TECHNICAL MEMORANDUM

X-321

PERFORMANCE, STABILITY, AND CONTROL CHARACTERISTICS AT TRANSONIC SPEEDS OF THREE V/STOL AIRPLANE CONFIGURATIONS WITH WINGS OF VARIABLE SWEEP

By Arvo A. Luoma and William J. Alford, Jr.

Langley Research Center
Langley Field, Va.

[redacted]

NATIONAL AERONAUTICS AND SPACE ADMINISTRATION
WASHINGTON
October 1960

[redacted]

NATIONAL AERONAUTICS AND SPACE ADMINISTRATION

TECHNICAL MEMORANDUM X-321

PERFORMANCE, STABILITY, AND CONTROL CHARACTERISTICS AT TRANSONIC SPEEDS OF THREE V/STOL AIRPLANE CONFIGURATIONS WITH WINGS OF VARIABLE SWEEP*

By Arvo A. Luoma and William J. Alford, Jr.

SUMMARY

29461

An investigation of the performance, longitudinal stability and control, and lateral stability of three V/STOL variable-wing-sweep airplane configurations with wing outboard panels swept 25°, 50°, and 75° was made in the Langley 8-foot transonic pressure tunnel. Data were obtained for an angle-of-attack range at Mach numbers from 0.60 to 1.30.

The general effects of wing sweep and Mach number on the aerodynamic characteristics of the three models investigated were similar and show the same trends as have been reported for other configurations employing a similar variable-sweep wing. The maximum lift-drag ratios are somewhat lower than those for contemporary configurations which do not have V/STOL capabilities. The aerodynamic-center shift for both wing sweep angle and Mach number is somewhat improved over that for previous configurations and amounts to approximately 13 percent of the mean aerodynamic chord for a change from 25° of sweep at a Mach number of 0.60 to 75° of sweep for Mach numbers near 2.0. For 25° of sweepback, the lowest sweep angle investigated, longitudinal instability occurs at moderate lift coefficients. Although the models were directionally stable for low and moderate angles of attack, they became unstable in the neighborhood of 10° to 12°.

Author

INTRODUCTION

The National Aeronautics and Space Administration has made extensive wind-tunnel studies to provide aerodynamic data for variable-wing-sweep airplane configurations suitable for multiple missions which would combine long-range subsonic flight for ferry (or loiter), efficient supersonic performance, and good landing and take-off characteristics. The

*Title, Unclassified.

[redacted]

results of these studies, in which a variable-sweep wing was developed which employed an outboard pivot to minimize the aerodynamic-center shift with wing-sweep changes, are presented in references 1 to 7. In order to add the capability of a rather long range of low-level supersonic flight, the wing-sweep range was increased to approximately 110° so that a large portion of the wing lay on the fuselage, and in order to assure low wave drag, the configurations were designed according to the area-rule concept of reference 8. The results of this study are presented in reference 9.

In order to provide airplanes with V/STOL capability, which enables them to operate from locations with limited ground facilities or from devastated areas, variable-sweep configurations have been designed around a proposed vectored lift-thrust engine. These engines have jet-exit nozzles which rotate through angles of approximately 120°, from straight back for forward flight to about 30° ahead of the vertical for low-speed operation.

The purpose of the present paper is to provide information on the performance, longitudinal stability and control, and lateral stability characteristics of three V/STOL variable-wing-sweep airplane configurations with wing outboard panels swept 25°, 50°, and 75°. Force and moment data were obtained for an angle-of-attack range at Mach numbers from 0.60 to 1.30. In order to expedite publication, the data are presented without analysis. The longitudinal characteristics of two of these configurations at a Mach number of 1.97 are presented in reference 10, and the longitudinal and lateral characteristics of the third configuration at a Mach number of 2.2 are presented in reference 11.

SYMBOLS

The lift and drag data are referred to the wind axes; the other force and moment data are referred to the body axes. The origin of the wind and body axes for the three models investigated herein is shown in figures 1 to 3. This location was on the body reference line and was positioned longitudinally to give a static margin of 5 percent mean aerodynamic chord at a Mach number of 0.60 for each of the models with the wings swept 25°. All the data presented herein were based on the planform dimensions of the wings with 75° of sweep. The symbols used are defined as follows:

A aspect ratio of wing, b^2/S

$A_{e,l}$ duct exit area (total) on body sides

$A_{e,2}$ duct exit area at end of body

A_p projected area (total) of duct inlet on plane perpendicular to reference line of body

b span of wing

C_D external drag coefficient, $\frac{\text{External drag}}{q_\infty S}$

$C_{D,i}$ internal drag coefficient,

$$\left[\frac{w_1}{q_\infty S}\left(V_\infty - V_{e,1}\cos\alpha\cos\theta\right) - C_{p,e,1}\frac{A_{e,1}}{S}\cos\alpha\cos\theta\right] + \left[\frac{w_2}{q_\infty S}\left(V_\infty - V_{e,2}\cos\alpha\right) - C_{p,e,2}\frac{A_{e,2}}{S}\cos\alpha\right]$$

$C_{D,o}$ zero-lift external drag coefficient

C_L lift coefficient, $\frac{\text{Lift}}{q_\infty S}$

C_Y lateral-force coefficient, $\frac{\text{Lateral force}}{q_\infty S}$

C_l rolling-moment coefficient, $\frac{\text{Rolling moment}}{q_\infty S b}$

C_m pitching-moment coefficient, $\frac{\text{Pitching moment}}{q_\infty S \bar{c}}$

C_n yawing-moment coefficient, $\frac{\text{Yawing moment}}{q_\infty S b}$

$C_{p,e,1}$ pressure coefficient of flow in duct at duct exit on body sides

$C_{p,e,2}$ pressure coefficient of flow in duct at duct exit at end of body

$\bar{c}$ mean aerodynamic chord of wing

L/D lift-drag ratio, C_L/C_D

$(L/D)_{max}$ maximum value of lift-drag ratio

M Mach number of undisturbed stream

q_∞ dynamic pressure of undisturbed stream, $\frac{1}{2}\rho_\infty V_\infty^2$

R Reynolds number, based on $\bar{c}$

S	wing area
$V_{e,1}$	velocity of flow in duct at duct exit on body sides
$V_{e,2}$	velocity of flow in duct at duct exit at end of body
V_∞	velocity of undisturbed stream
w	total mass flow in duct, $w_1 + w_2$
w_1	mass flow in duct at duct exit on body sides
w_2	mass flow in duct at duct exit at end of body
w/w_∞	mass-flow ratio based on projected area of inlet, $w/\rho_\infty V_\infty A_p$
α	angle of attack of model, based on reference line of body
β	angle of sideslip of model
δ_h	horizontal-tail deflection, positive direction when trailing edge is down
Λ	sweep angle of wing, based on sweep of leading edge of outer panel
θ	angle between plane of duct exit on body sides and lateral axis (see fig. 3)
ρ_∞	mass density of undisturbed stream

$C_{L_\alpha} = \frac{dC_L}{d\alpha}$ per deg

$C_{m_{C_L}} = \frac{dC_m}{dC_L}$

$C_{m_{\delta_h}} = \frac{dC_m}{d\delta_h}$ per deg

$C_{n_\beta} = \frac{dC_n}{d\beta}$ per deg

$C_{l_\beta} = \frac{dC_l}{d\beta}$ per deg

$C_{Y_\beta} = \frac{dC_Y}{d\beta}$ per deg

Components of models:

B	body (including canopy and air inlets)
H	horizontal tail
V	vertical tail
W_1	wing for which $\Lambda = 25^\circ$
W_2	wing for which $\Lambda = 51.3^\circ$ (models I and II) or $\Lambda = 50^\circ$ (model III)
W_3	wing for which $\Lambda = 75^\circ$

APPARATUS AND METHODS

Tunnel

The investigation was made in the Langley 8-foot transonic pressure tunnel. This tunnel can be operated over a range of total pressures.

Models

The models tested in the present investigation are identified herein as models I, II, and III. Three-view drawings of the models are shown in figures 1 to 3, and photographs of the models are shown as figures 4 to 6. Some of the geometric characteristics of the models are presented in table I. Models I and II were 1/10 scale and model III was 1/20 scale.

All three models were designed for internal flow. Model I, which had four duct exits with two located on each side of the body (fig. 4(b)), represents a four-point vectored-thrust V/STOL arrangement. The presumed advantage of this type of configuration is good longitudinal and lateral stability at low forward speeds due to the symmetrical nozzle arrangement

with respect to the airplane center of gravity. The disadvantages of such a configuration are the large wetted area associated with the large inlets, necessary for low-speed flight, and the difficulty in obtaining a refined area distribution. It is estimated that supersonic speeds in the neighborhood of $M = 1.8$ should be obtainable with this type of configuration. Model II (fig. 5(b)) represents a three-point vectored-thrust V/STOL arrangement. The forward part of this configuration from the nose to the first set of nozzles is identical to model I. The third rotatable nozzle (not represented on the model) would be located on the fuselage center line just ahead of the space provided for the afterburner section. The advantages of this configuration are the cleaner aerodynamic design and higher supersonic speed potential, estimated to be approximately $M = 2.2$, due to the addition of the afterburner. Model III (fig. 6(b)) represents an STOL design with two rotatable nozzles near the center of gravity to minimize stability problems in the low-speed mode. The nose section is considerably longer than that of models I and II and, therefore, closer to the optimum fineness ratio. In addition, a better area distribution was obtained (fig. 7) and it is estimated that it should be capable of operation near a Mach number of 2.5.

Three wings of identical plan form and with sweep angles of the outboard panels varying from 25° to 75° were tested on each model. The pivot point about which the outer panel of the wing was swept was located laterally at 51.1 percent of the semispan of the 75° swept wing. The inboard (fixed) panel of the wings had a leading-edge sweep of 60°. The airfoil sections (parallel to the root chord) were NACA 65A004.5 for the inboard panel and NACA 65A006 for the outboard panel at $\Lambda = 25^\circ$. The wings had 0° dihedral and incidence and were positioned 2.90 inches above the body reference line for models I and II and 1.40 inches for model III.

The leading-edge sweep of the horizontal and vertical tails was 45° for model I and 60° for models II and III. The dihedral of the horizontal tail was 0° for model I and -15° for models II and III. The horizontal tails were of the all-movable type.

The longitudinal distribution of cross-sectional area of the three models is shown in figure 7. The cross-sectional area has been reduced by 80 percent of the inlet projected area A_p to account for internal flow.

Instrumentation

An internally housed six-component strain-gage balance was used for determining the overall forces and moments on the models. A strain-gage

attitude transmitter used for getting the no-load angle of attack of the model was housed in the extension of the model sting.

A static-pressure orifice located within the chamber surrounding the strain-gage balance was connected to a pressure transducer. Two rakes of total-pressure tubes were used at the duct exits when mass-flow and internal-drag measurements were made. Static-pressure tubes were located on the duct wall at the duct exit.

The overall forces and moments on the model, the angle of attack, and the static pressure in the chamber surrounding the strain-gage balance were recorded electronically on punch cards for all configurations. During the mass-flow runs, the rake total pressures and the duct-exit static pressures were measured by use of a multiple-tube manometer containing tetrabromoethane. All manometer tubes were photographed simultaneously.

TESTS, CORRECTIONS, AND ACCURACY

Tests

All the tests were made with transition fixed by narrow strips of No. 80 carborundum grains shellacked to the wing and tail surfaces at 10 percent of the chord (streamwise) and to the body at 10 percent of the length.

The effect of wing sweep, horizontal-tail deflection, and model components on the aerodynamic forces and moments was determined. Most of the tests were made at an angle of sideslip of 0°. The configuration with the 75° swept wing (BW_3VH at $\delta_h = 0^\circ$ for models I, II, and III) and the configuration with the 25° swept wing (BW_1VH at $\delta_h = 0^\circ$ for model III) were also investigated at an angle of sideslip of 5°.

All the configurations were investigated for an angle-of-attack range at five Mach numbers from 0.60 to 1.20. The configurations with the 50° (or 51.3°) and 75° swept wings were also tested at a Mach number of 1.3 at zero sideslip. The zero-lift drag of some of the configurations was obtained also at several intermediate Mach numbers. The total pressure at which models I and II were investigated was 800 lb/sq ft for Mach numbers from 0.60 to 0.90 and 600 lb/sq ft for Mach numbers from 0.95 to 1.30. The total pressure at which model III was investigated was 1,350 lb/sq ft for Mach numbers from 0.60 to 0.90 and 1,000 lb/sq ft for Mach numbers from 0.95 to 1.30. Some zero-lift drag data were also obtained at a total pressure of 2,120 lb/sq ft for several of the configurations of Model III. The Reynolds number range of the investigation is shown in figure 8.

All the configurations were investigated with internal flow in the models. The mass flow and internal drag of the configuration with the 75° swept wing (BW_3VH at $\delta_h = 0°$) for each of the three models was measured. Internal-flow data were obtained for the angle-of-attack range at Mach numbers from 0.60 to 1.30.

Corrections

The external-drag coefficient C_D was corrected by adjusting the static pressure in the balance chamber and at the body base to the free-stream value. The external-drag coefficient also includes the correction for the internal-drag coefficient $C_{D,i}$. The internal-drag coefficient measured for configuration BW_3VH ($\delta_h = 0°$) for a given model was used in correcting all the configurations of that model.

Data presented herein at supersonic Mach numbers consist of zero-lift drag data at Mach numbers of 1.01, 1.02, and 1.03 and of force and moment data taken for the angle-of-attack range at Mach numbers of 1.2 and 1.3. At Mach numbers of 1.01 to 1.03 for all three models and at a Mach number of 1.2 for models I and II the flow over the models was subject to influence by wall-reflected disturbances. Model III was clear of wall-reflected disturbances at a Mach number of 1.2 and all three models were clear of wall-reflected disturbances at a Mach number of 1.3. Wall-reflected disturbances usually increase the drag at Mach numbers near 1.03 and reduce the drag at Mach numbers near 1.2. The variation of pitching moment with angle of attack at a Mach number of 1.2 shows some irregularities and slope changes for model I which are at variance to those shown by the remainder of the data and which presumably are caused by wall-reflected disturbances. Plots shown herein of faired performance and stability parameters against Mach number are believed to indicate the general trends at those Mach numbers where wall-reflected disturbances are present. No corrections have been made to the data for wall-reflected disturbances except to the extent of the partial correction for wall-reflected disturbances inherent in the base-pressure correction.

A buoyancy correction was made at a Mach number of 1.3. This correction consisted of reducing the measured drag coefficients at a Mach number of 1.3 by 0.0039 for model I, 0.0040 for model II, and 0.0014 for model III. At the other Mach numbers no buoyancy correction was required.

No sting interference corrections have been made to the data except to the extent of the partial correction for sting interference inherent in the base-pressure correction.

Accuracy

The estimated accuracy of the data based primarily on the static calibrations and the repeatability of the data was as follows:

C_L	±0.01
C_D	±0.001
C_m	±0.002
C_n	±0.0003
C_l	±0.001
C_Y	±0.006
α, deg	±0.1
β, deg	±0.1
M	±0.003

PRESENTATION OF RESULTS

The basic data are presented in figures 9 to 22. Figures 9 to 21 consist of plots of lift coefficient against angle of attack, drag coefficient against lift coefficient, pitching-moment coefficient against angle of attack and lift coefficient, and lift-drag ratio against lift coefficient. Figure 22 is a plot of internal drag coefficient and mass-flow ratio against angle of attack and Mach number. An index of these figures is given in the following outline:

	Figure
Model I:	
Effect of horizontal-tail deflection for -	
Configuration BW_1VH ($\Lambda = 25^\circ$)	9
Configuration BW_3VH ($\Lambda = 75^\circ$)	10
Effect of wing sweep for -	
Configuration BWVH; $\delta_h = 0^\circ$	11
Configuration BWV (horizontal tail off)	12
Model II:	
Effect of horizontal-tail deflection for -	
Configuration BW_1VH ($\Lambda = 25^\circ$)	13
Configuration BW_3VH ($\Lambda = 75^\circ$)	14
Effect of wing sweep for -	
Configuration BWVH; $\delta_h = -0.2^\circ$	15
Configuration BWV (horizontal tail off)	16

[redacted]

	Figure
Model III:	
Effect of horizontal-tail deflection for -	
Configuration BW_1VH ($\Lambda = 25^\circ$)	17
Configuration BW_3VH ($\Lambda = 75^\circ$)	18
Effect of wing sweep for -	
Configuration BWVH; $\delta_h = 0^\circ$	19
Configuration BW (horizontal and vertical tails off)	20
Body alone characteristics	21
Models I, II, and III:	
Internal drag and mass flow for configuration BW_3VH ($\Lambda = 75^\circ$); $\delta_h = 0^\circ$	22

Summary data on performance, stability, and control are presented in figures 23 to 33. The summary figures on performance and longitudinal stability and control (figs. 23 to 30) are plotted against Mach number. The summary figures on lateral stability (figs. 31 and 32) are plotted against angle of attack and Mach number. A direct comparison of the performance and longitudinal stability of models I, II, and III is given in figure 33. An index of these figures is given in the following outline:

	Figure
Effect of wing sweep on zero-lift drag:	
Configuration BWVH; $\delta_h = 0^\circ$	23
Configurations BWV and BW; $\delta_h = 0^\circ$	24
Zero-lift drag of body alone (model III)	25
Effect of wing sweep on lift-curve slope for configuration BWVH; $\delta_h = 0^\circ$	26
Effect of wing sweep on maximum lift-drag ratio for configuration BWVH; $\delta_h = 0^\circ$	27
Effect of wing sweep on static longitudinal stability derivative for configuration BWVH; $\delta_h = 0^\circ$	28
Variation of static longitudinal stability derivative with angle of sweep for configuration BWVH; $\delta_h = 0^\circ$	29
Effect of wing sweep on horizontal-tail effectiveness for configuration BWVH; $\alpha = 0^\circ$	30
Lateral-stability derivatives:	
Configuration BW_3VH ($\Lambda = 75^\circ$); $\delta_h = 0^\circ$	31
Configurations BW_1VH ($\Lambda = 25^\circ$) and BW_3VH ($\Lambda = 75^\circ$) with $\delta_h = 0^\circ$ of model III	32
Comparison of longitudinal characteristics of models I, II, and III for configuration BW_3VH ($\Lambda = 75^\circ$); $\delta_h = 0^\circ$	33

SUMMARY OF RESULTS

In general, the effects of variation in wing sweep angle and Mach number on the aerodynamic characteristics of the three models investigated were similar and show the same trends as have been reported for other configurations employing a similar variable-sweep wing. (See refs. 1 to 7.) The maximum lift-drag ratios are somewhat lower than those for contemporary configurations which do not have V/STOL capability because of the large fuselage drag resulting from the large cross-sectional and wetted areas associated with the engine inlets required for low-speed operation in the V/STOL modes. At transonic speeds, although there are sizeable reductions in zero-lift drag with increases in wing sweep angles from 25° to 75°, improvements in maximum lift-drag ratio are not realized due to the increase in drag due to lift accompanying wing-sweep increases. Increasing the wing sweep angle produced large reductions in the lift-curve slope which would be beneficial from a gust acceleration standpoint for high-speed low-level flight.

The aerodynamic-center travel with both wing sweep angle and Mach number is somewhat improved over that for previous configurations and amounts to approximately 13 percent of the mean aerodynamic chord accompanying a change from $\Lambda = 25^\circ$ at $M = 0.60$ to $\Lambda = 75^\circ$ for Mach numbers near 2.0. For the lowest sweep angle investigated, $\Lambda = 25^\circ$, longitudinal instability occurs at moderate lift coefficients. Although the models were directionally stable for low and moderate angles of attack, they generally became unstable in the neighborhood of 10° to 12°.

Langley Research Center,
National Aeronautics and Space Administration,
Langley Field, Va., June 9, 1960.

[redacted]

REFERENCES

1. Alford, William J., Jr., and Henderson, William P.: An Exploratory Investigation of the Low-Speed Aerodynamic Characteristics of Variable-Wing-Sweep Airplane Configurations. NASA TM X-142, 1959.

2. Alford, William J., Jr., Luoma, Arvo A., and Henderson, William P.: Wind-Tunnel Studies at Subsonic and Transonic Speeds of a Multiple-Mission Variable-Wing-Sweep Airplane Configuration. NASA TM X-206, 1959.

3. Spearman, M. Leroy, and Foster, Gerald V.: Stability and Control Characteristics at a Mach Number of 2.01 of a Variable-Wing-Sweep Configuration With Outboard Wing Panels Swept Back 75°. NASA TM X-32, 1959.

4. Spearman, M. Leroy, and Foster, Gerald V.: Effects of Various Modifications on the Supersonic Stability Characteristics of a Variable-Wing-Sweep Configuration at a Mach Number of 2.01. NASA TM X-260, 1960.

5. Foster, Gerald V.: Stability and Control Characteristics at Mach Numbers of 2.50, 3.00, and 3.71 of a Variable-Wing-Sweep Configuration With Outboard Wing Panels Swept Back 75°. NASA TM X-267, 1960.

6. Foster, Gerald V.: Effects of Spoiler-Slot-Deflector Control on the Aerodynamic Characteristics at a Mach Number of 2.01 of a Variable-Wing-Sweep Configuration With the Outer Wing Panels Swept Back 75°. NASA TM X-273, 1960.

7. Spencer, Bernard, Jr.: Stability and Control Characteristics at Low Subsonic Speeds of an Airplane Configuration Having Two Types of Variable-Sweep Wings. NASA TM X-303, 1960.

8. Whitcomb, Richard T.: A Study of the Zero-Lift Drag-Rise Characteristics of Wing-Body Combinations Near the Speed of Sound. NACA Rep. 1273, 1956. (Supersedes NACA RM L52H08.)

9. Bielat, Ralph P., Robins, A. Warner, and Alford, William J., Jr.: The Transonic Aerodynamic Characteristics of Two Variable-Sweep Airplane Configurations Capable of Low-Level Supersonic Attack. NASA TM X-304, 1960.

10. Foster, Gerald V., and Morris, Odell A.: Aerodynamic Characteristics in Pitch at a Mach Number of 1.97 of Two Variable-Wing-Sweep V/STOL Configurations With Outboard Wing Panels Swept Back 75°. NASA TM X-322, 1960.

[redacted]

11. Foster, Gerald V., and Morris, Odell A.: Static Longitudinal and Lateral Aerodynamic Characteristics at a Mach Number of 2.20 of a Variable-Wing-Sweep STOL Configuration. NASA TM X-329, 1960.

TABLE I.- GEOMETRIC CHARACTERISTICS OF MODELS

Model I:	
Wing with $\Lambda = 25^{\circ}$ -	
Area, S, sq ft	2.7295
Span, b, in.	44.98
Mean aerodynamic chord, $\bar{c}$, in.	12.39
Aspect ratio, A	5.148
Wing with $\Lambda = 51.3^{\circ}$ -	
Area, S, sq ft	2.608
Span, b, in.	37.32
Mean aerodynamic chord, $\bar{c}$, in.	13.16
Aspect ratio, A	3.70
Wing with $\Lambda = 75^{\circ}$ -	
Area, S, sq ft	2.4991
Span, b, in.	26.112
Mean aerodynamic chord, $\bar{c}$, in.	15.6335
Aspect ratio, A	1.894
Duct -	
Projected inlet area, A_p, sq ft	0.1100
Exit area -	
On body sides, $A_{e,1}$, sq ft	0.0978
At body base, $A_{e,2}$, sq ft	0.0
Total, sq ft	0.0978
Duct exit angle, θ, deg	27.5
Model II:	
Wing with $\Lambda = 25^{\circ}$ -	
Area, S, sq ft	2.7295
Span, b, in.	44.98
Mean aerodynamic chord, $\bar{c}$, in.	12.39
Aspect ratio, A	5.148
Wing with $\Lambda = 51.3^{\circ}$ -	
Area, S, sq ft	2.608
Span, b, in.	37.32
Mean aerodynamic chord, $\bar{c}$, in.	13.16
Aspect ratio, A	3.70
Wing with $\Lambda = 75^{\circ}$ -	
Area, S, sq ft	2.4991
Span, b, in.	26.112
Mean aerodynamic chord, $\bar{c}$, in.	15.6335
Aspect ratio, A	1.894
Duct -	
Projected inlet area, A_p, sq ft	0.1100
Exit area -	
On body sides, $A_{e,1}$, sq ft	0.0458
At body base, $A_{e,2}$, sq ft	0.0464
Total, sq ft	0.0922
Duct exit angle, θ, deg	27.5
Model III:	
Wing with $\Lambda = 25^{\circ}$ -	
Area, S, sq ft	0.682
Span, b, in.	22.70
Mean aerodynamic chord, $\bar{c}$, in.	6.195
Aspect ratio, A	5.148
Wing with $\Lambda = 50^{\circ}$ -	
Area, S, sq ft	0.654
Span, b, in.	18.94
Mean aerodynamic chord, $\bar{c}$, in.	6.508
Aspect ratio, A	3.81
Wing with $\Lambda = 75^{\circ}$ -	
Area, S, sq ft	0.625
Span, b, in.	13.056
Mean aerodynamic chord, $\bar{c}$, in.	7.817
Aspect ratio, A	1.894
Duct -	
Projected inlet area, A_p, sq ft	0.0275
Exit area -	
On body sides, $A_{e,1}$, sq ft	0.0133
At body base, $A_{e,2}$, sq ft	0.0133
Total, sq ft	0.0266
Duct exit angle, θ, deg	27.5

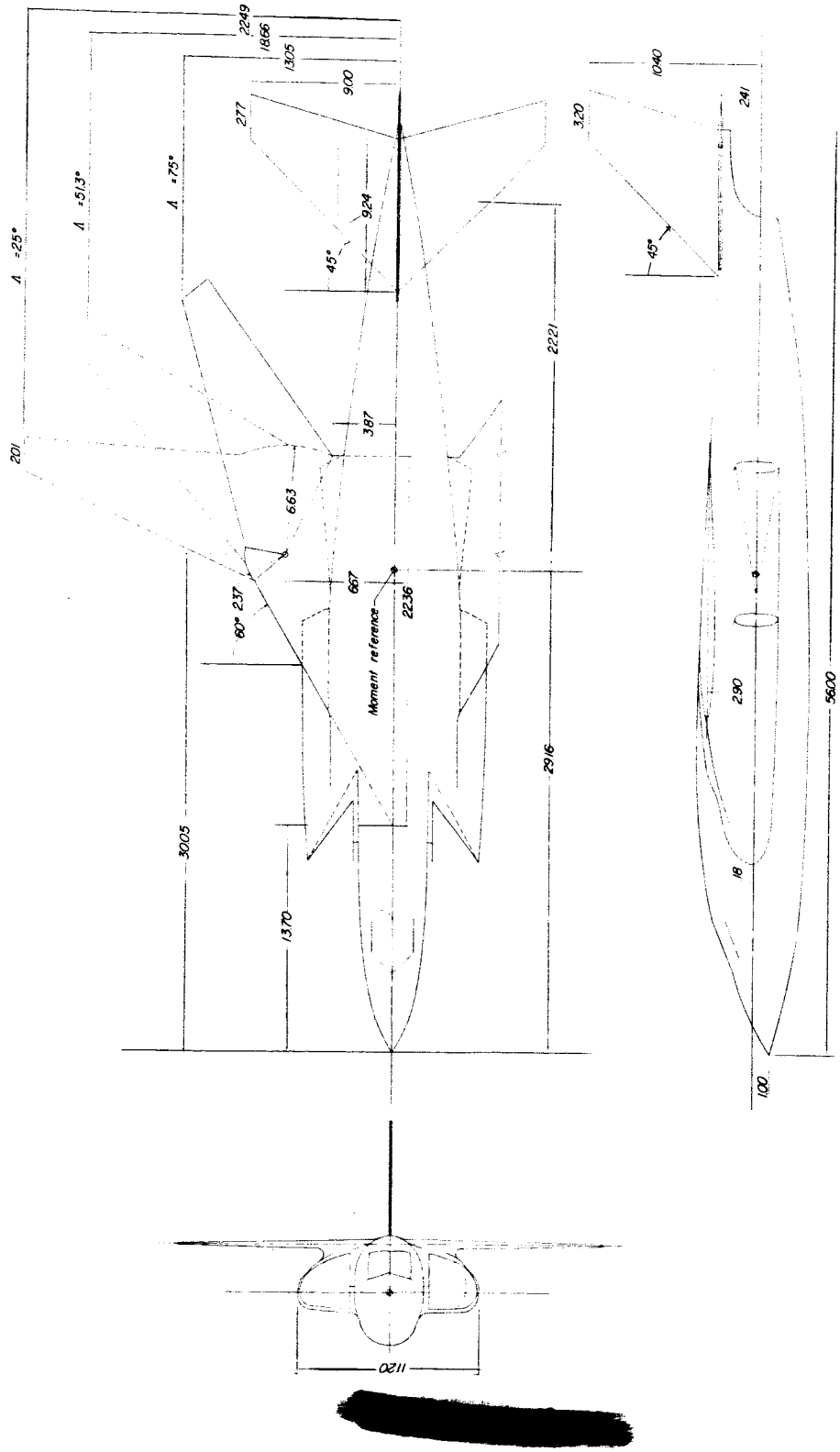

Figure 1.- Drawing of model I. All dimensions in inches unless otherwise noted.

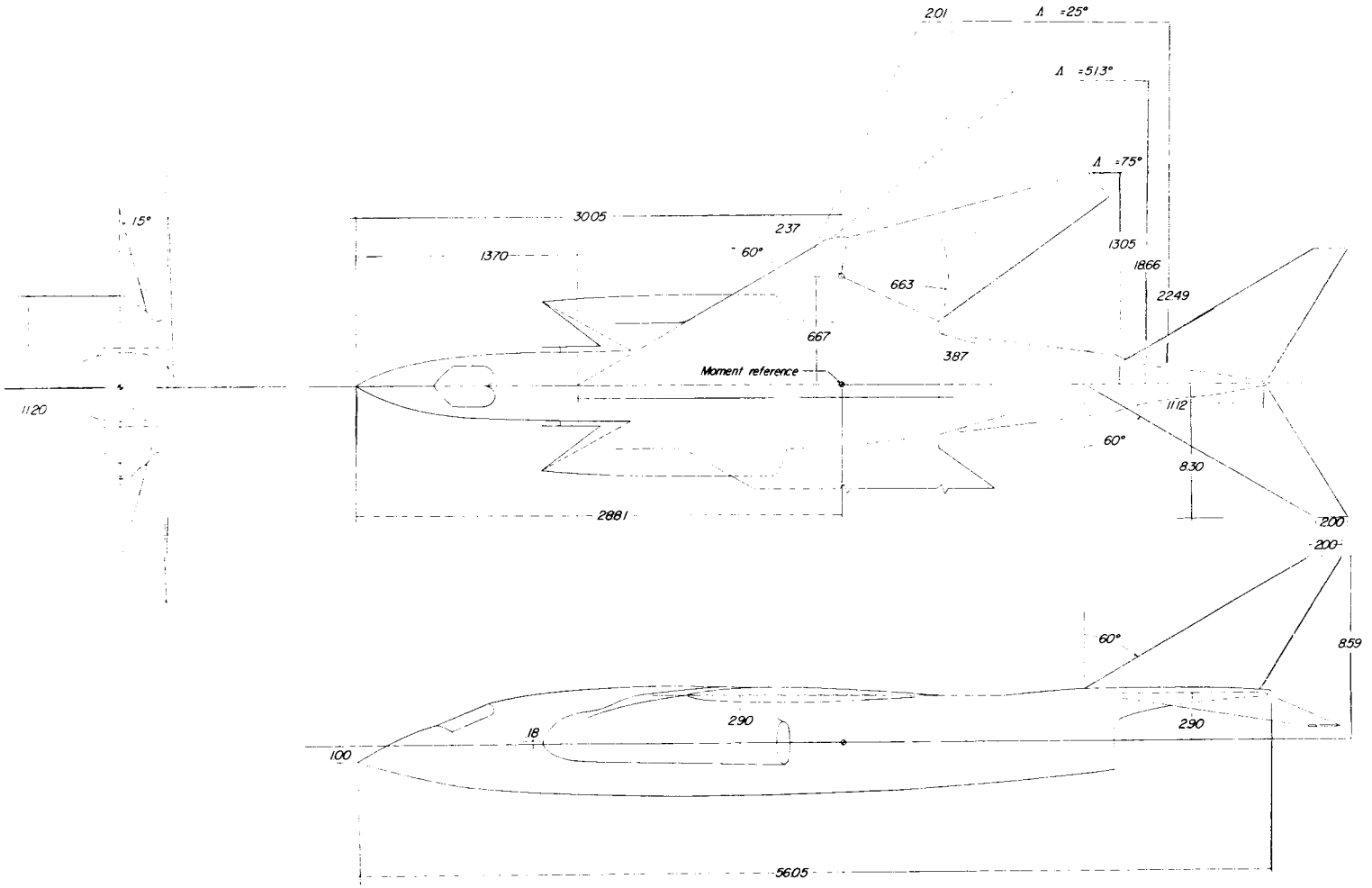

Figure 2.- Drawing of model II. All dimensions in inches unless otherwise noted.

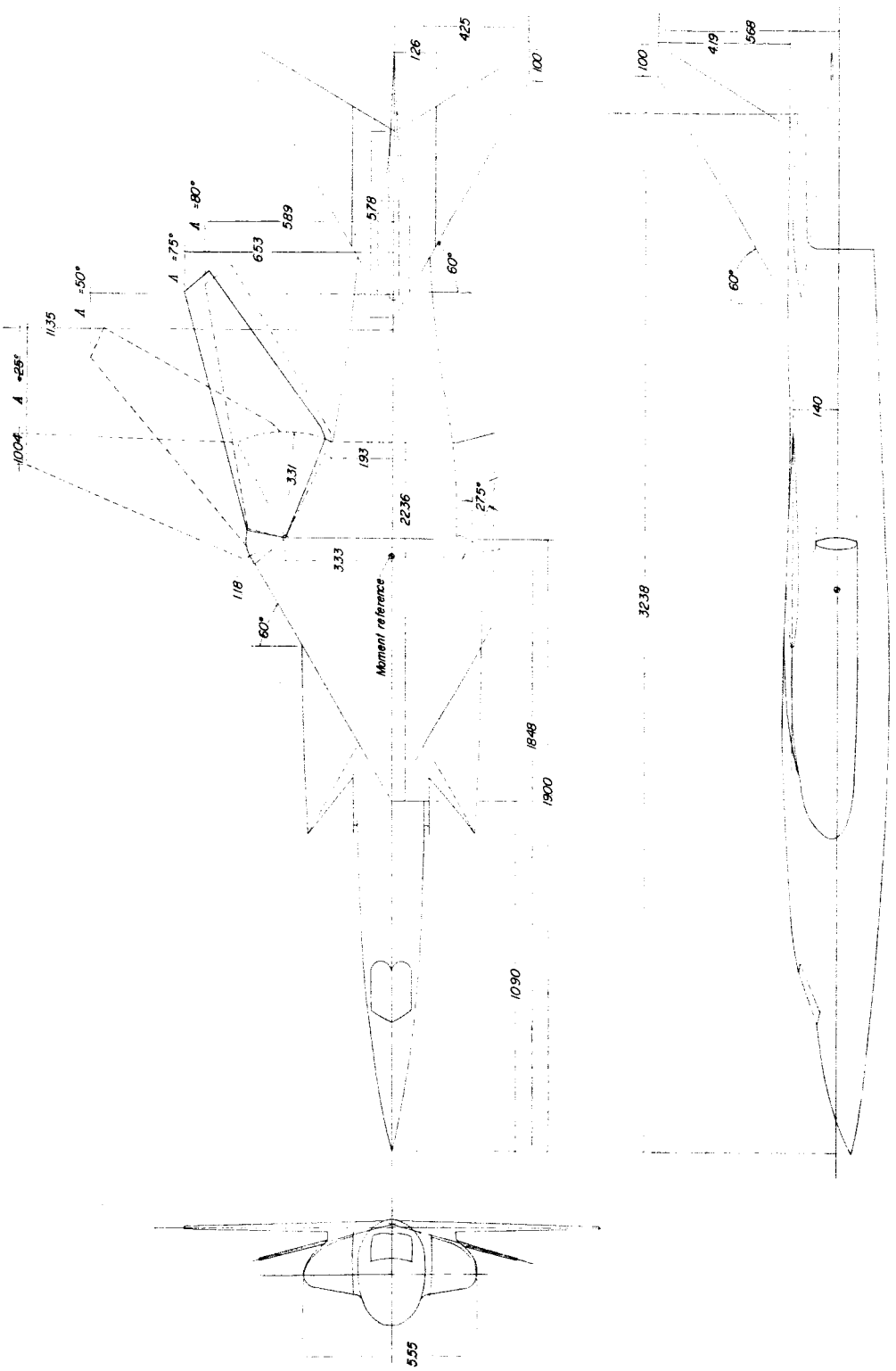

Figure 3.- Drawing of model III. All dimensions in inches unless otherwise noted.

[redacted]

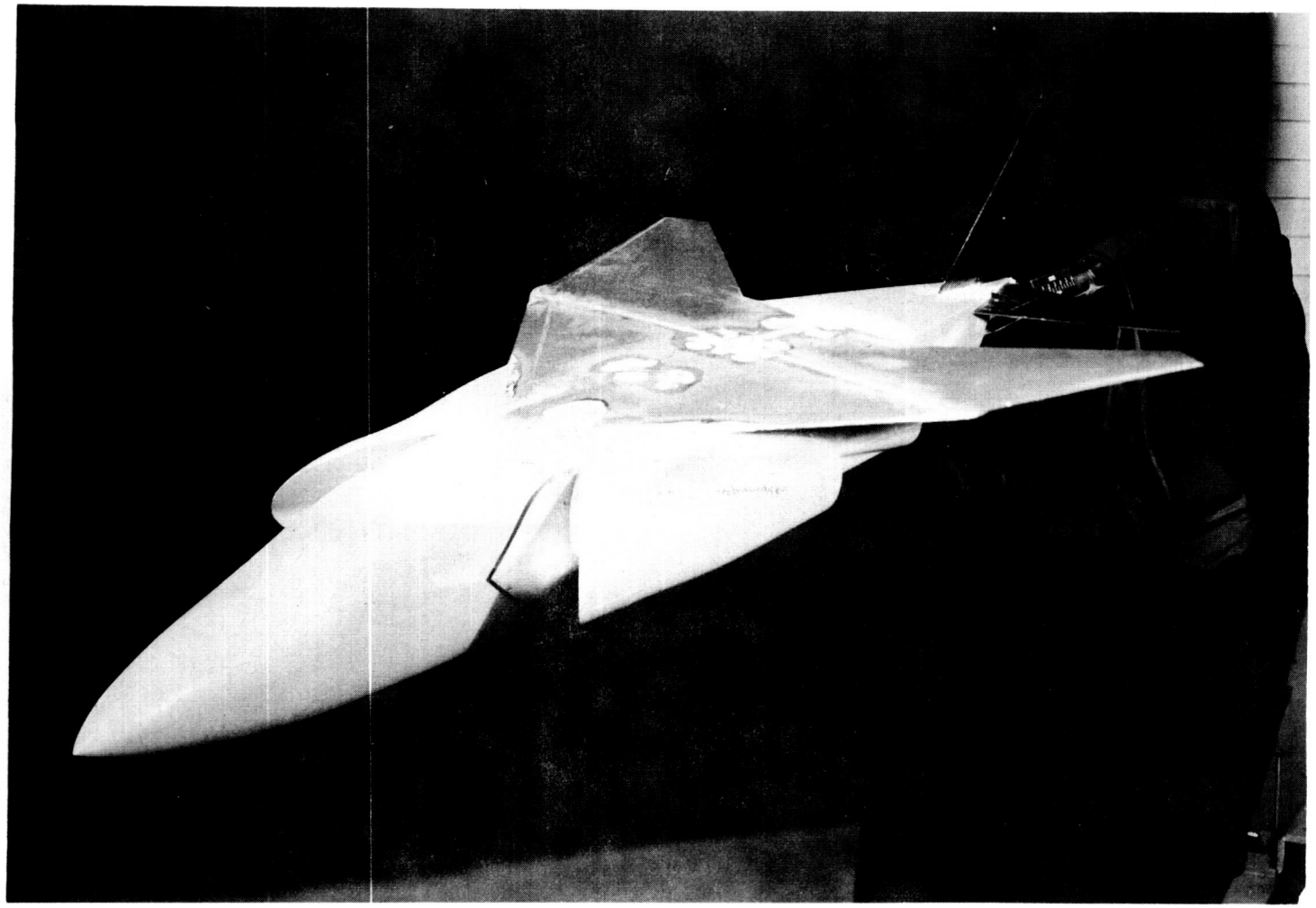

(a) Three-quarter front view. L-60-2984

Figure 4.- Photographs of model I. Configuration BW_3VH ($\Lambda = 75^\circ$).

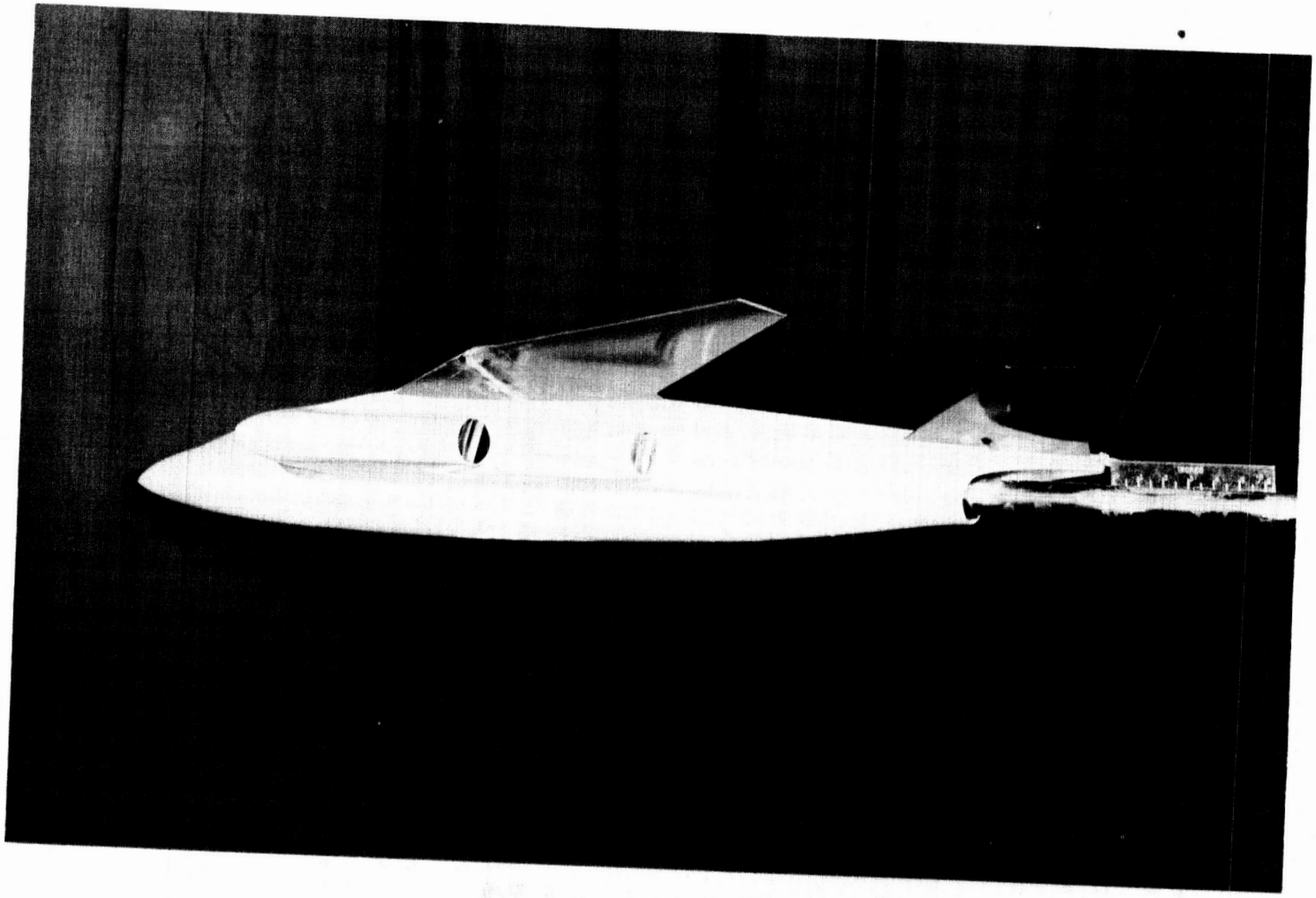

(b) Three-quarter rear view. L-60-2985

Figure 4.- Concluded.

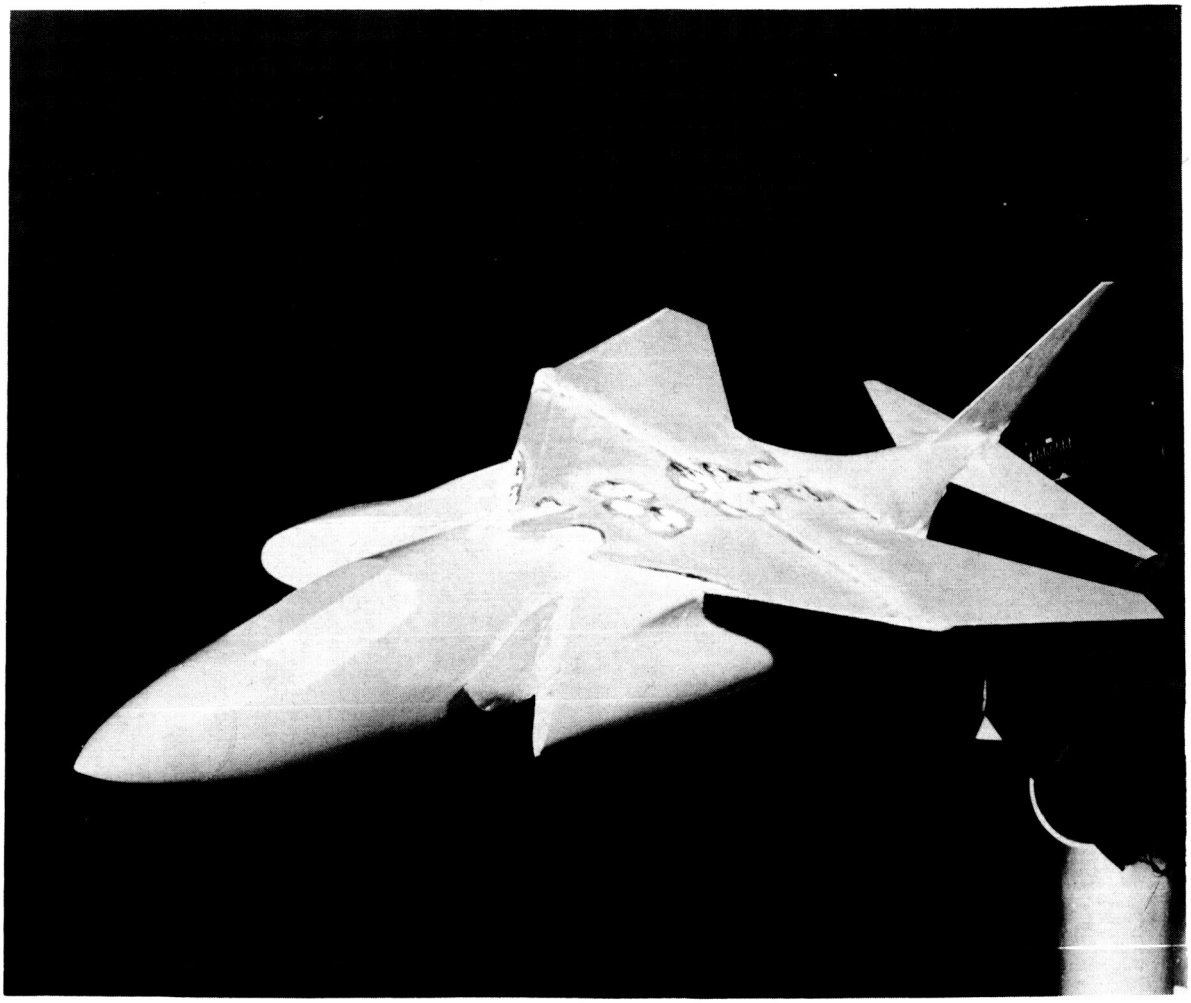

(a) Three-quarter front view. L-60-2987

Figure 5.- Photographs of model II. Configuration BW_3VH ($\Lambda = 75^{\circ}$).

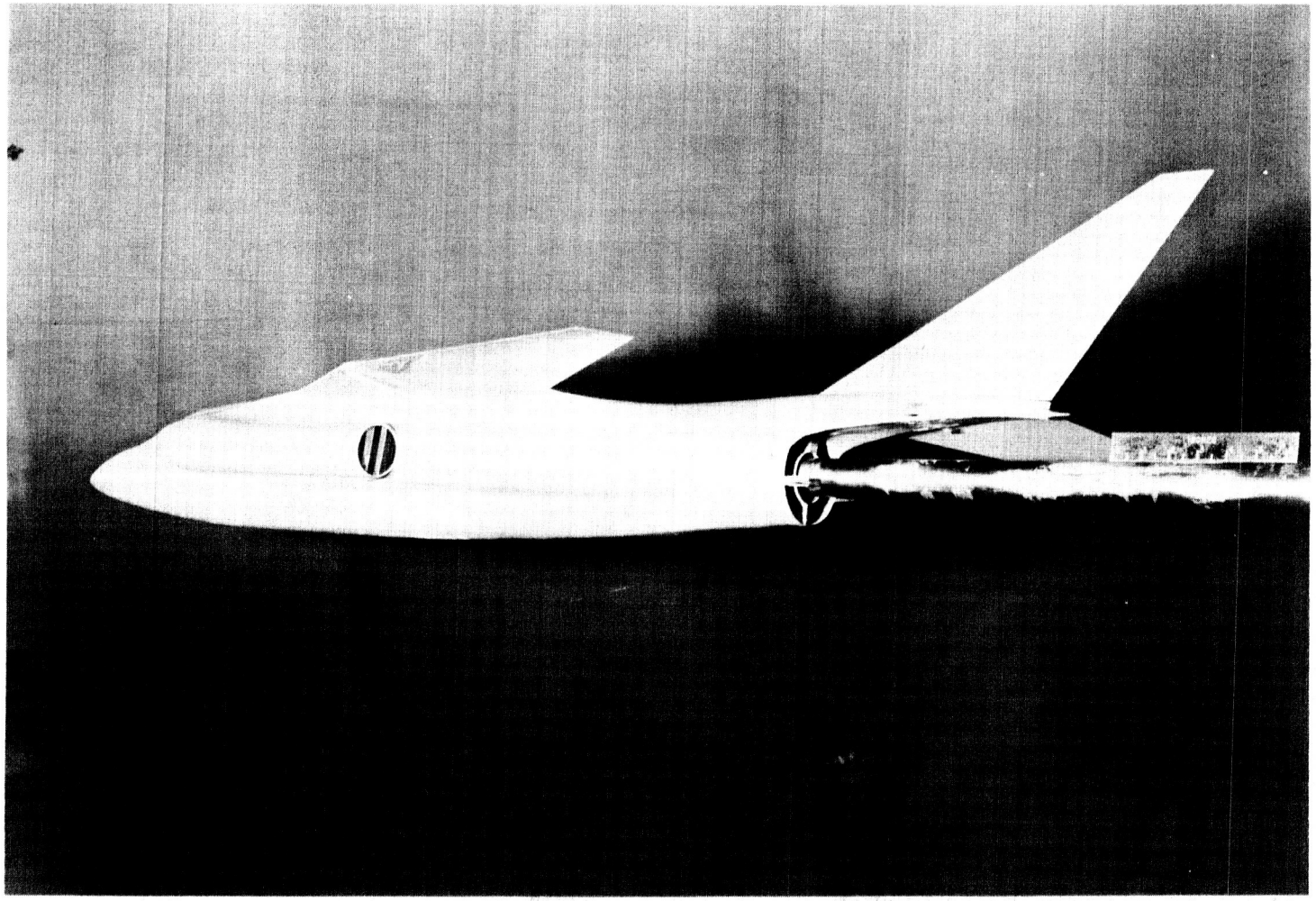

(b) Three-quarter rear view. L-60-2988

Figure 5.- Concluded.

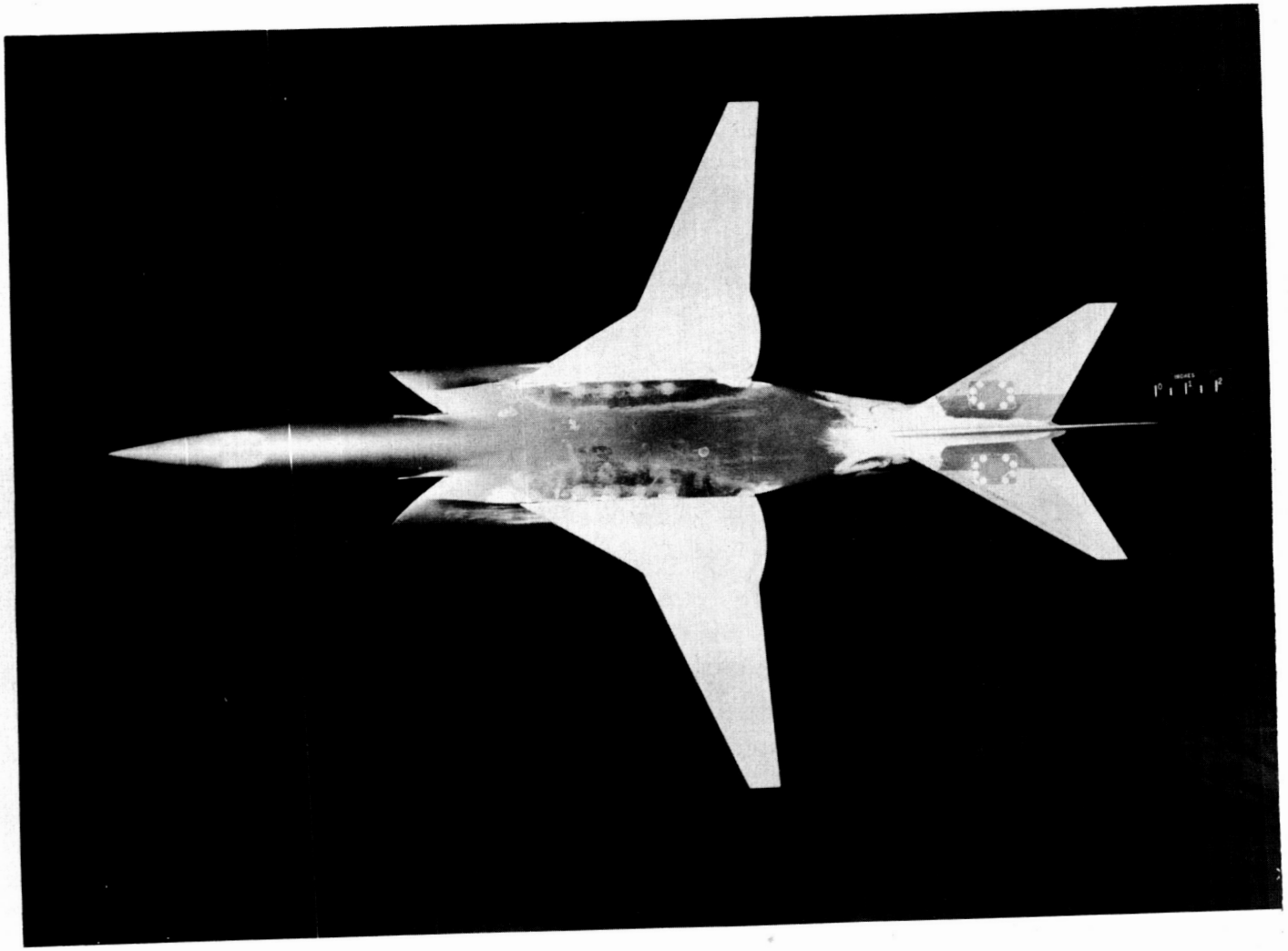

(a) Plan view of BW_1VH ($\Lambda = 25^{\circ}$). L-60-3113

Figure 6.- Photographs of model III.

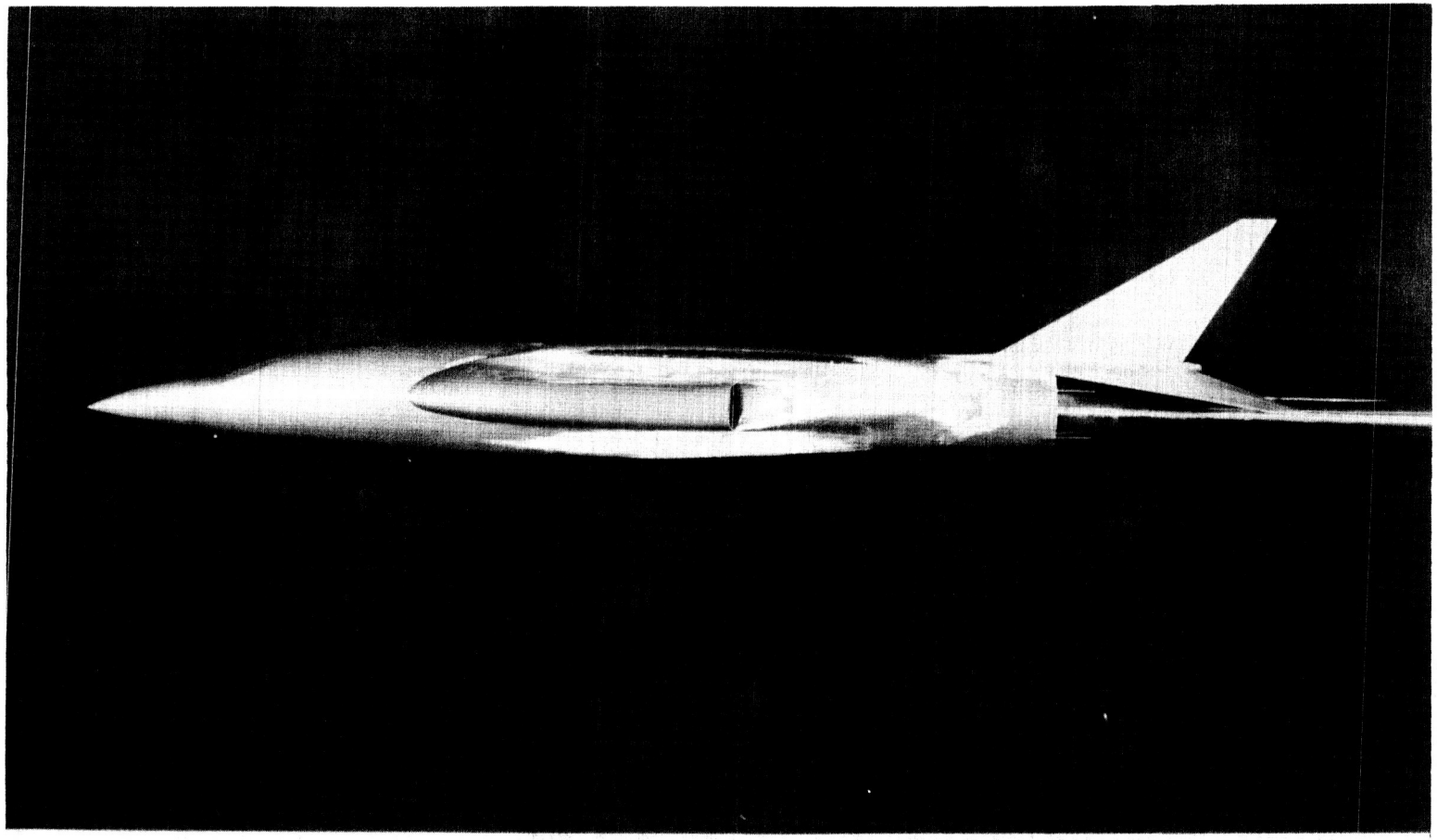

(b) Side view of BW_1VH ($\Lambda = 25^\circ$). L-60-3082

Figure 6.- Continued.

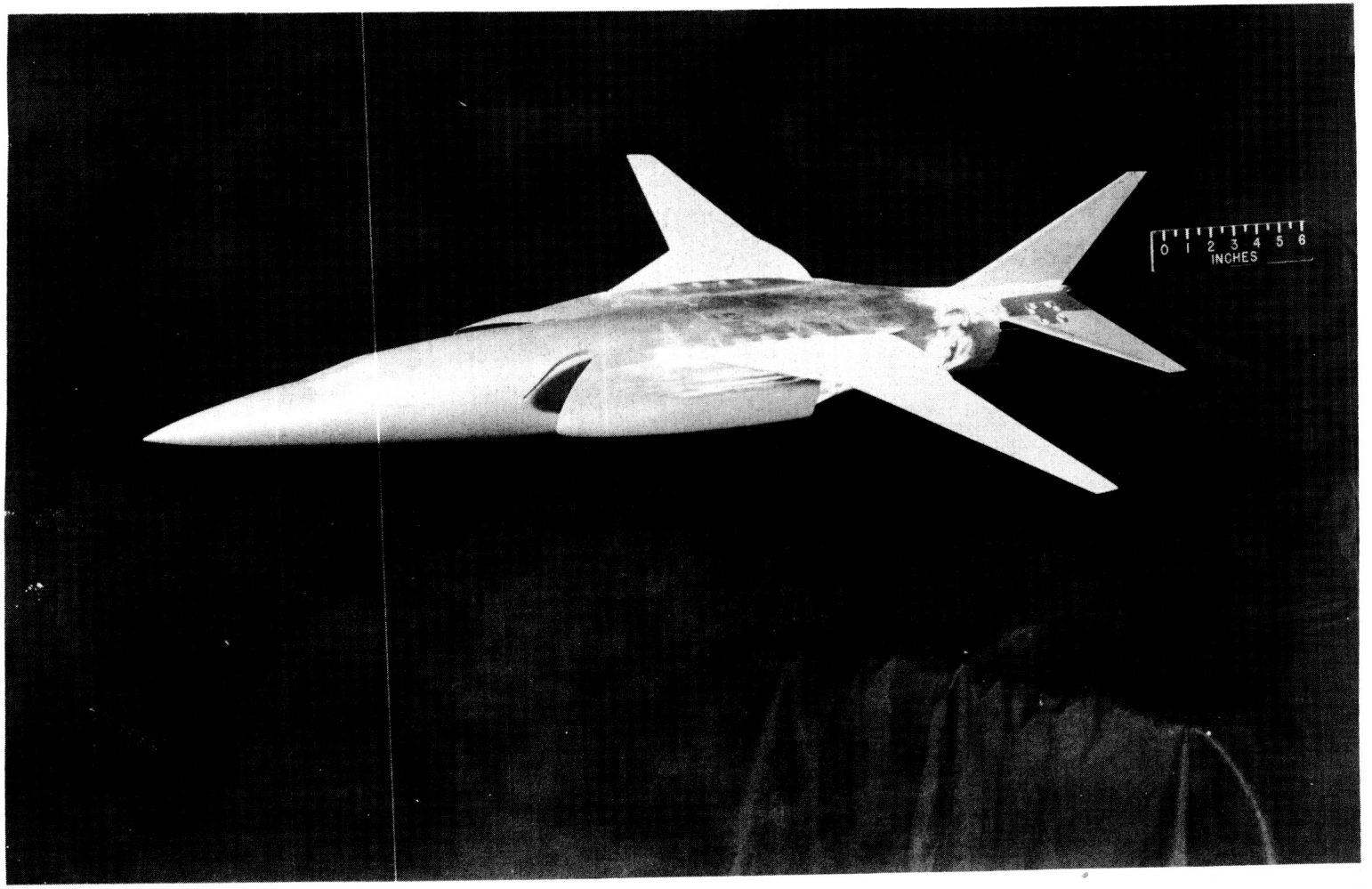

(c) Three-quarter front view of BW_1VH ($\Lambda = 25^\circ$). L-60-3114

Figure 6.- Continued.

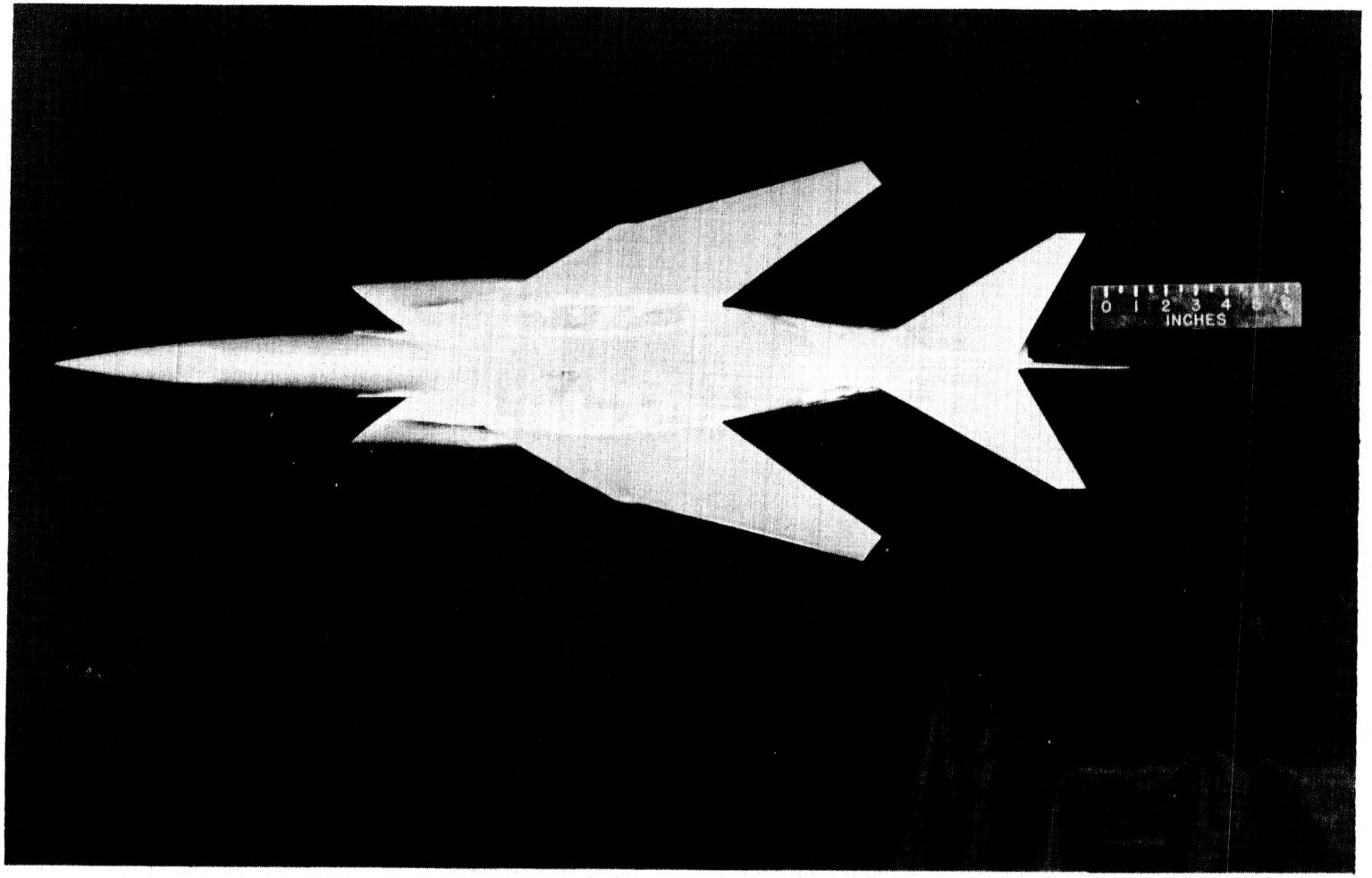

(d) Plan view of BW_3VH ($\Lambda = 75^\circ$). L-60-3115

Figure 6.- Continued.

(e) Three-quarter front view of BW_3VH ($\Lambda = 75^\circ$). L-60-3116

Figure 6.- Concluded.

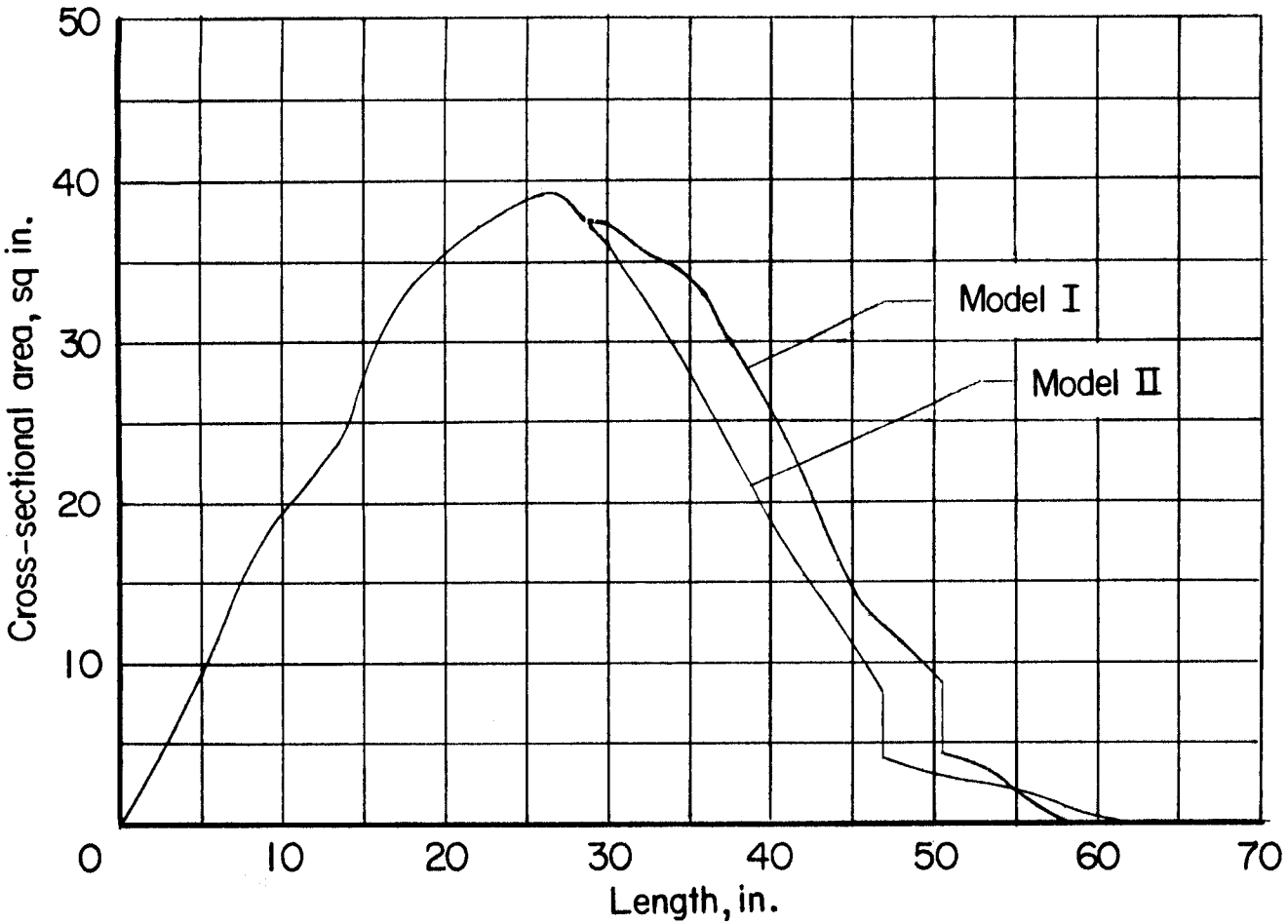

(a) Models I and II.

Figure 7.- Longitudinal distribution of normal cross-sectional area of models. Configuration BW_3VH.

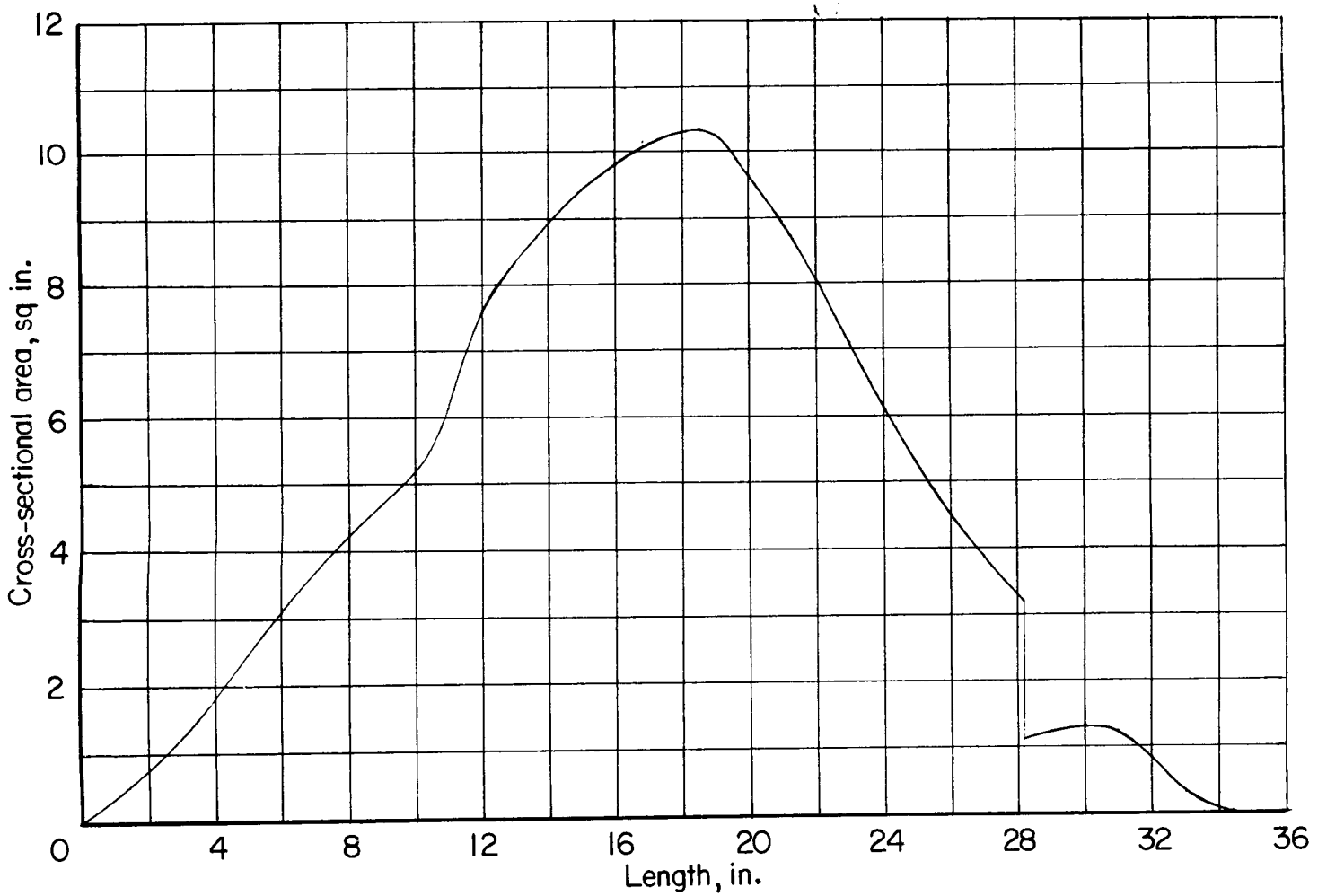

(b) Model III.

Figure 7.- Concluded.

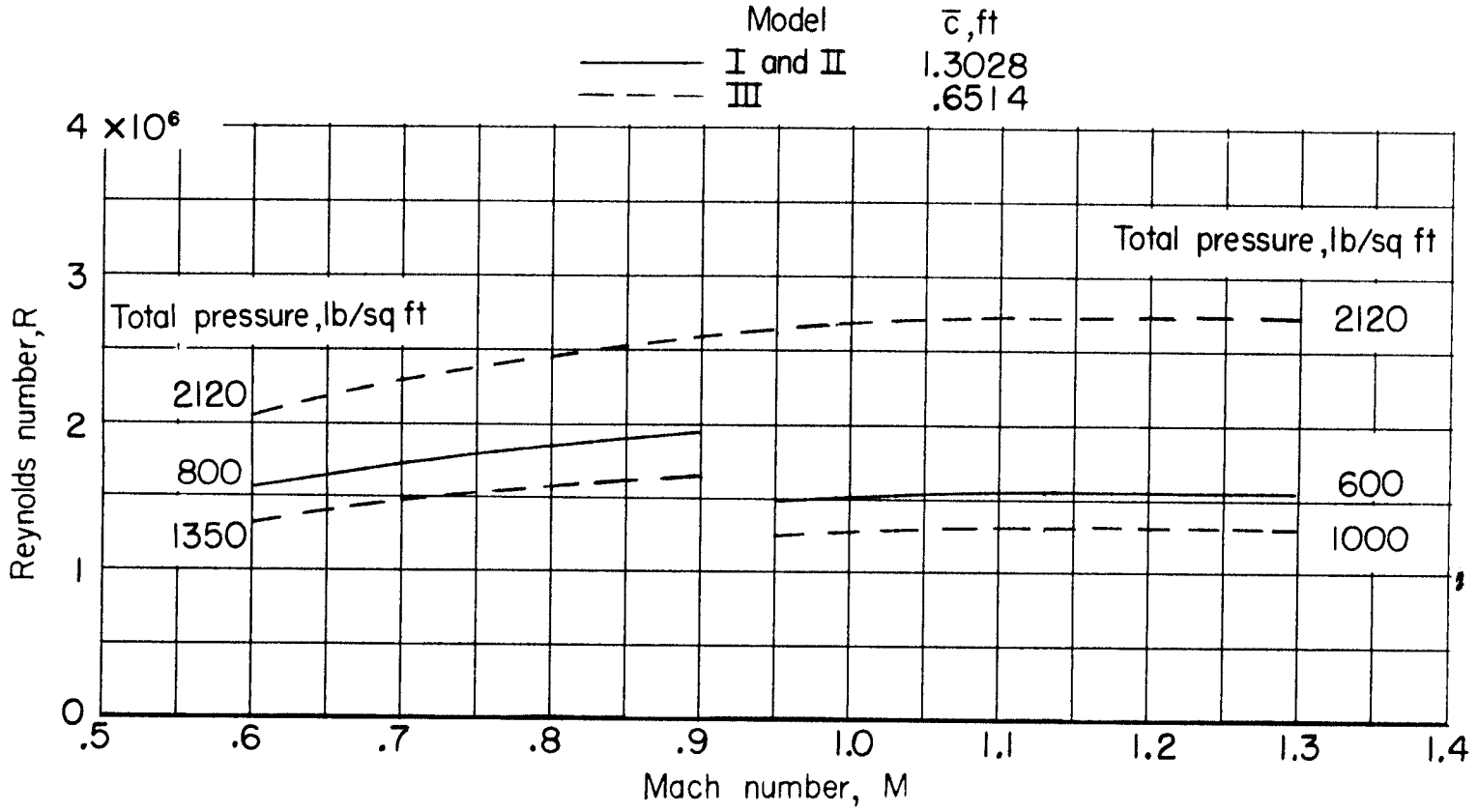

Figure 8.- Variation of Reynolds number (based on $\bar{c}$) with Mach number.

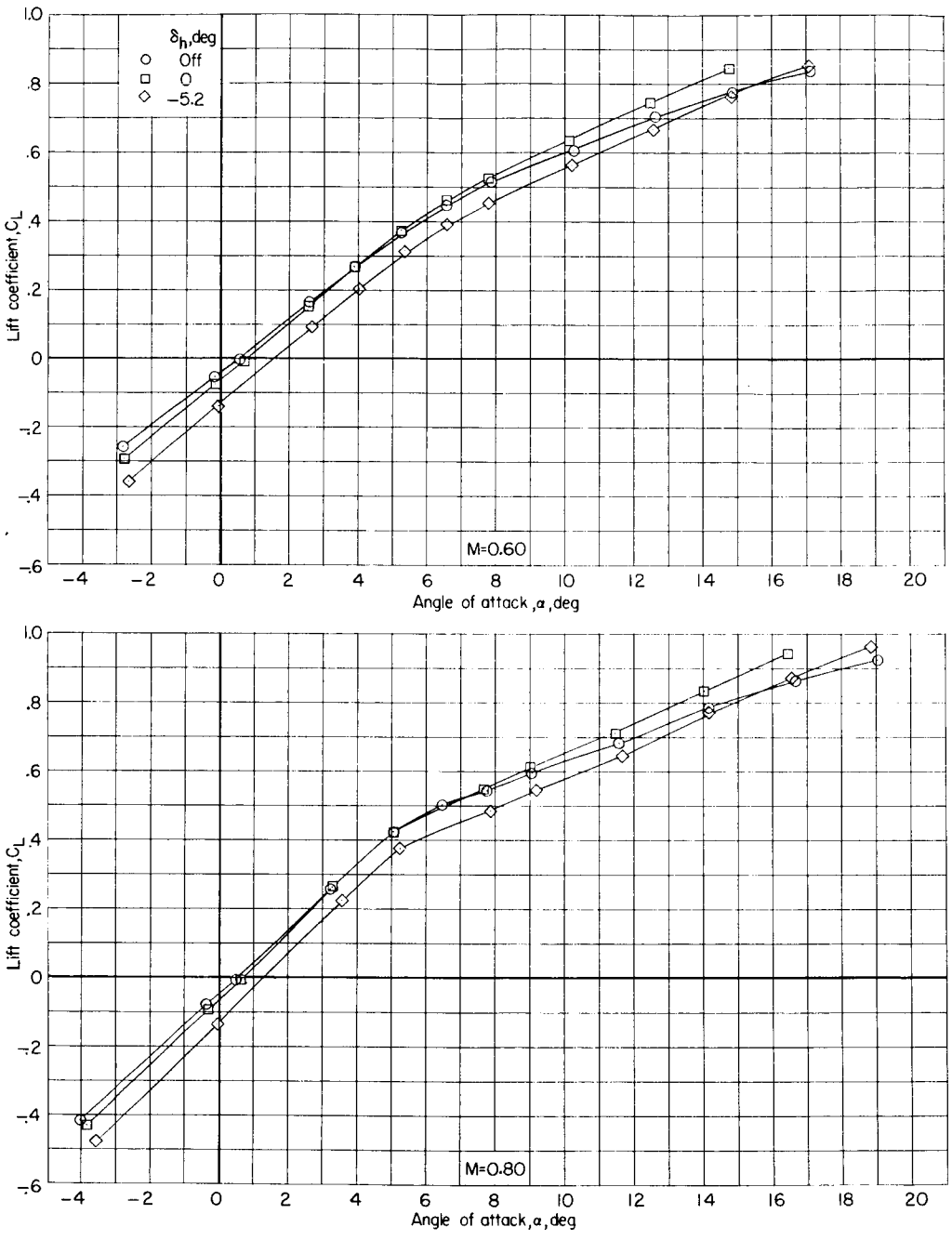

(a) C_L against α.

Figure 9.- Effect of horizontal-tail deflection on longitudinal aerodynamic characteristics of model I with 25° swept wing. Configuration BW_1VH.

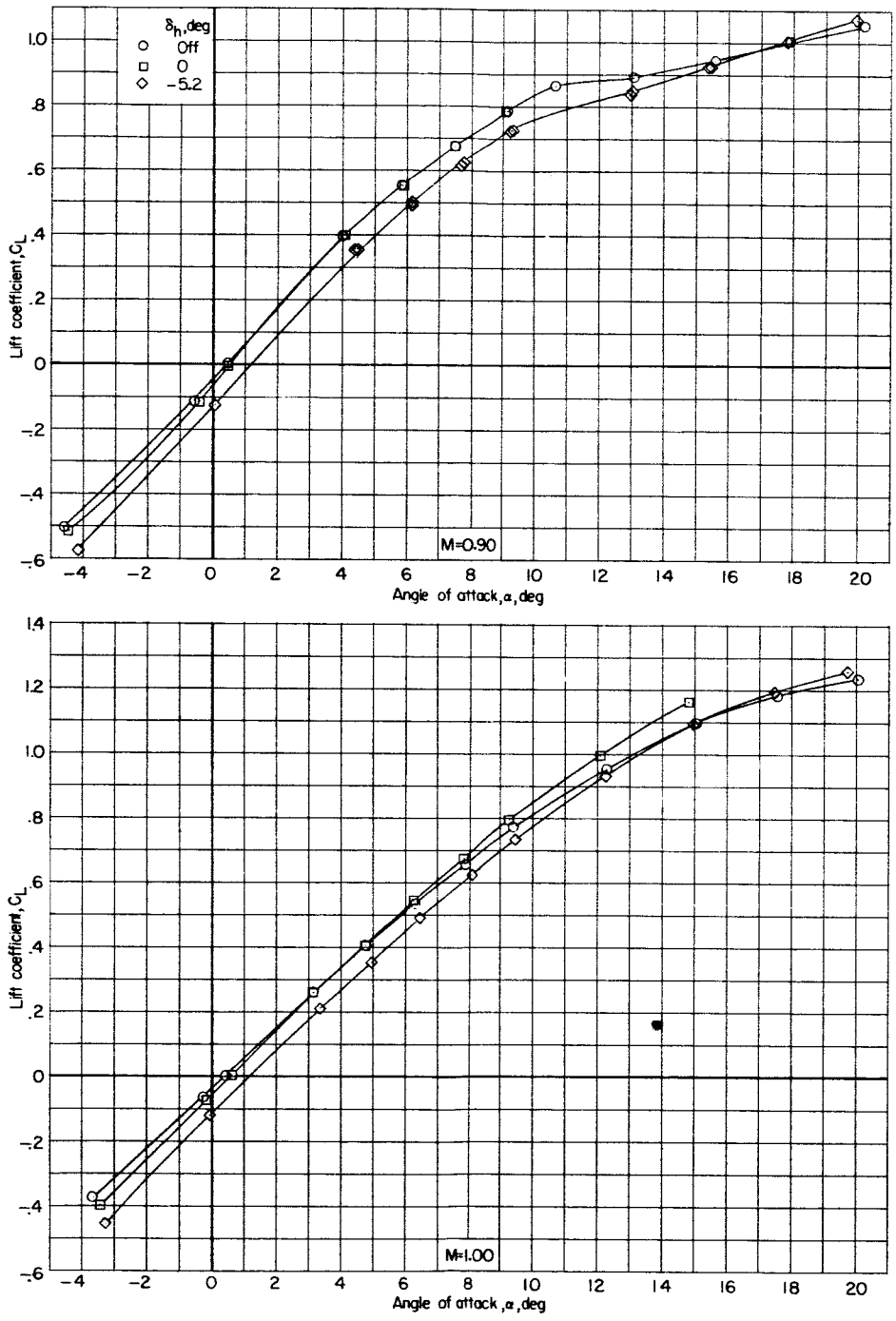

(a) Continued.

Figure 9.- Continued.

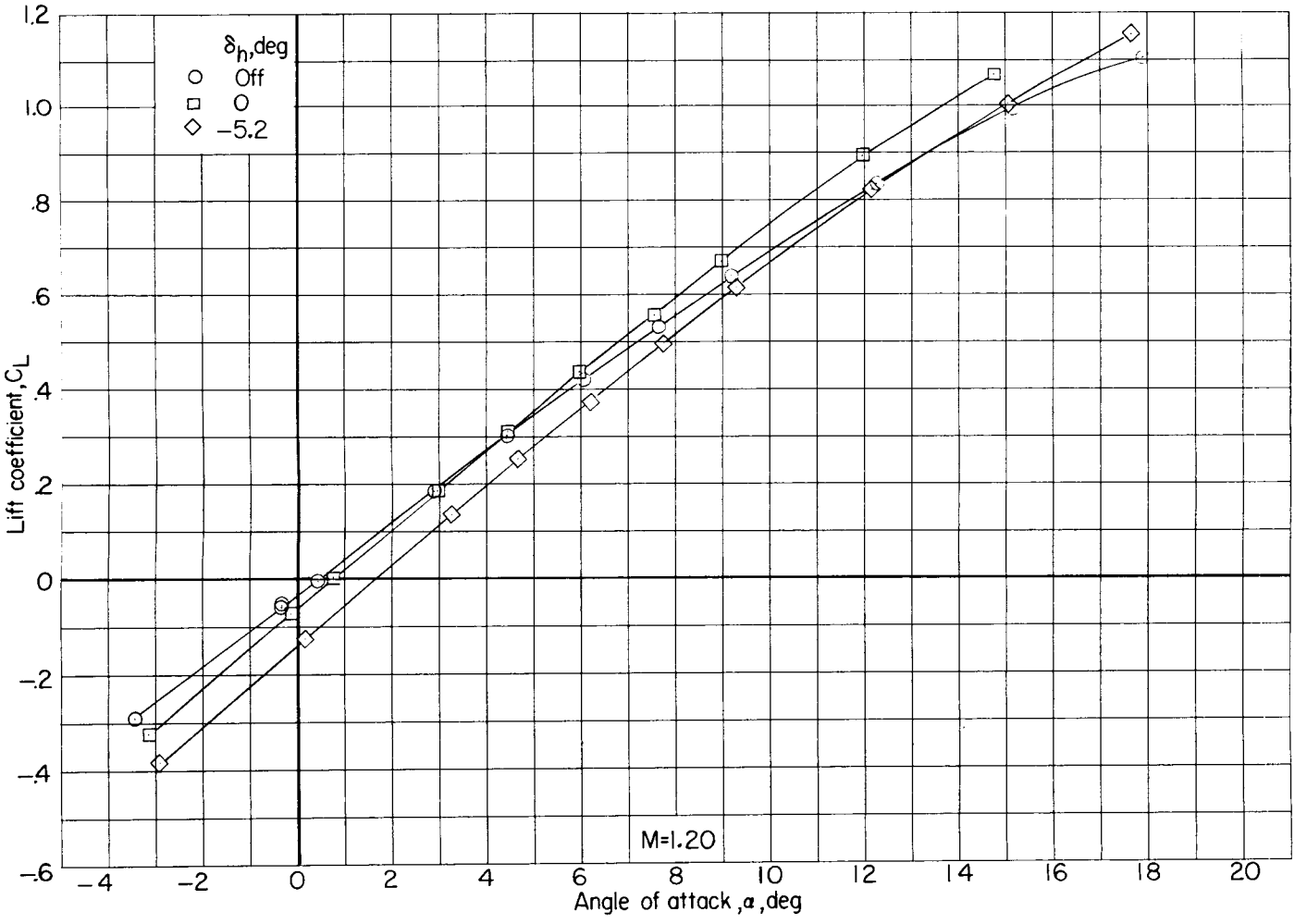

(a) Concluded.

Figure 9.- Continued.

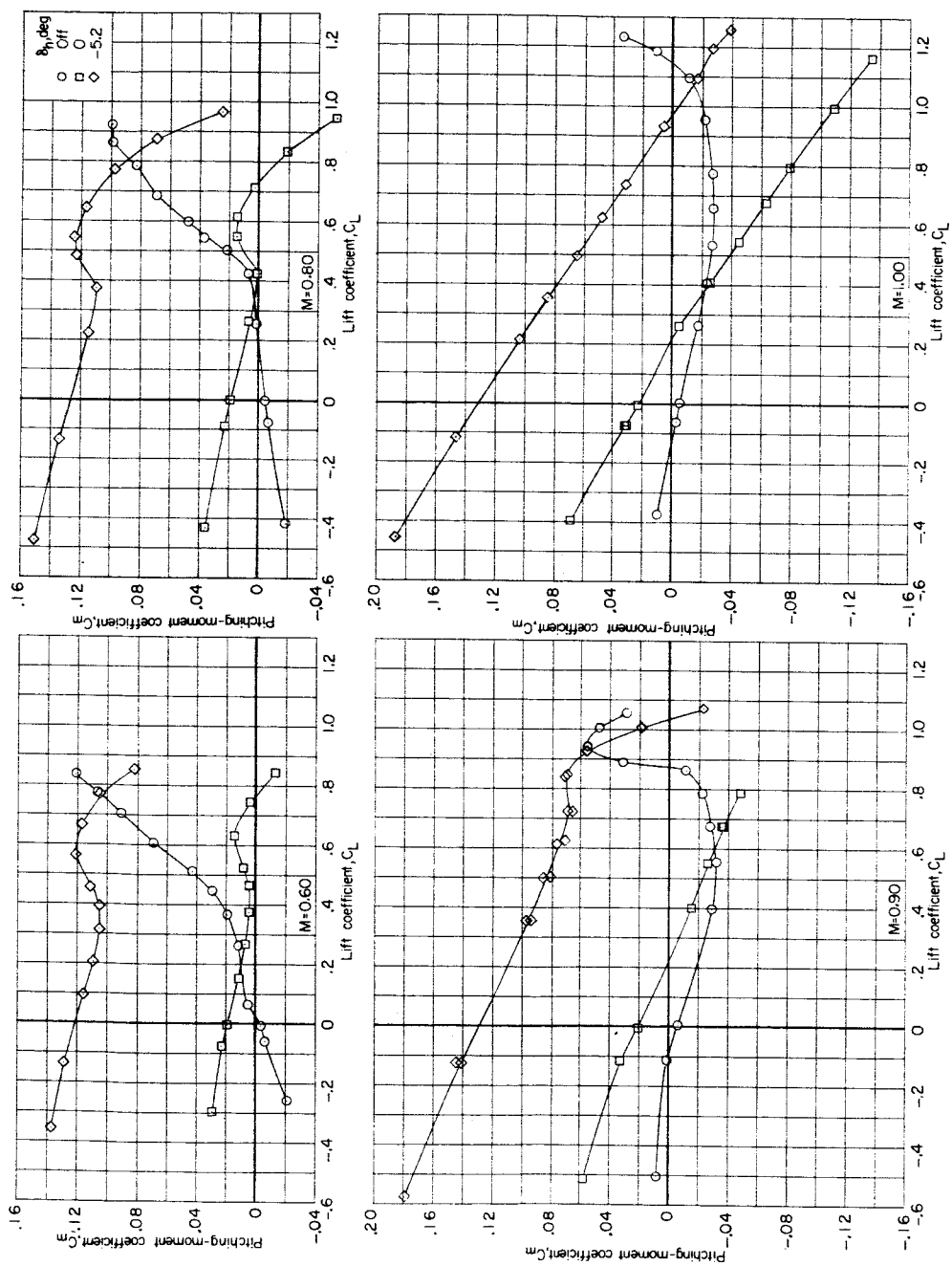

(b) C_m against C_L.

Figure 9.- Continued.

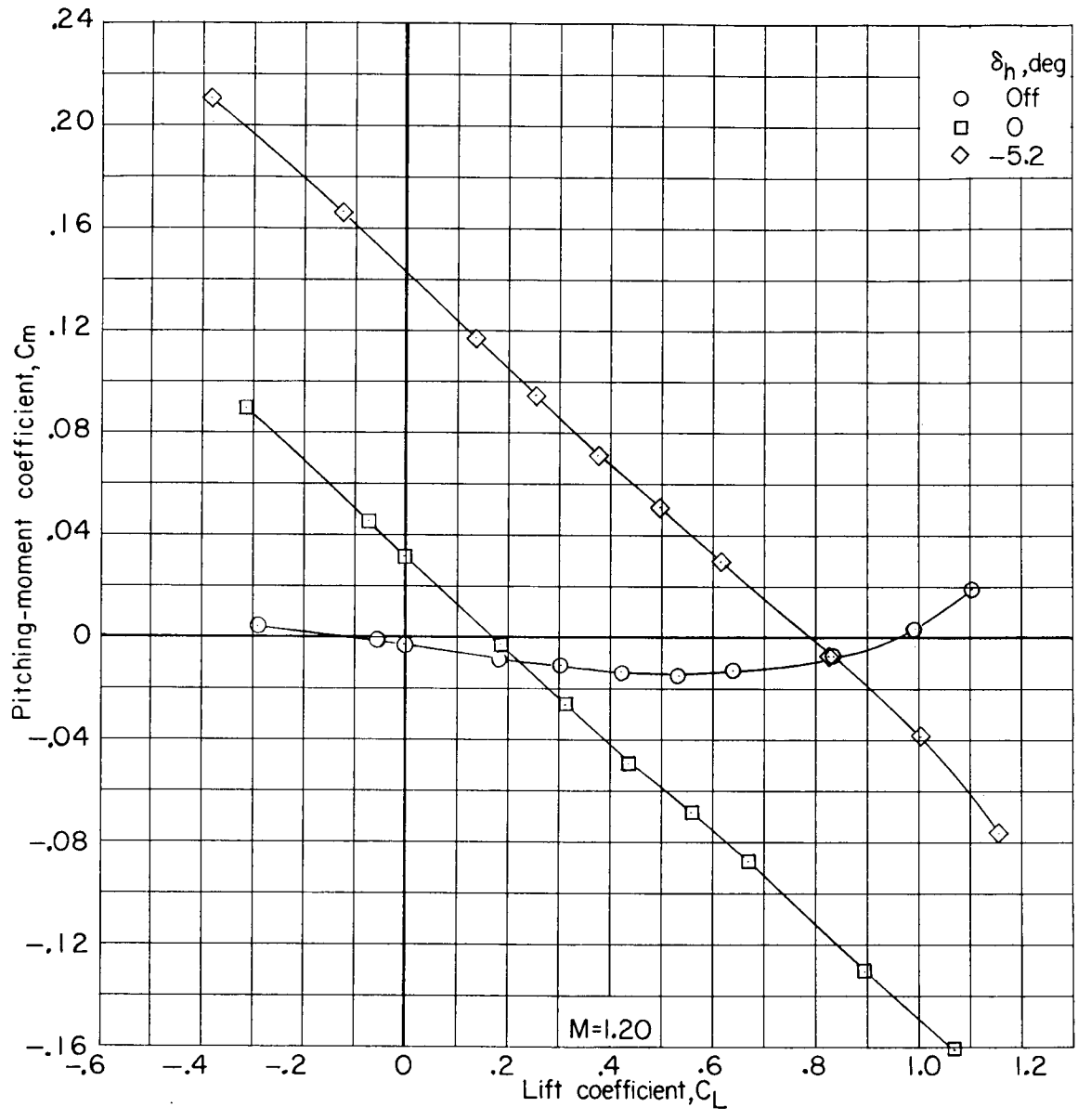

(b) Concluded.

Figure 9.- Continued.

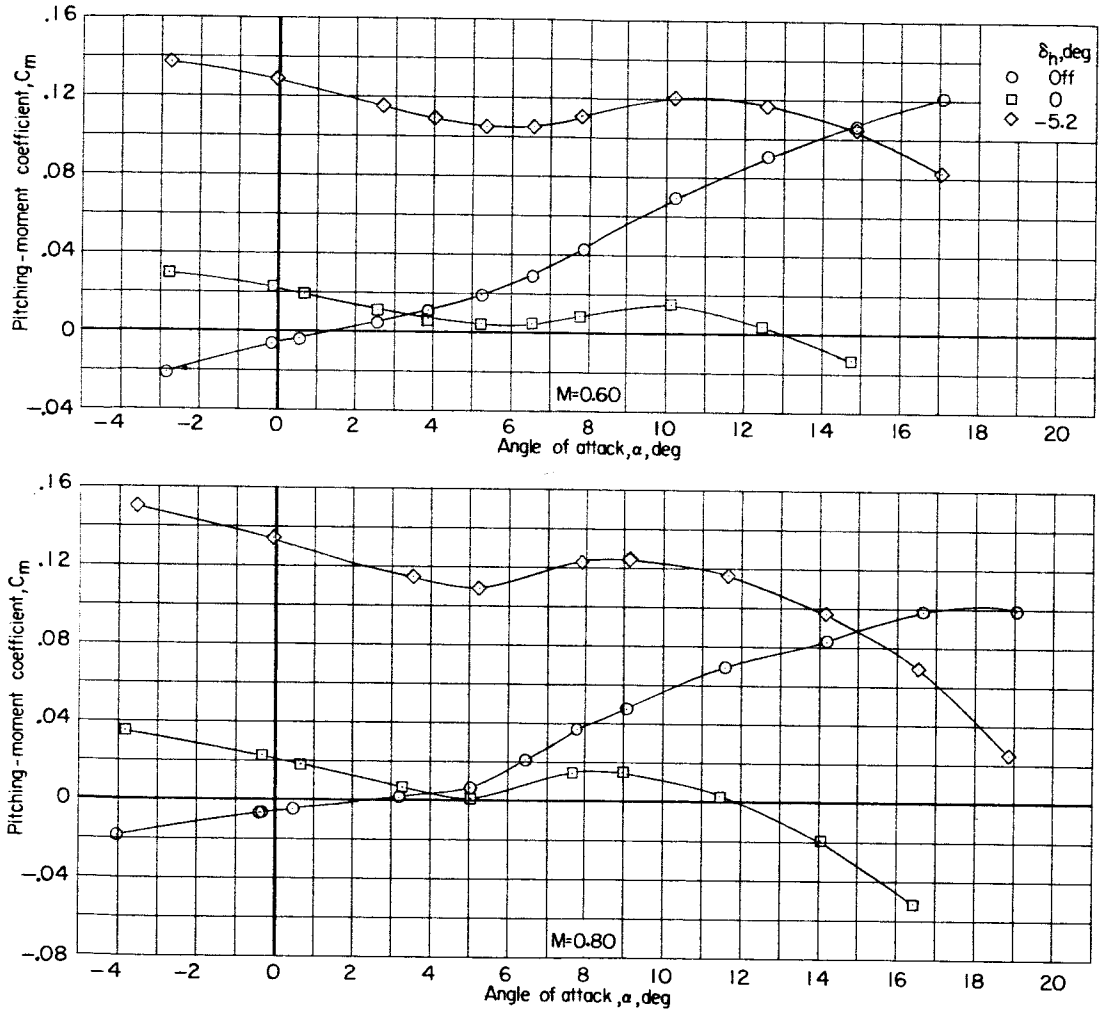

(c) C_m against α.

Figure 9.- Continued.

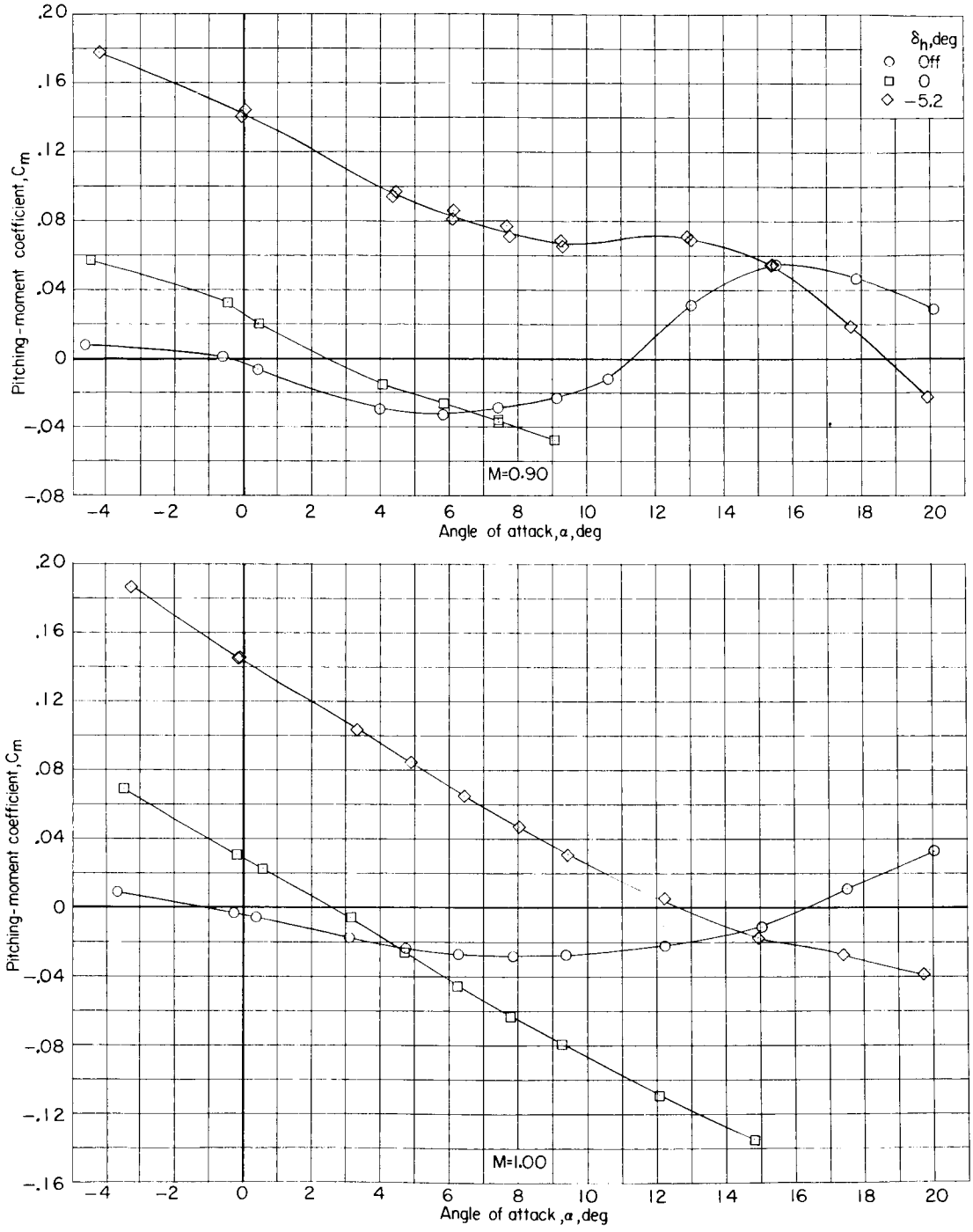

(c) Continued.

Figure 9.- Continued.

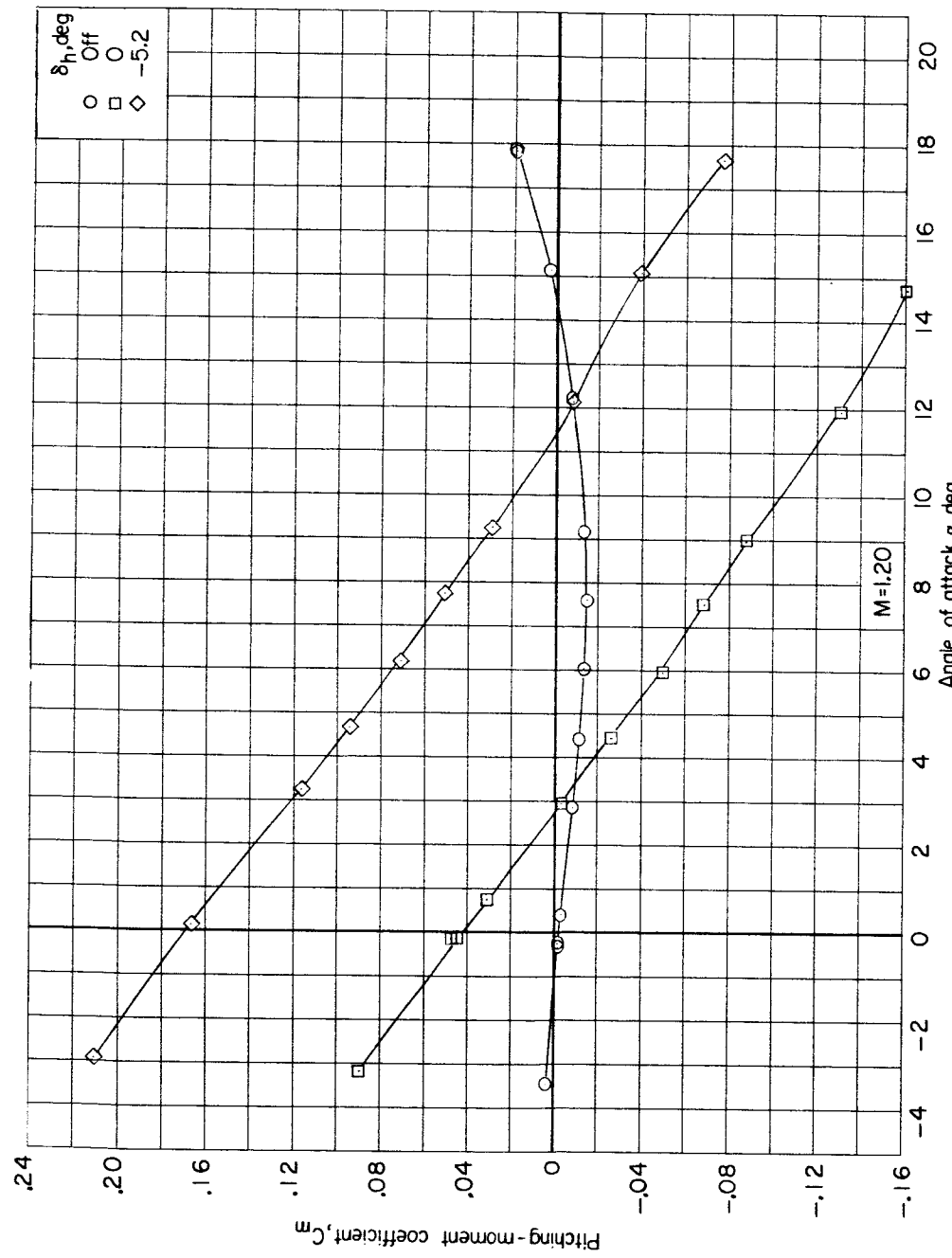

(c) Concluded.

Figure 9.- Continued.

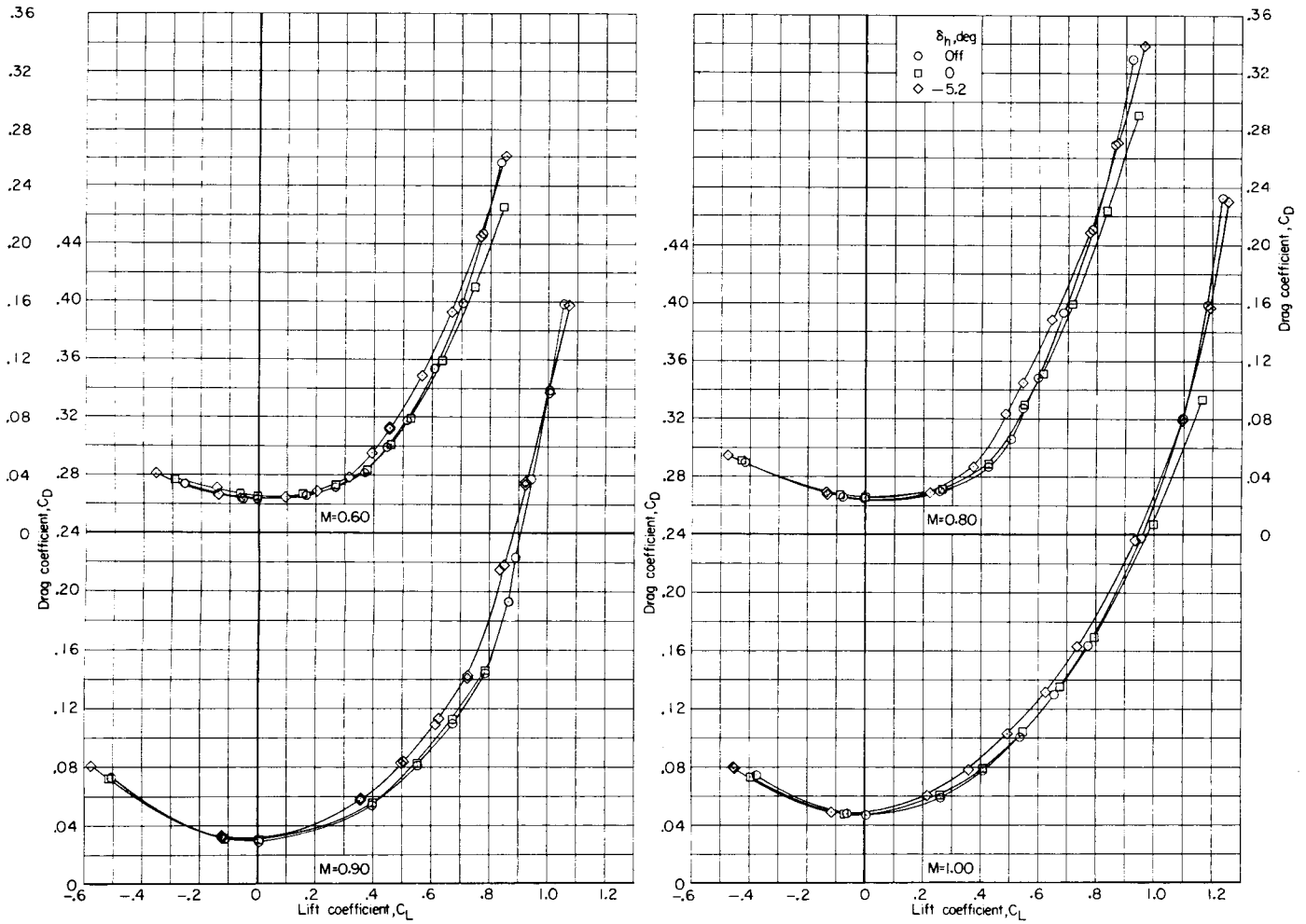

(d) C_D against C_L.

Figure 9.- Continued.

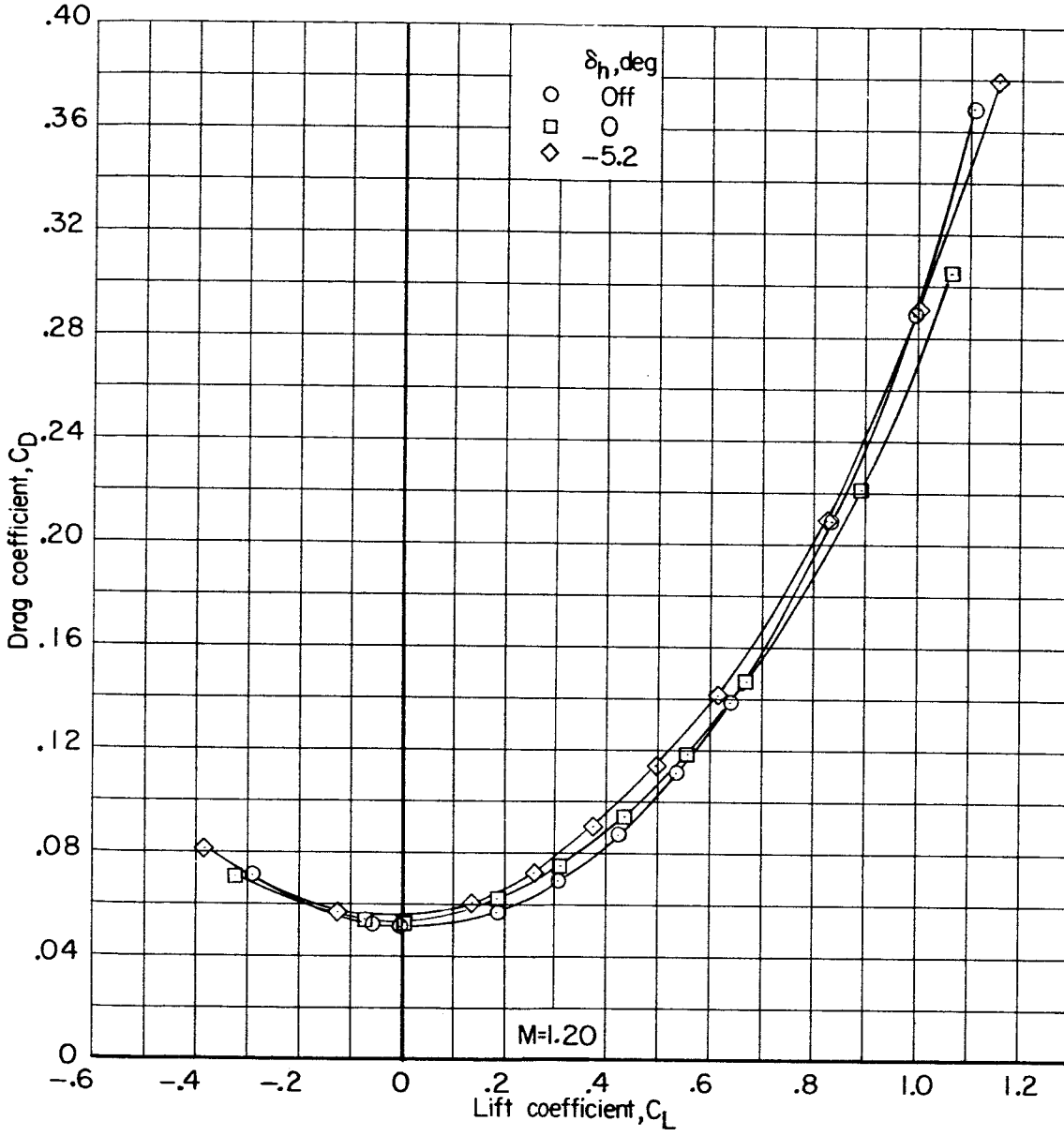

(d) Concluded.

Figure 9.- Continued.

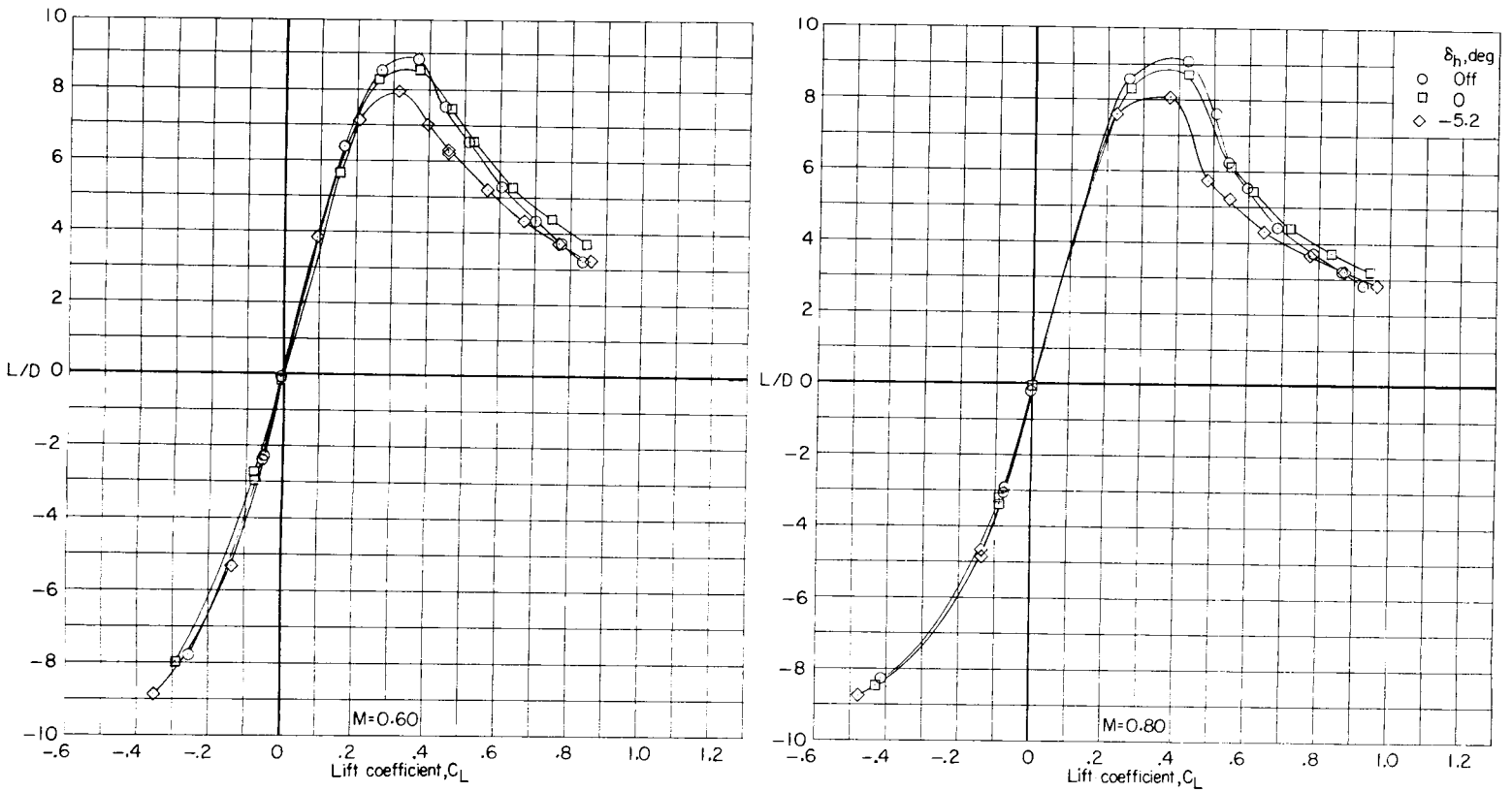

(e) L/D against C_L.

Figure 9.- Continued.

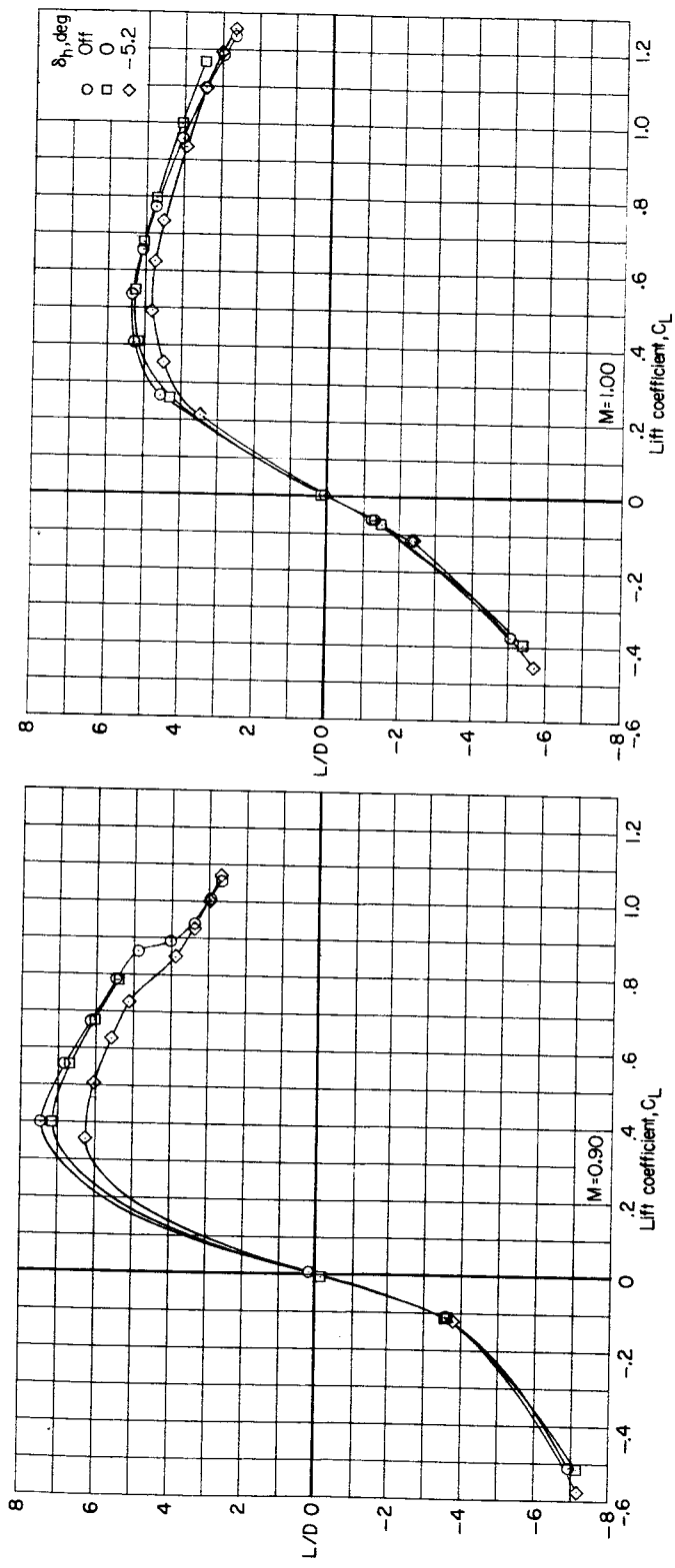

(e) Continued.

Figure 9.- Continued.

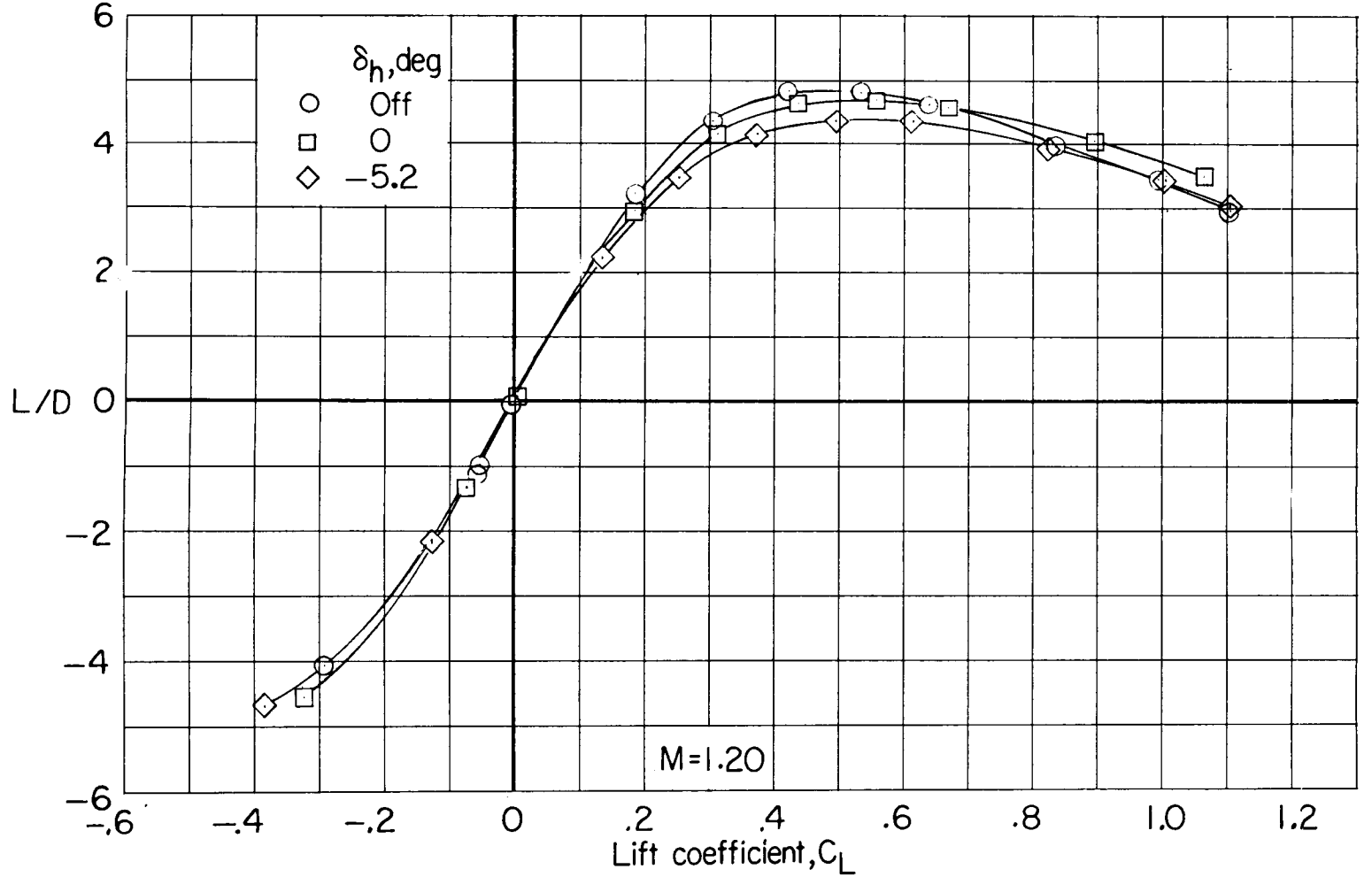

(e) Concluded.

Figure 9.- Concluded.

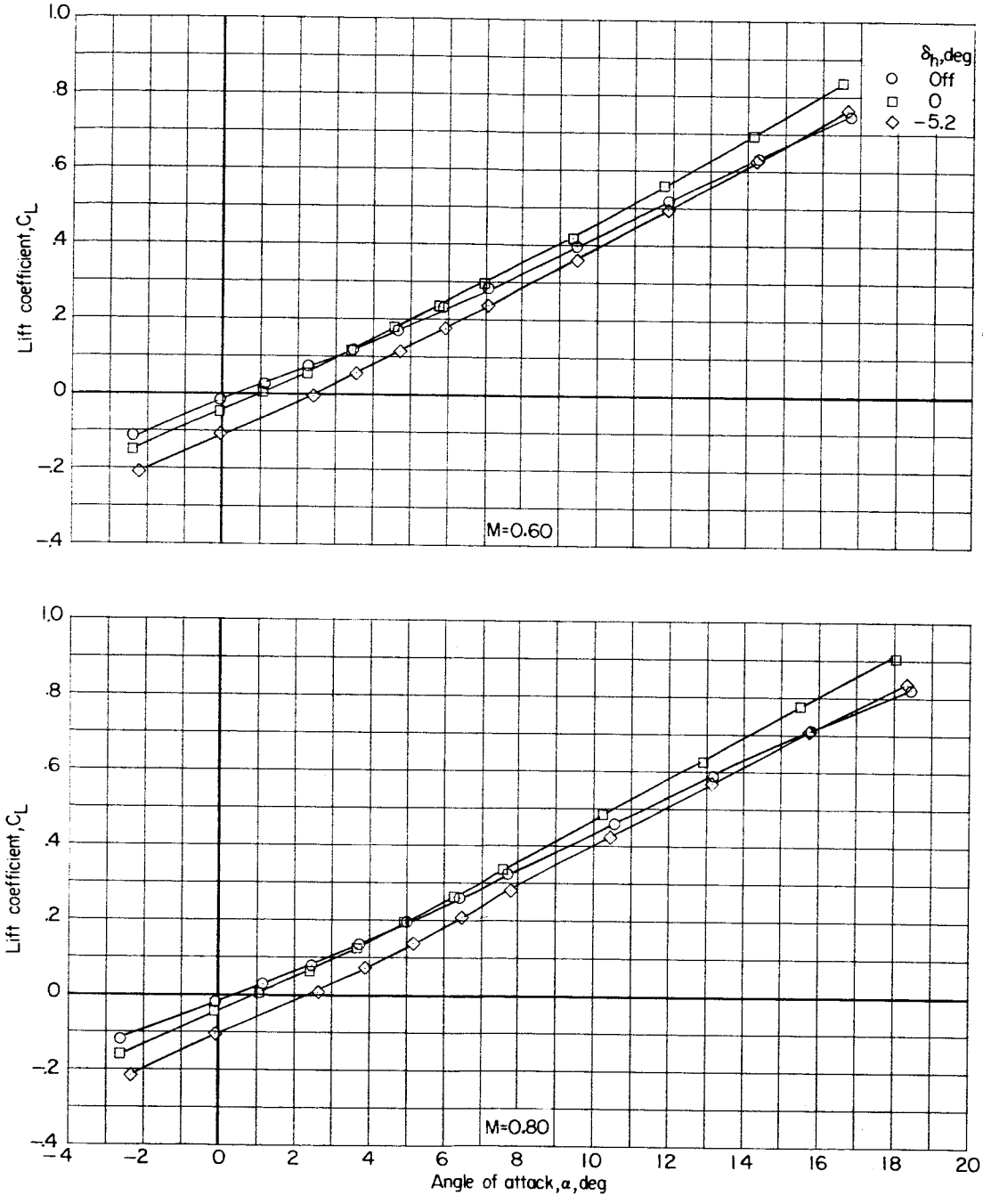

(a) C_L against α.

Figure 10.- Effect of horizontal-tail deflection on longitudinal aerodynamic characteristics of model I with 75° swept wing. Configuration BW_3VH.

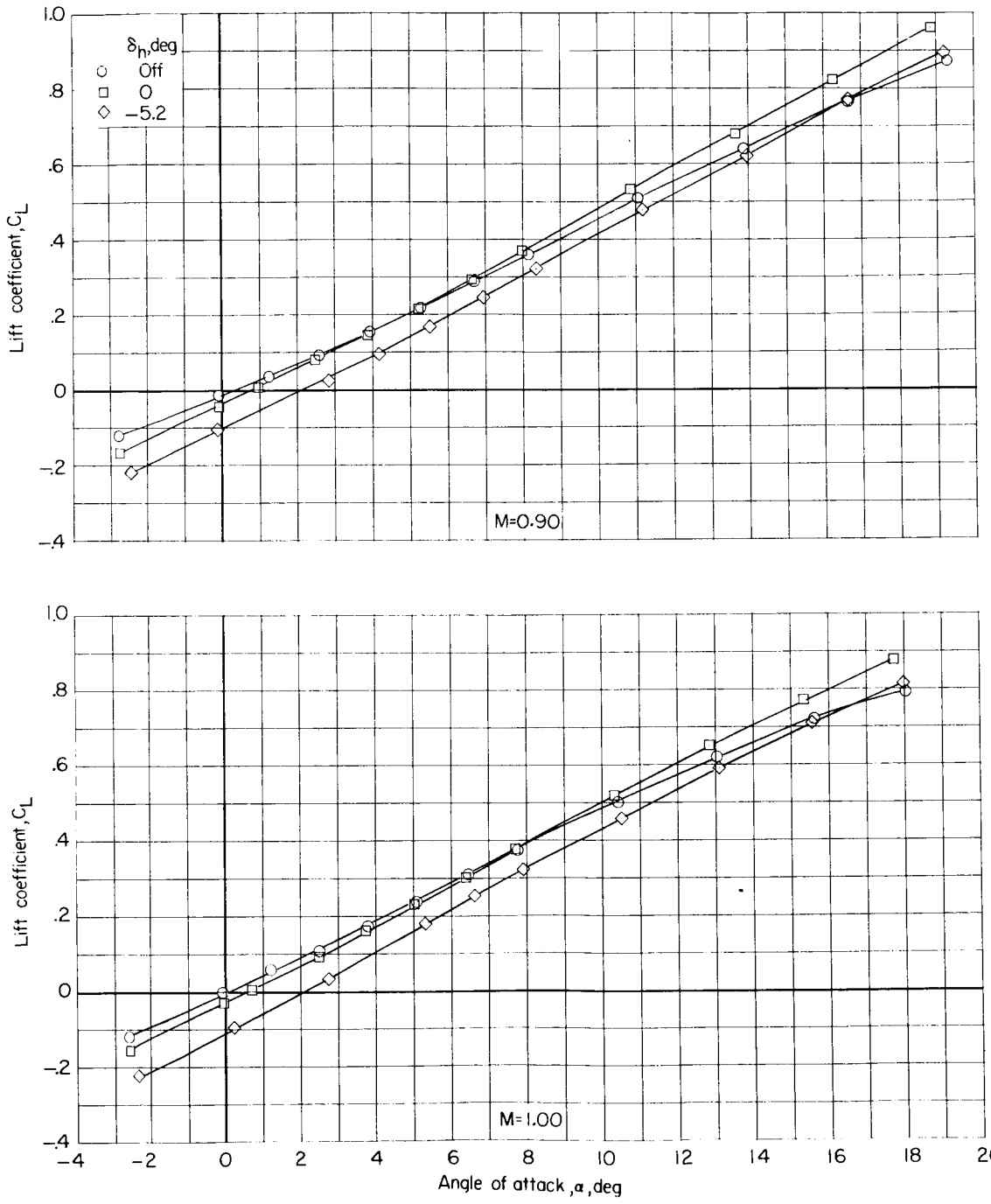

(a) Continued.

Figure 10.- Continued.

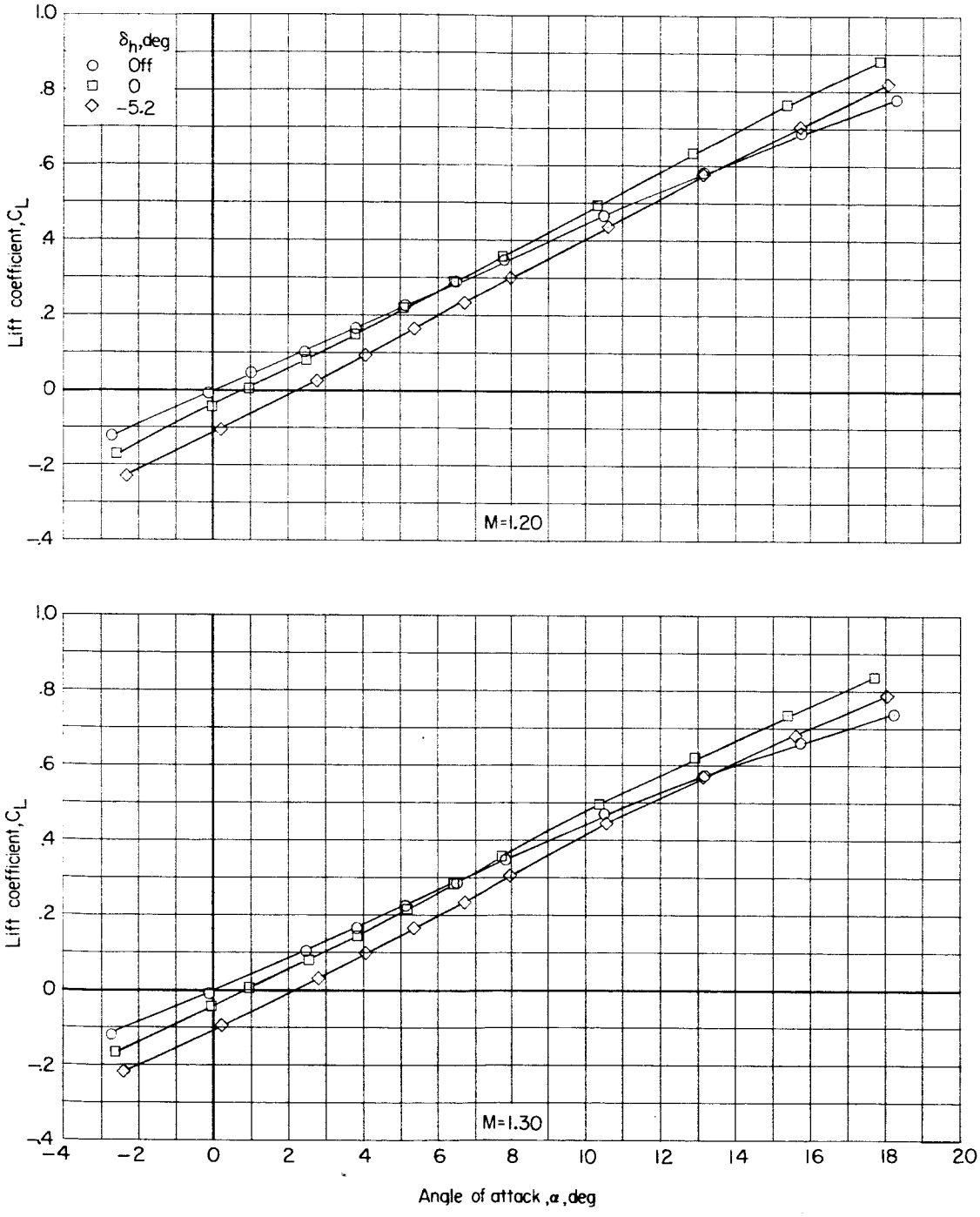

(a) Concluded.

Figure 10.- Continued.

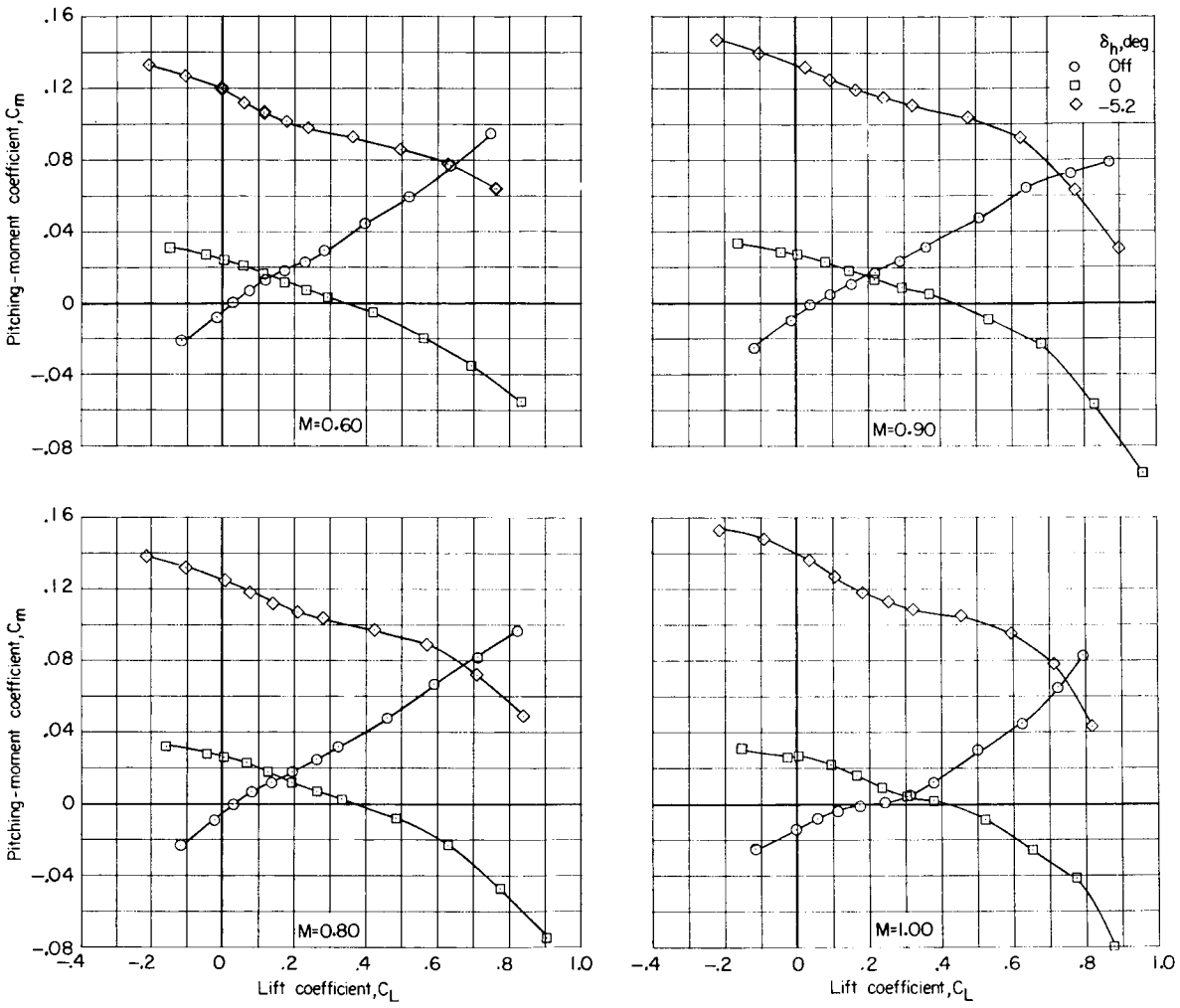

(b) C_m against C_L.

Figure 10.- Continued.

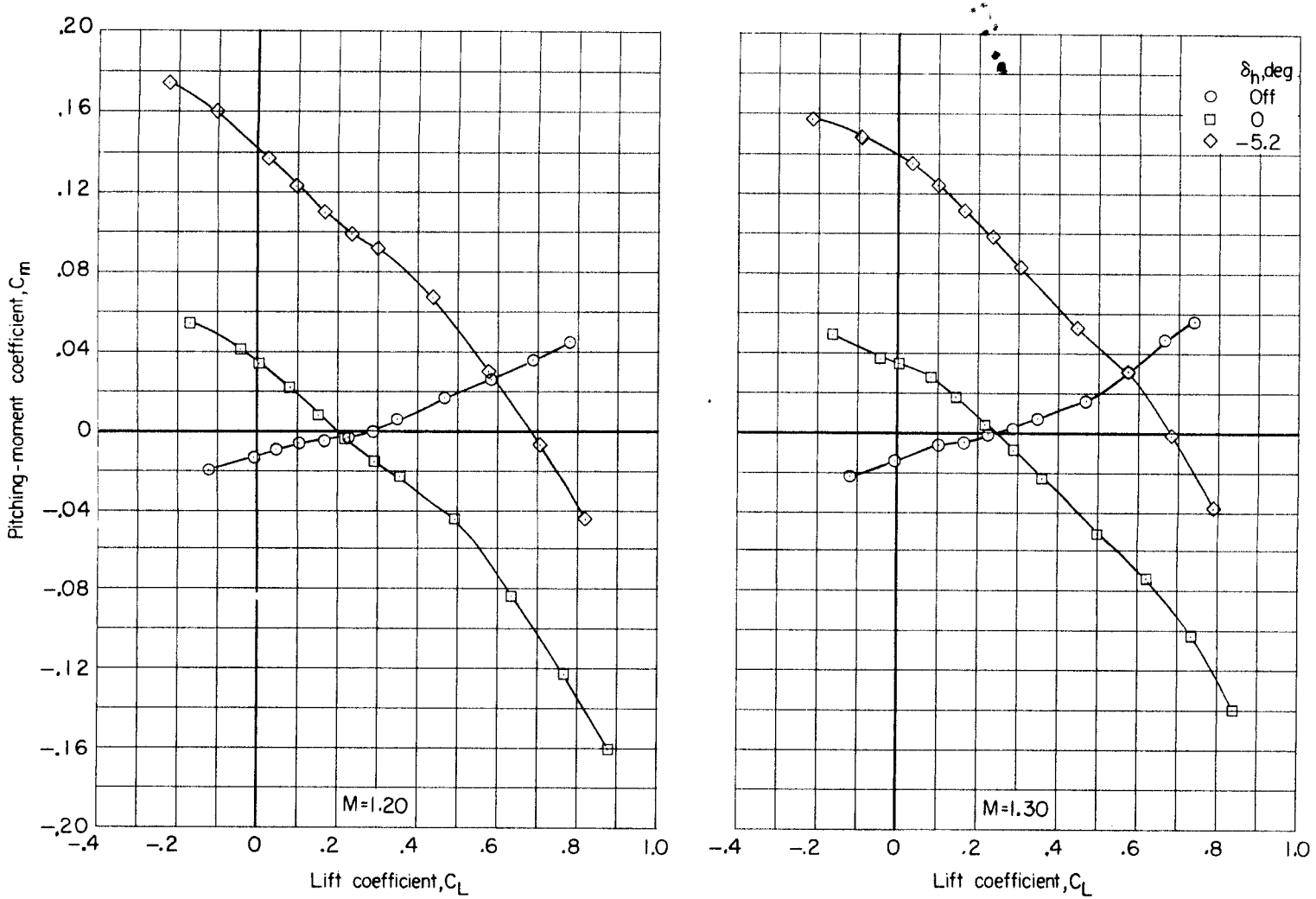

(b) Concluded.

Figure 10.- Continued.

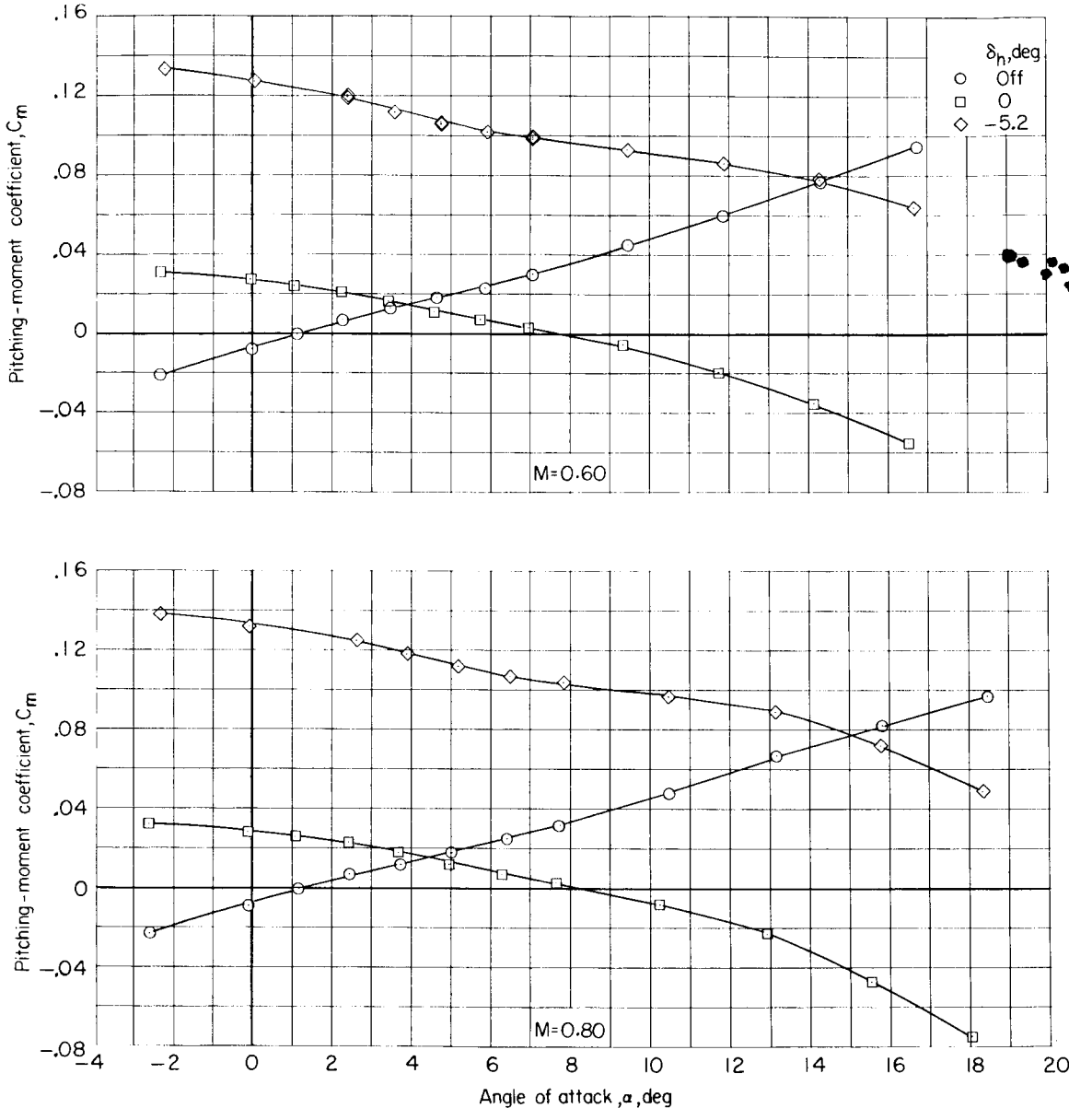

(c) C_m against α.

Figure 10.- Continued.

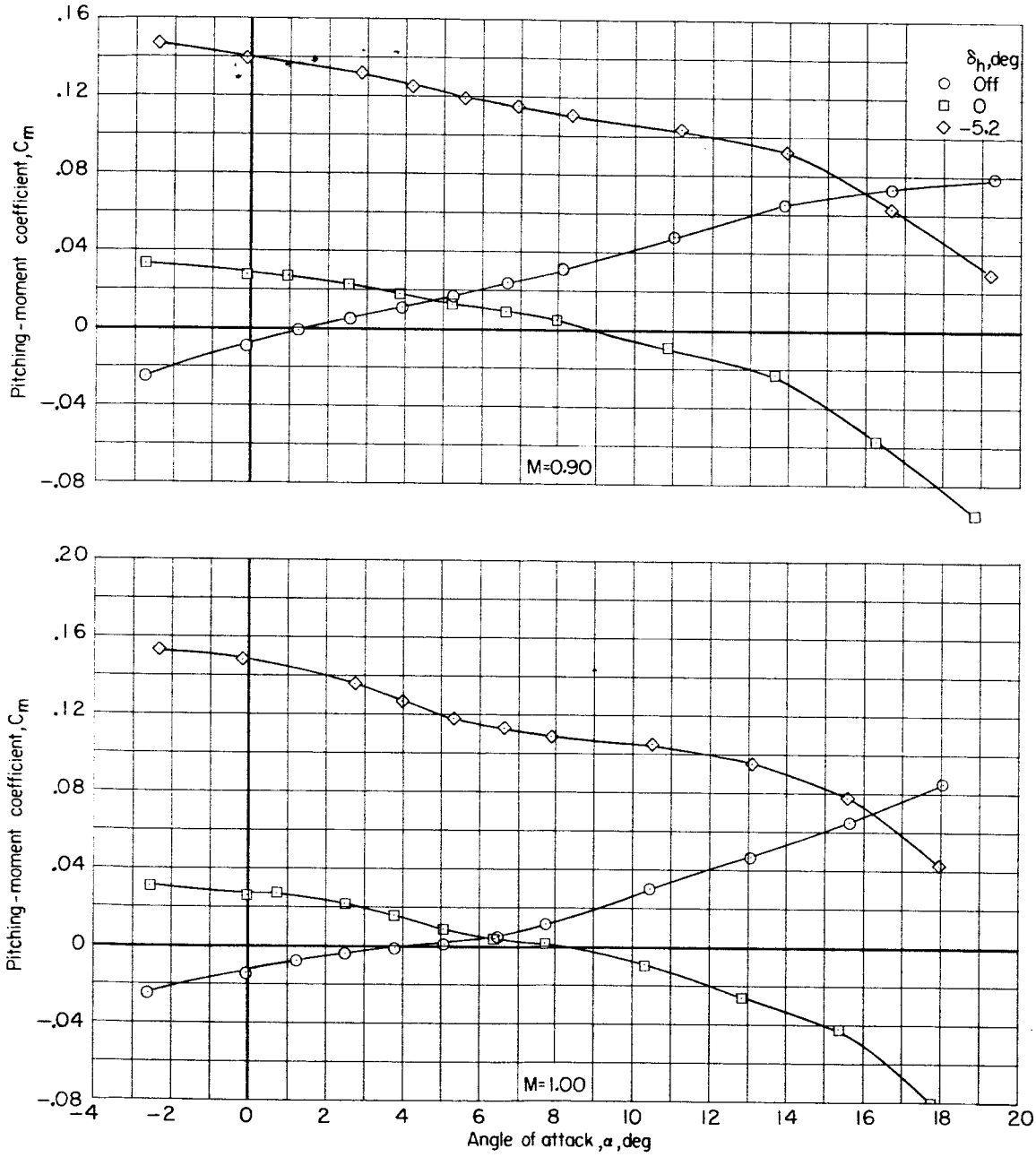

(c) Continued.

Figure 10.- Continued.

[redacted]

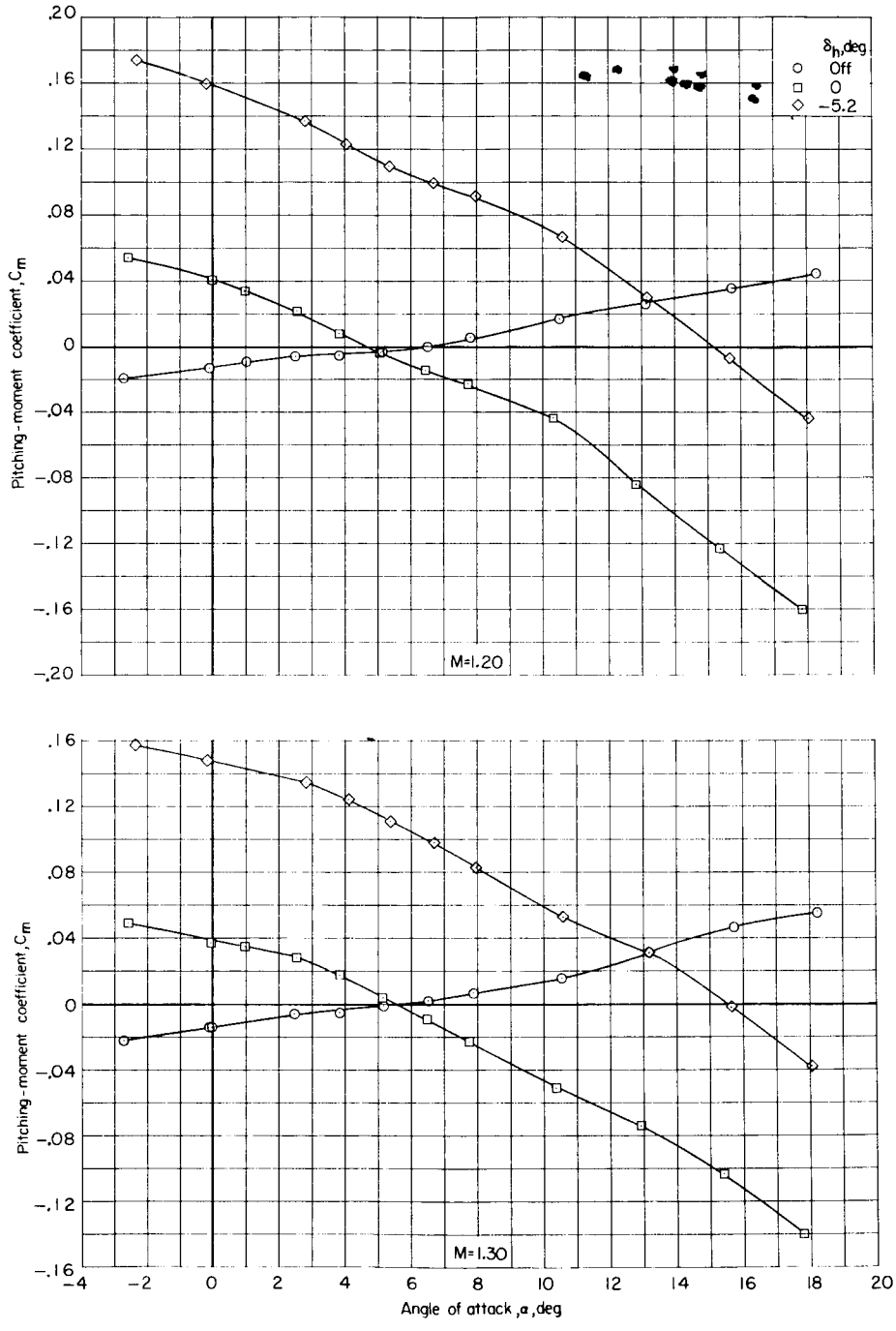

(c) Concluded.

Figure 10.- Continued.

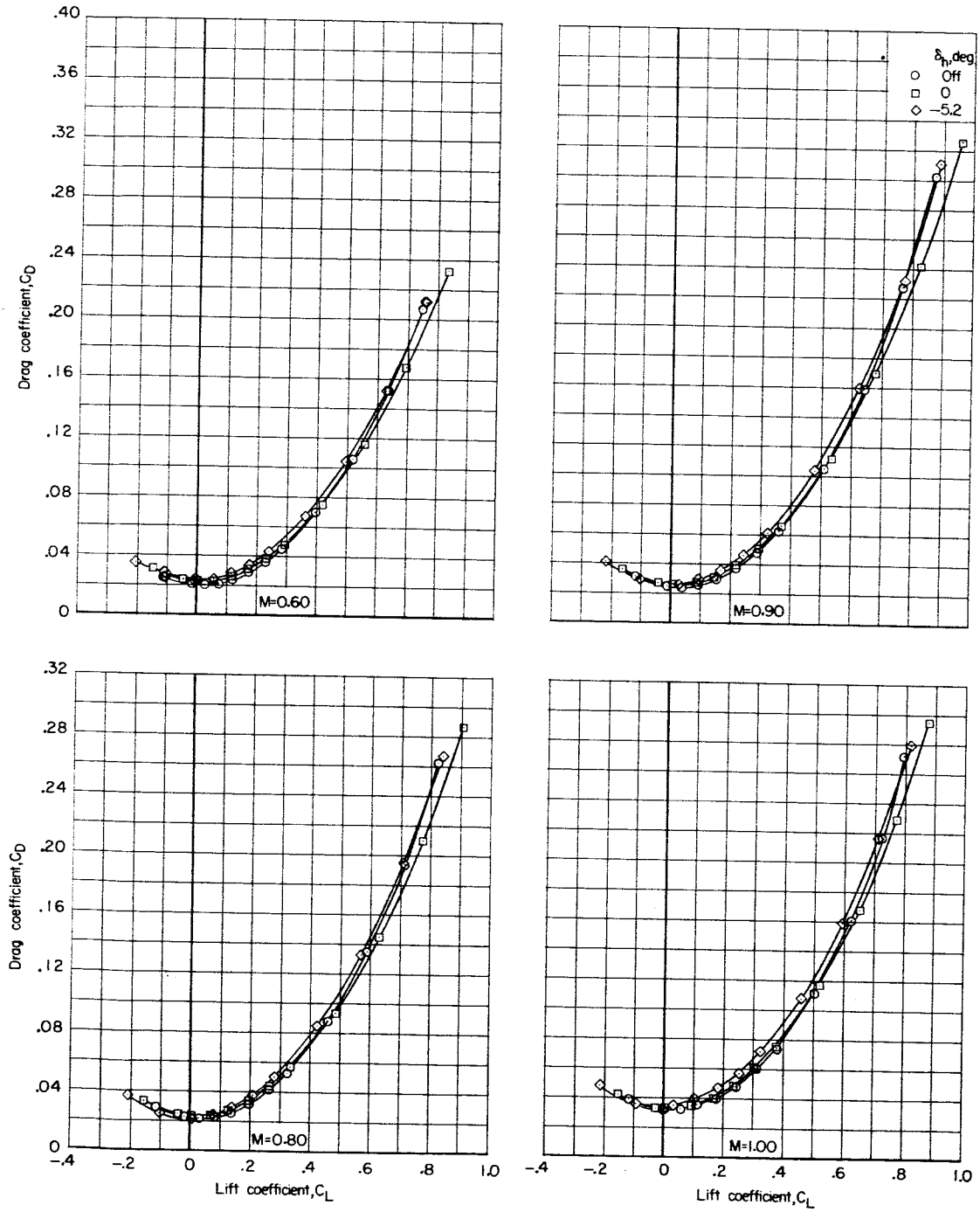

(d) C_D against C_L.

Figure 10.- Continued.

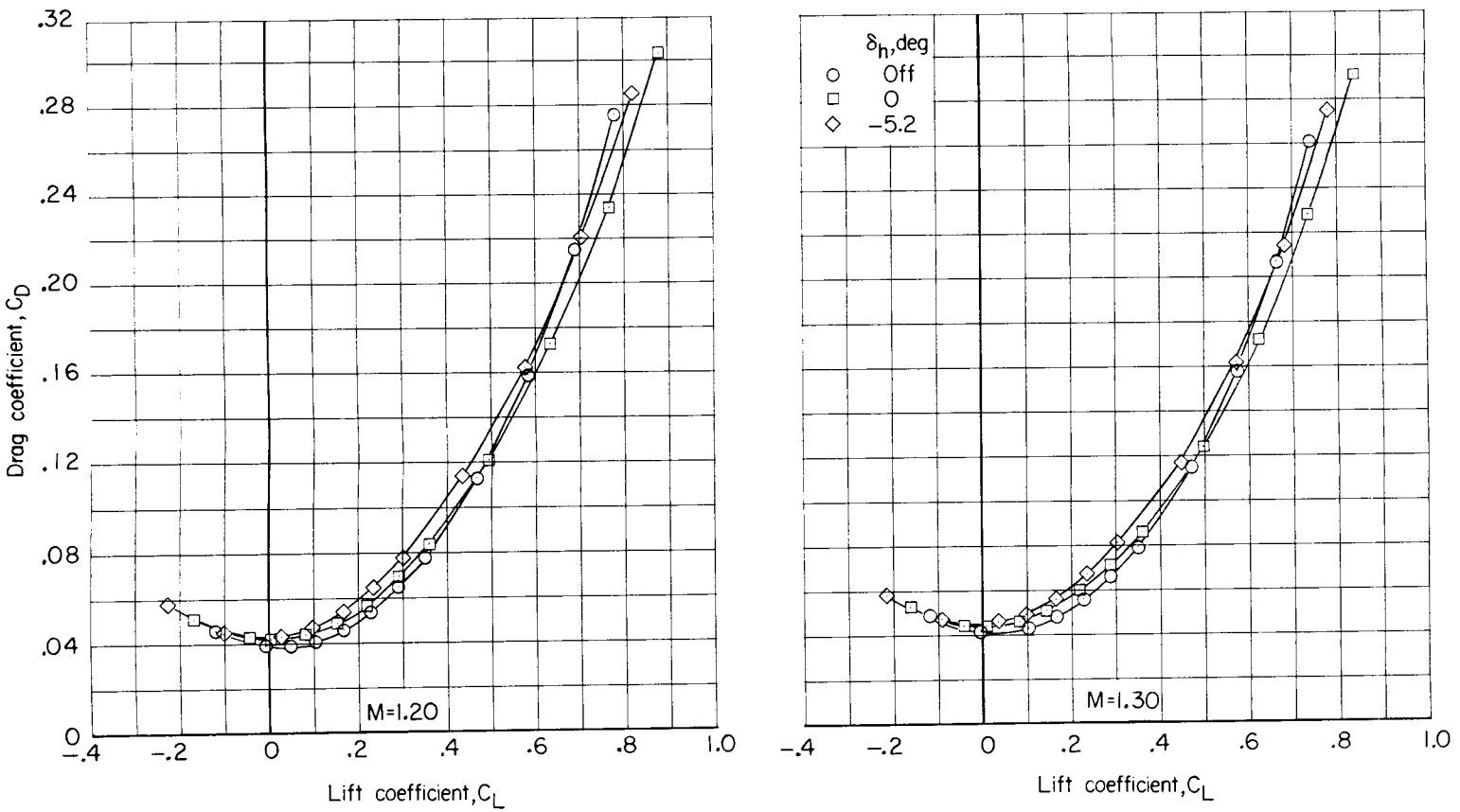

(d) Concluded.

Figure 10.- Continued.

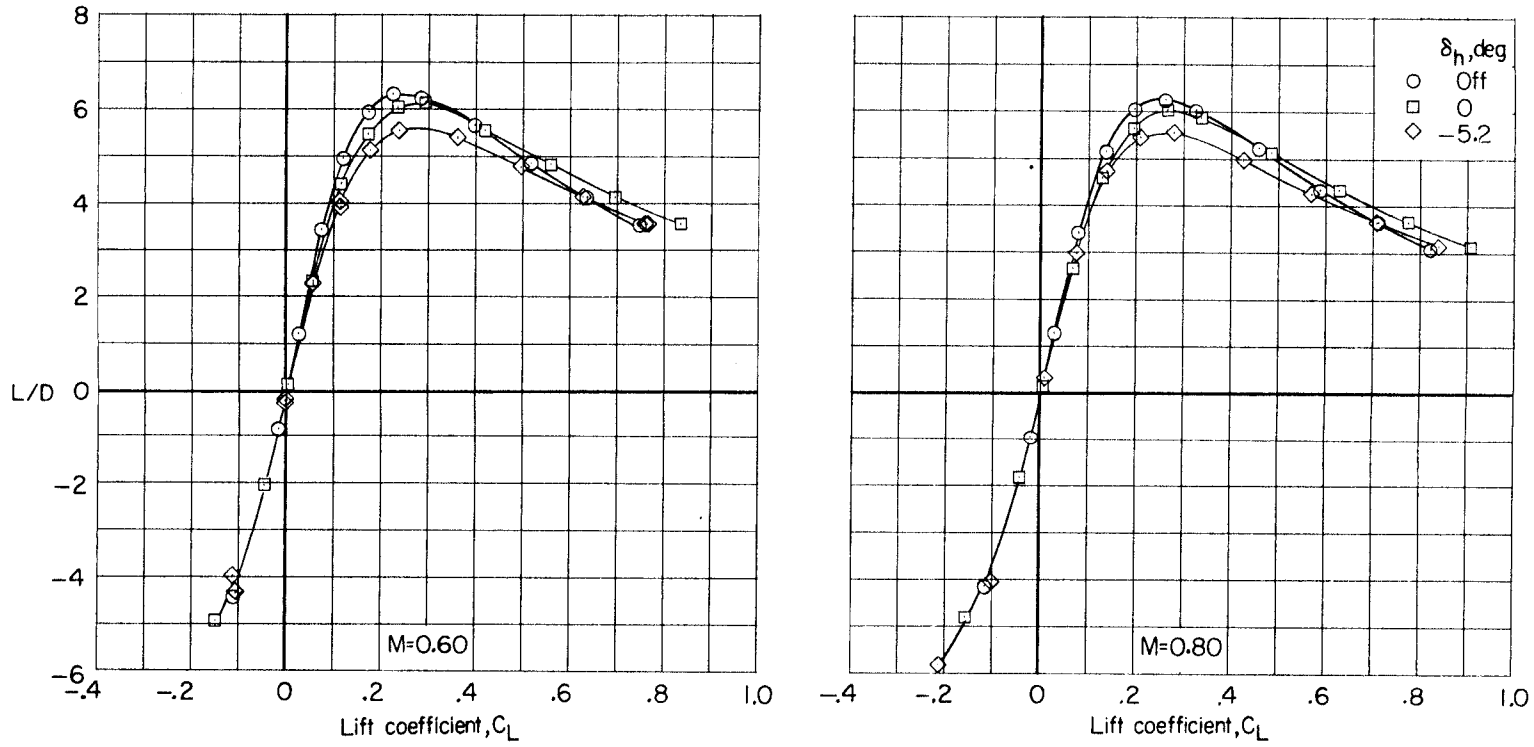

(e) L/D against C_L.

Figure 10.- Continued.

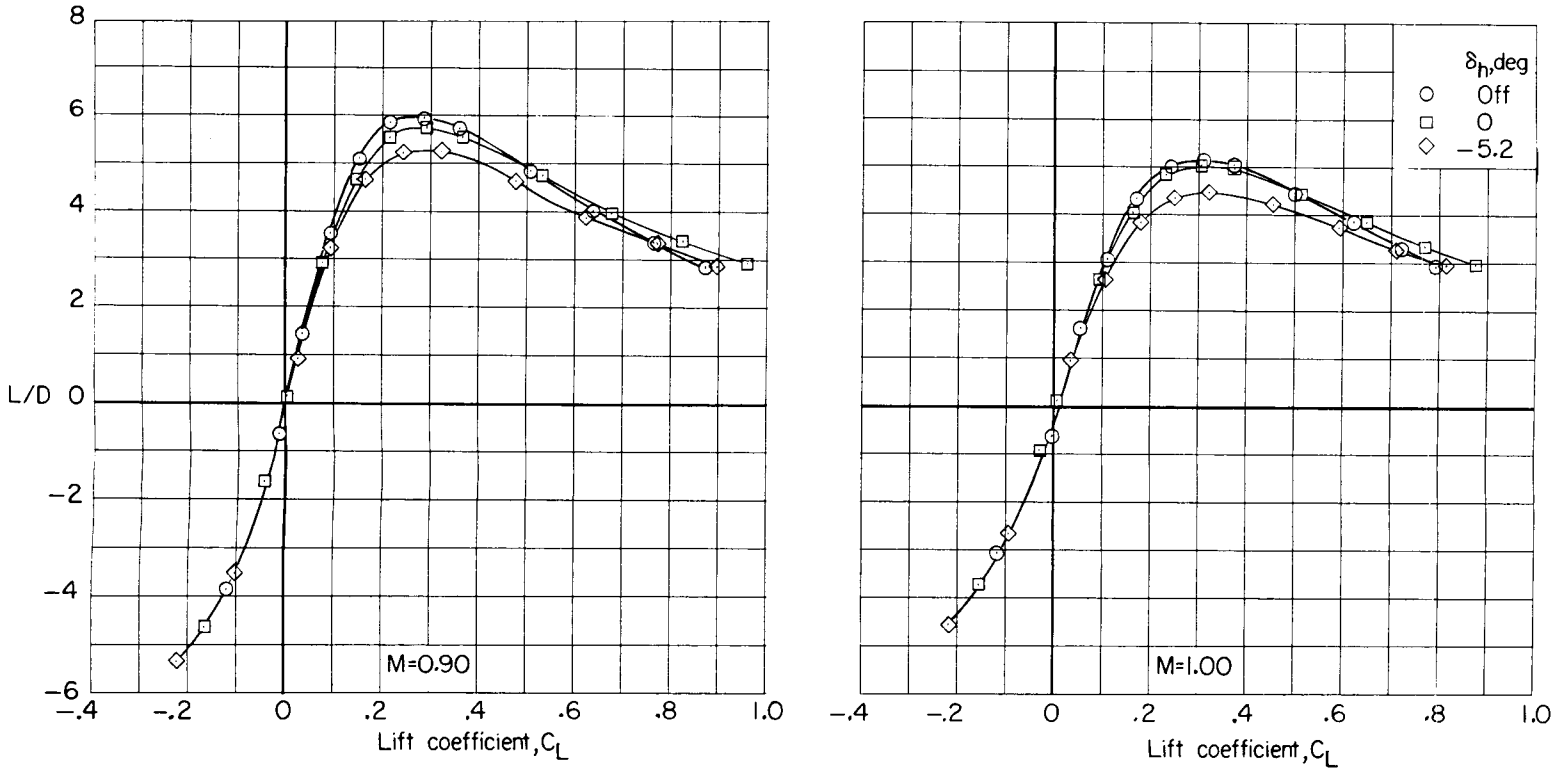

(e) Continued.

Figure 10.- Continued.

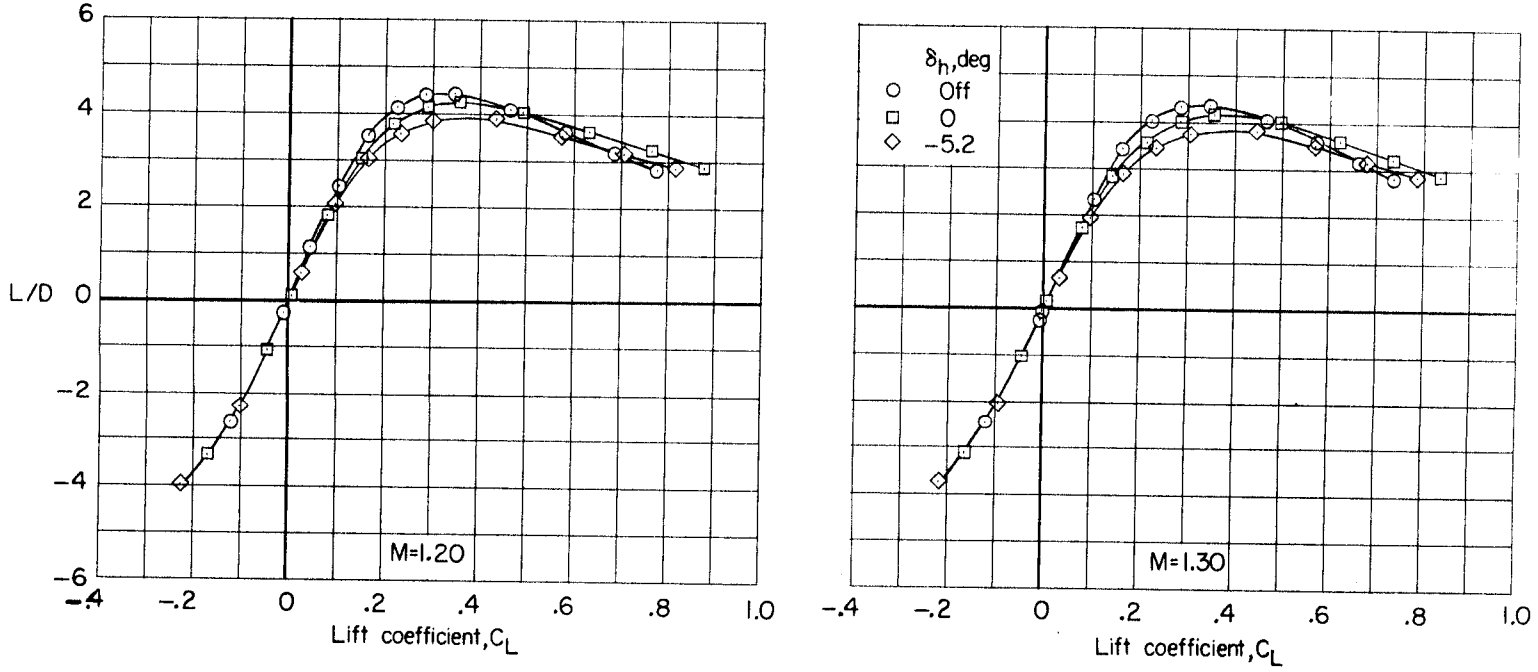

(e) Concluded.

Figure 10.- Concluded.

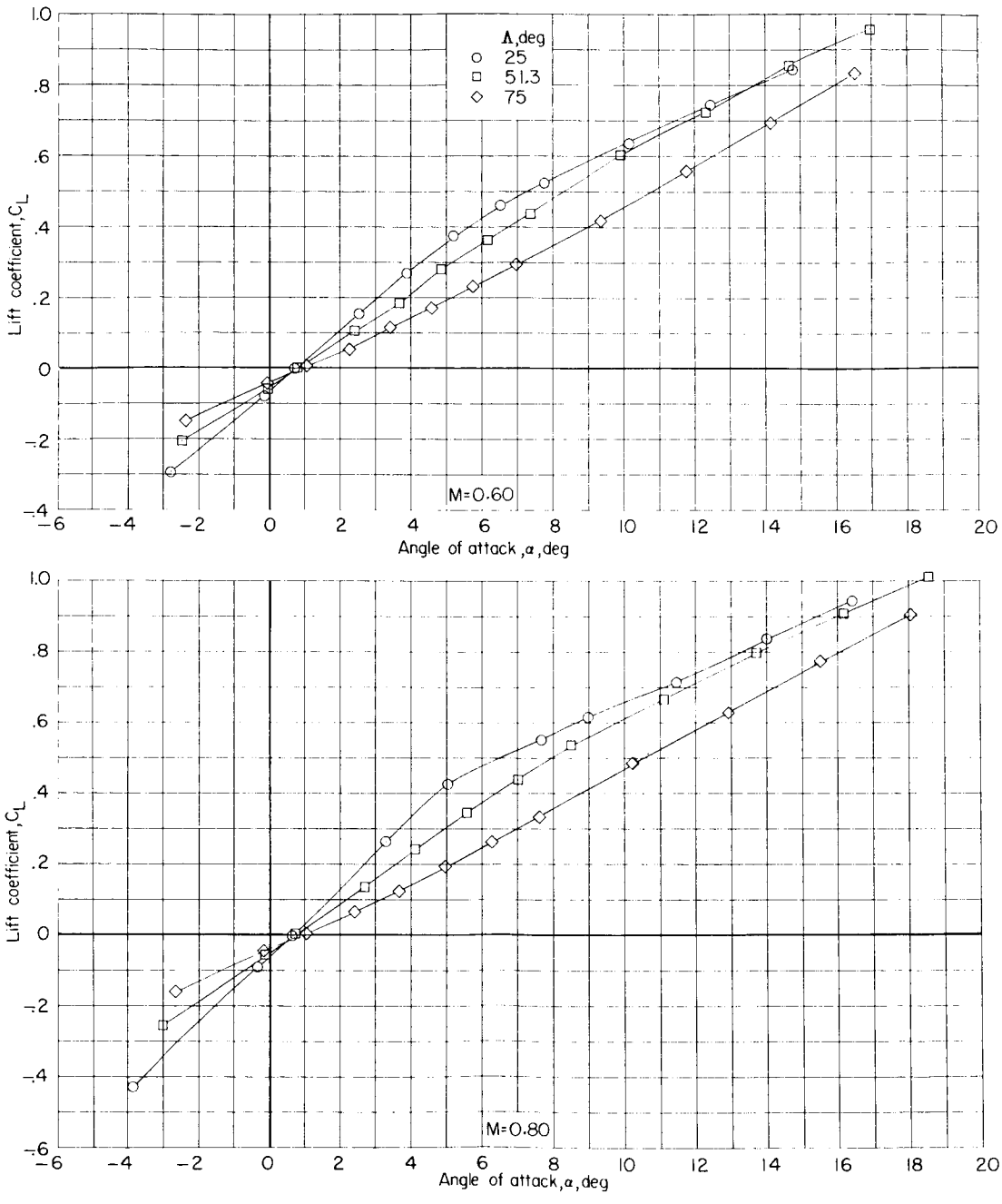

(a) C_L against α.

Figure 11.- Effect of wing sweep on longitudinal aerodynamic characteristics of model I. Configuration BWVH; $\delta_h = 0^o$.

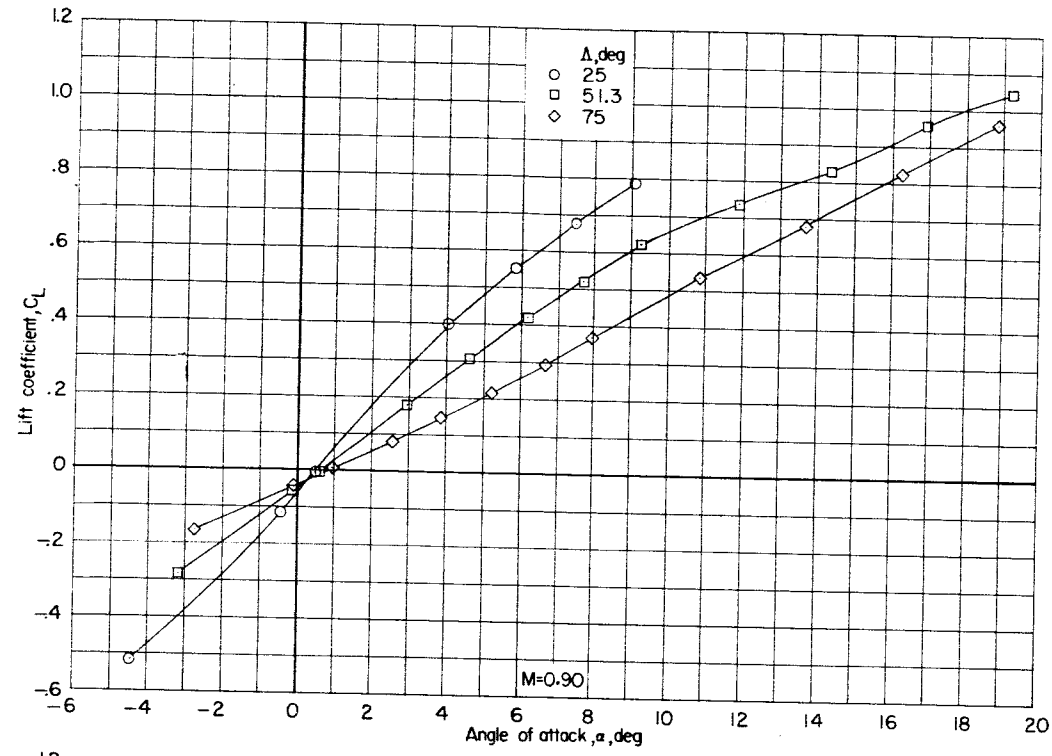

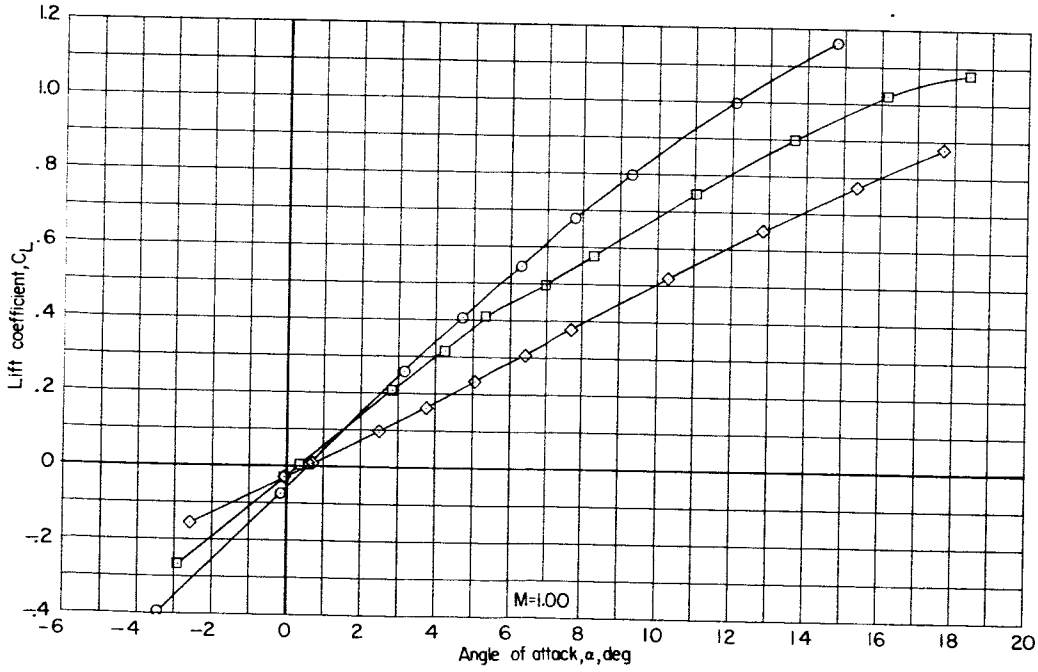

(a) Continued.

Figure 11.- Continued.

[redacted]

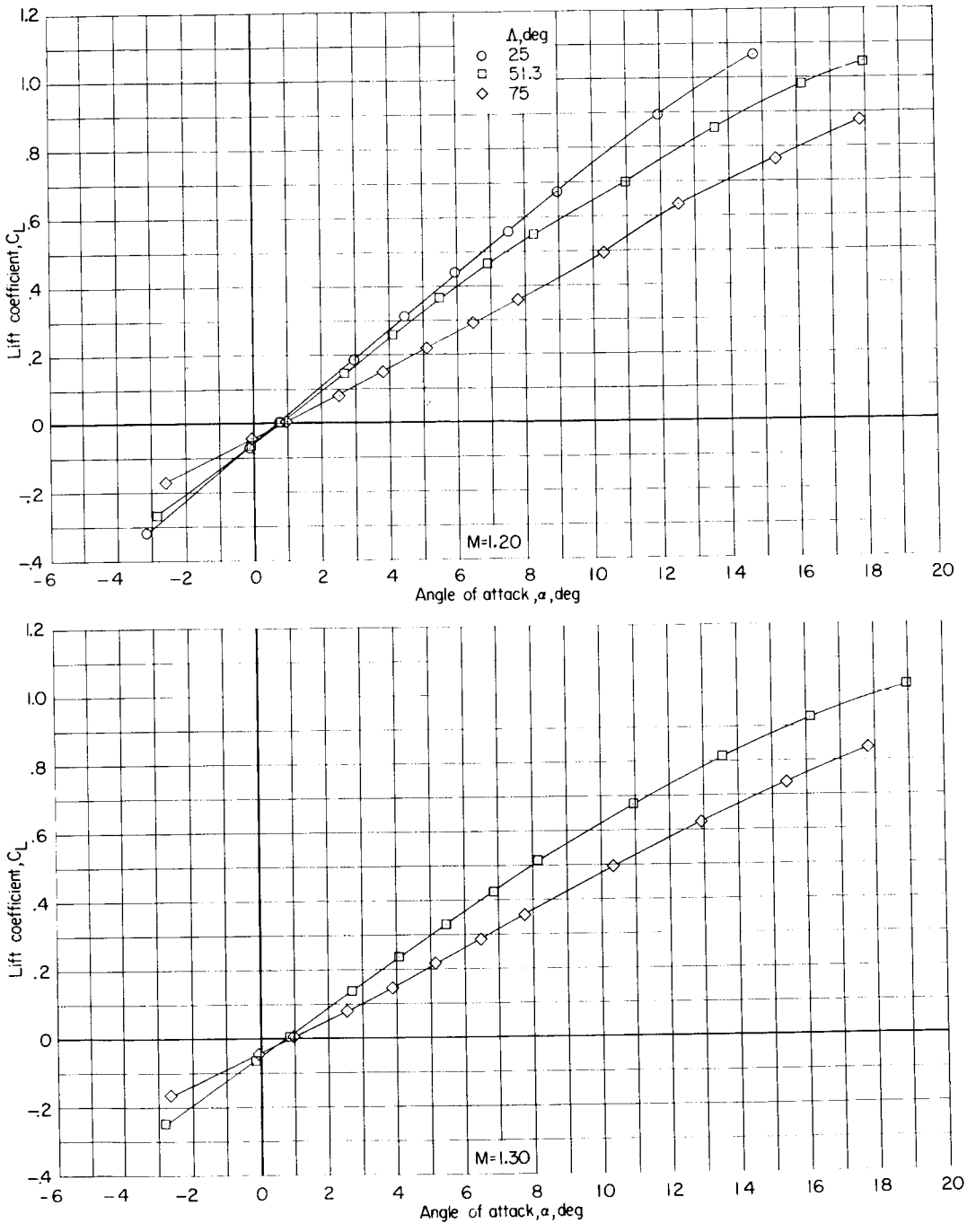

(a) Concluded.

Figure 11.- Continued.

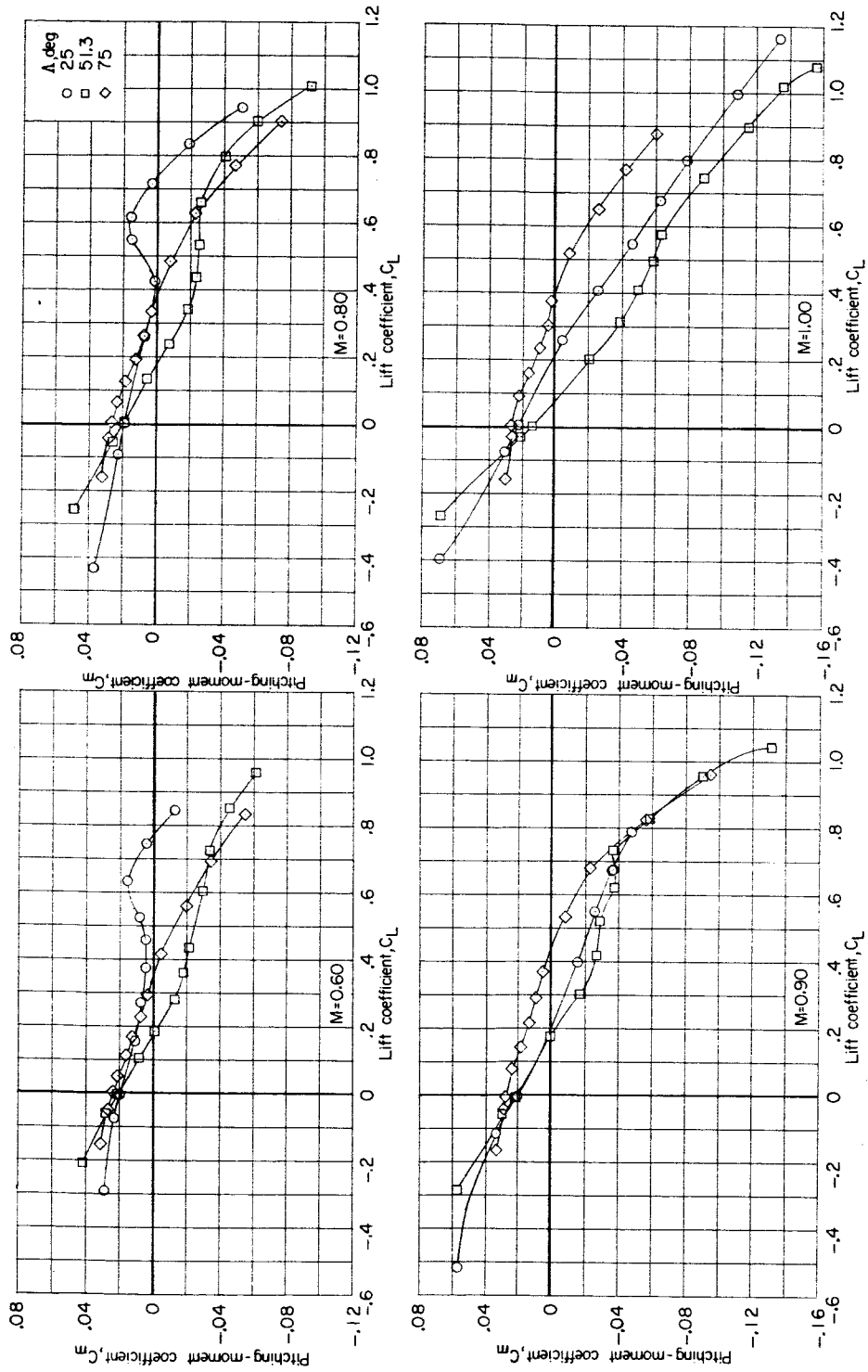

(b) C_m against C_L.

Figure 11.- Continued.

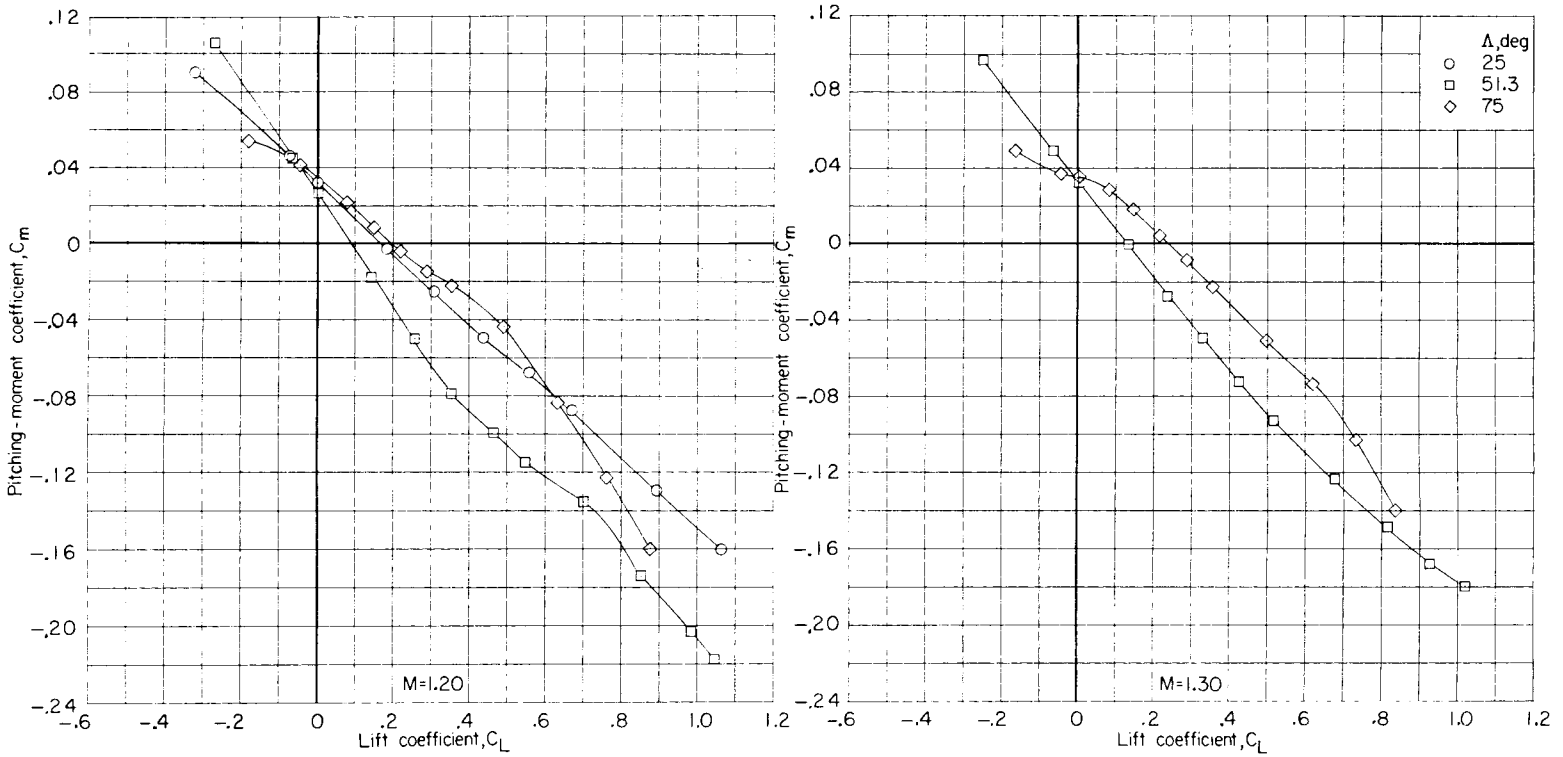

(b) Concluded.

Figure 11.- Continued.

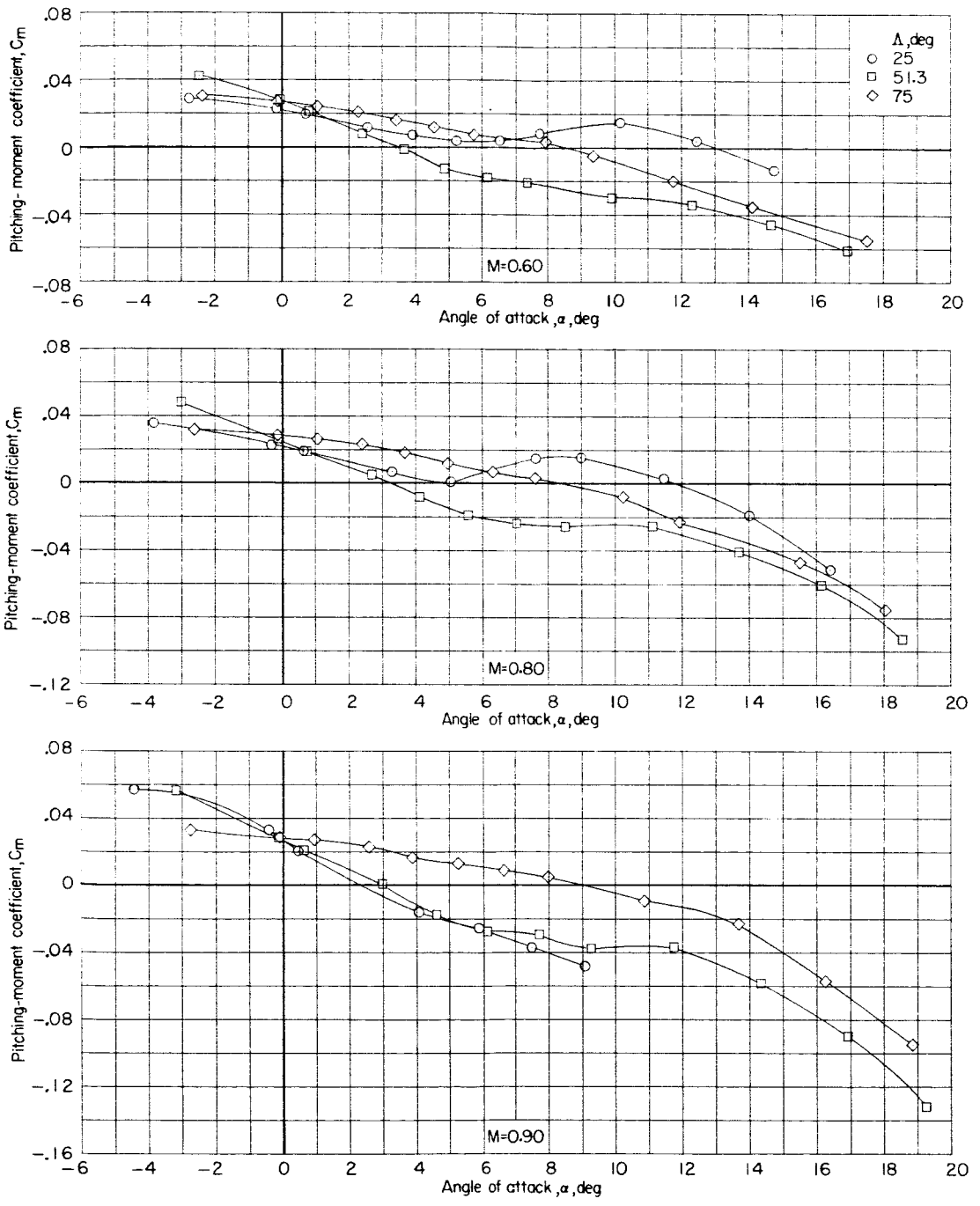

(c) C_m against α.

Figure 11.- Continued.

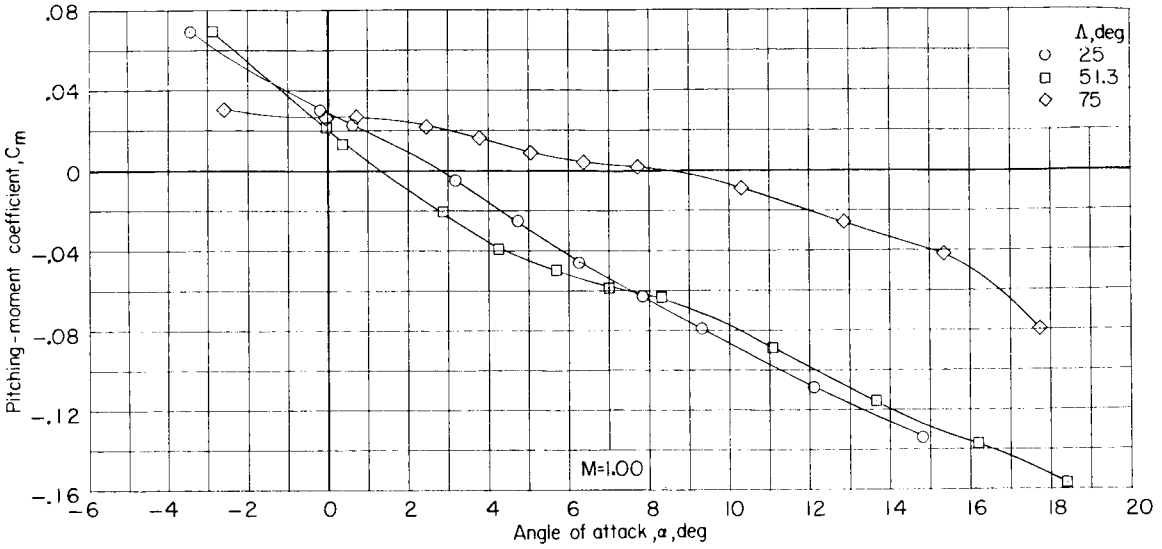

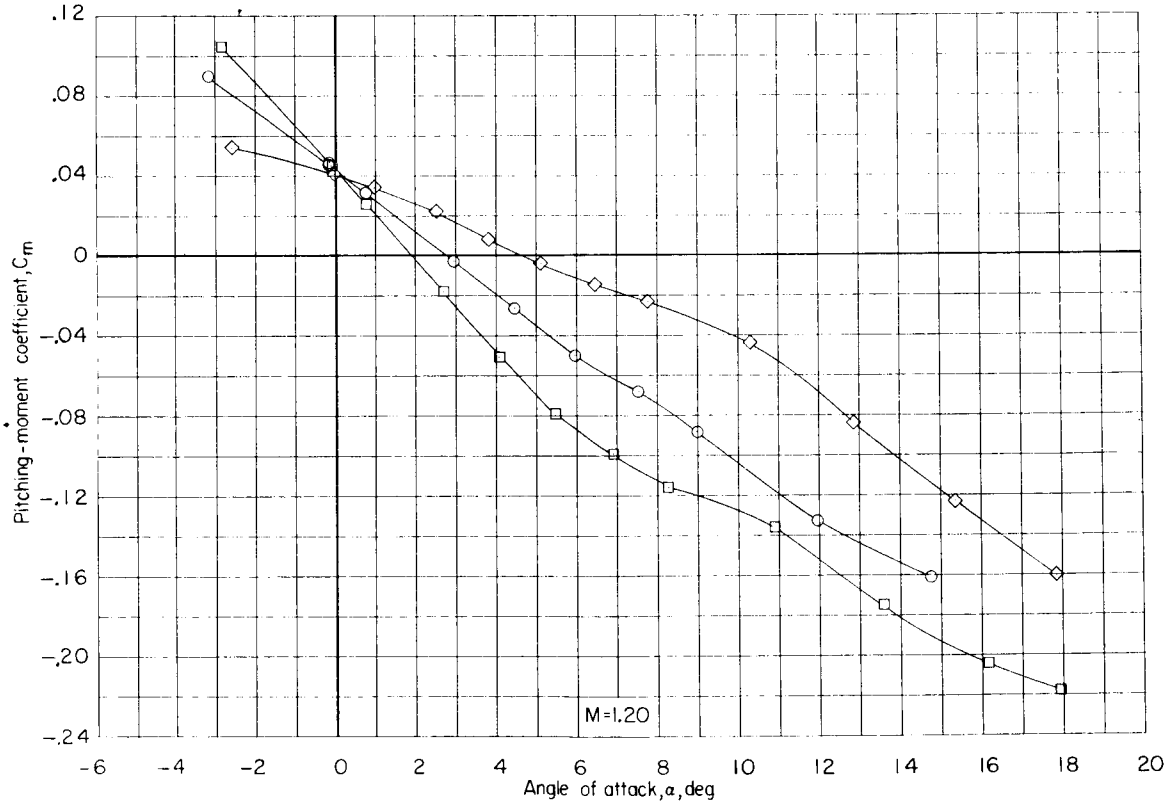

(c) Continued.

Figure 11.- Continued.

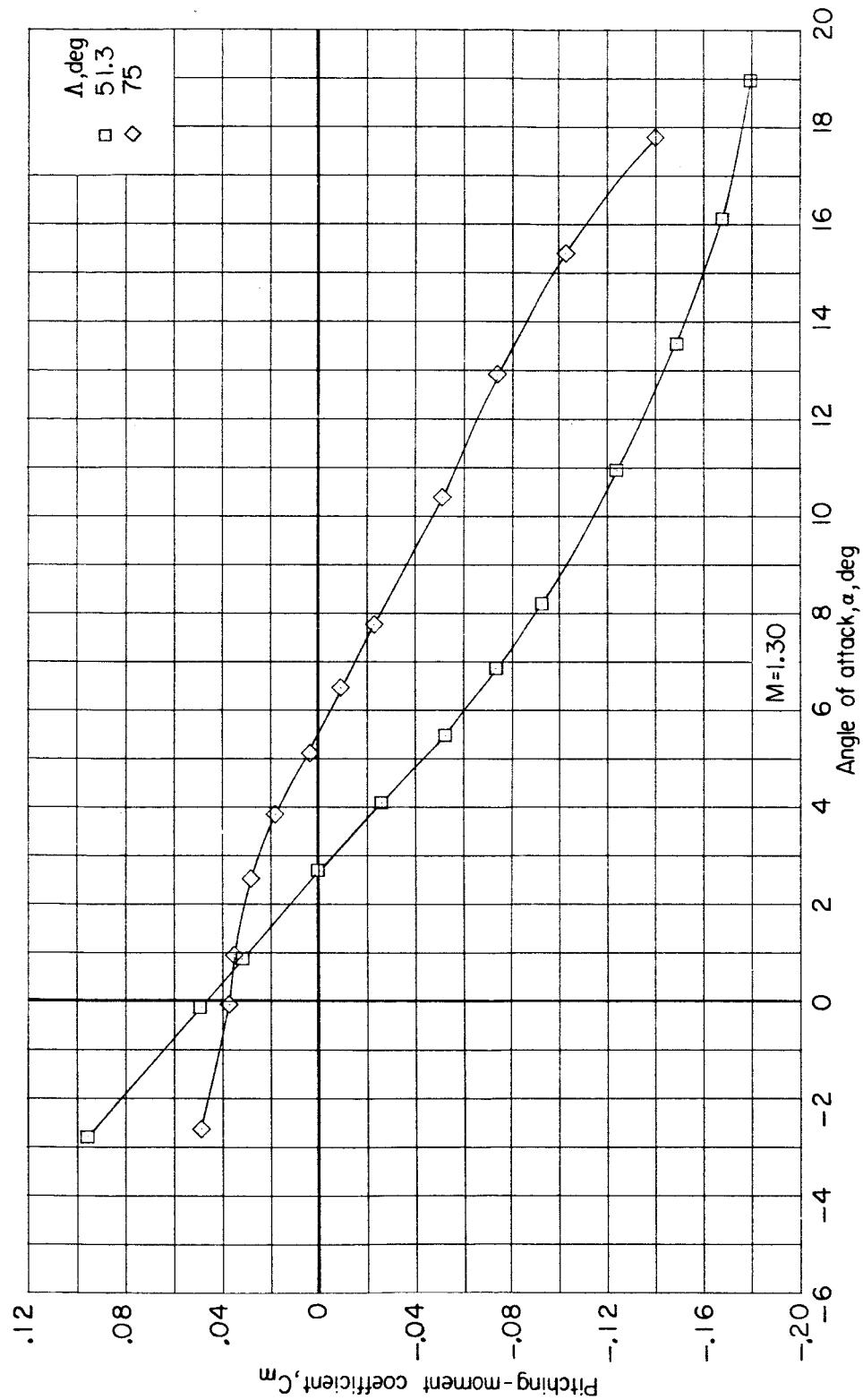

(c) Concluded.

Figure 11.- Continued.

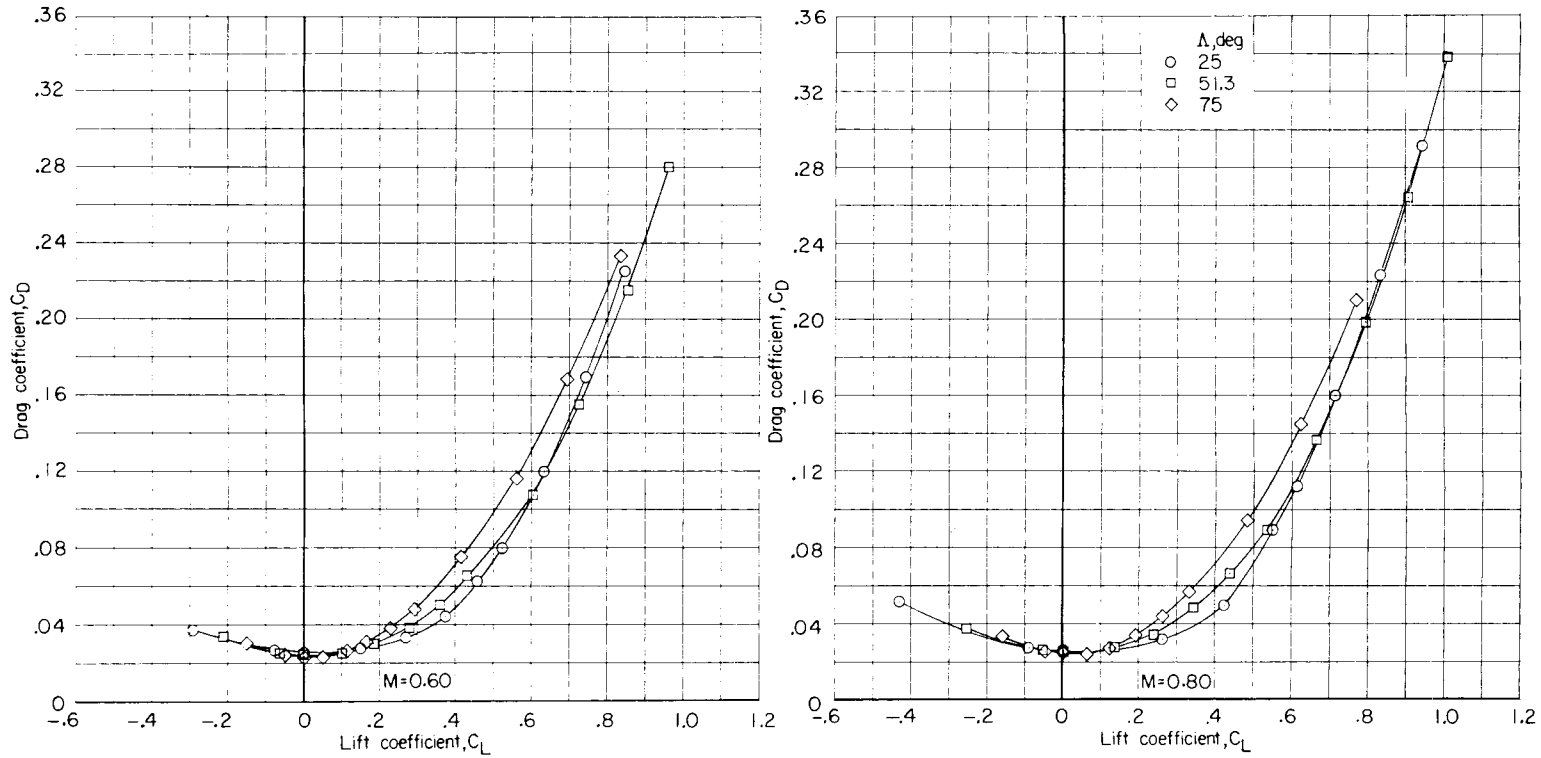

(d) C_D against C_L.

Figure 11.- Continued.

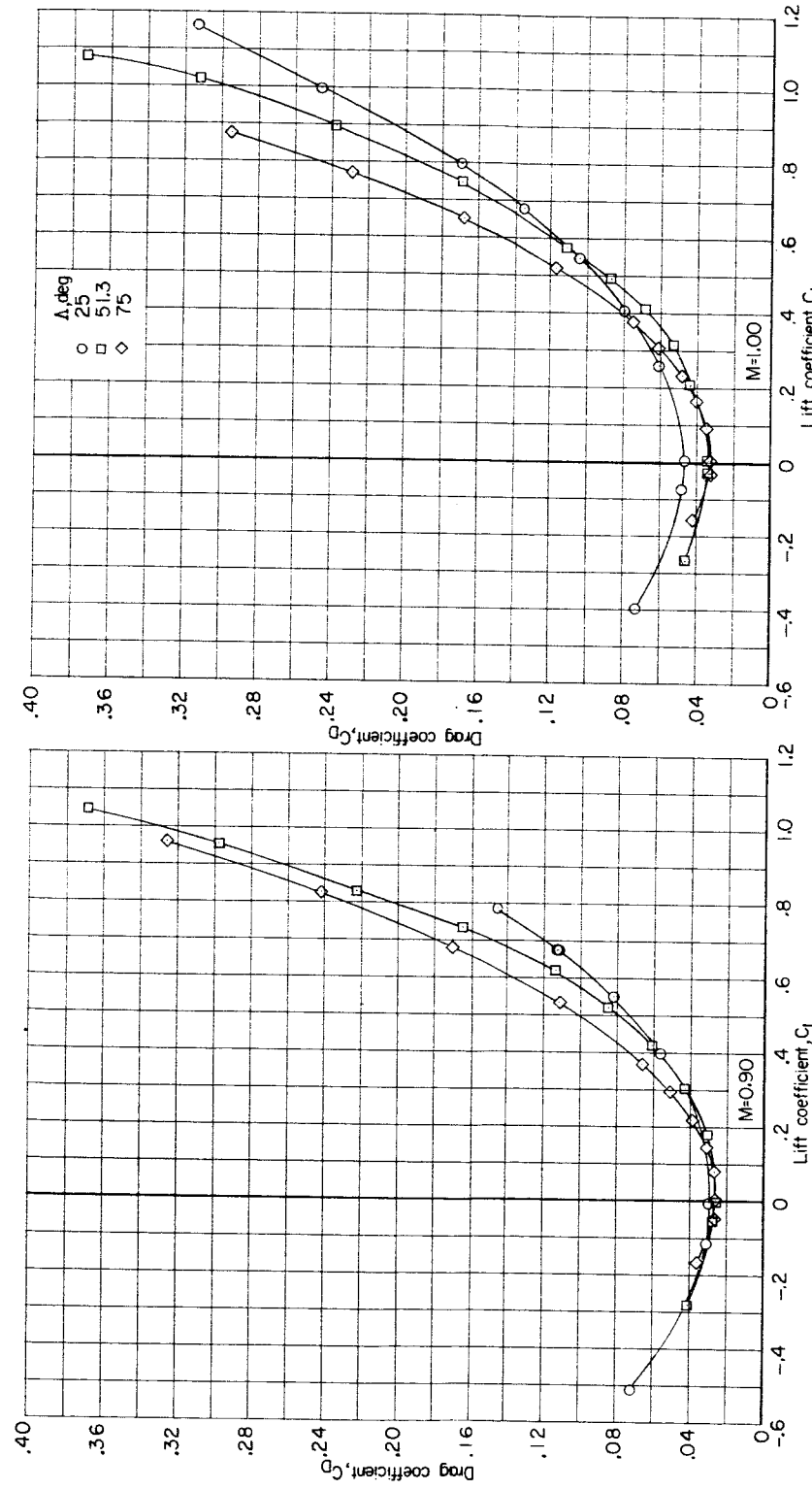

(d) Continued.

Figure 11.- Continued.

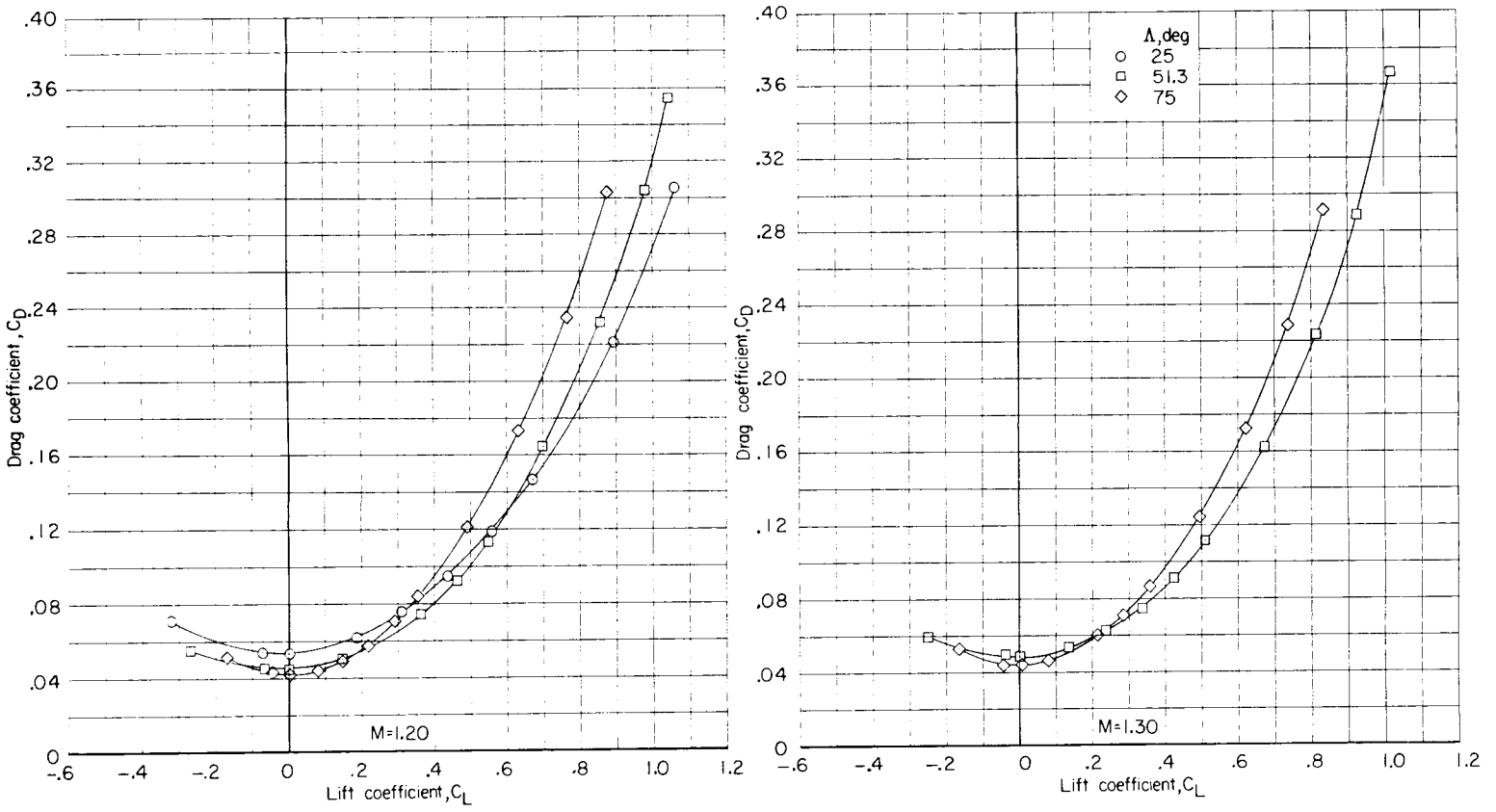

(d) Concluded.

Figure 11.- Continued.

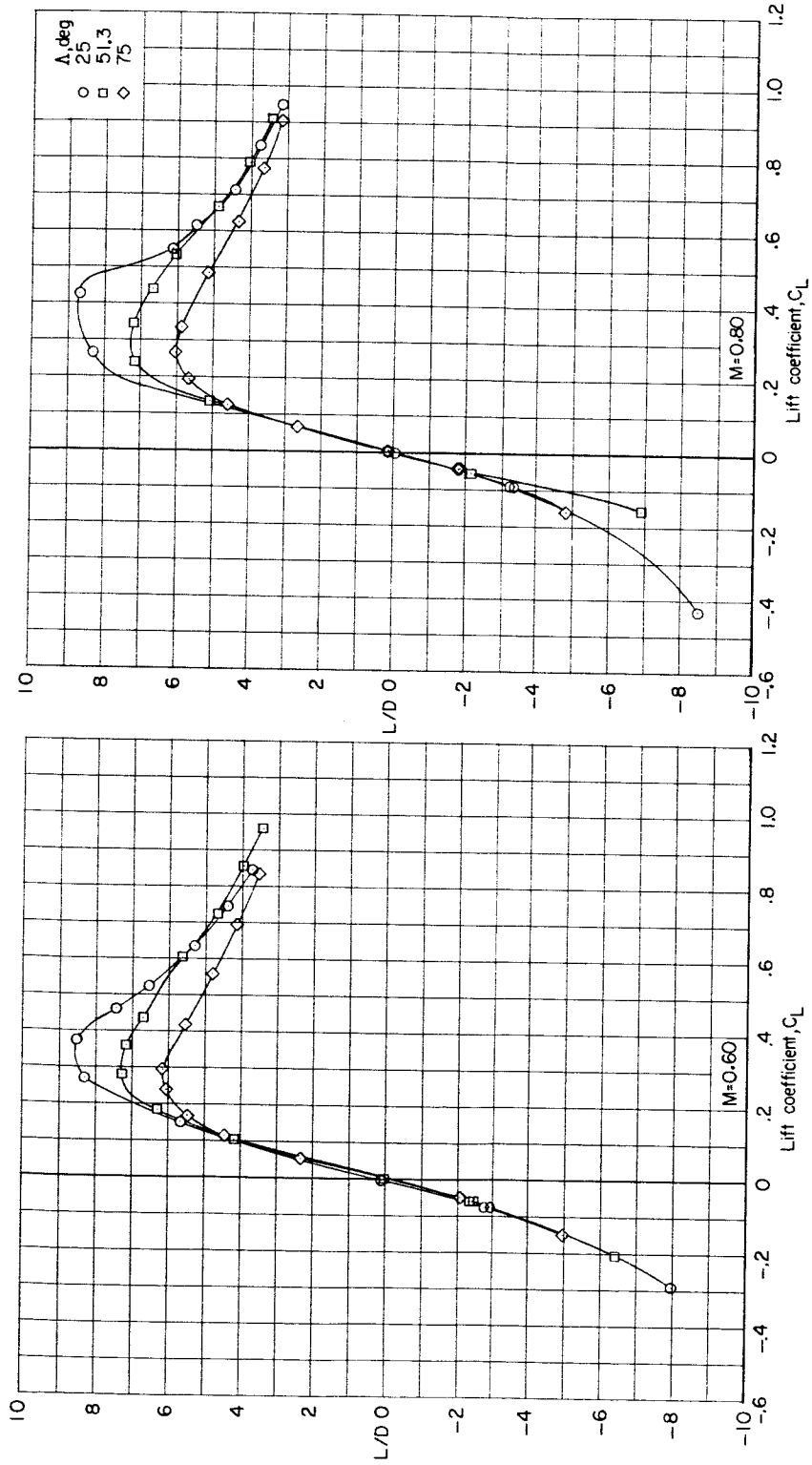

(e) L/D against C_L.

Figure 11.- Continued.

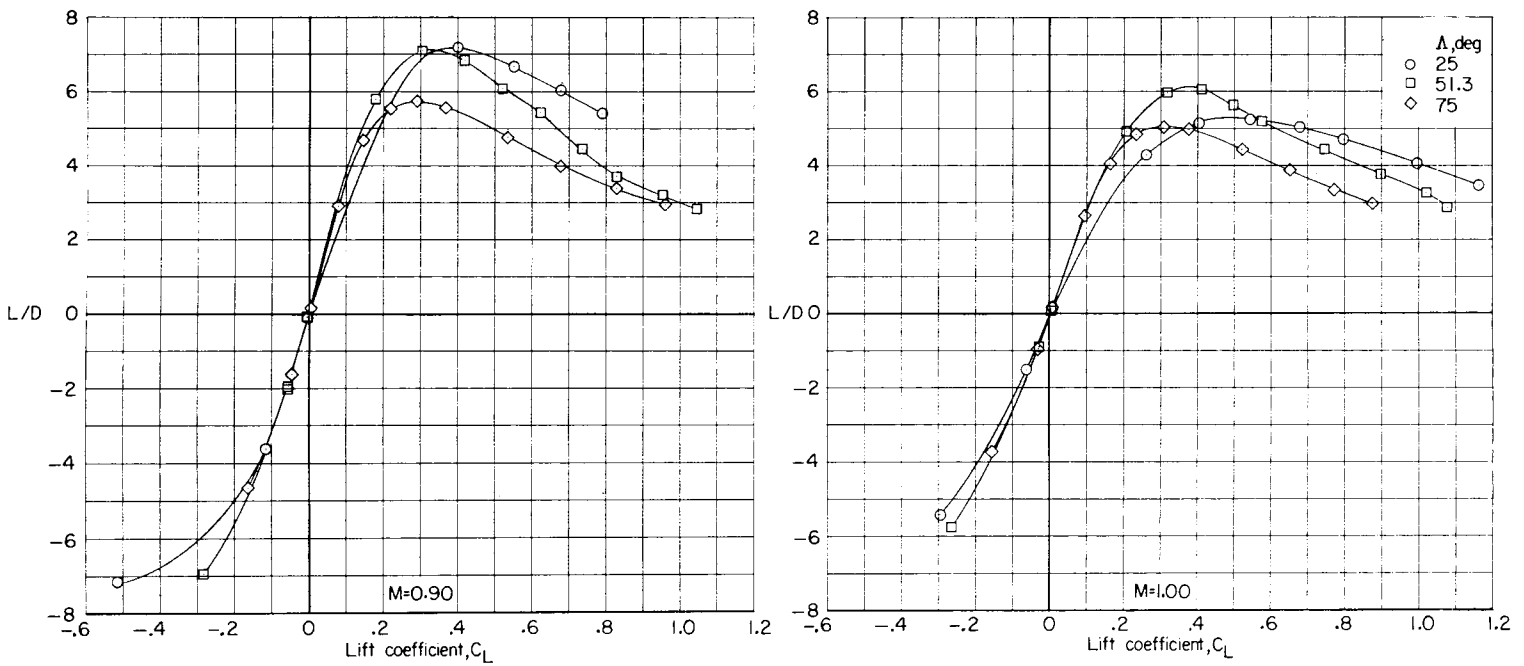

(e) Continued.

Figure 11.- Continued.

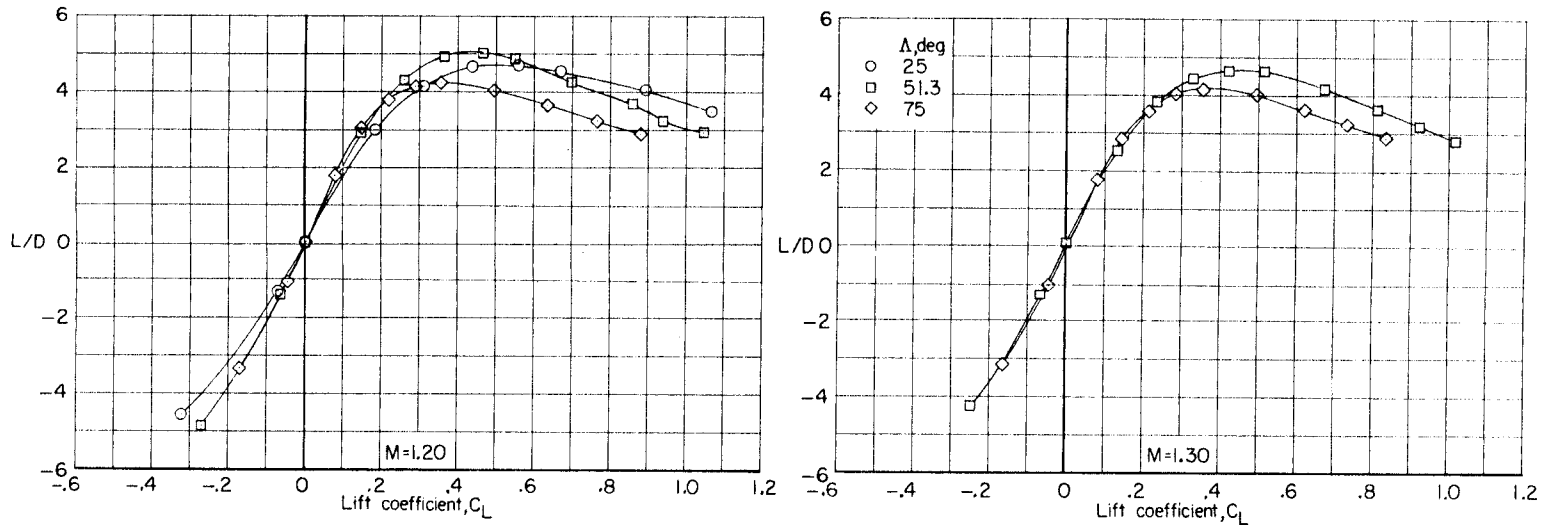

(e) Concluded.

Figure 11.- Concluded.

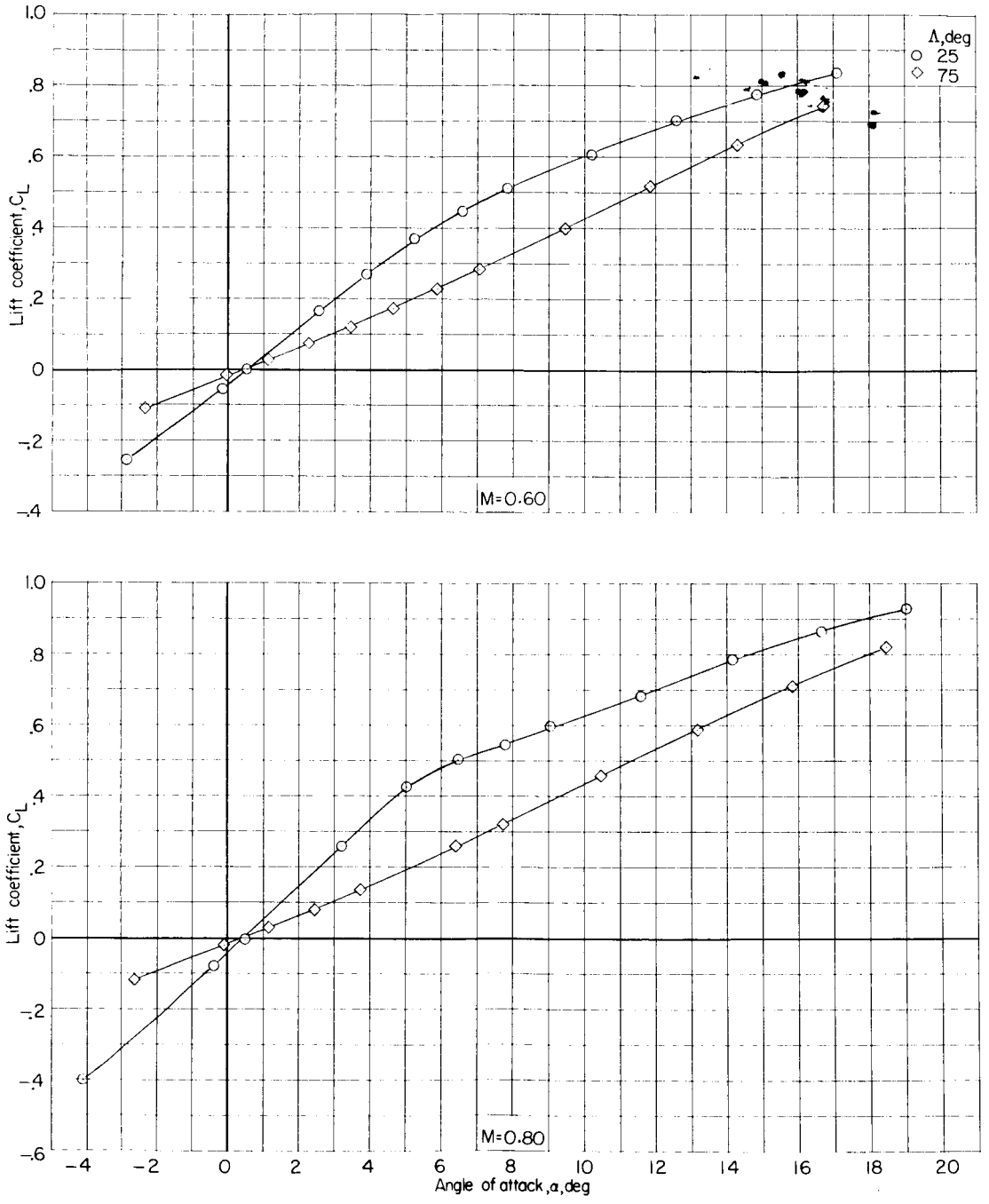

(a) C_L against α.

Figure 12.- Effect of wing sweep on longitudinal aerodynamic characteristics of model I with horizontal tail off. Configuration BWV.

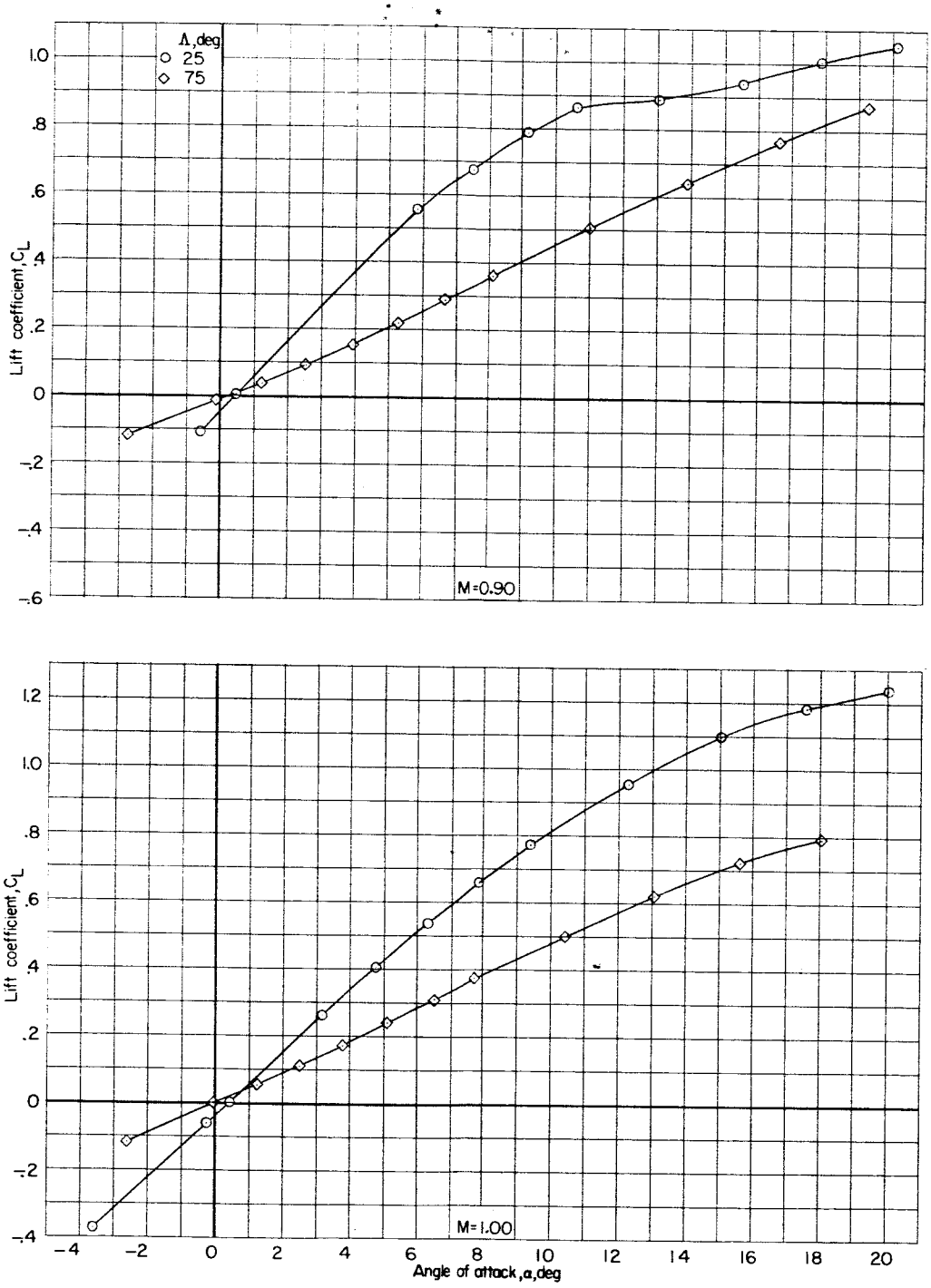

(a) Continued.

Figure 12.- Continued.

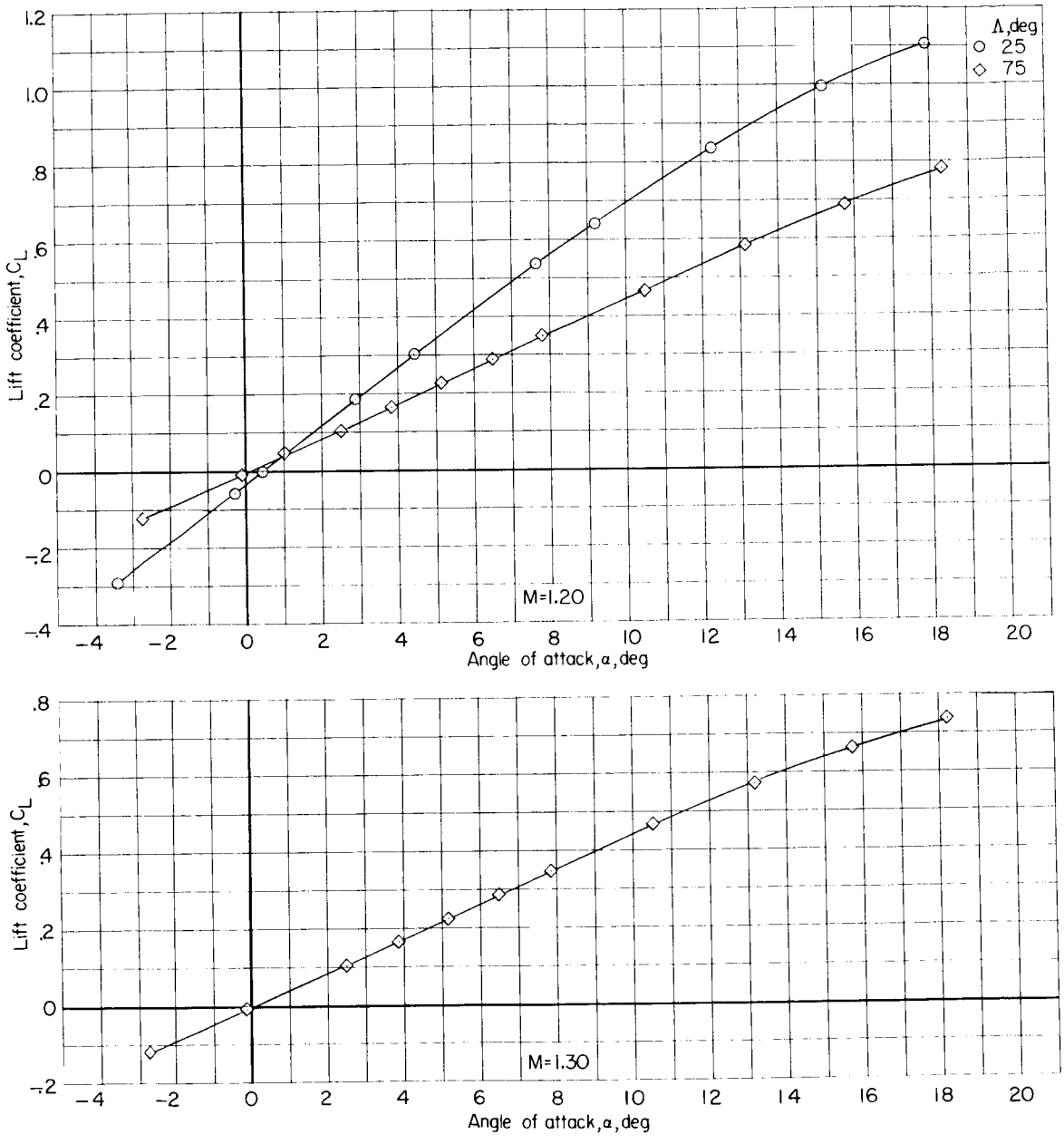

(a) Concluded.

Figure 12.- Continued.

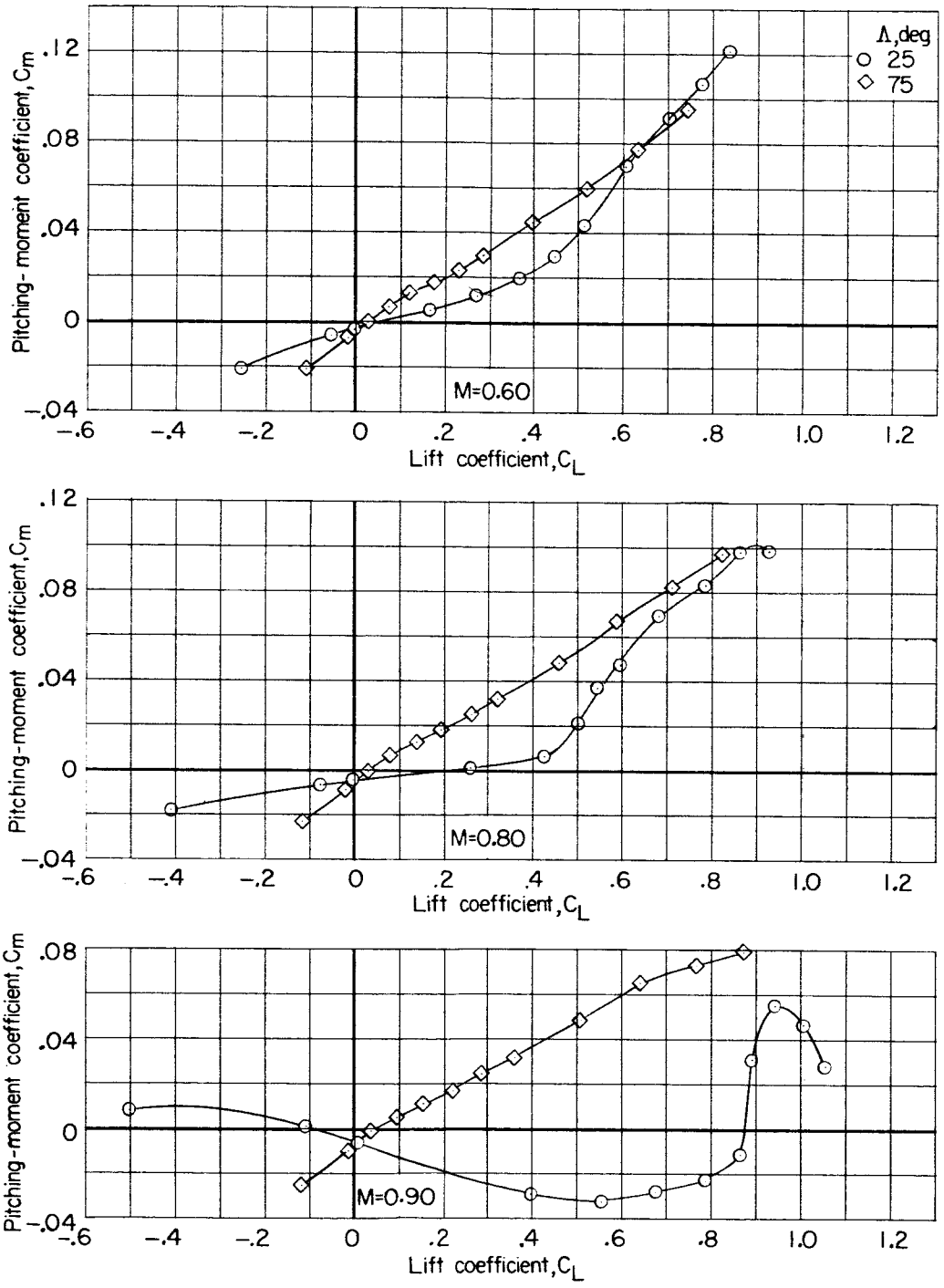

(b) C_m against C_L.

Figure 12.- Continued.

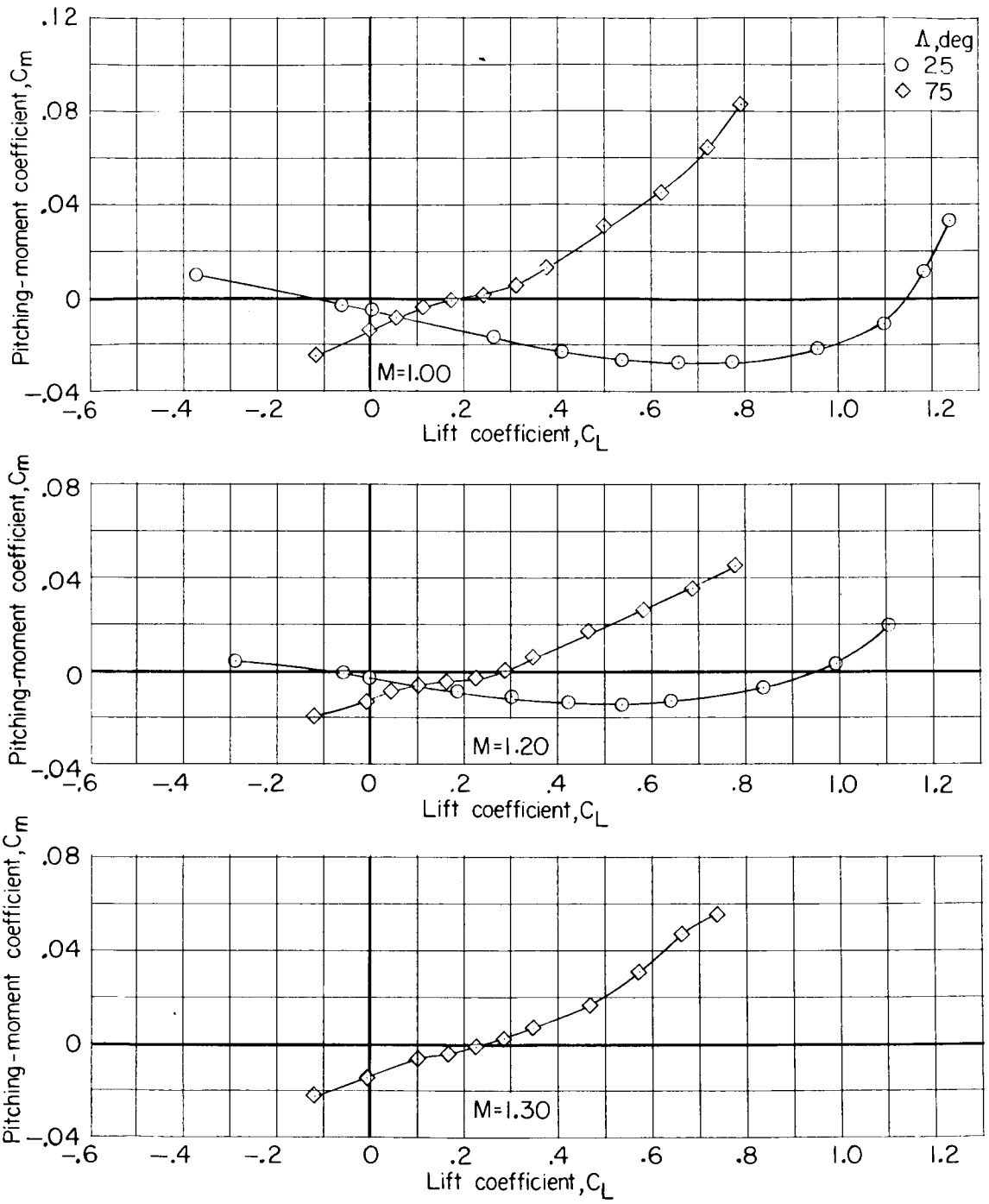

(b) Concluded.

Figure 12.- Continued.

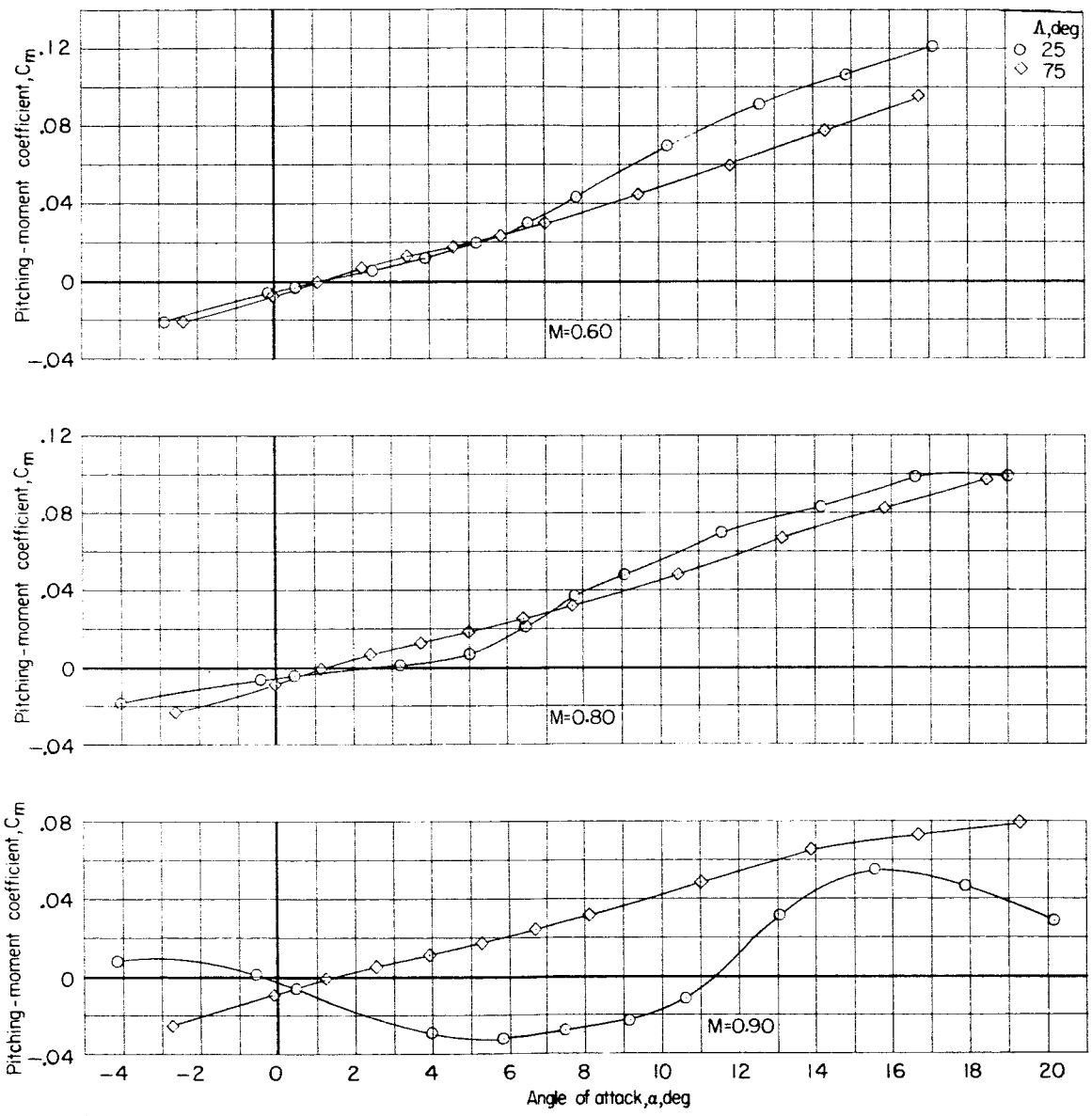

(c) C_m against α.

Figure 12.- Continued.

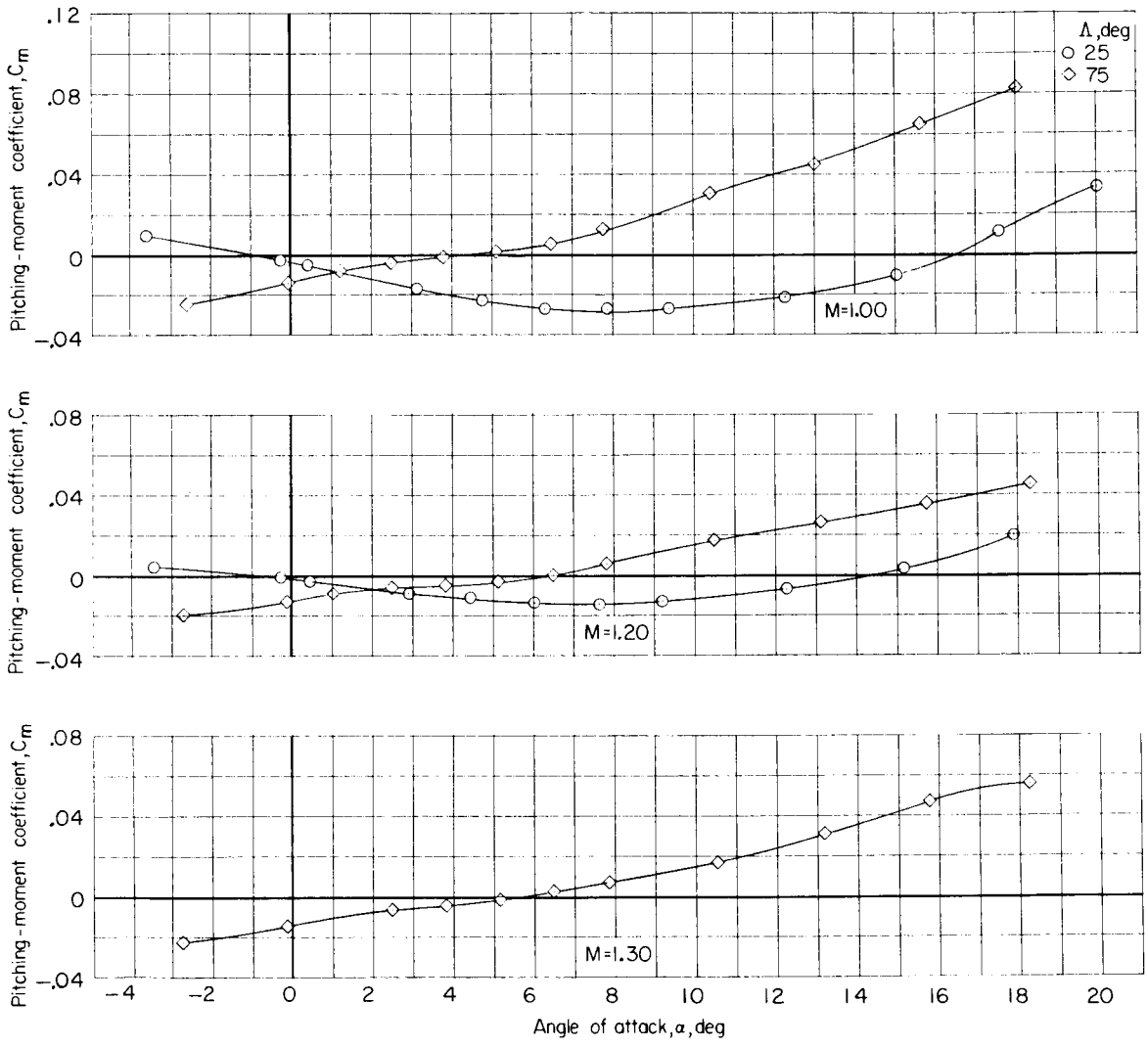

(c) Concluded.

Figure 12.- Continued.

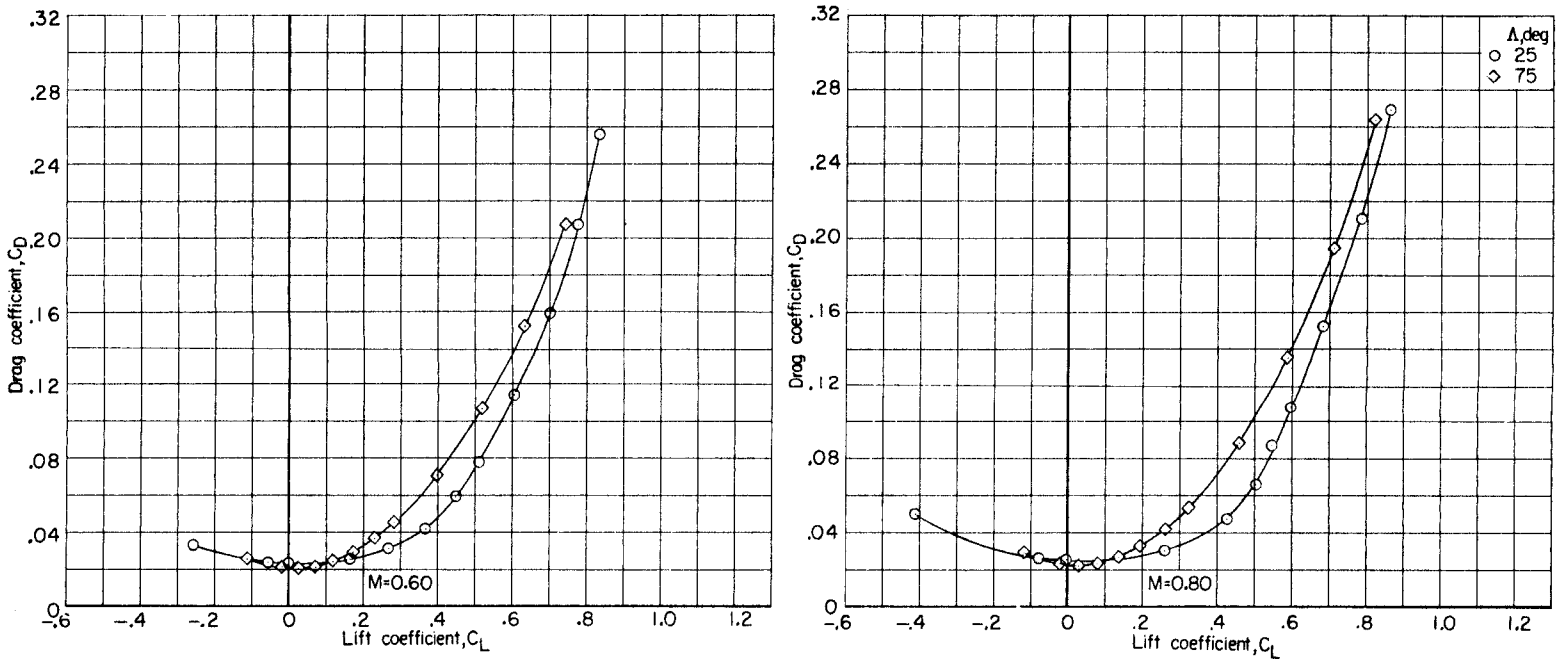

(d) C_D against C_L.

Figure 12.- Continued.

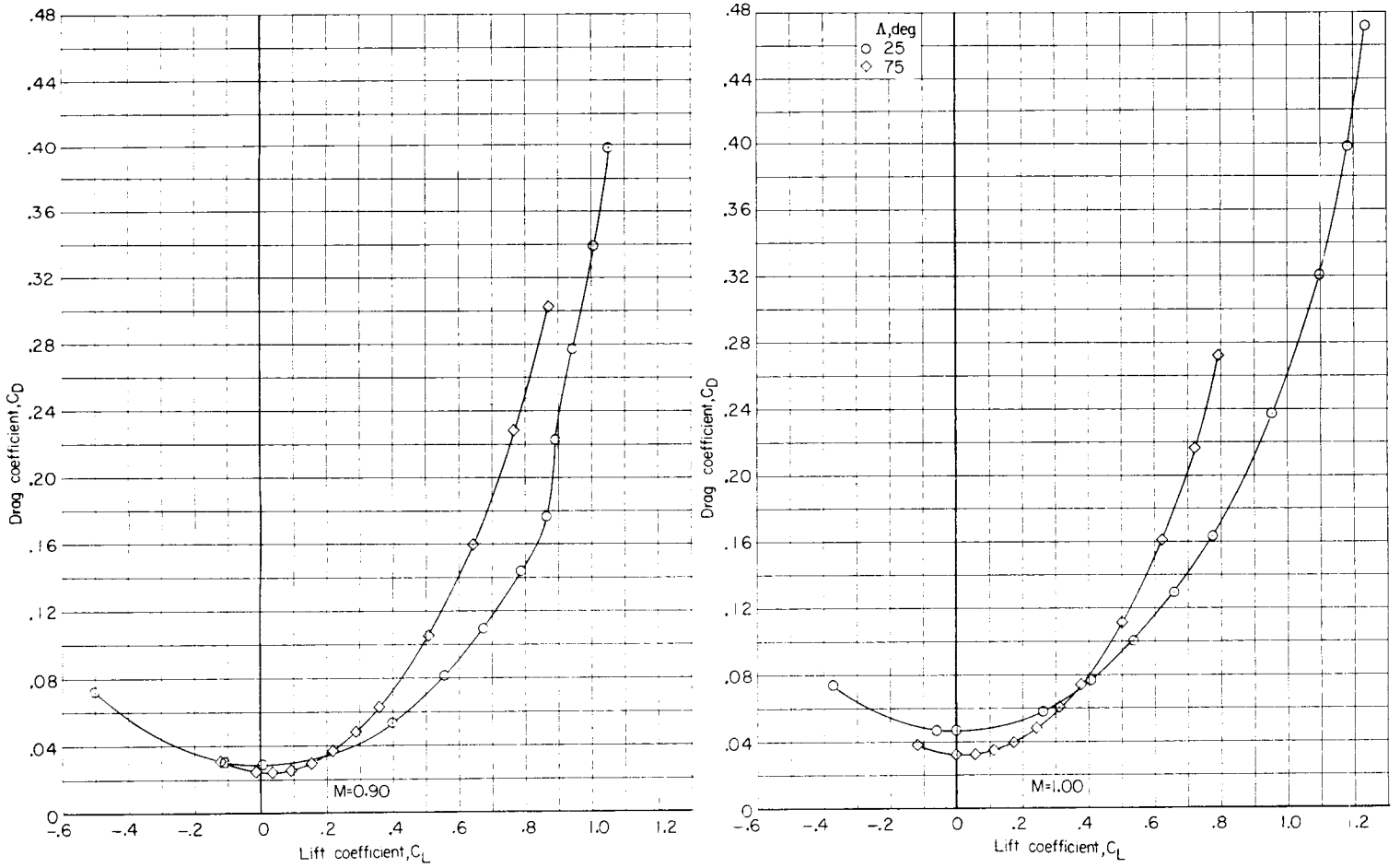

(d) Continued.

Figure 12.- Continued.

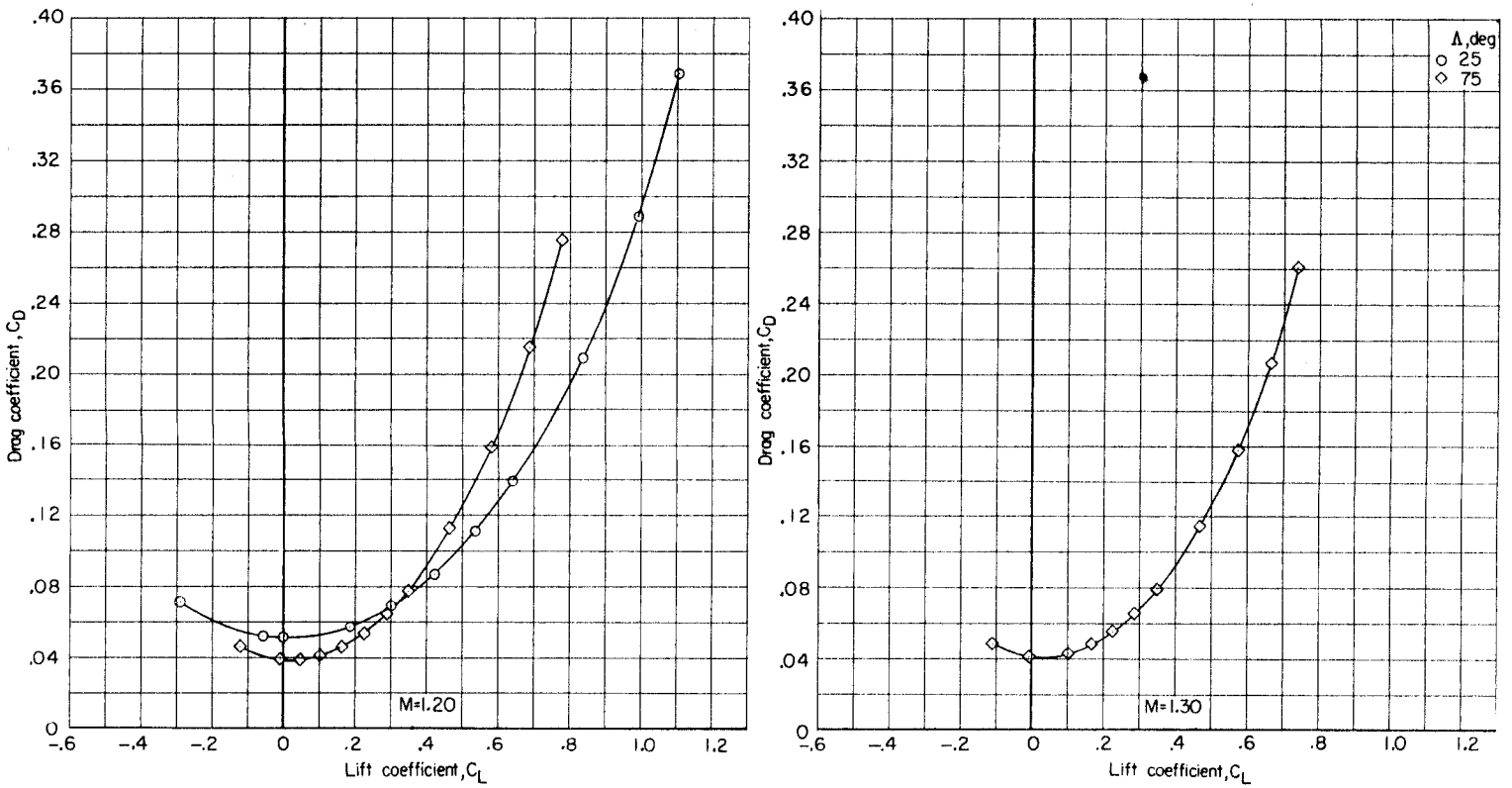

(d) Concluded.

Figure 12.- Continued.

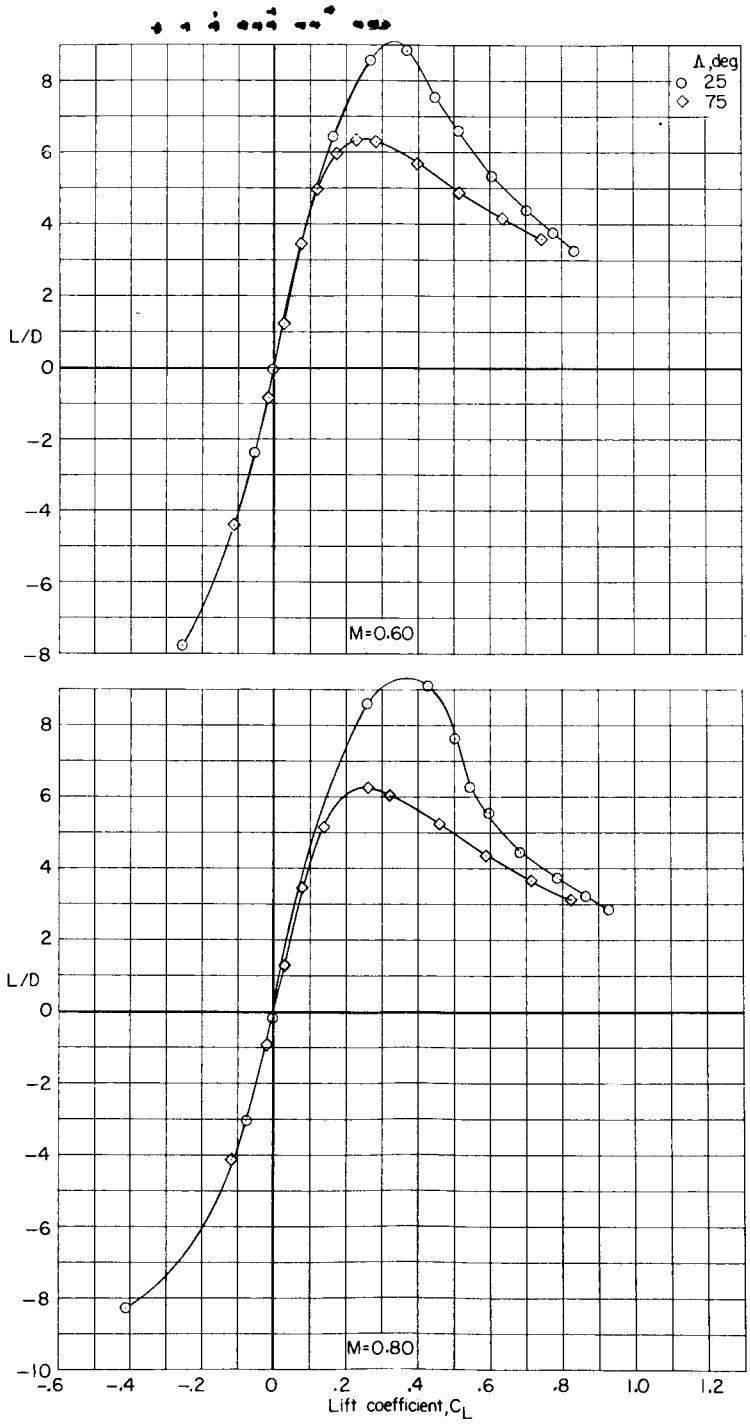

(e) L/D against C_L.

Figure 12.- Continued.

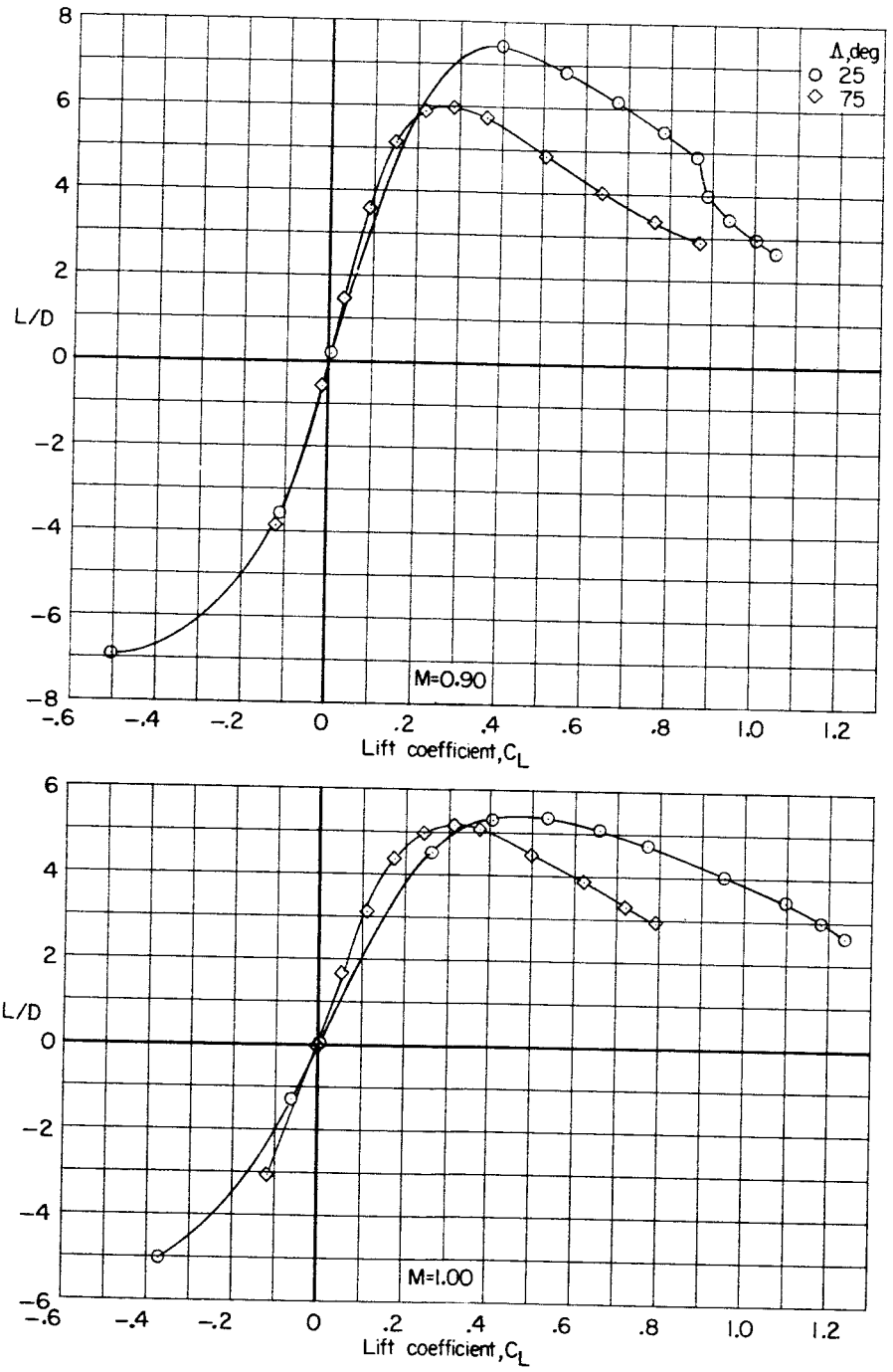

(e) Continued.

Figure 12.- Continued.

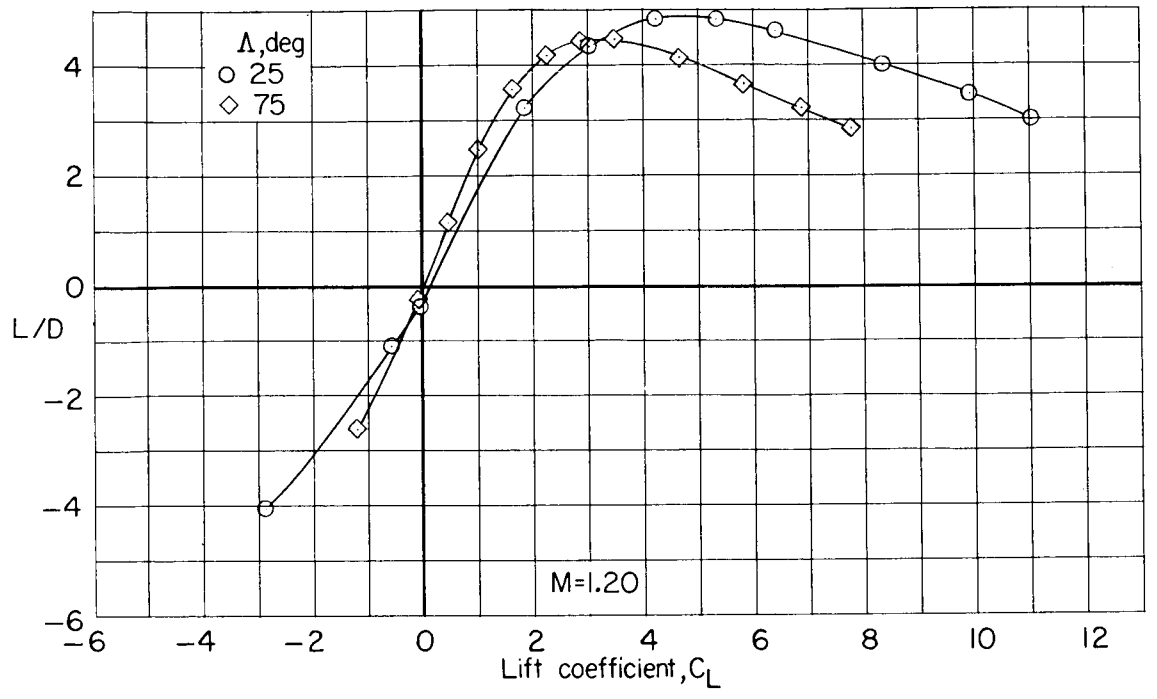

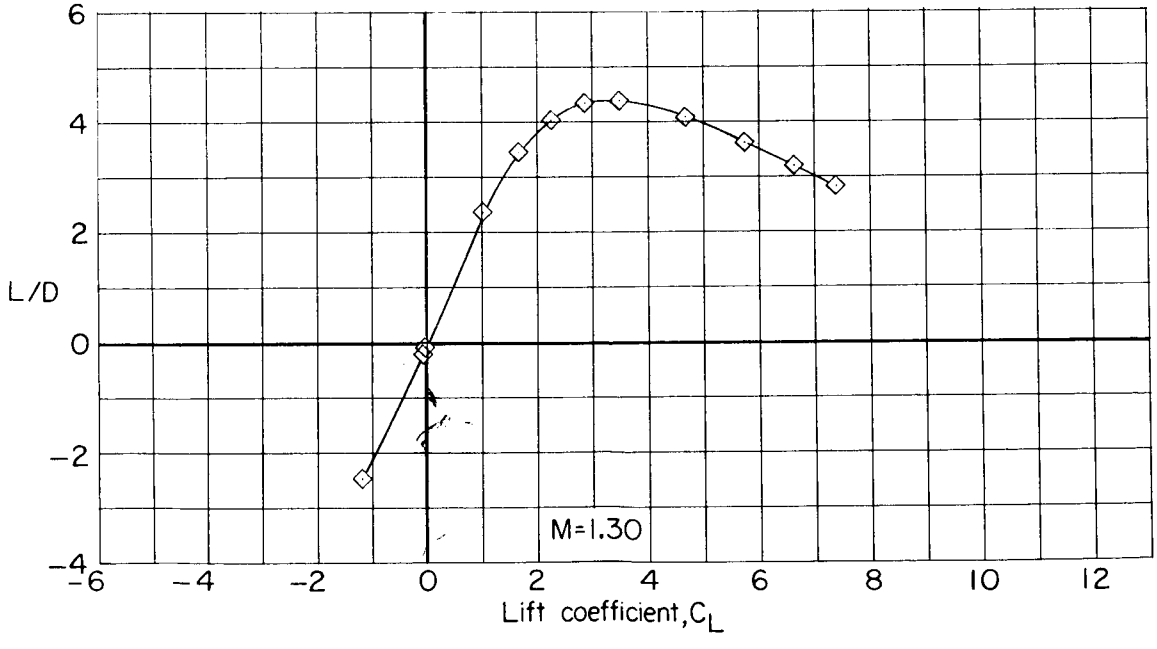

(e) Concluded.

Figure 12.- Concluded.

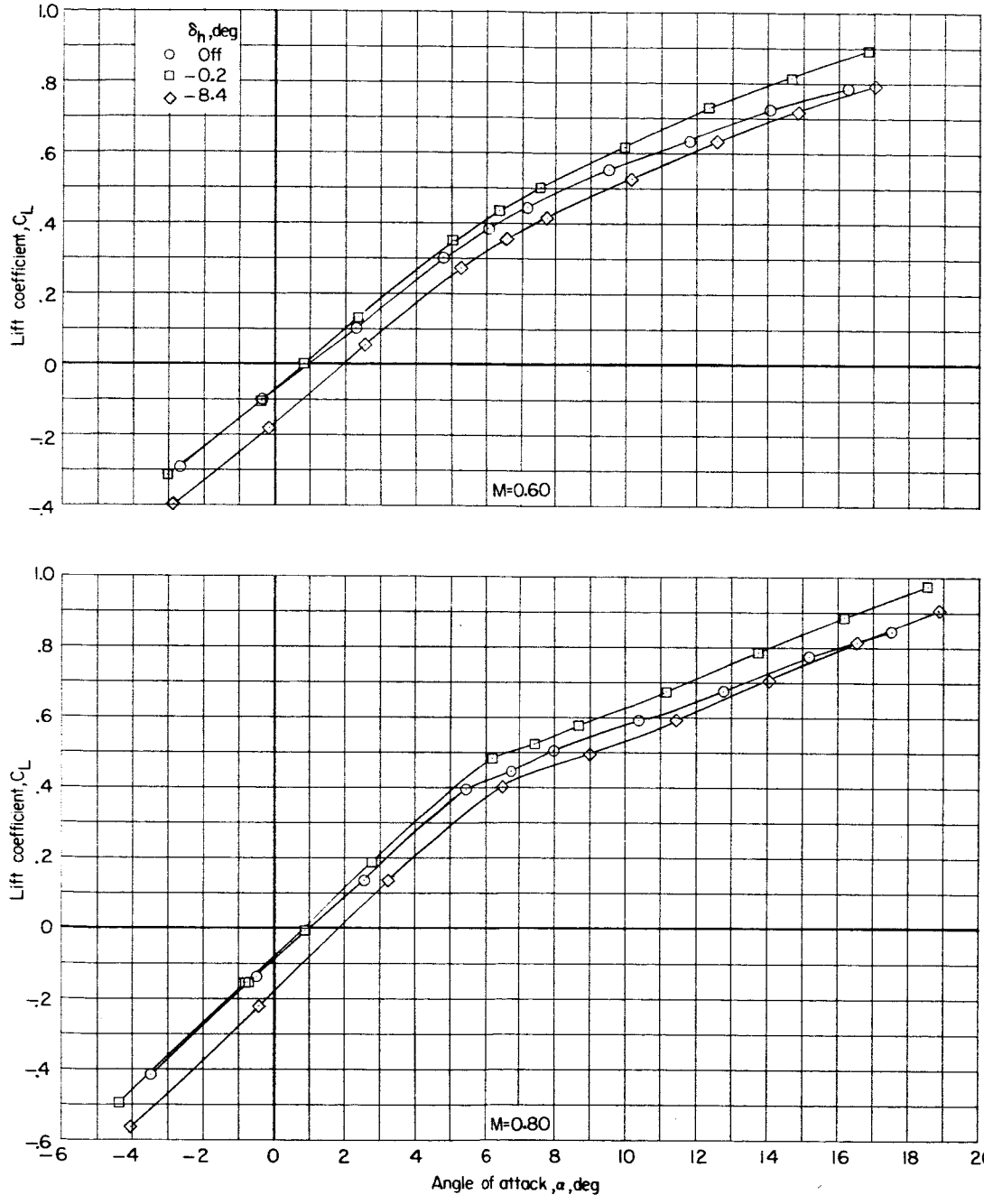

(a) C_L against α.

Figure 13.- Effect of horizontal-tail deflection on longitudinal aerodynamic characteristics of model II with 25° swept wing. Configuration BW_1VH.

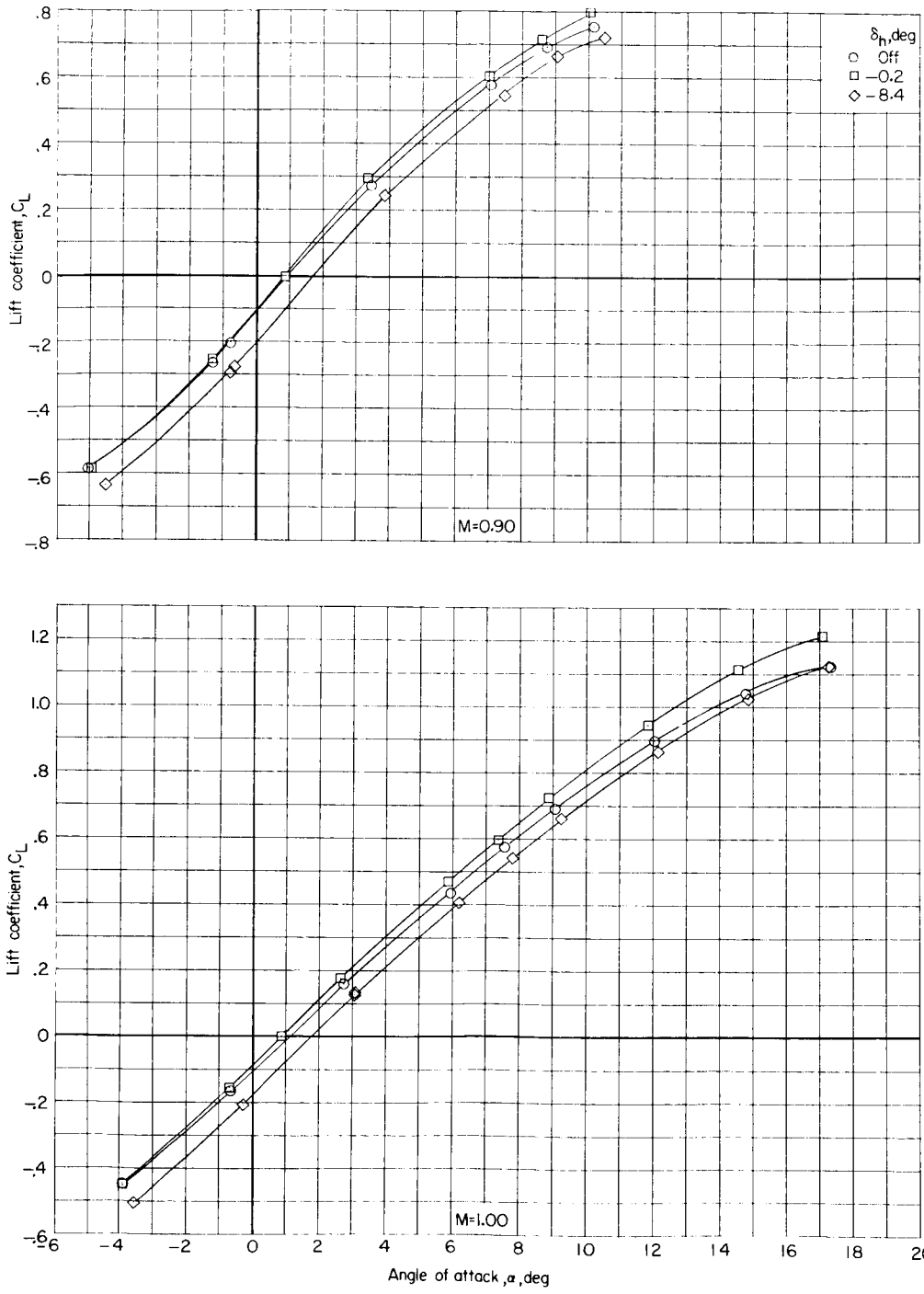

(a) Continued.

Figure 13.- Continued.

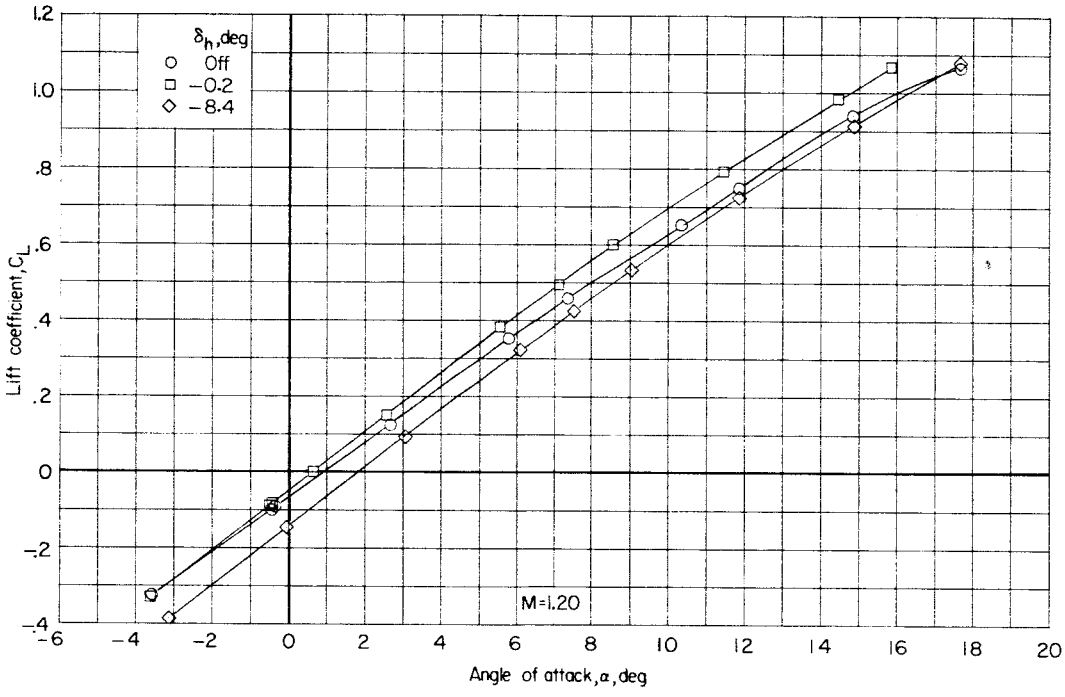

(a) Concluded.

Figure 13.- Continued.

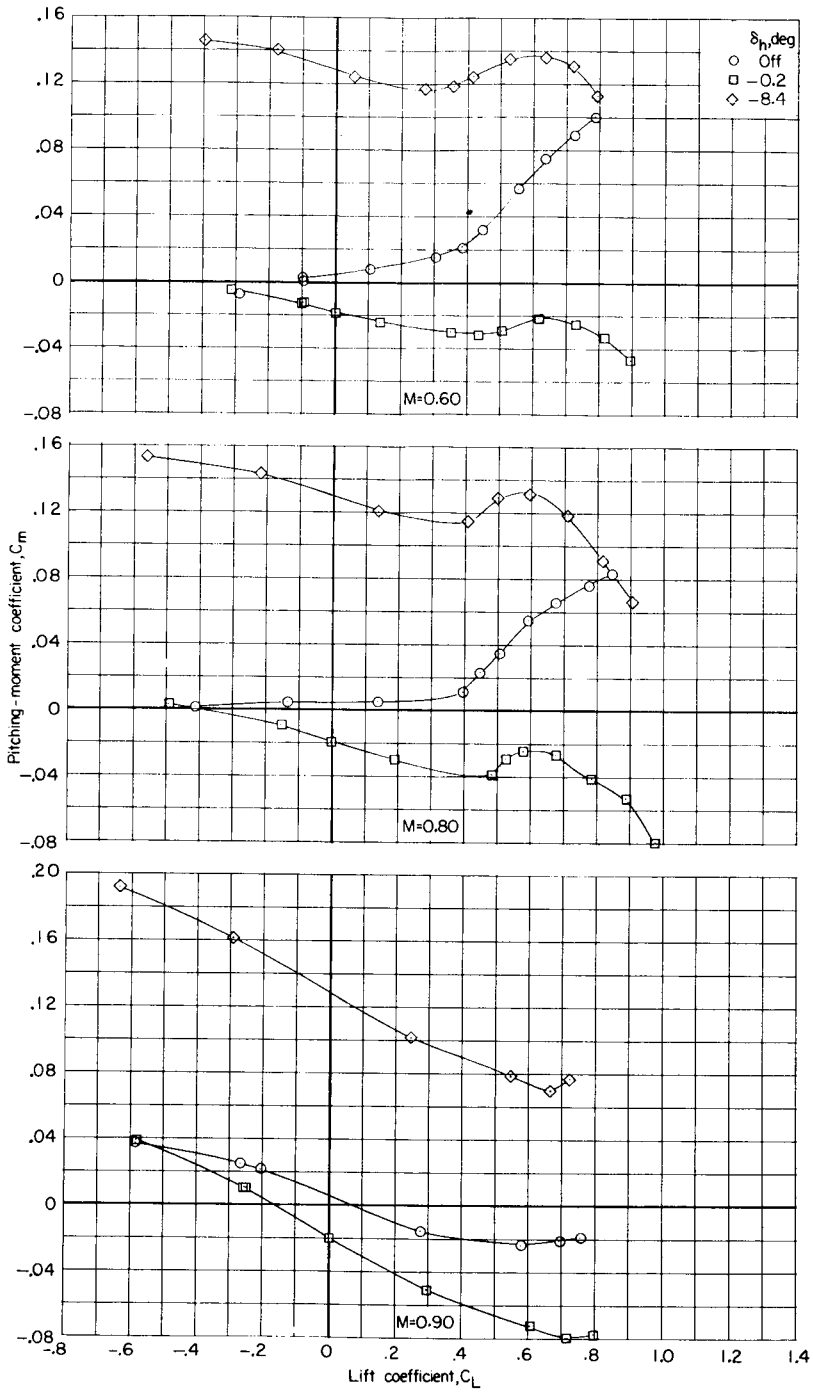

(b) C_m against C_L.

Figure 13.- Continued.

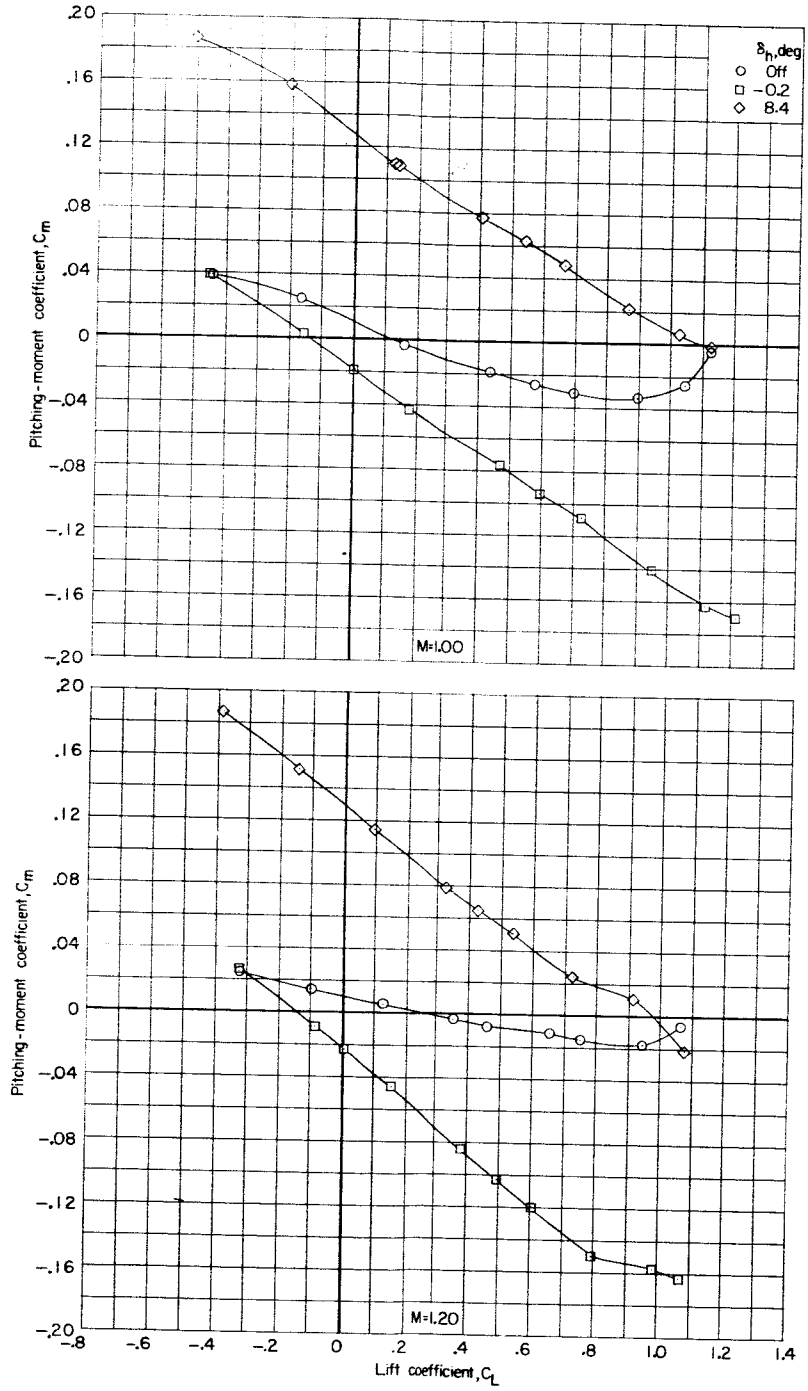

(b) Concluded.

Figure 13.- Continued.

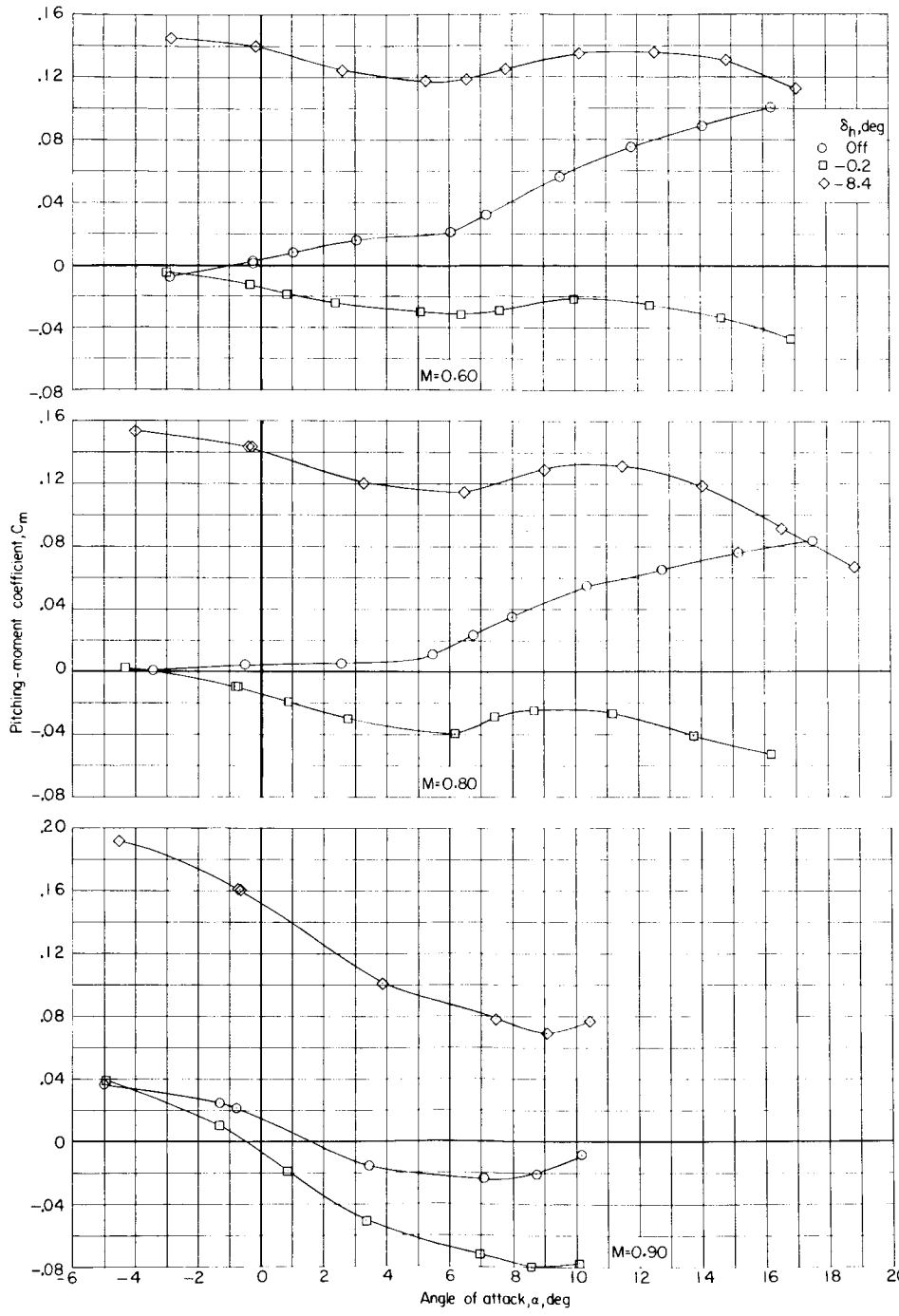

(c) C_m against α.

Figure 13.- Continued.

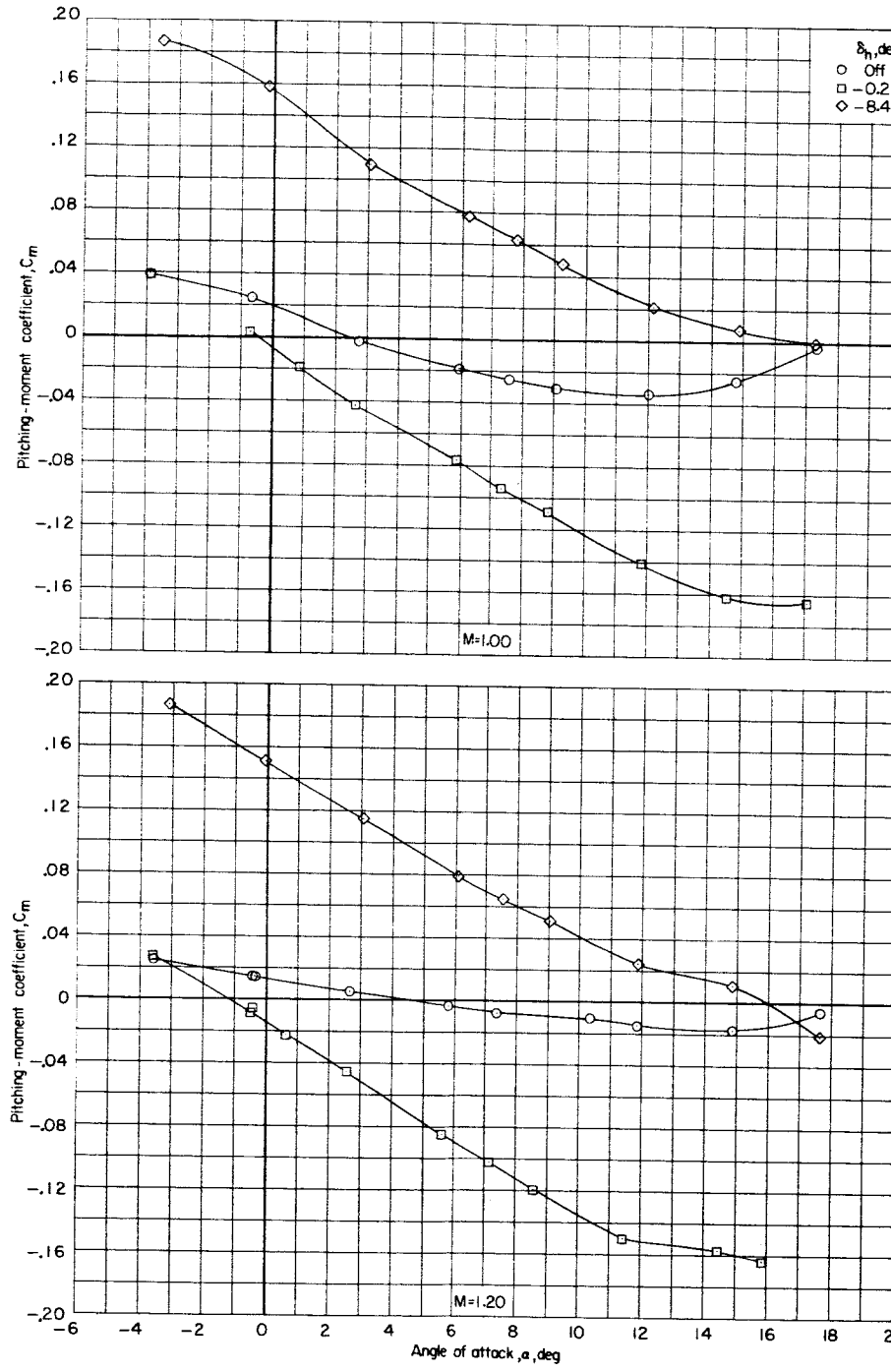

(c) Concluded.

Figure 13.- Continued.

[redacted]

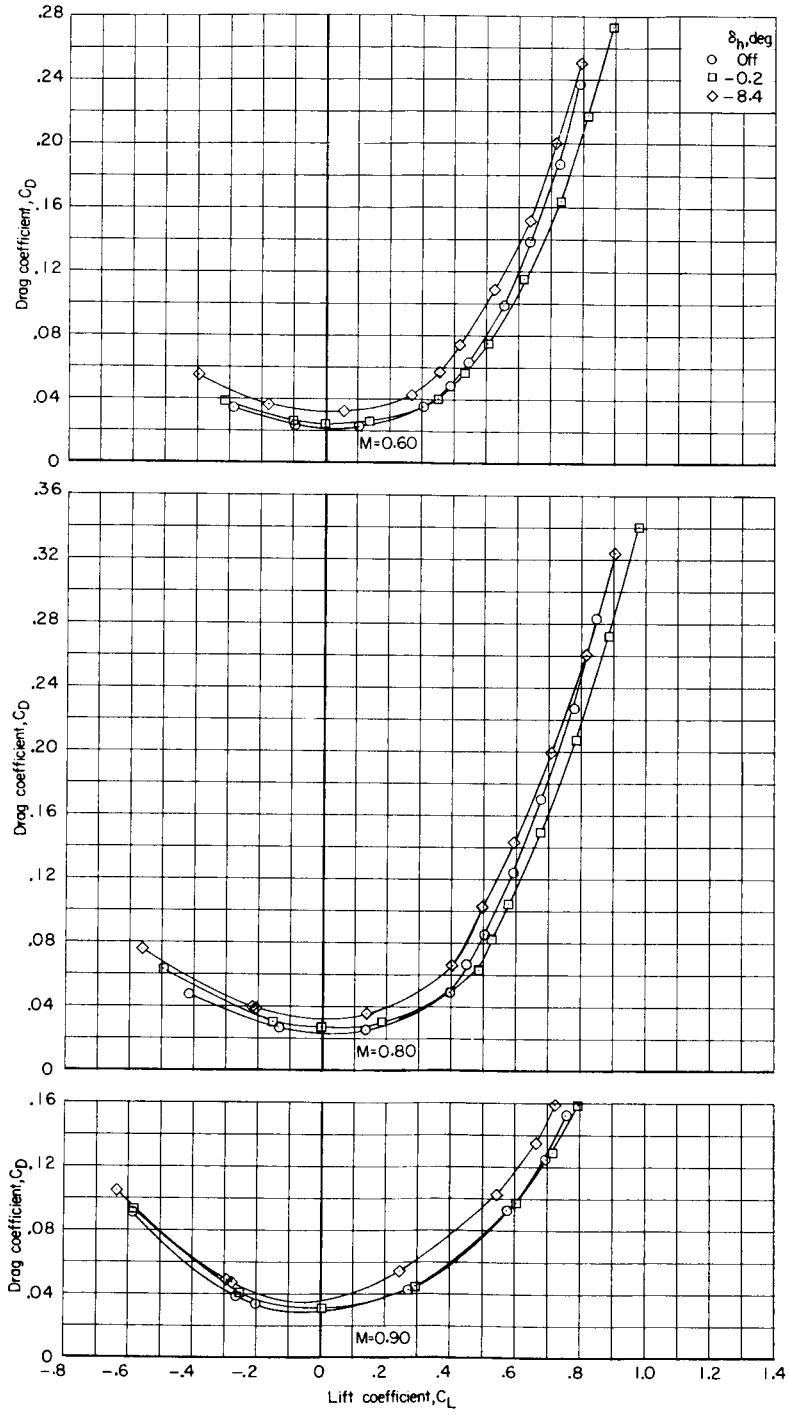

(d) C_D against C_L.

Figure 13.- Continued.

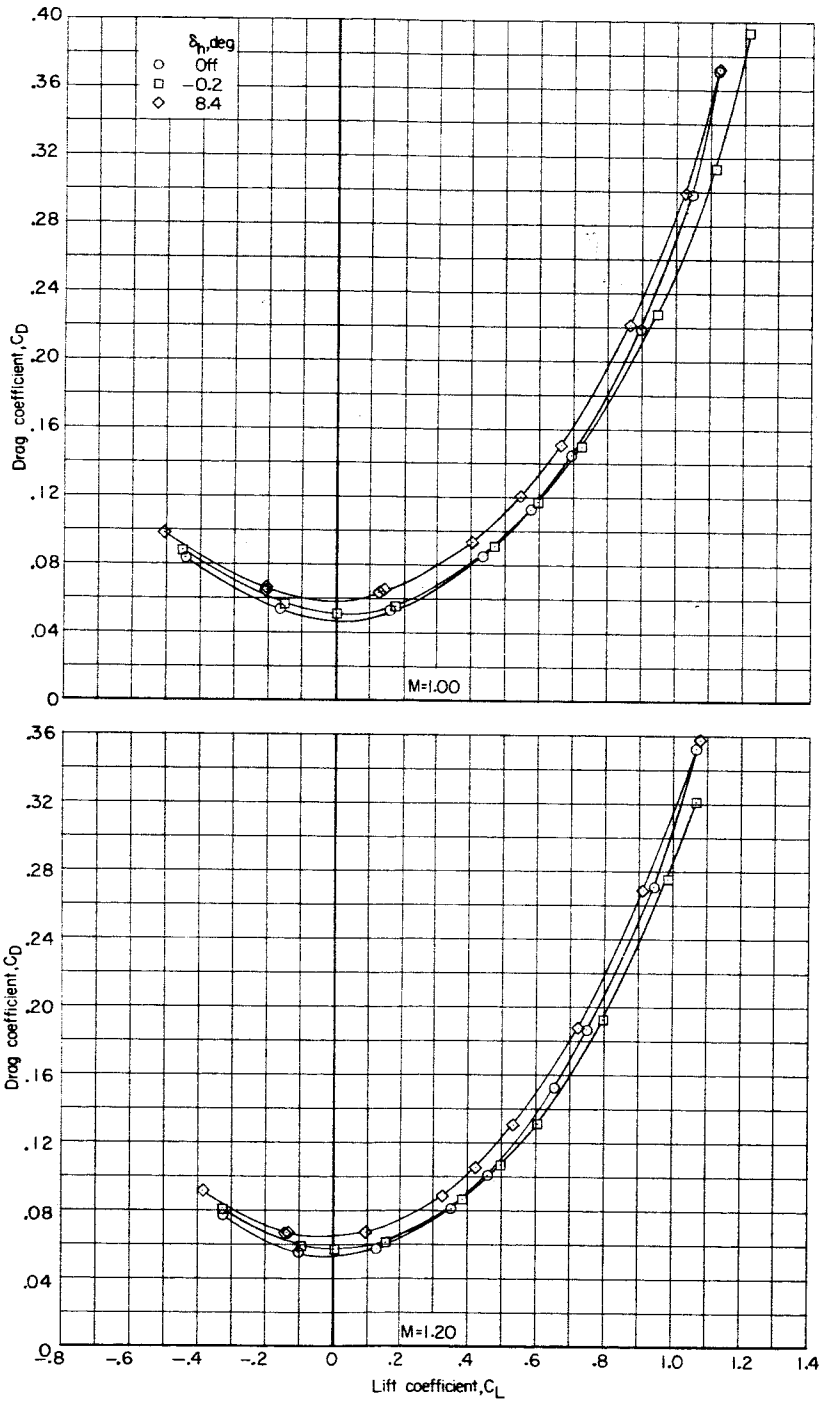

(d) Concluded.

Figure 13.- Continued.

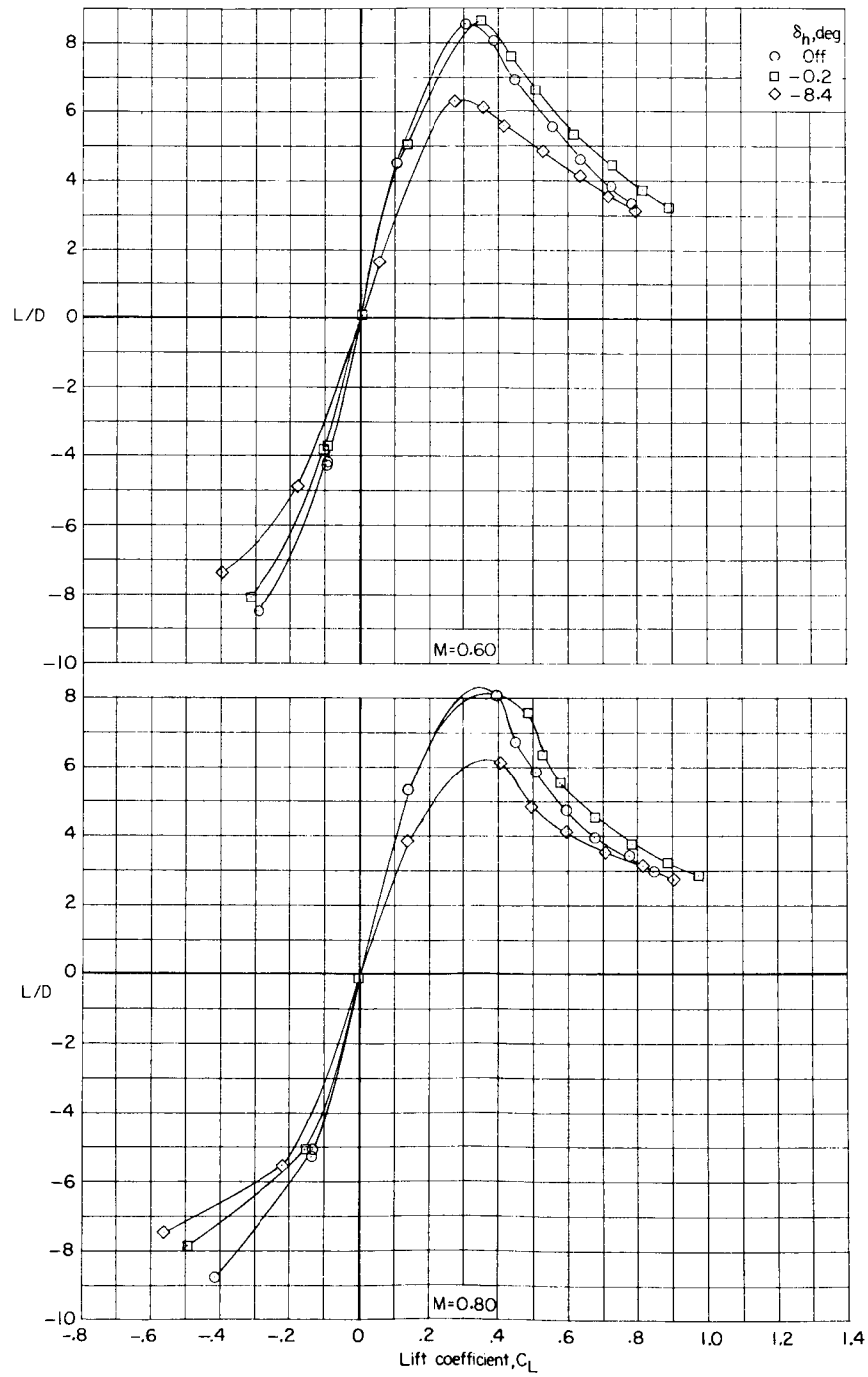

(e) L/D against C_L.

Figure 13.- Continued.

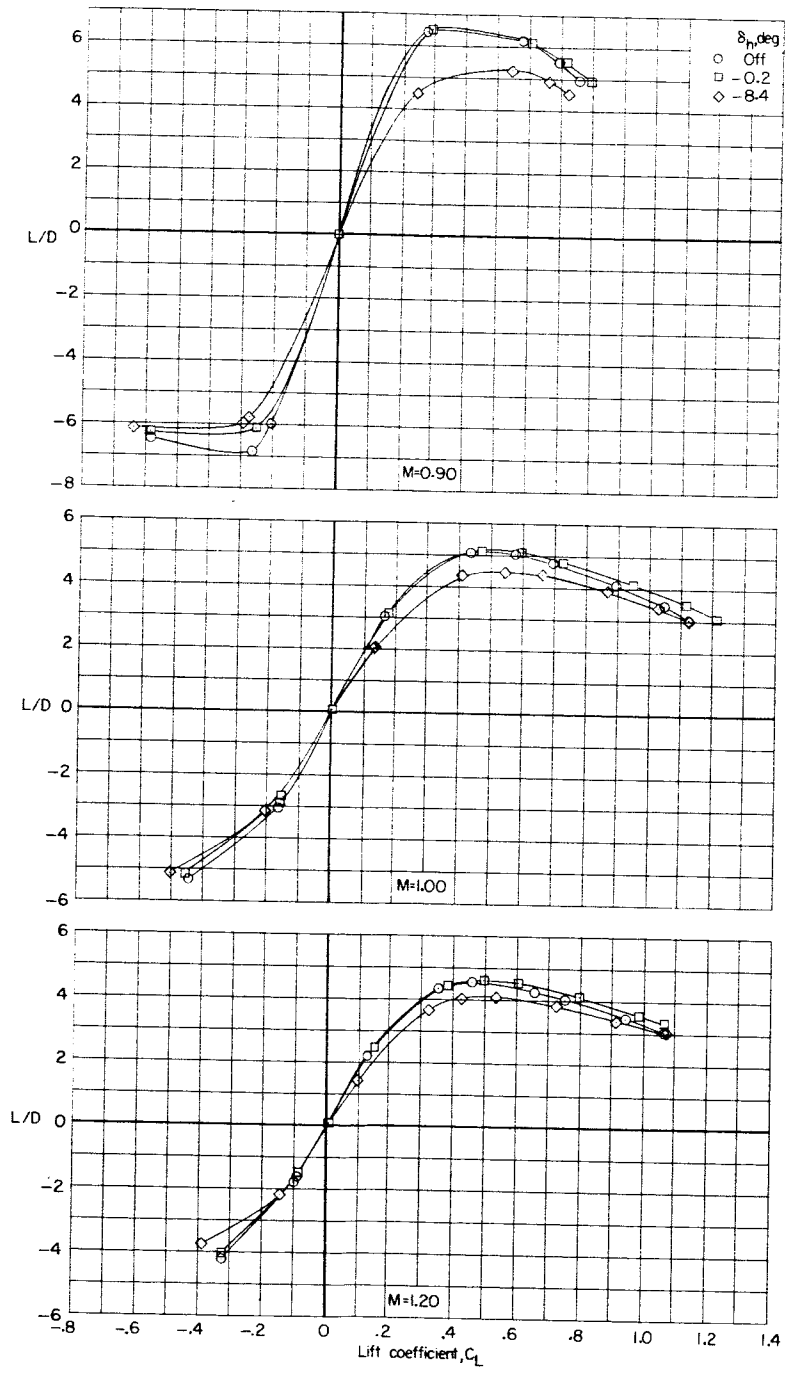

(e) Concluded.

Figure 13.- Concluded.

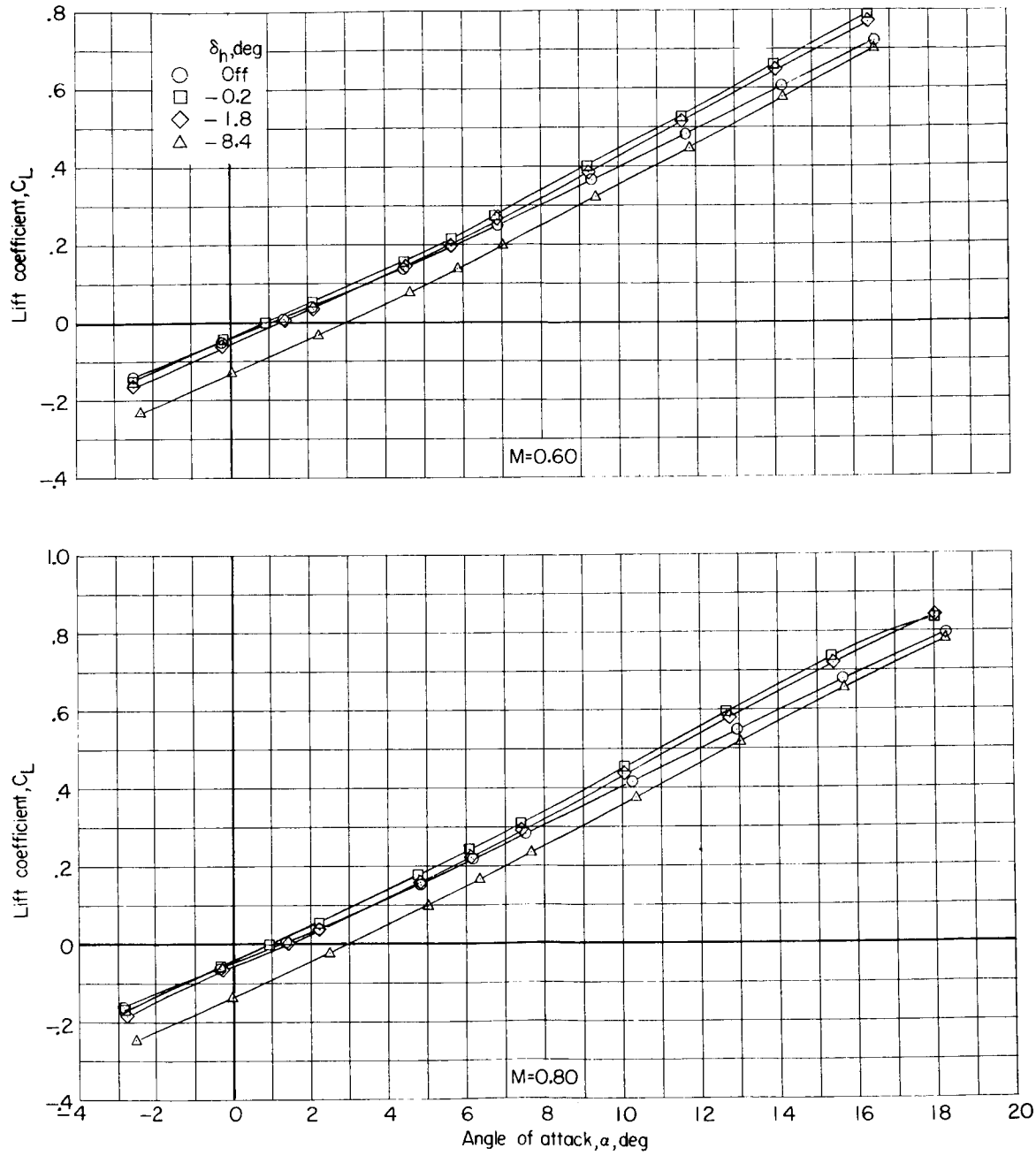

(a) C_L against α.

Figure 14.- Effect of horizontal-tail deflection on longitudinal aerodynamic characteristics of model II with 75° swept wing. Configuration BW_3VH.

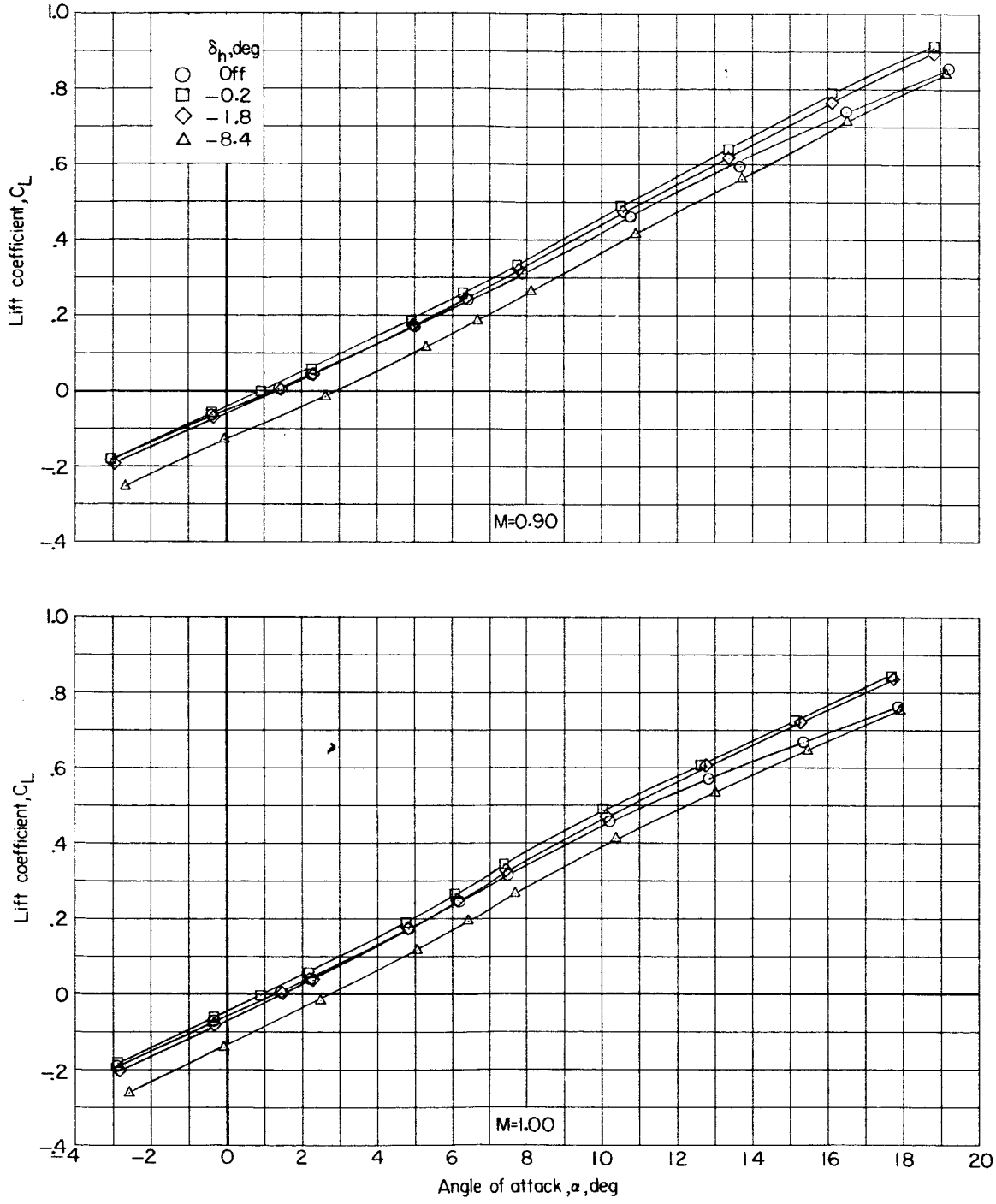

(a) Continued.

Figure 14.- Continued.

[redacted]

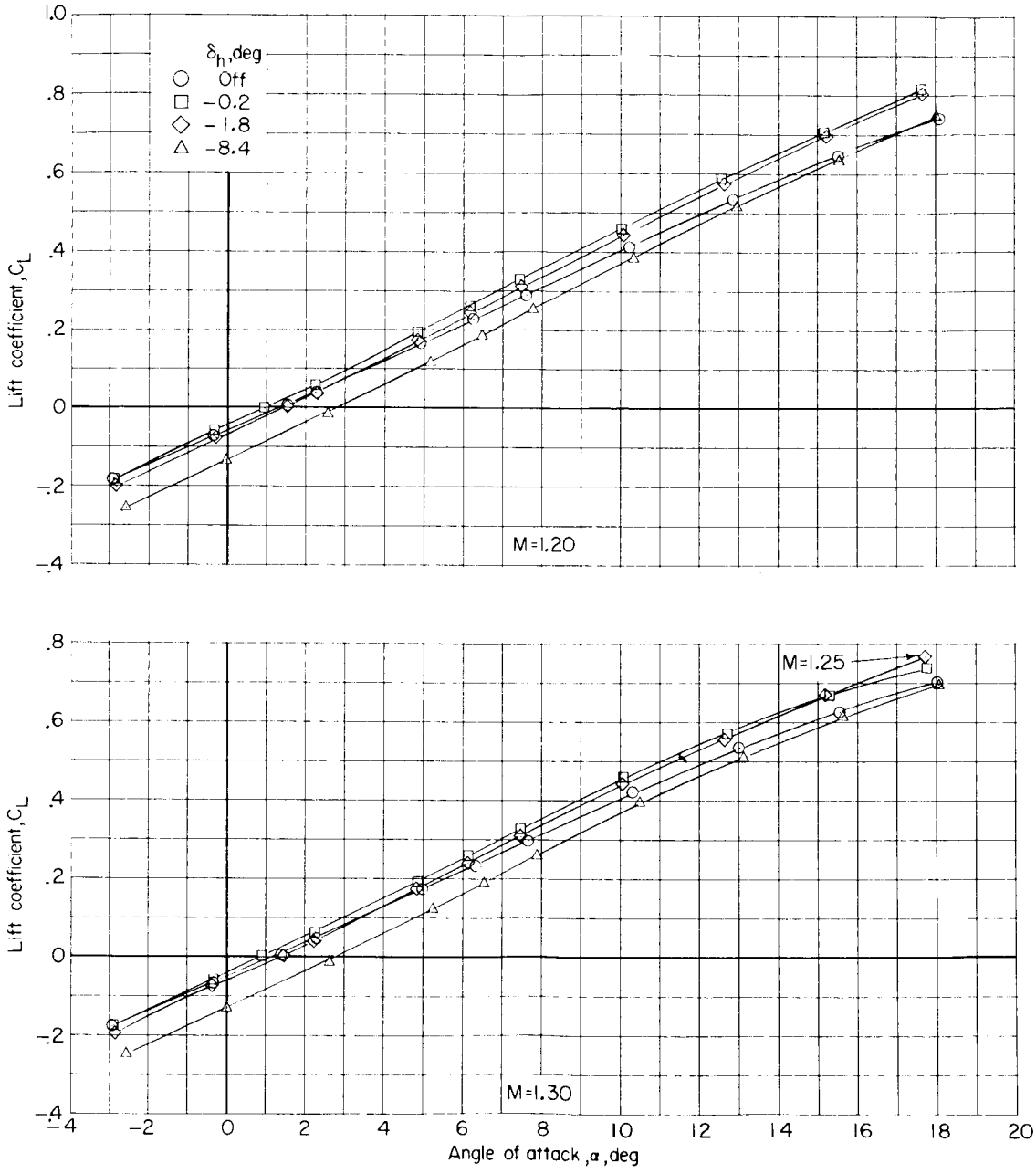

(a) Concluded.

Figure 14.- Continued.

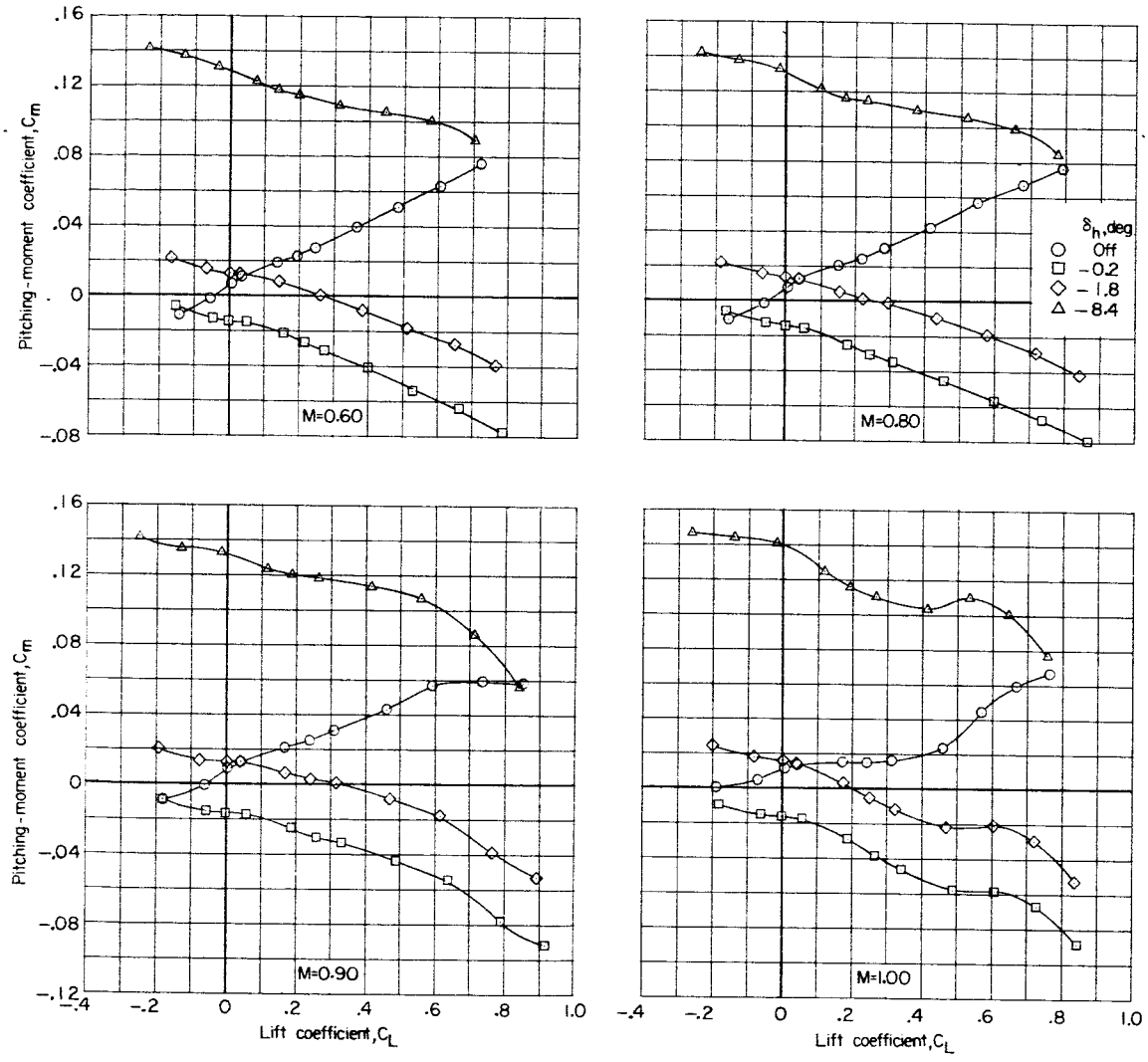

(b) C_m against C_L.

Figure 14.- Continued.

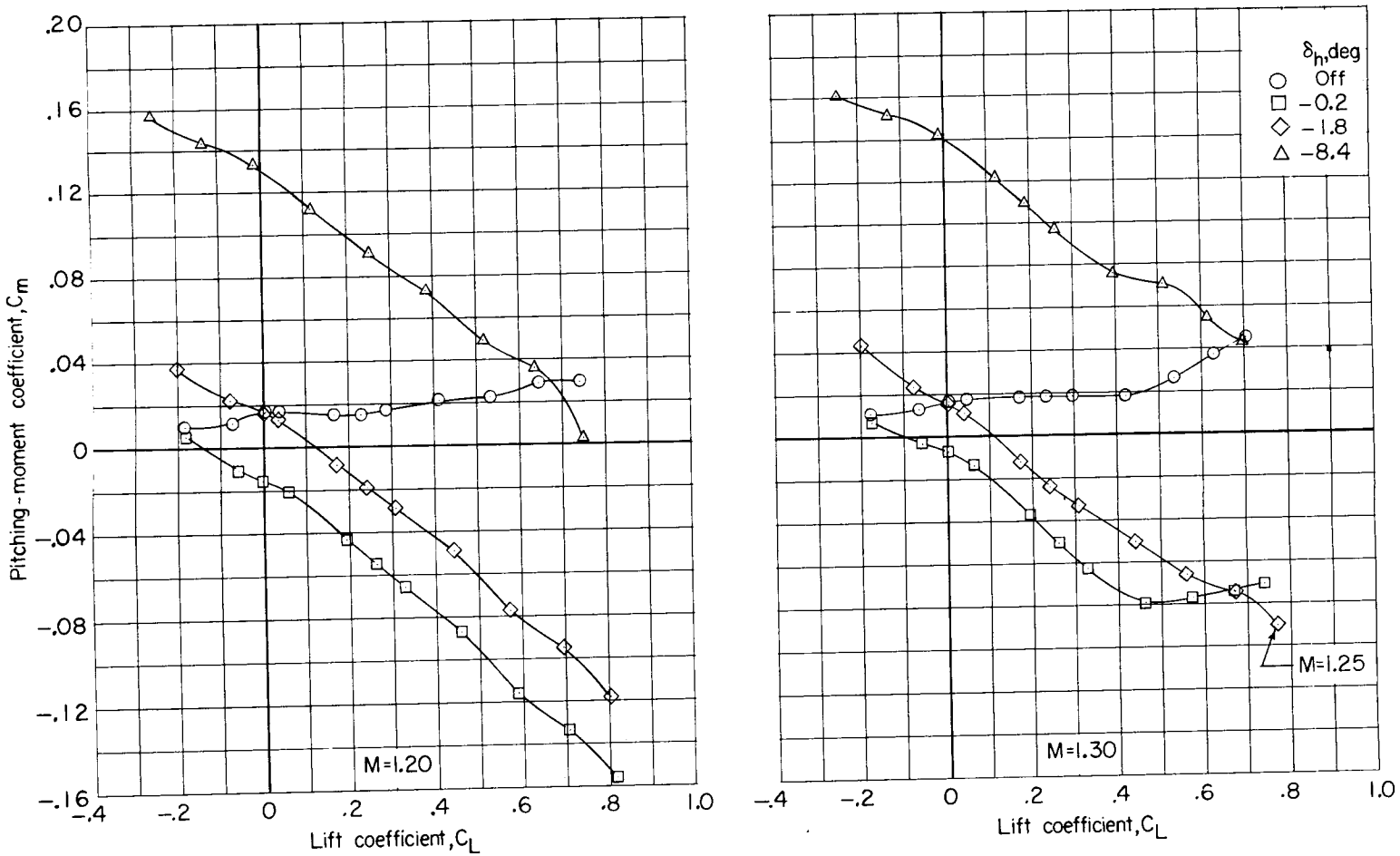

(b) Concluded.

Figure 14.- Continued.

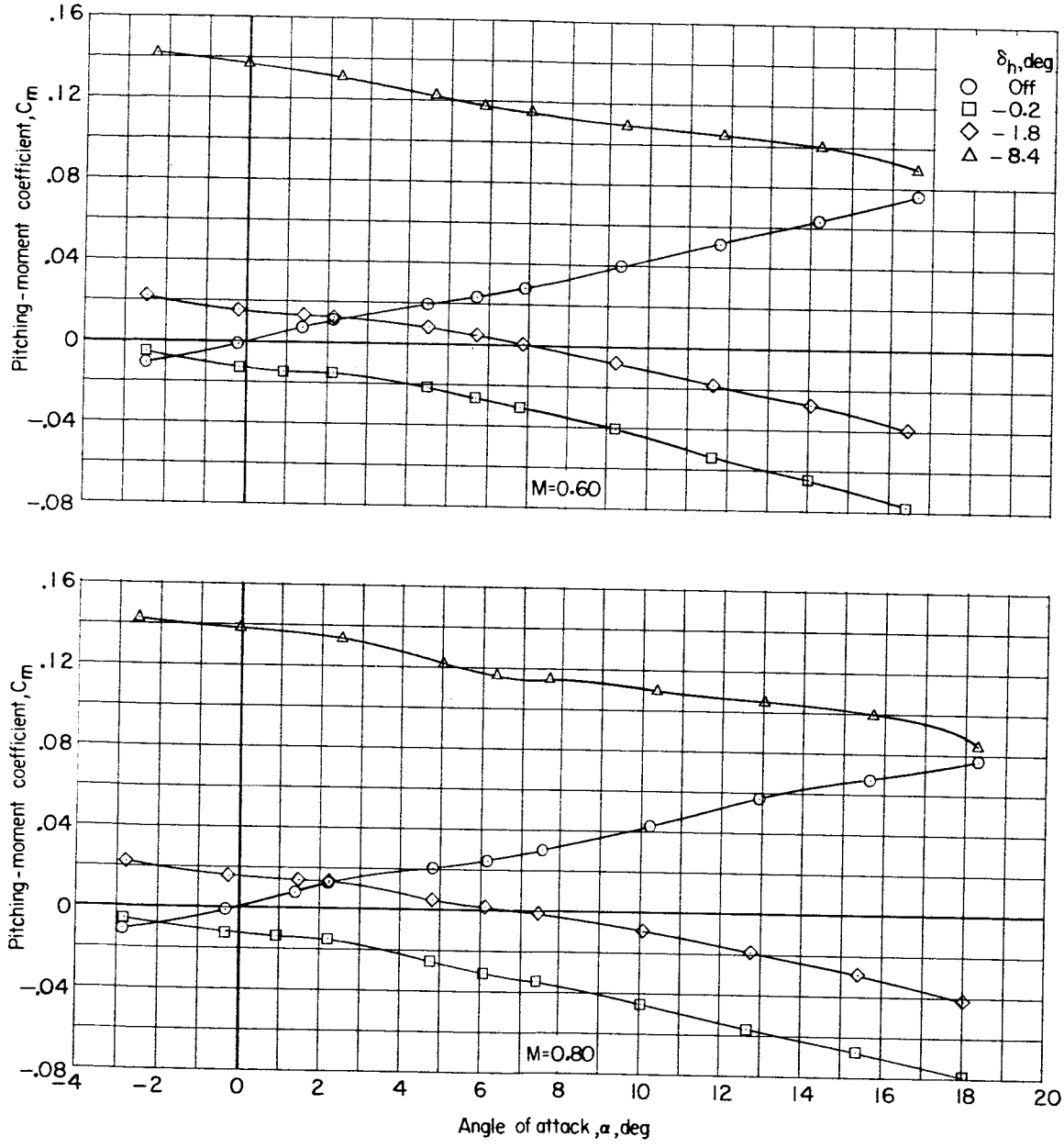

(c) C_m against α.

Figure 14.- Continued.

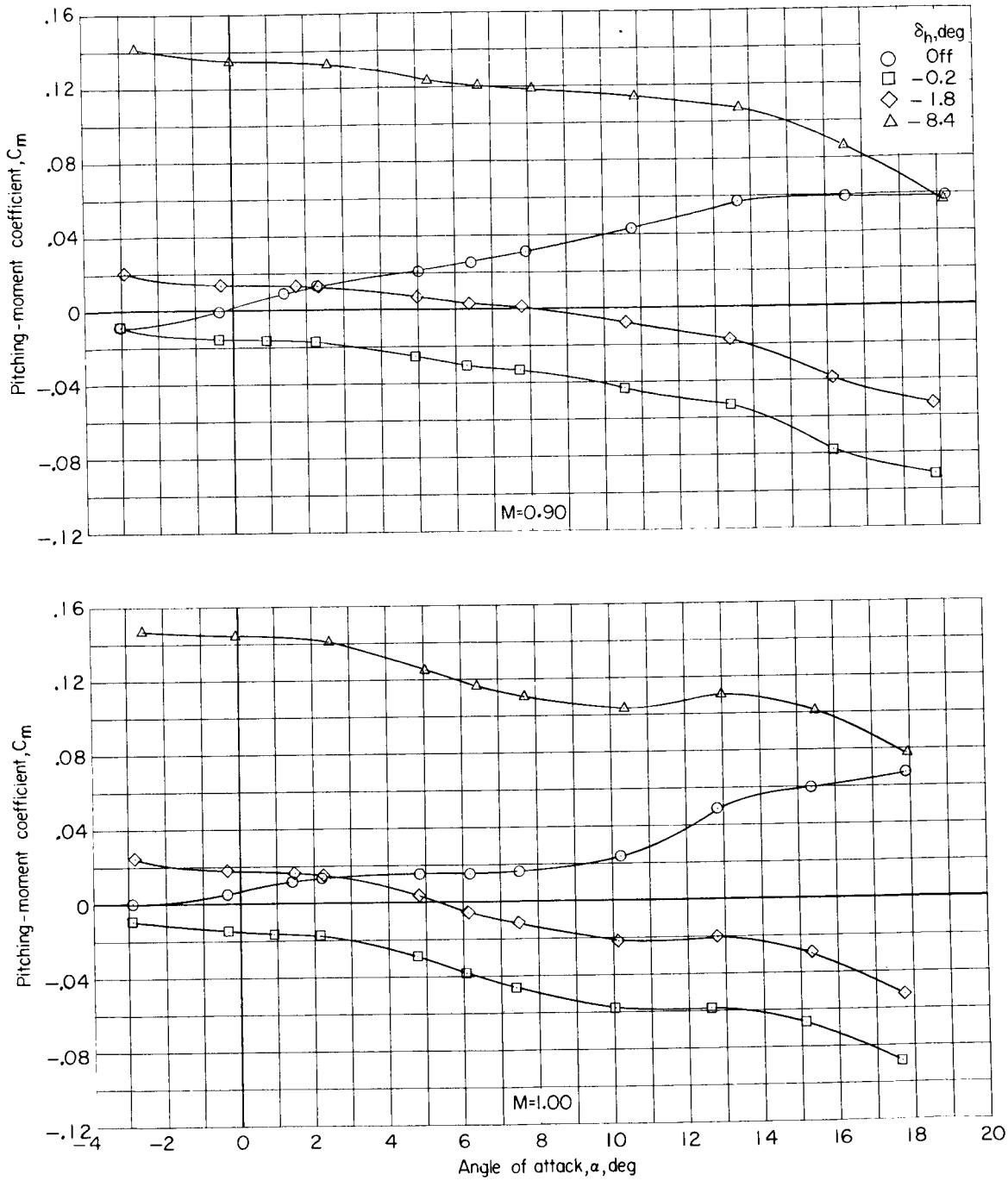

(c) Continued.

Figure 14.- Continued.

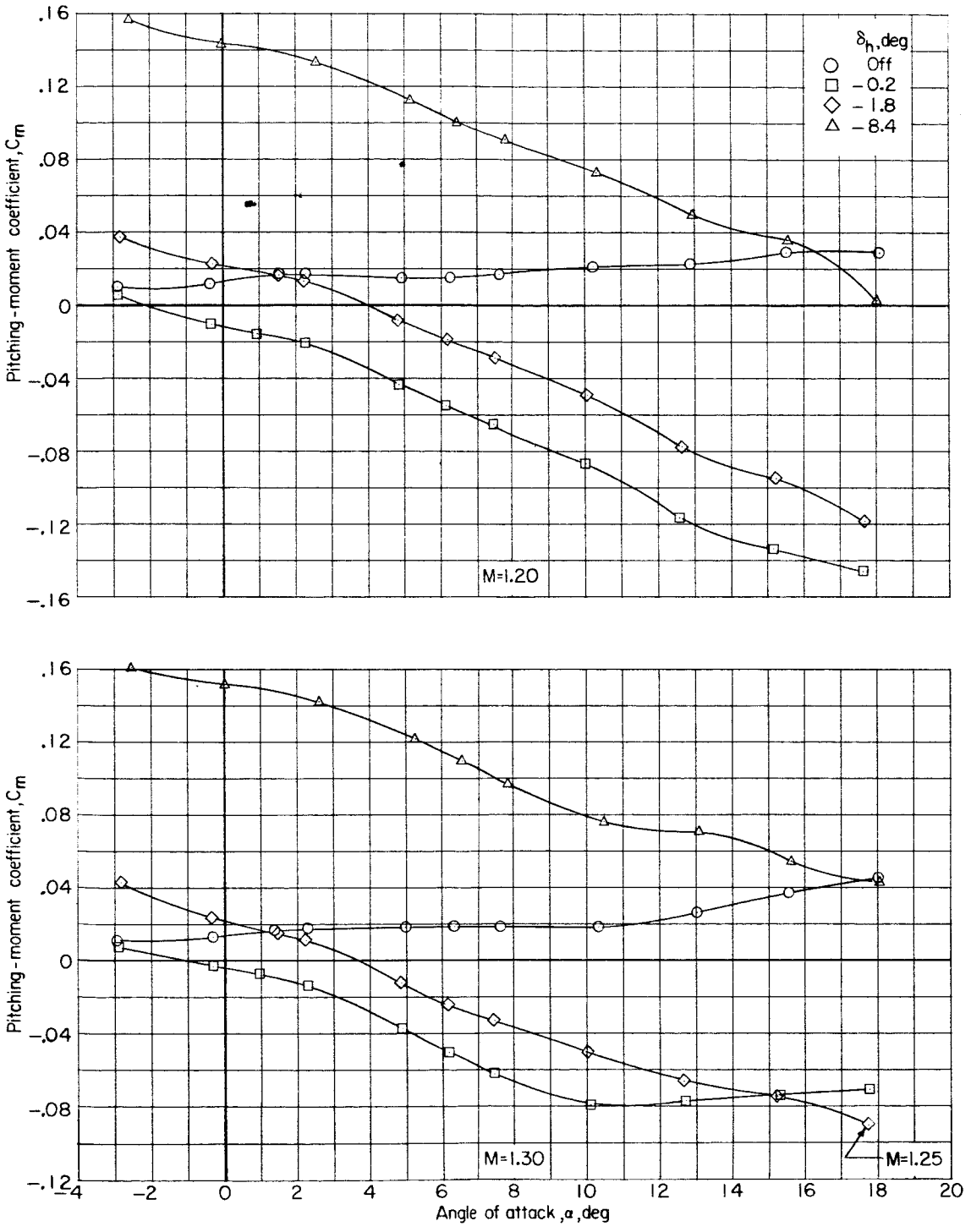

(c) Concluded.

Figure 14.- Continued.

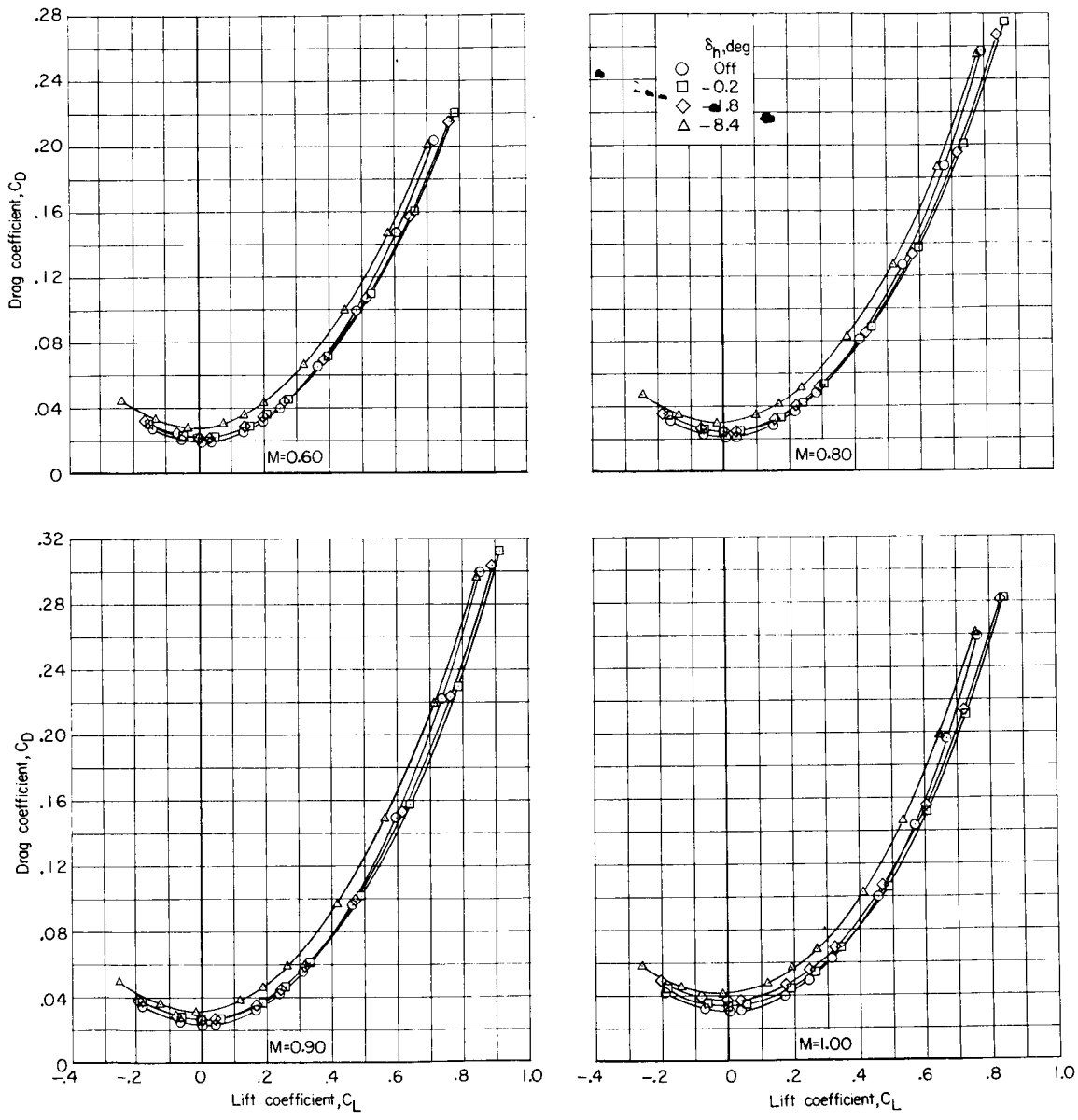

(d) C_D against C_L.

Figure 14.- Continued.

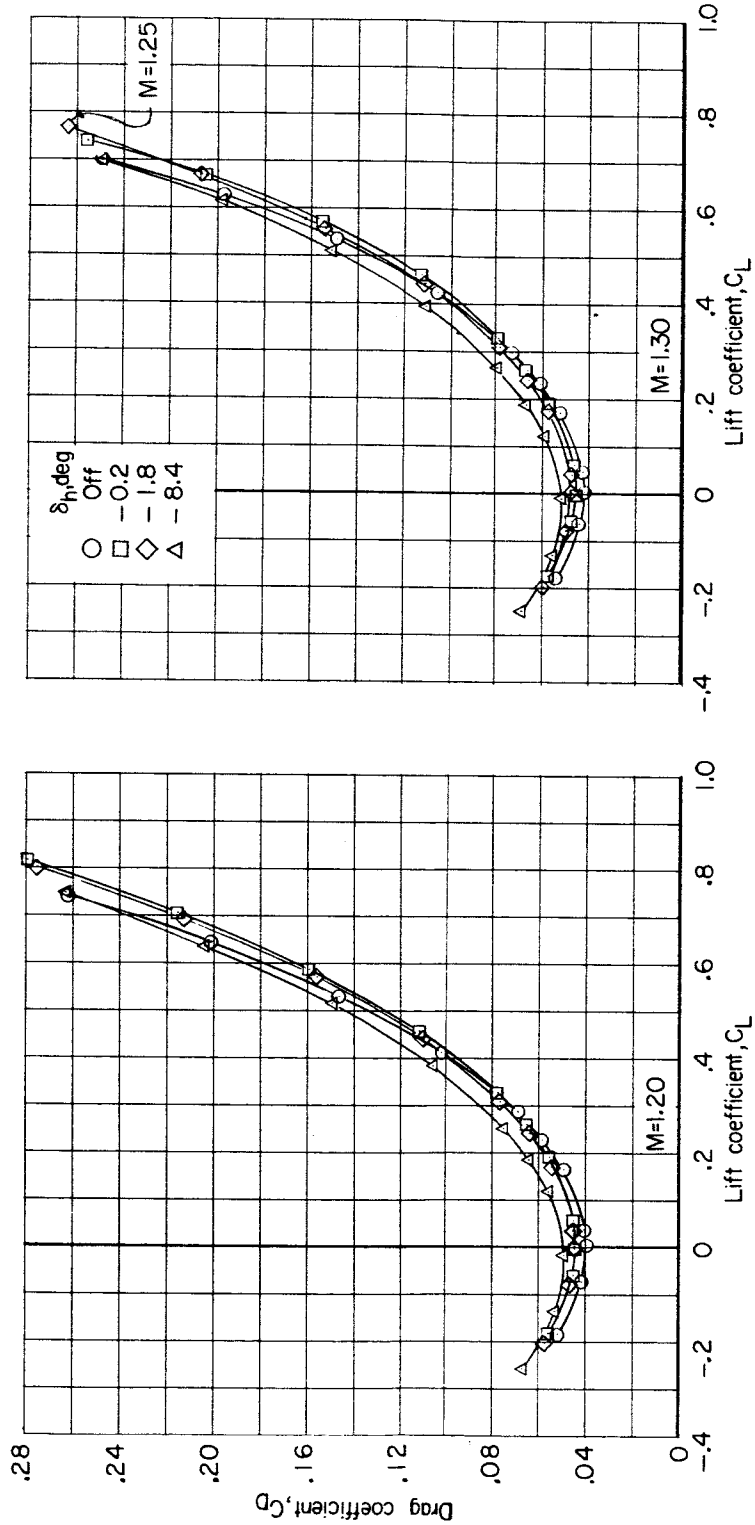

(d) Concluded.

Figure 14.- Continued.

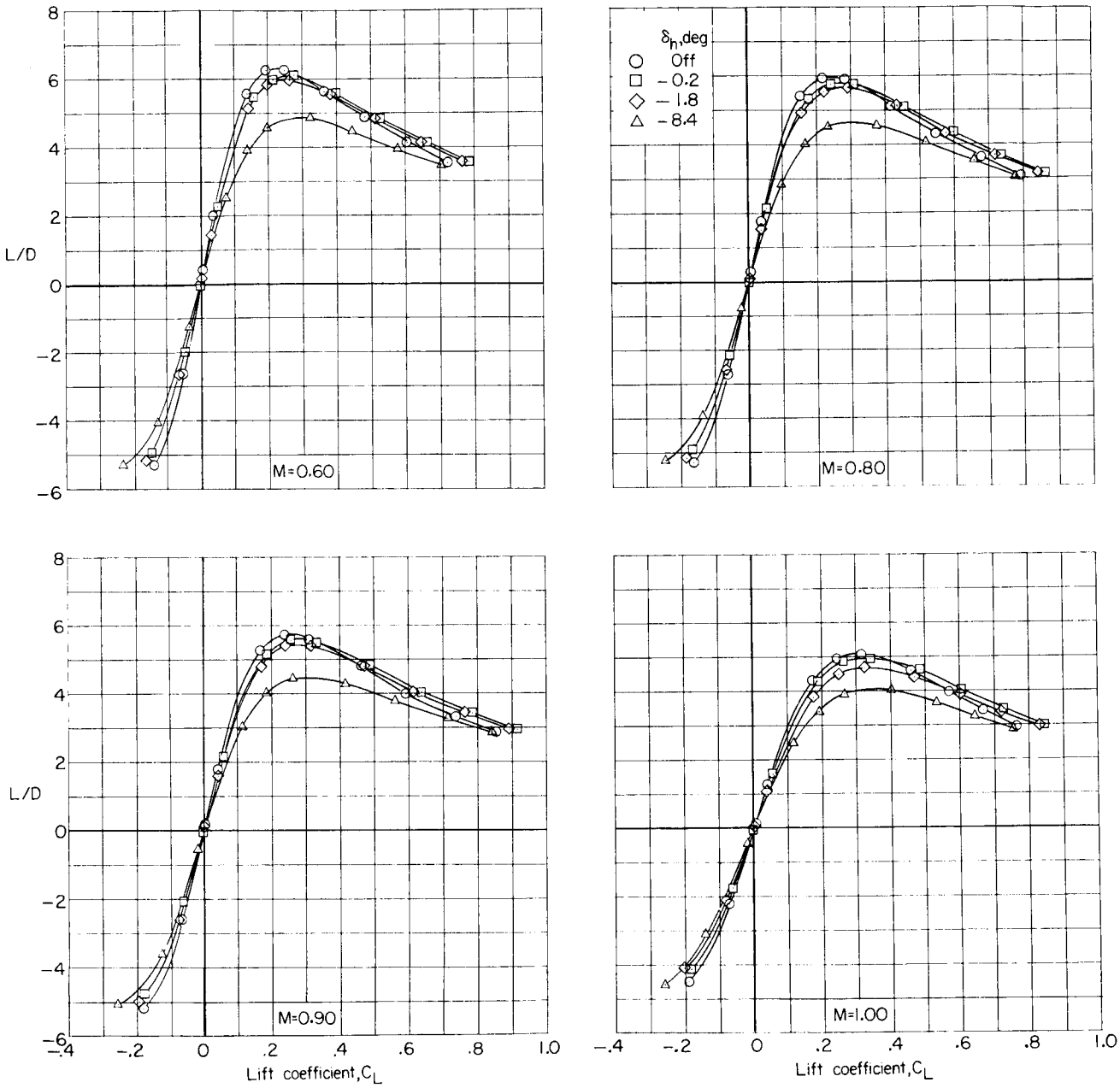

(e) L/D against C_L.

Figure 14.- Continued.

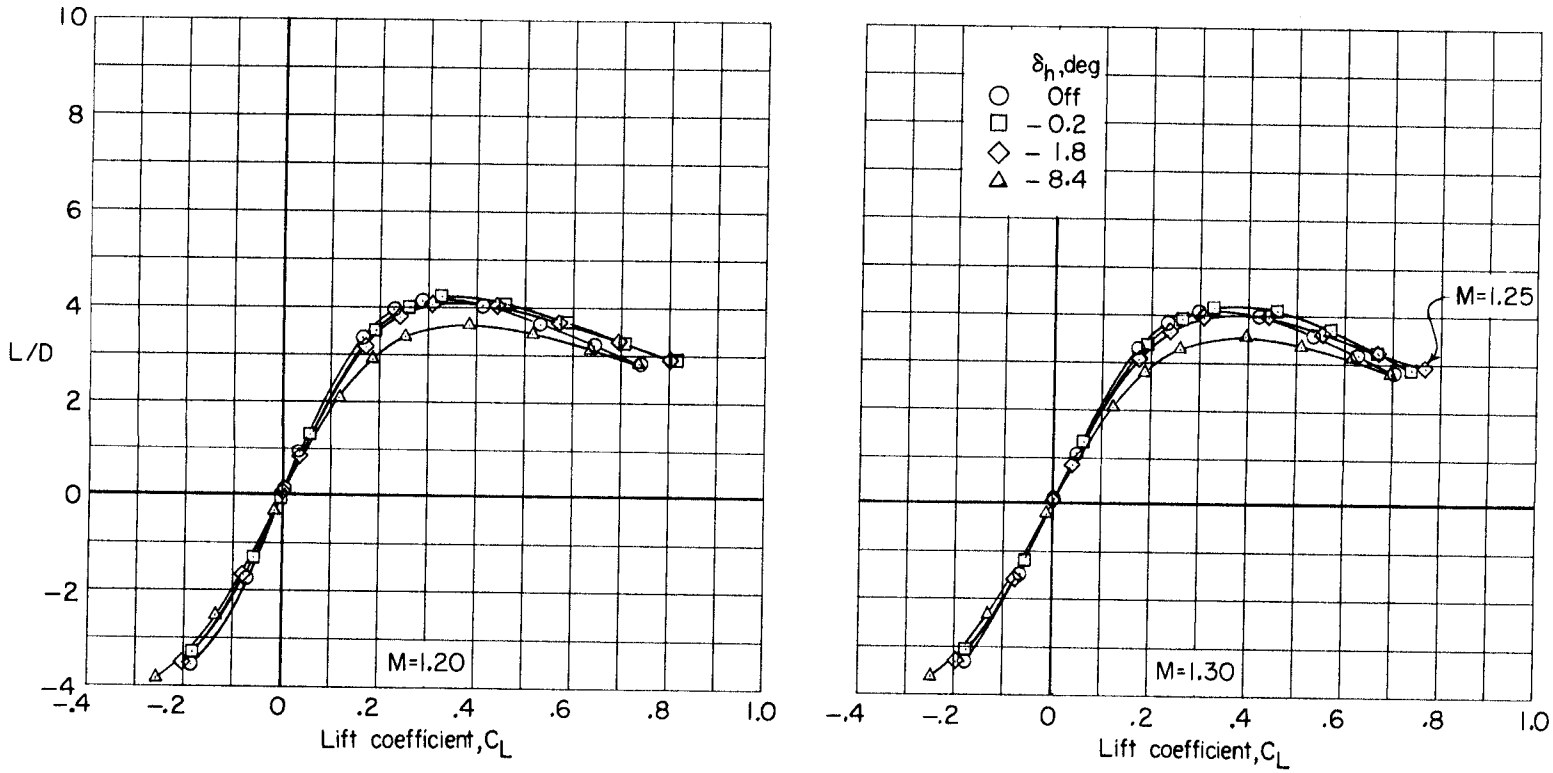

(e) Concluded.

Figure 14.- Concluded.

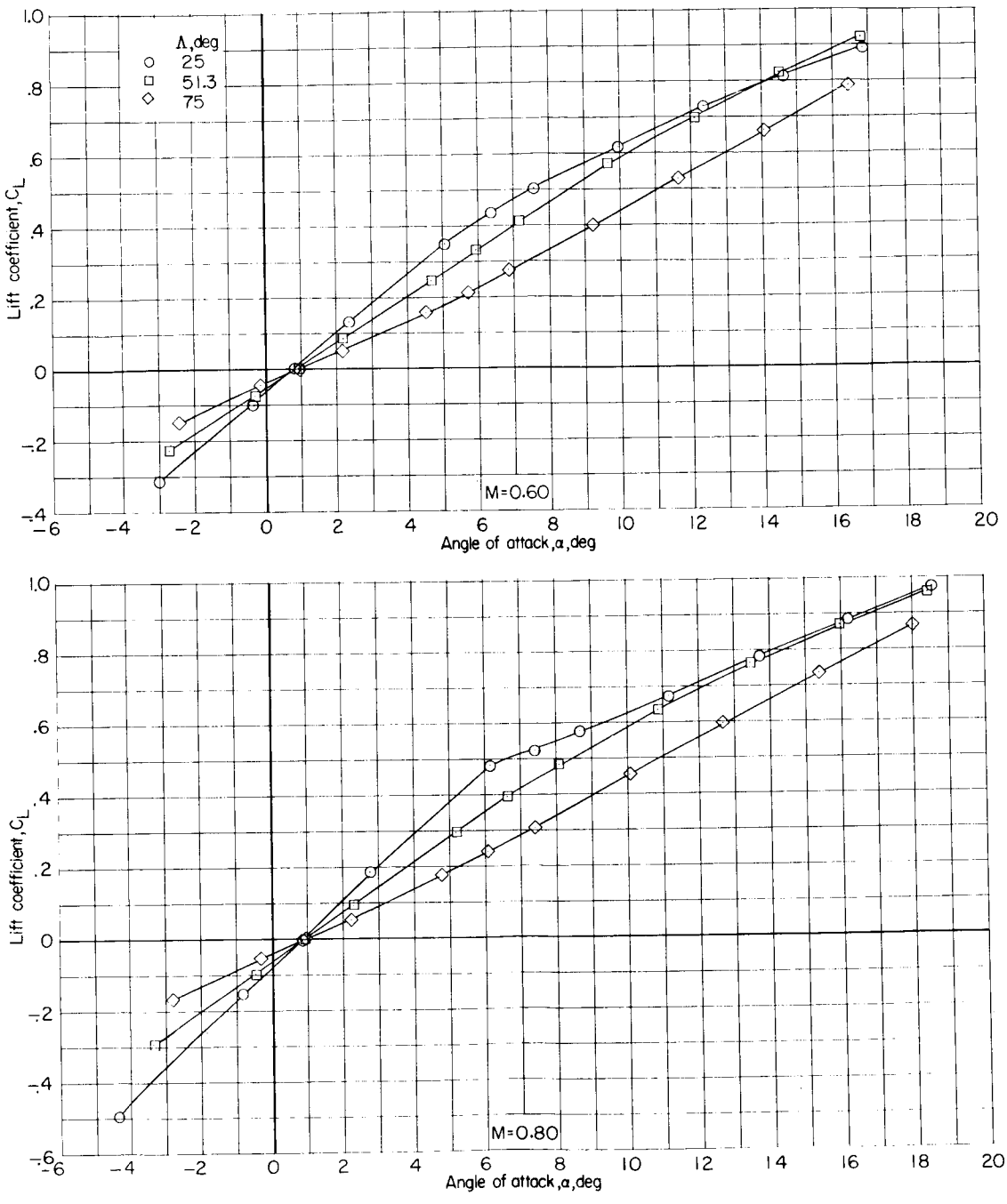

(a) C_L against α.

Figure 15.- Effect of wing sweep on longitudinal aerodynamic characteristics of model II. Configuration BWVH; $\delta_h = -0.2^o$.

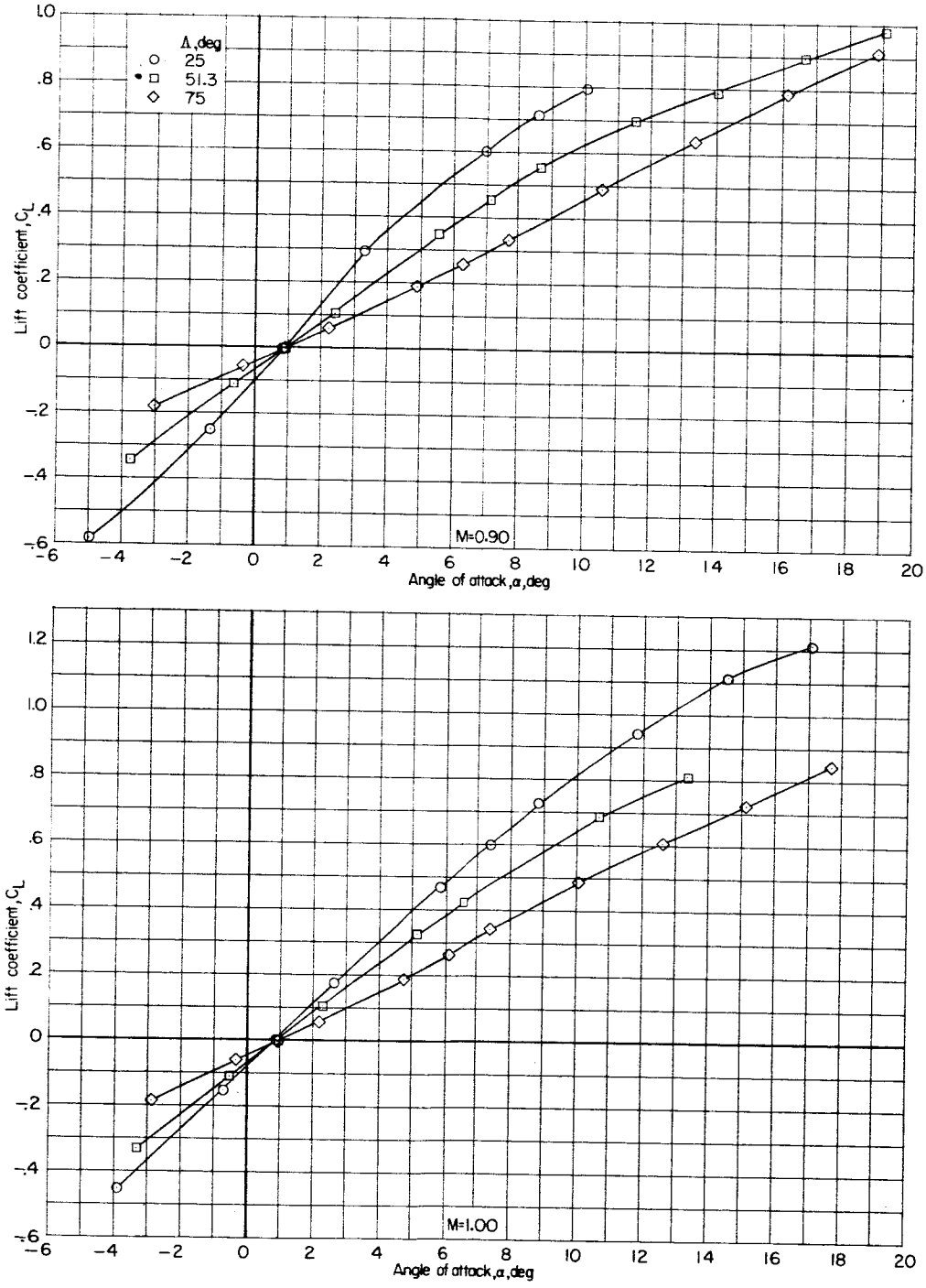

(a) Continued.

Figure 15.- Continued.

[redacted]

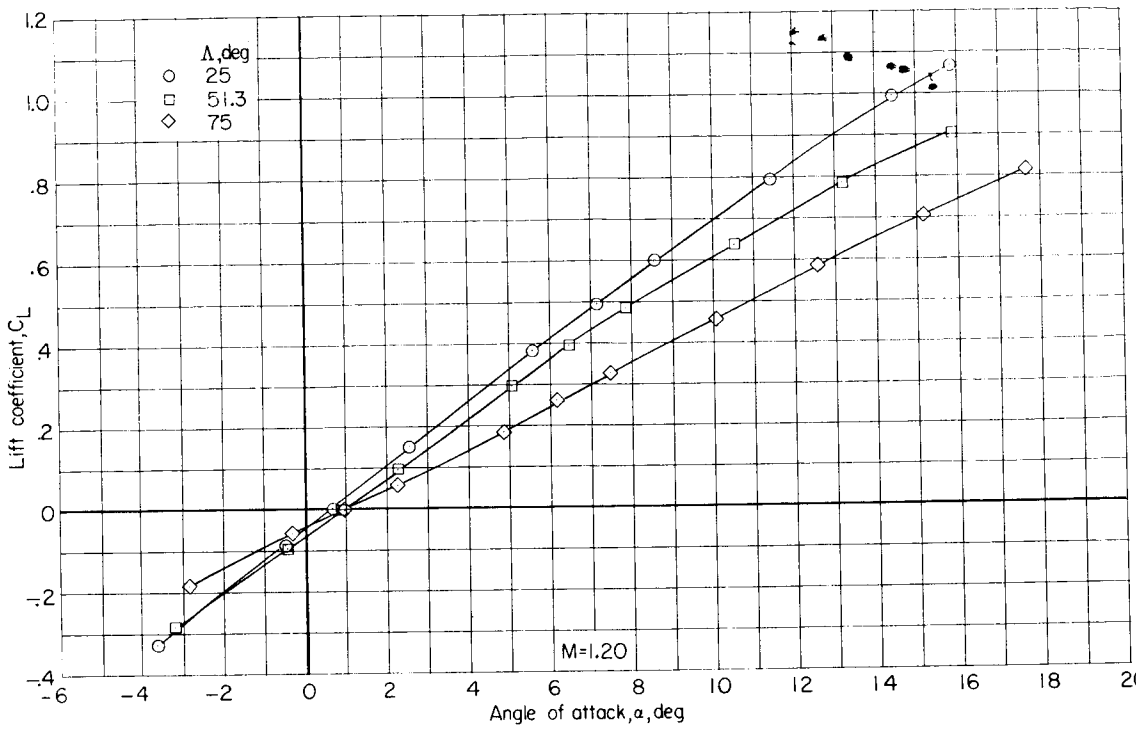

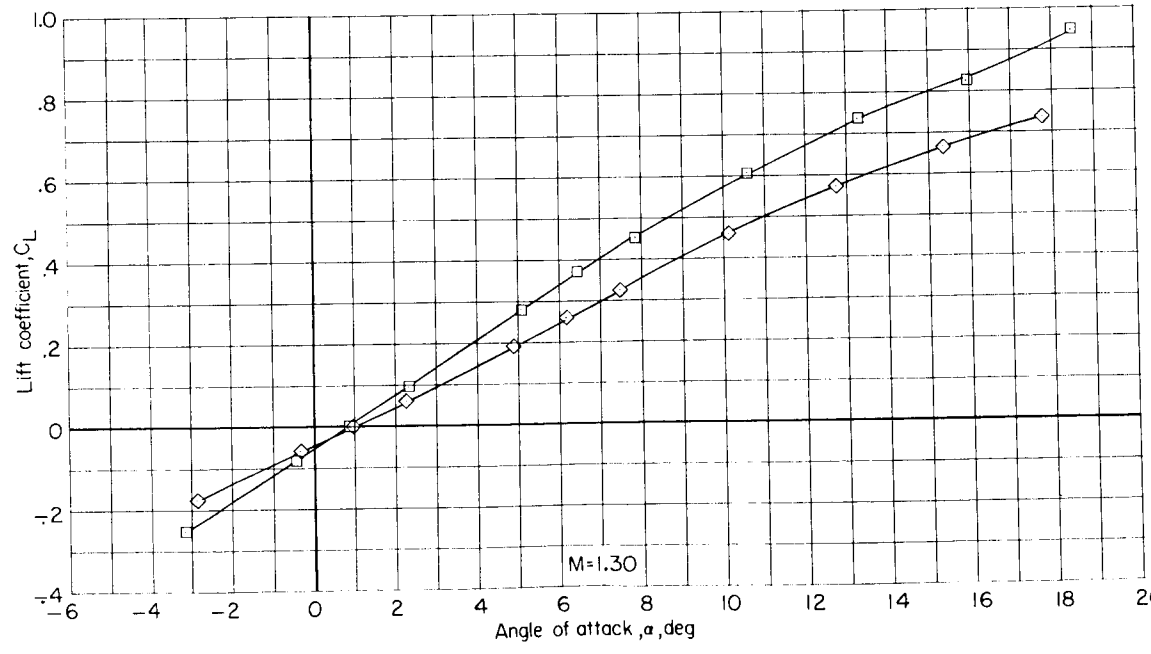

(a) Concluded.

Figure 15.- Continued.

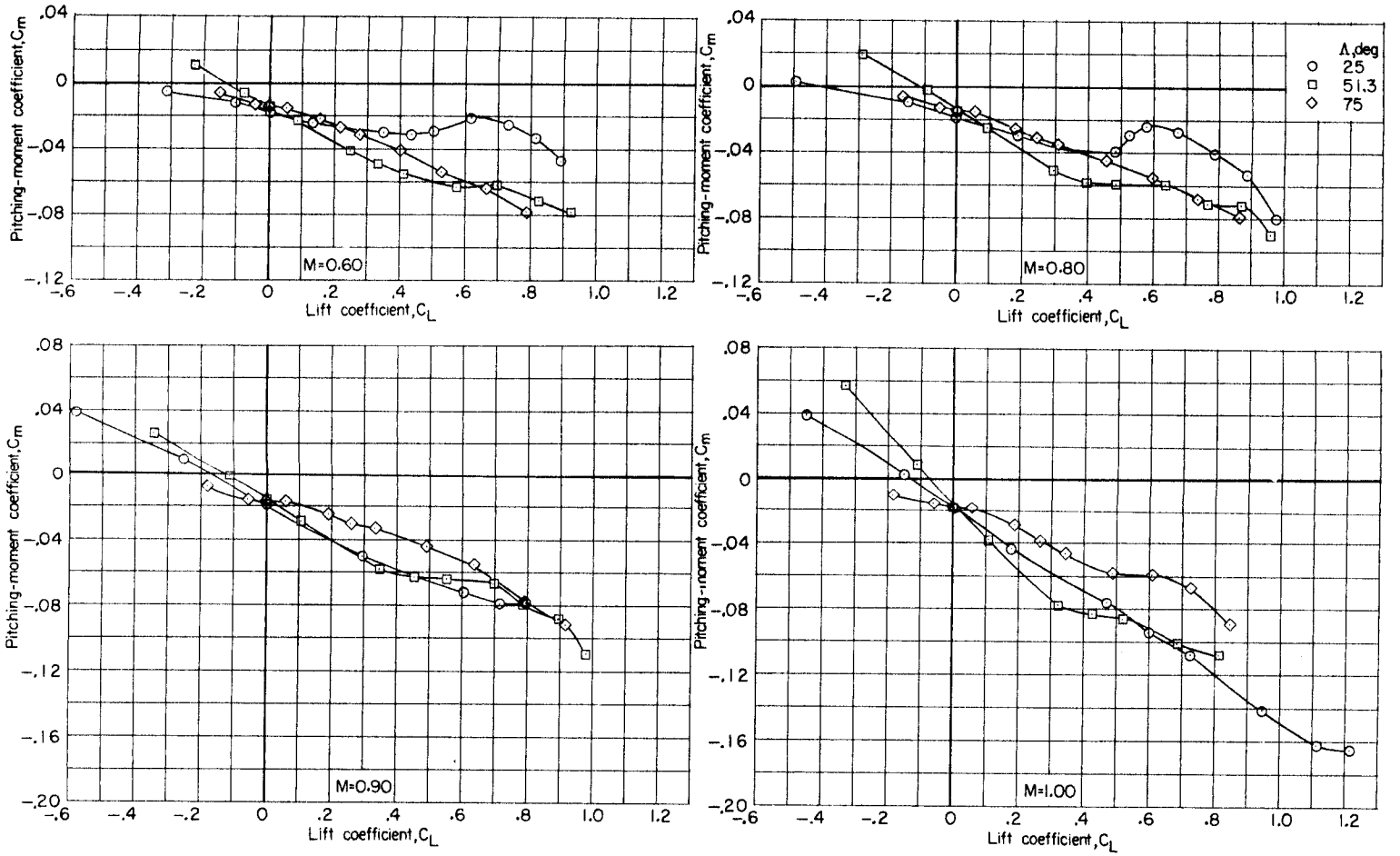

(b) C_m against C_L.

Figure 15.- Continued.

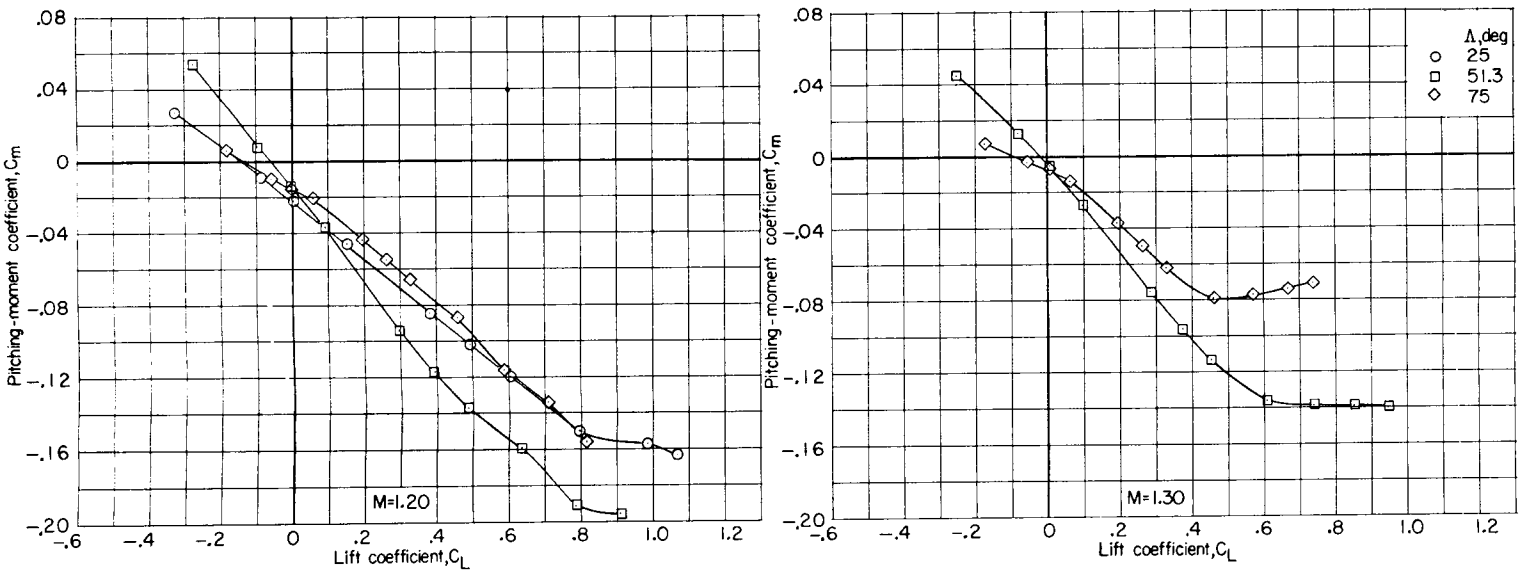

(b) Concluded.

Figure 15.- Continued.

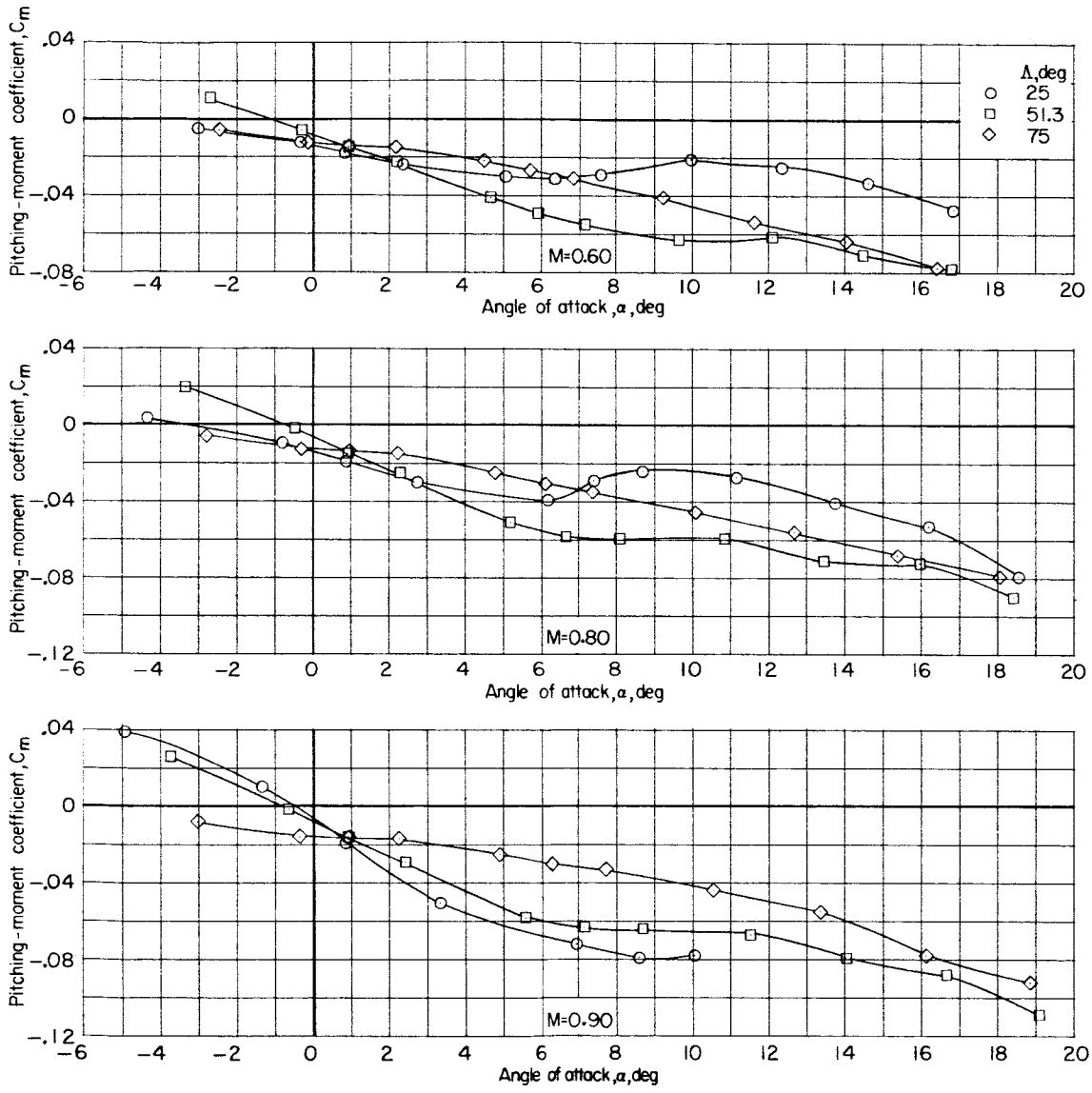

(c) C_m against α.

Figure 15.- Continued.

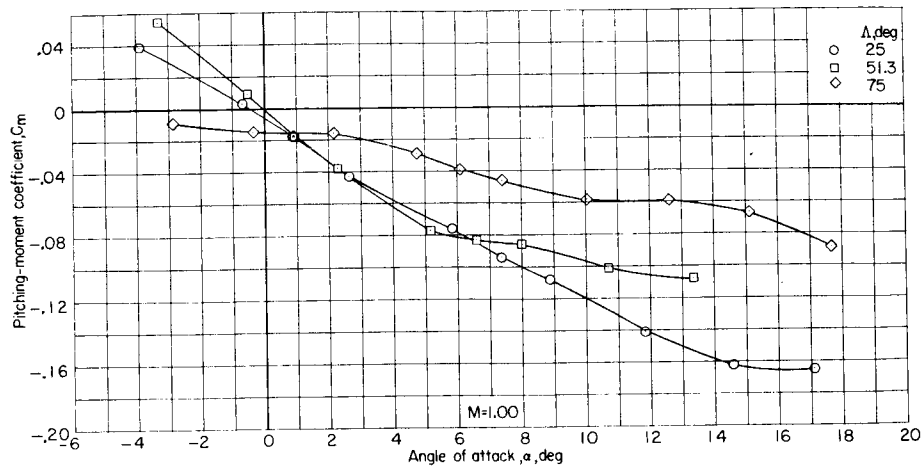

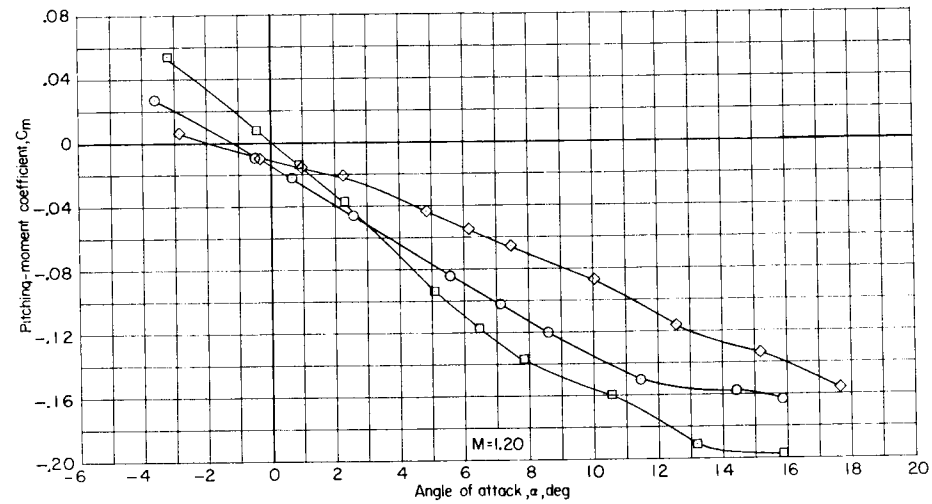

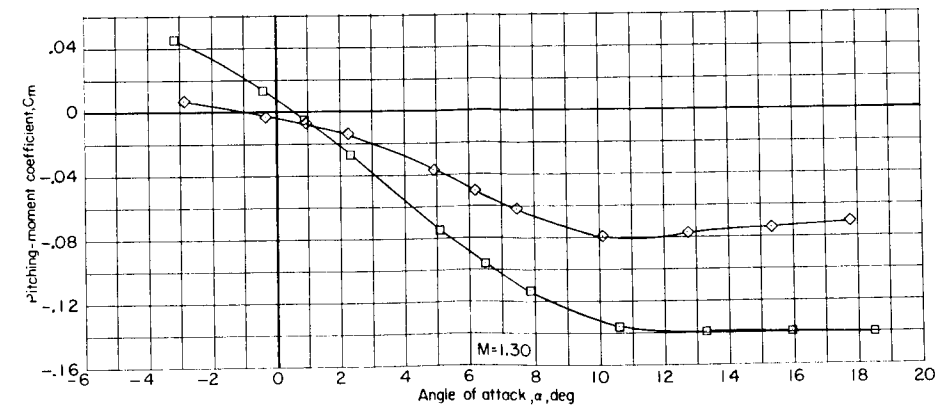

(c) Concluded.

Figure 15.- Continued.

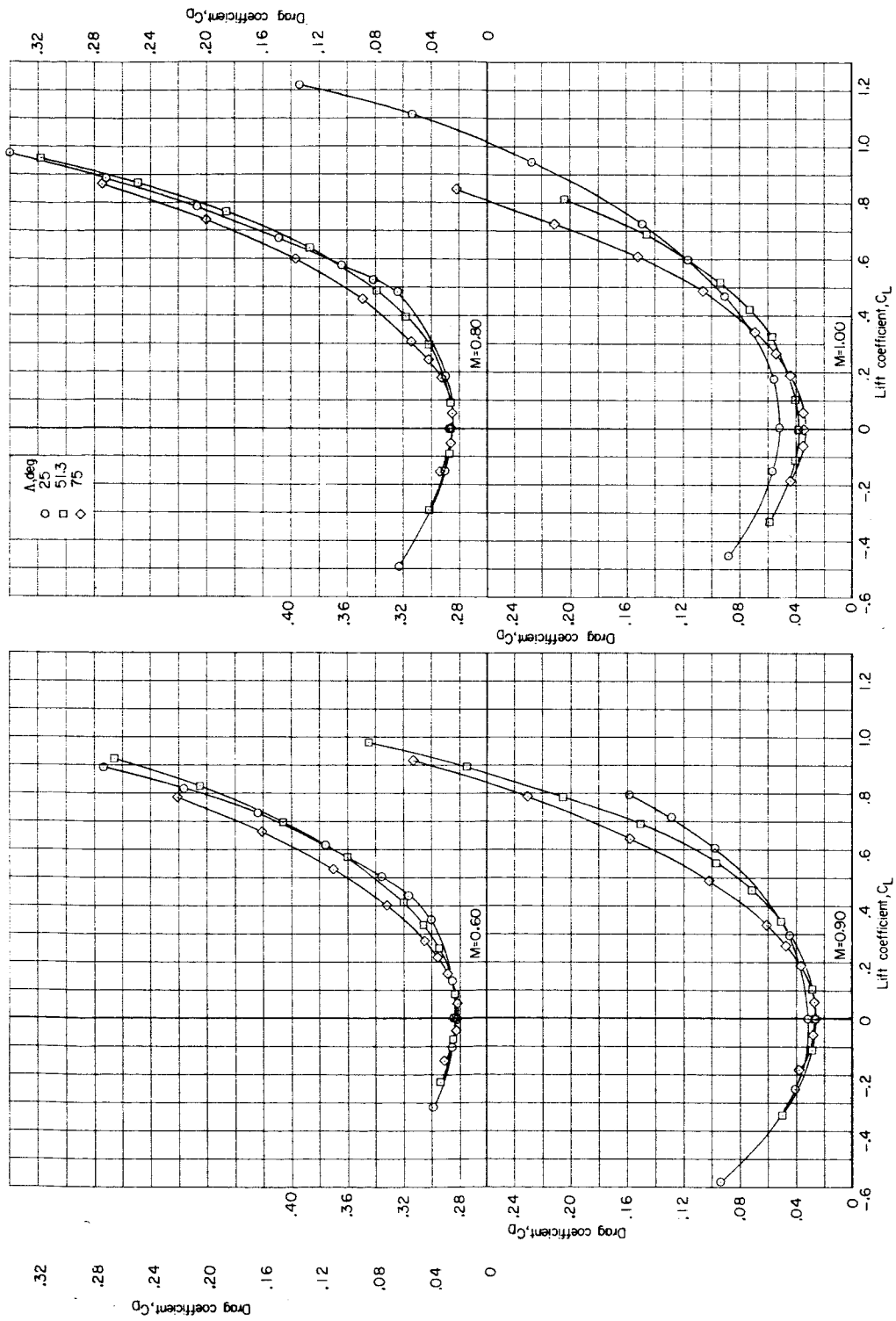

(d) C_D against C_L.

Figure 15.- Continued.

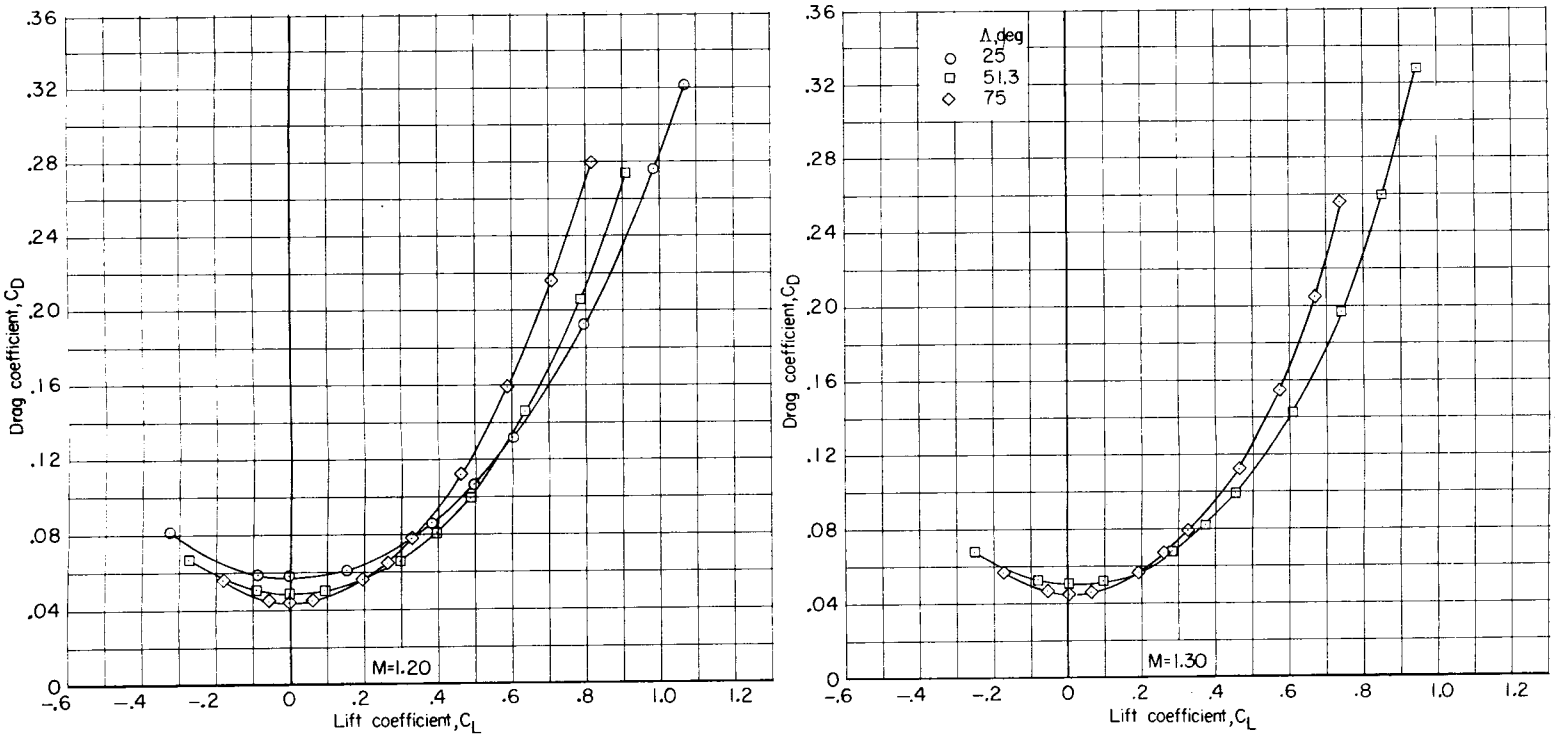

(d) Concluded.

Figure 15.- Continued.

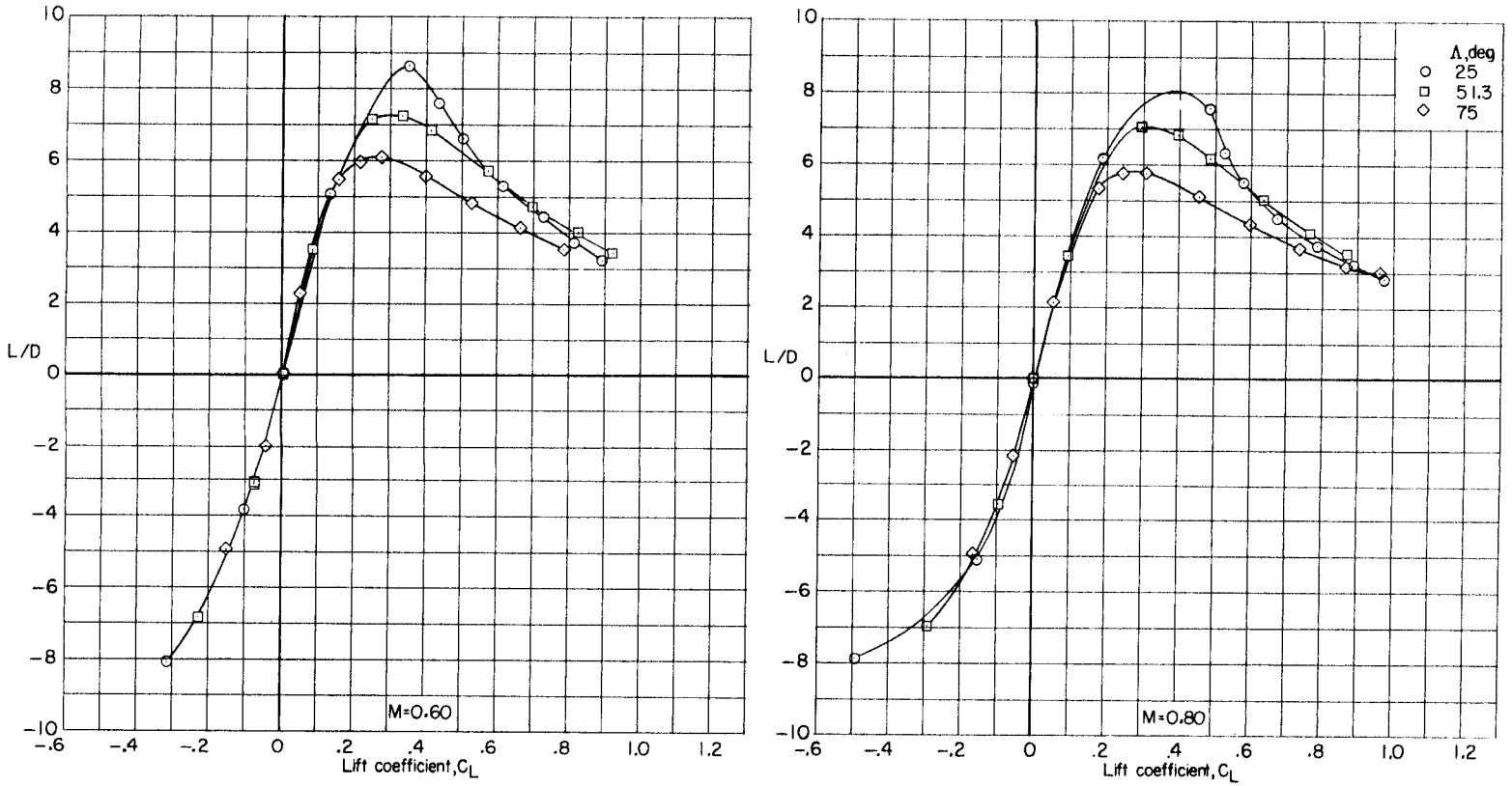

(e) L/D against C_L.

Figure 15.- Continued.

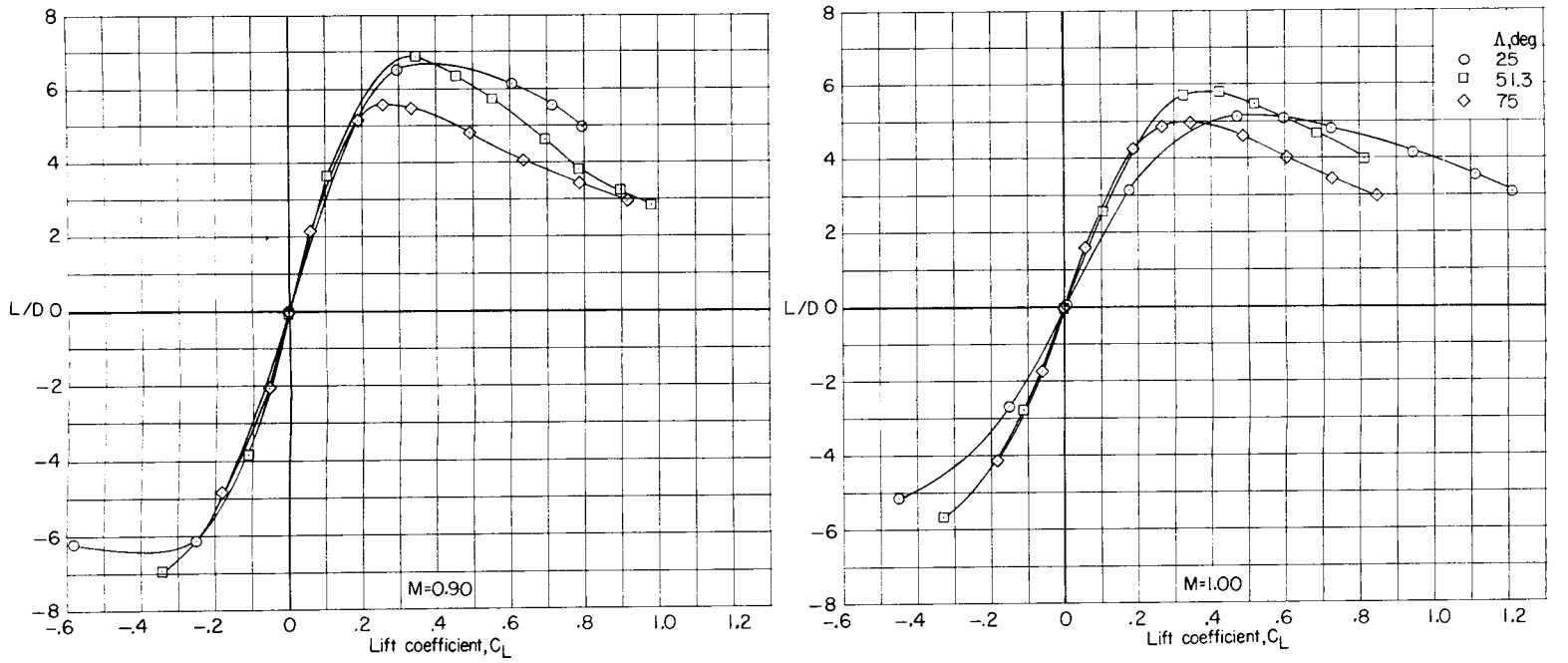

(e) Continued.

Figure 15.- Continued.

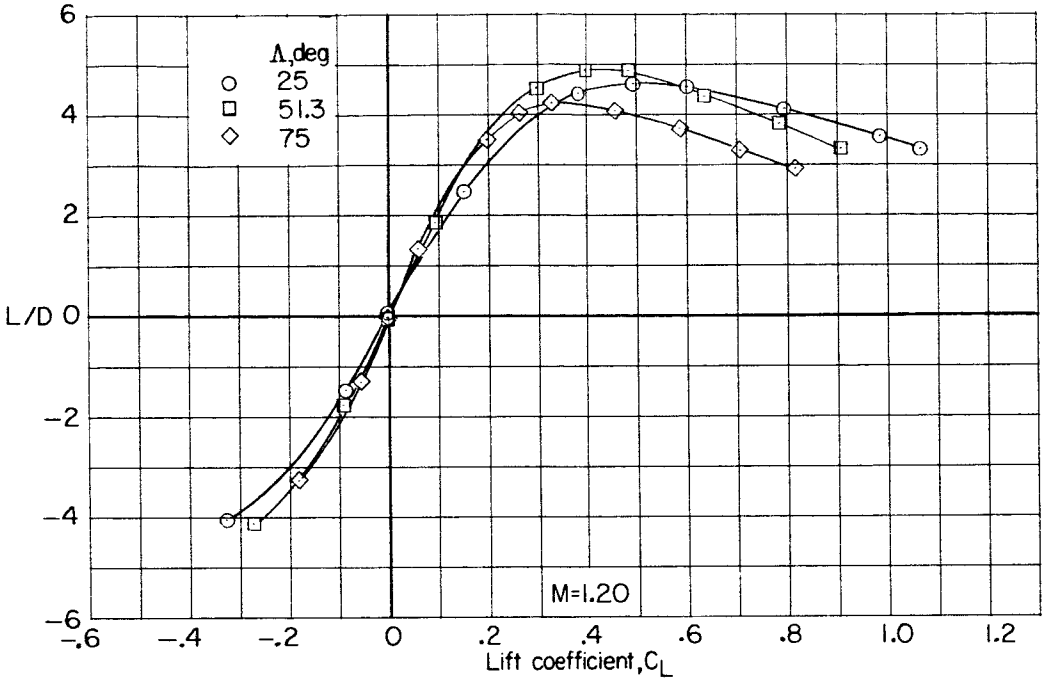

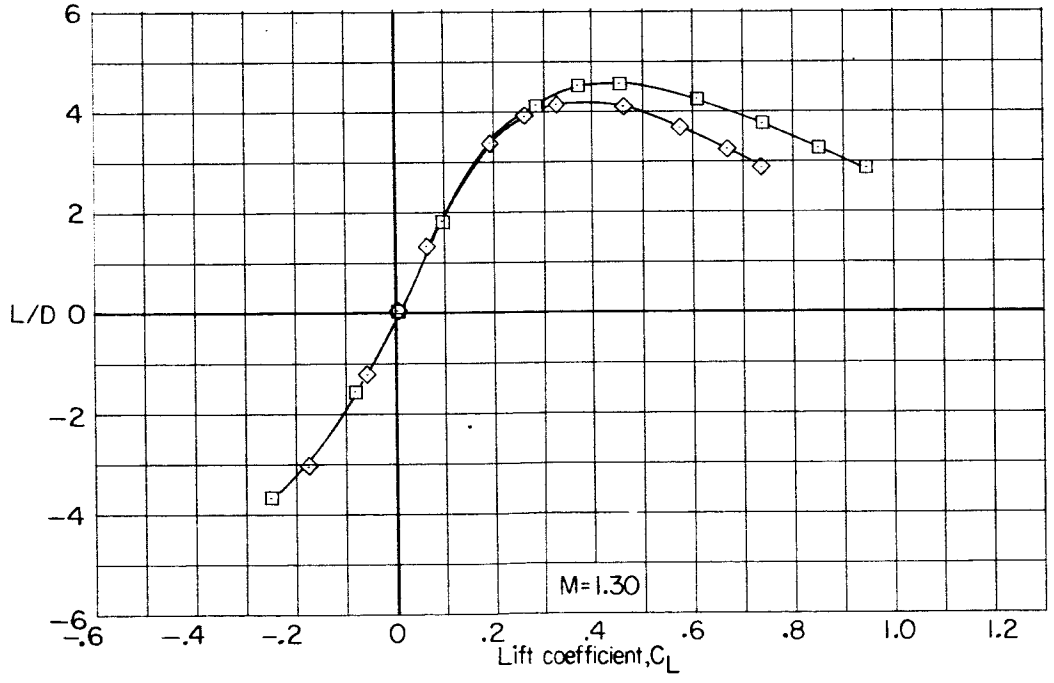

(e) Concluded.

Figure 15.- Concluded.

[redacted]

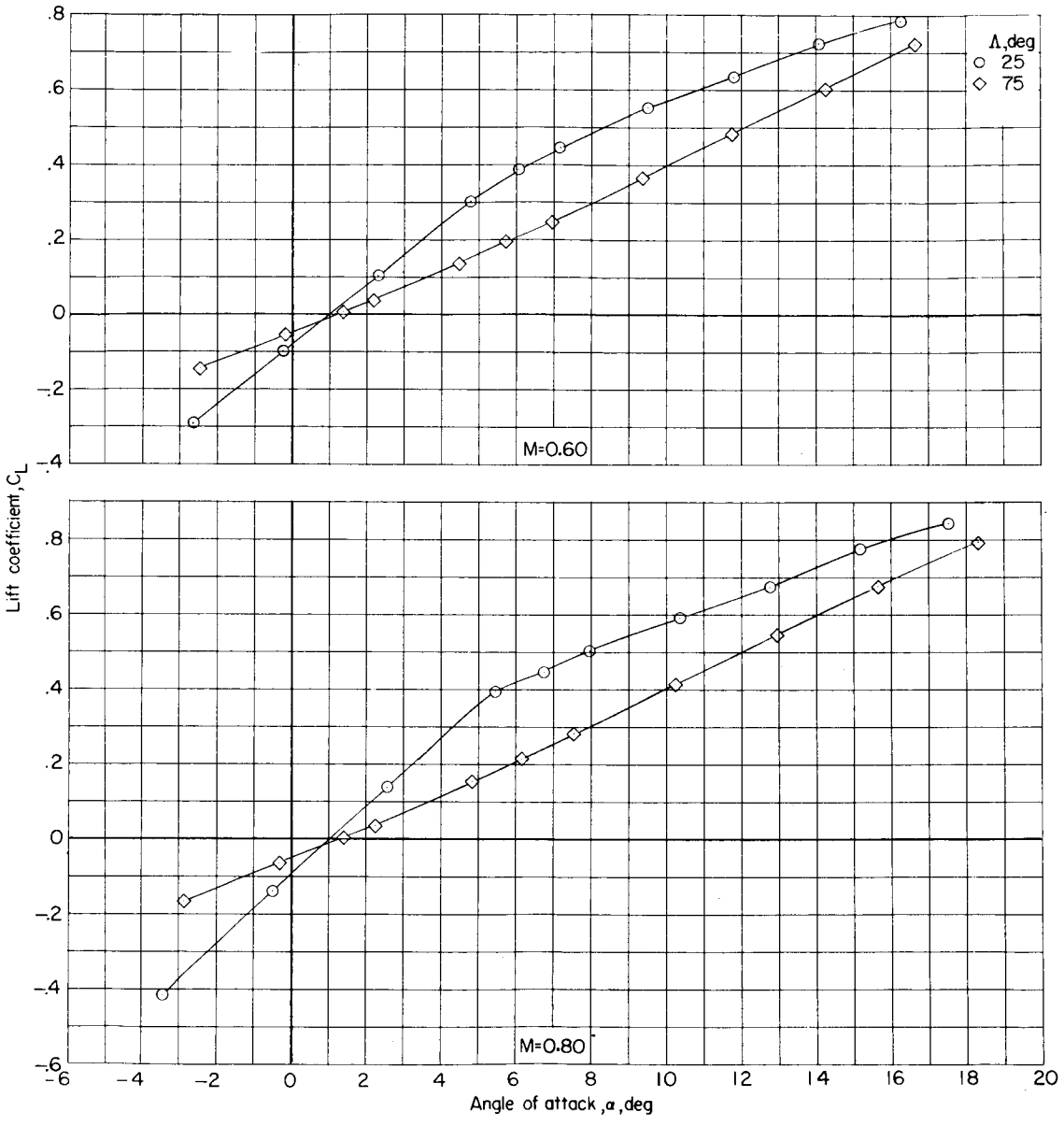

(a) C_L against α.

Figure 16.- Effect of wing sweep on longitudinal aerodynamic characteristics of model II with horizontal tail off. Configuration BWV.

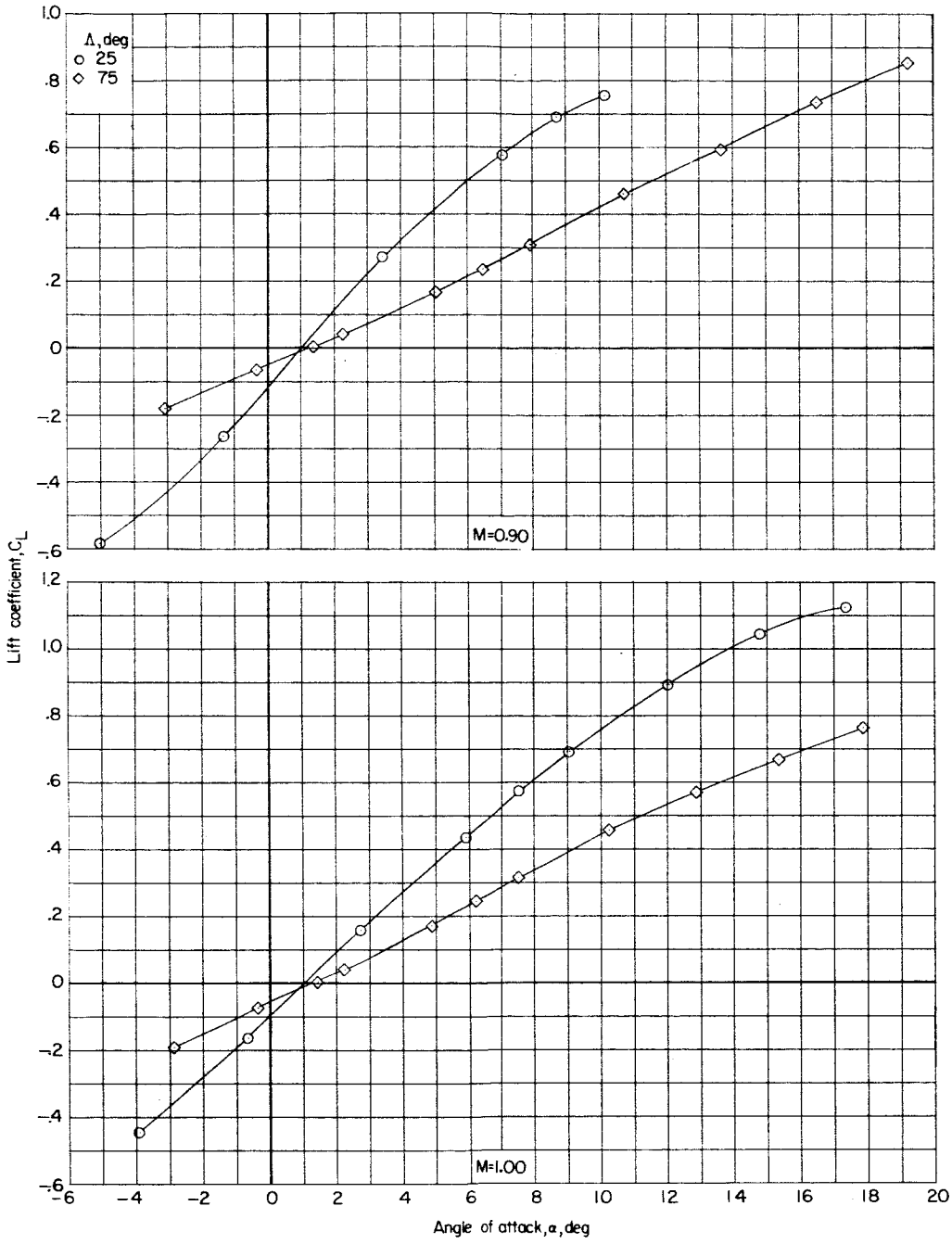

(a) Continued.

Figure 16.- Continued.

[redacted]

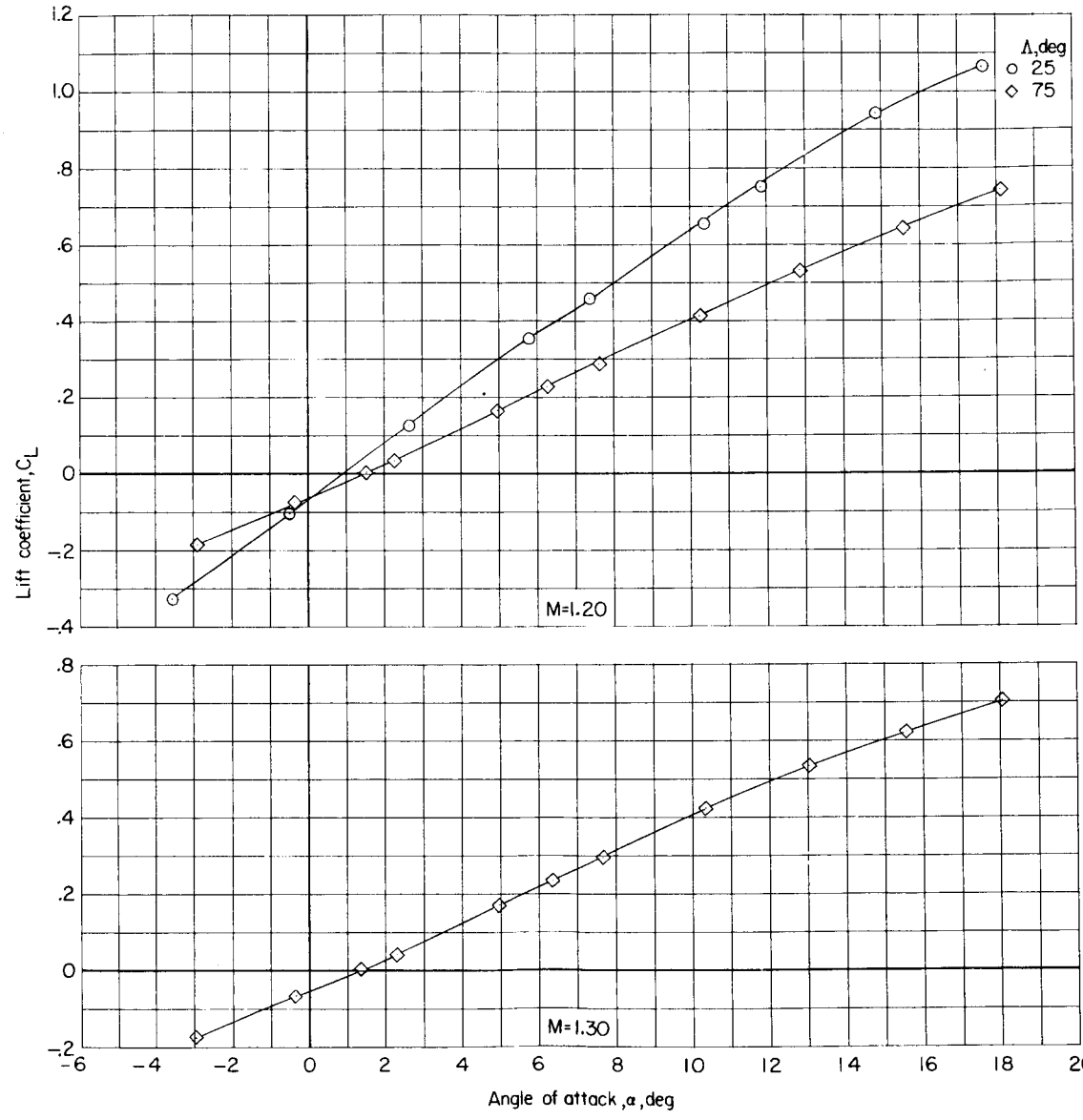

(a) Concluded.

Figure 16.- Continued.

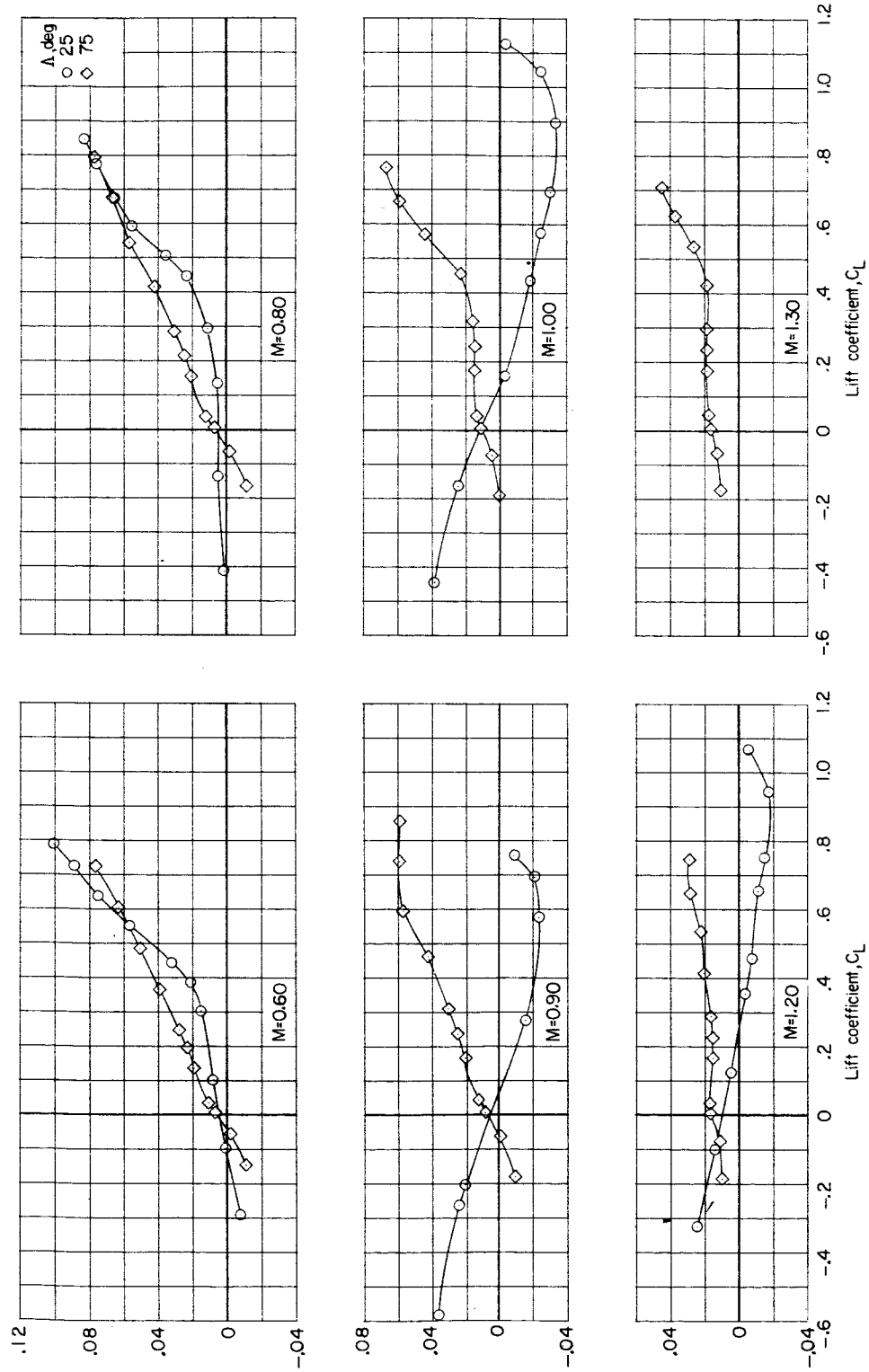

(b) C_m against C_L.

Figure 16.- Continued.

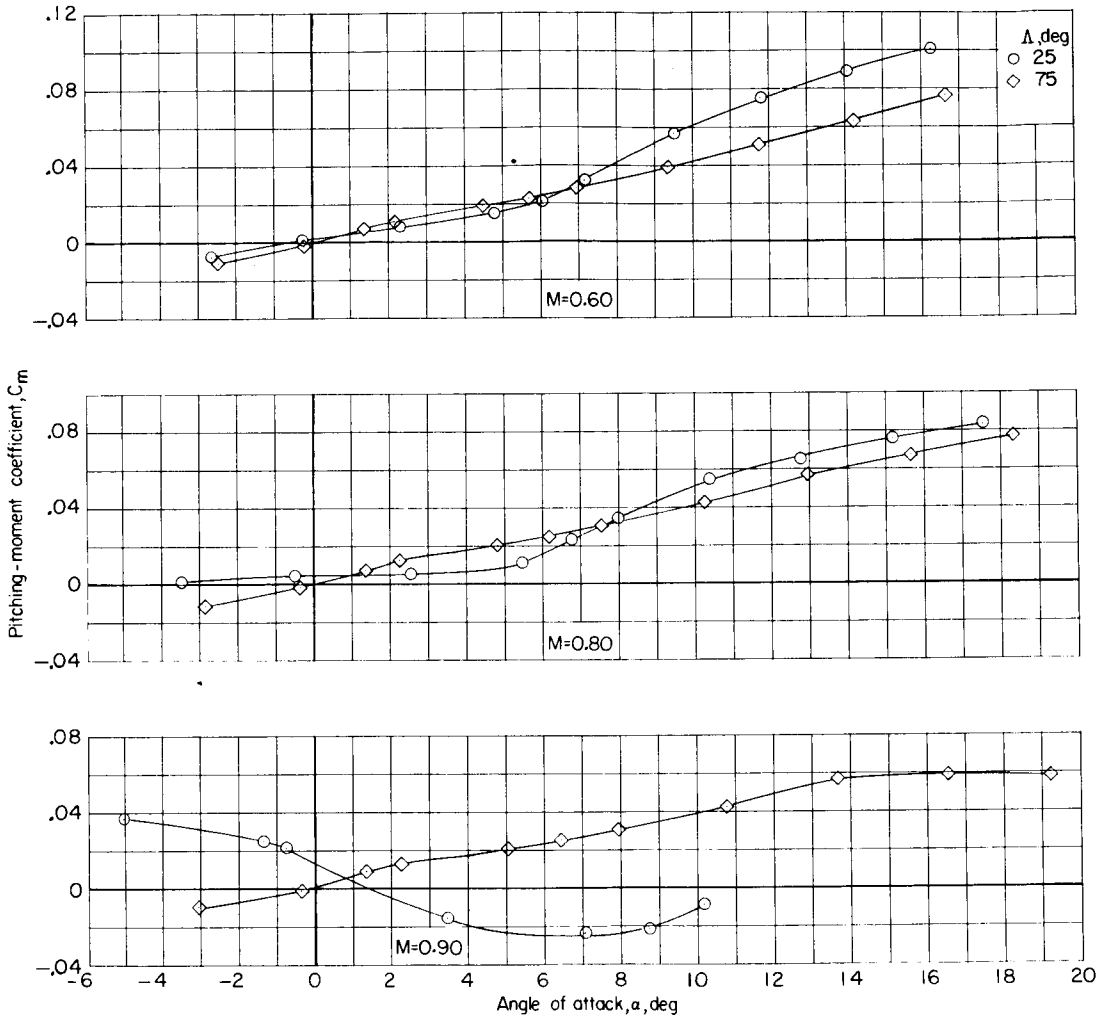

(c) C_m against α.

Figure 16.- Continued.

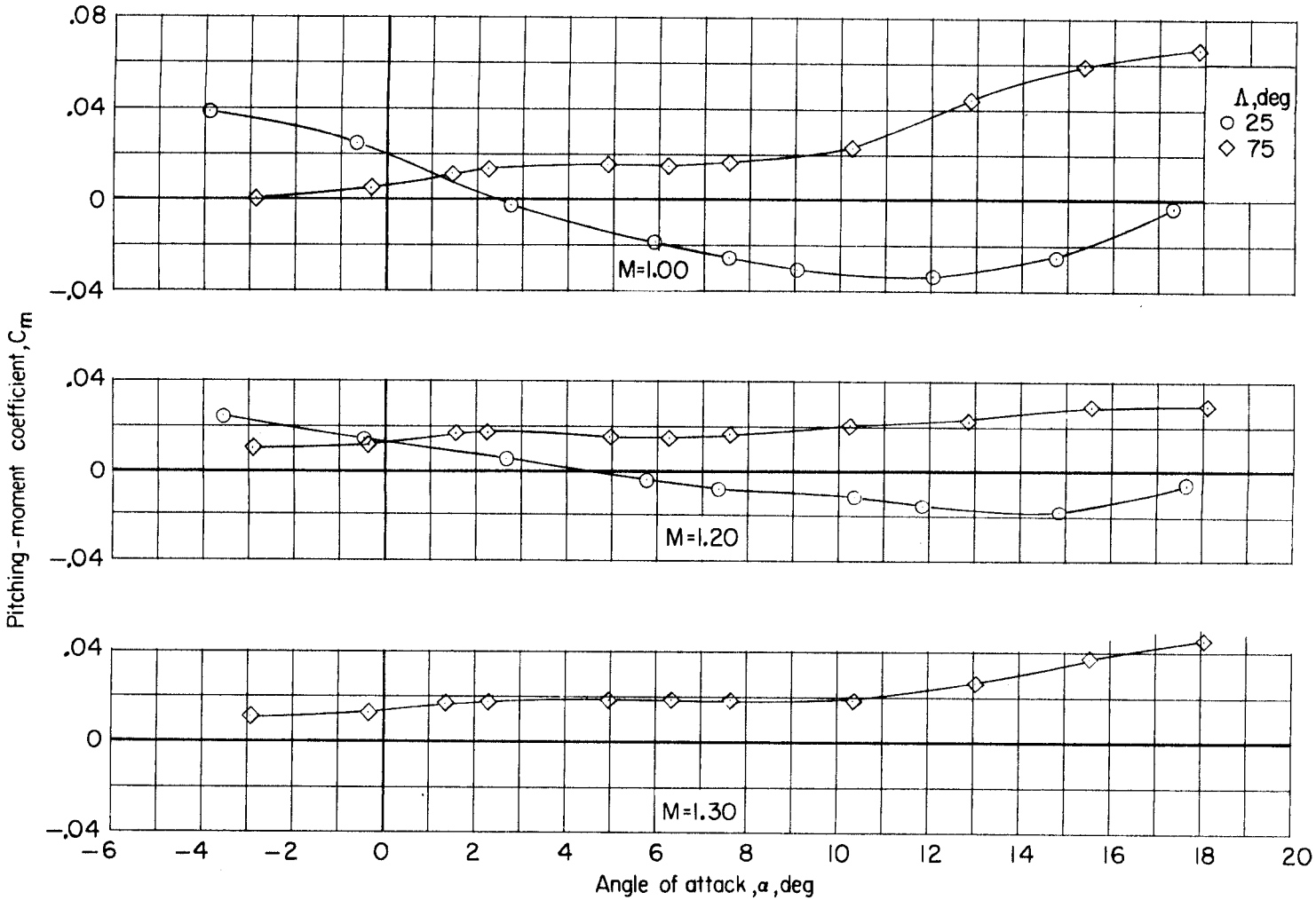

(c) Concluded.

Figure 16.- Continued.

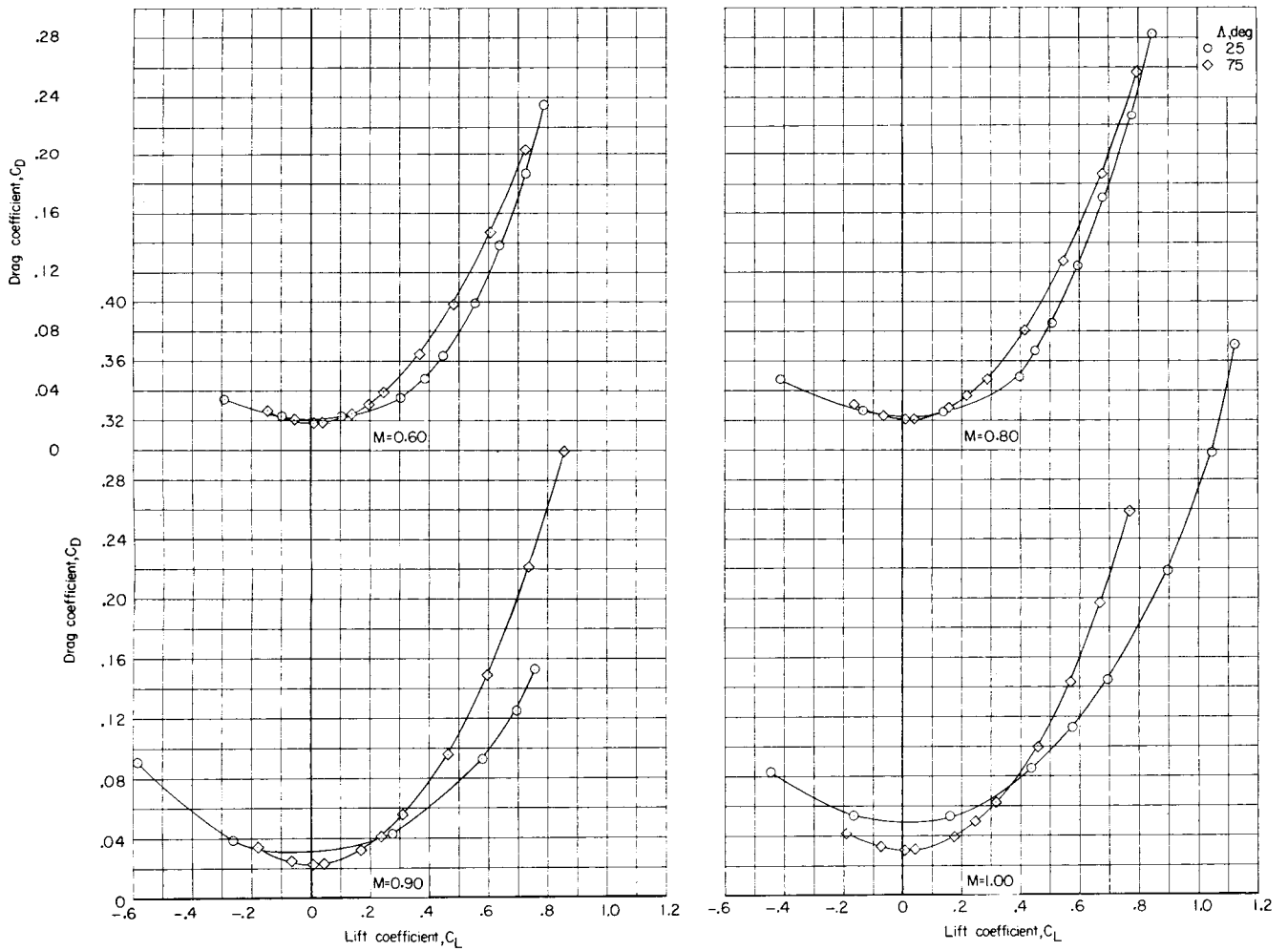

(d) C_D against C_L.

Figure 16.- Continued.

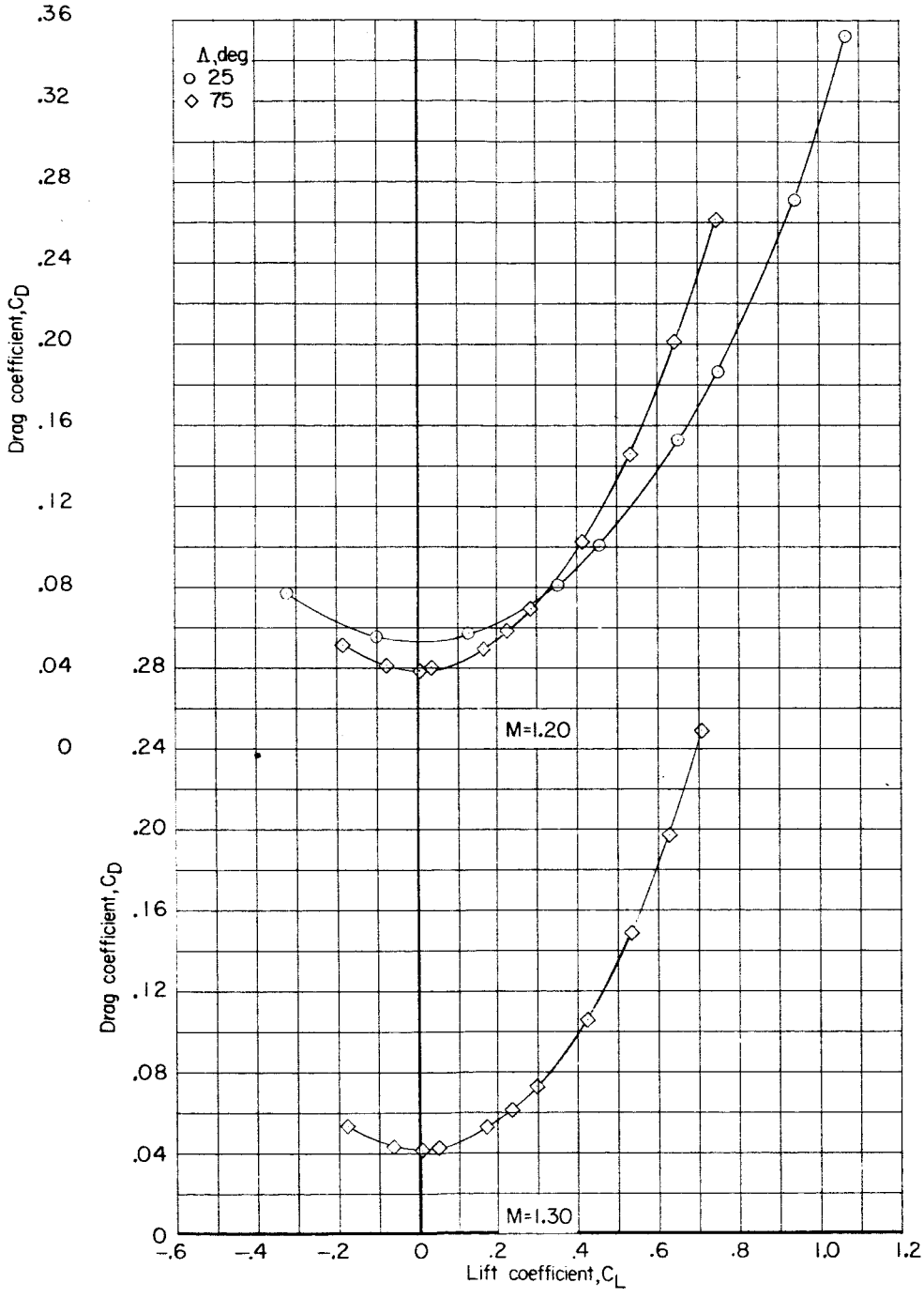

(d) Concluded.

Figure 16.- Continued.

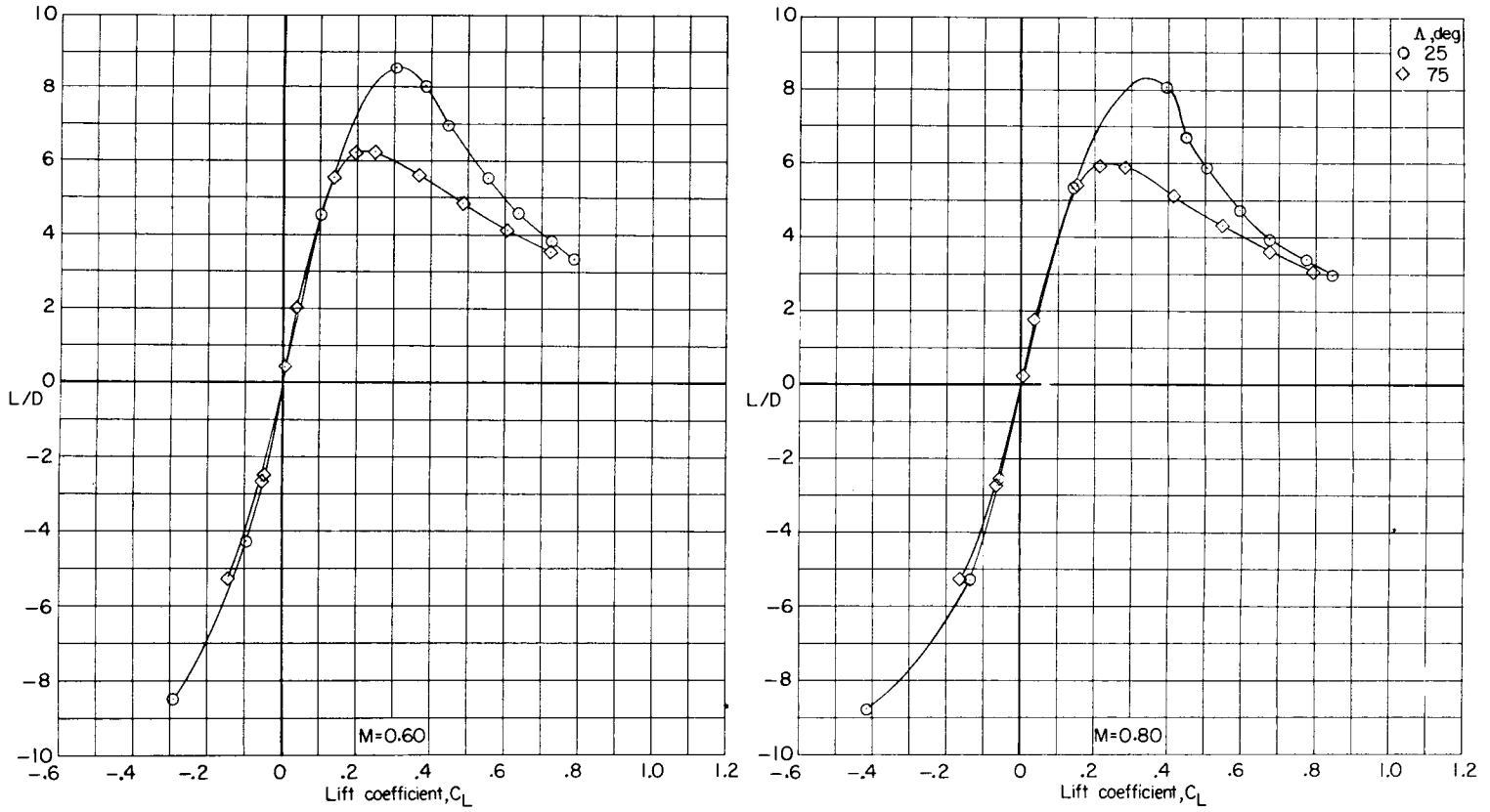

(e) L/D against C_L.

Figure 16.- Continued.

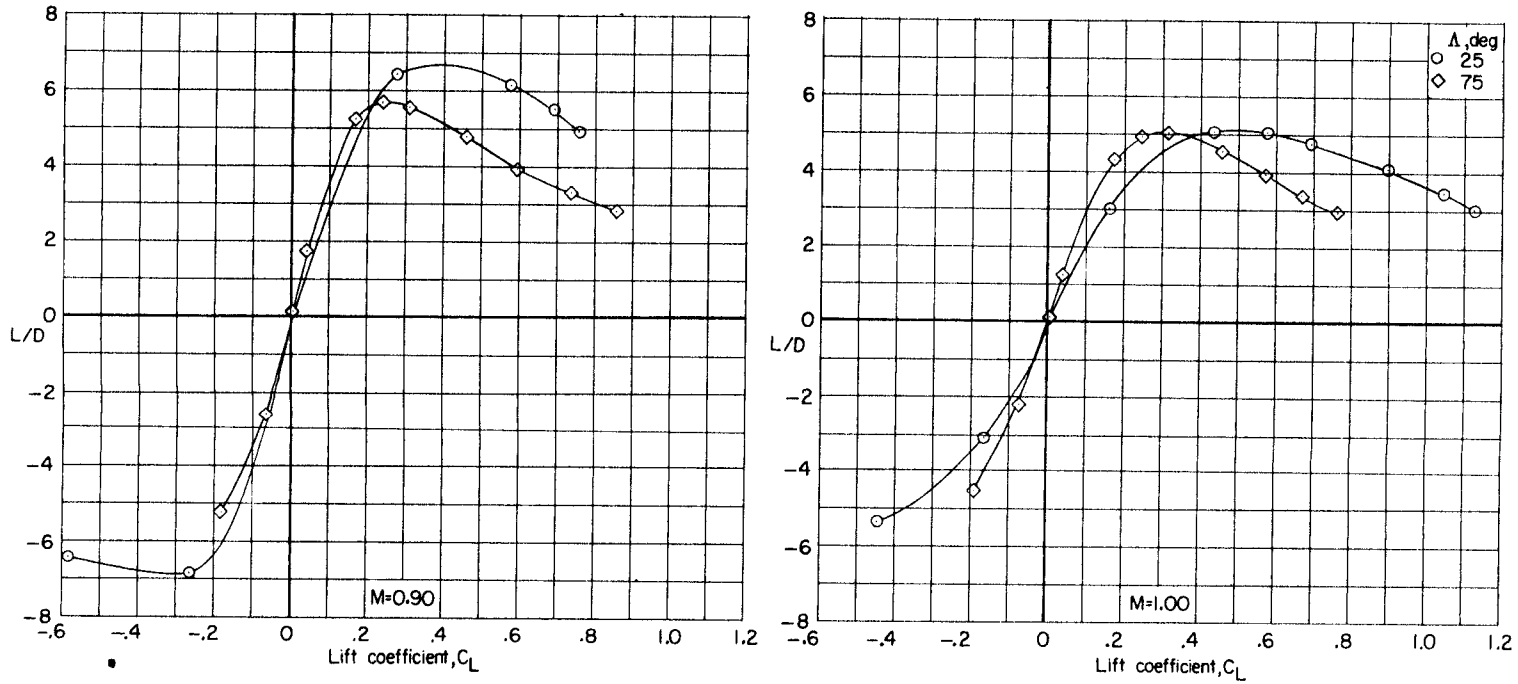

(e) Continued.

Figure 16.- Continued.

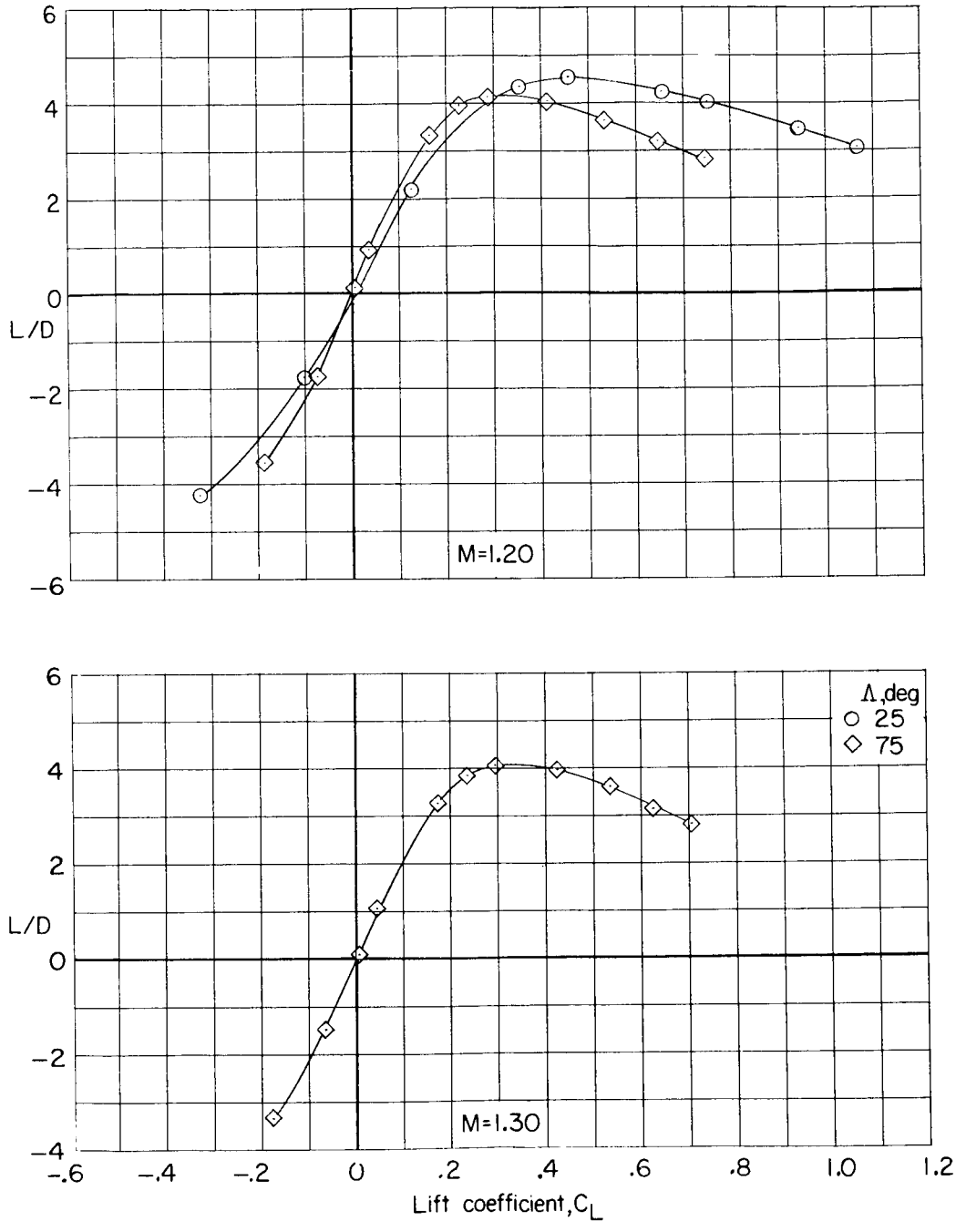

(e) Concluded.

Figure 16.- Concluded.

[redacted]

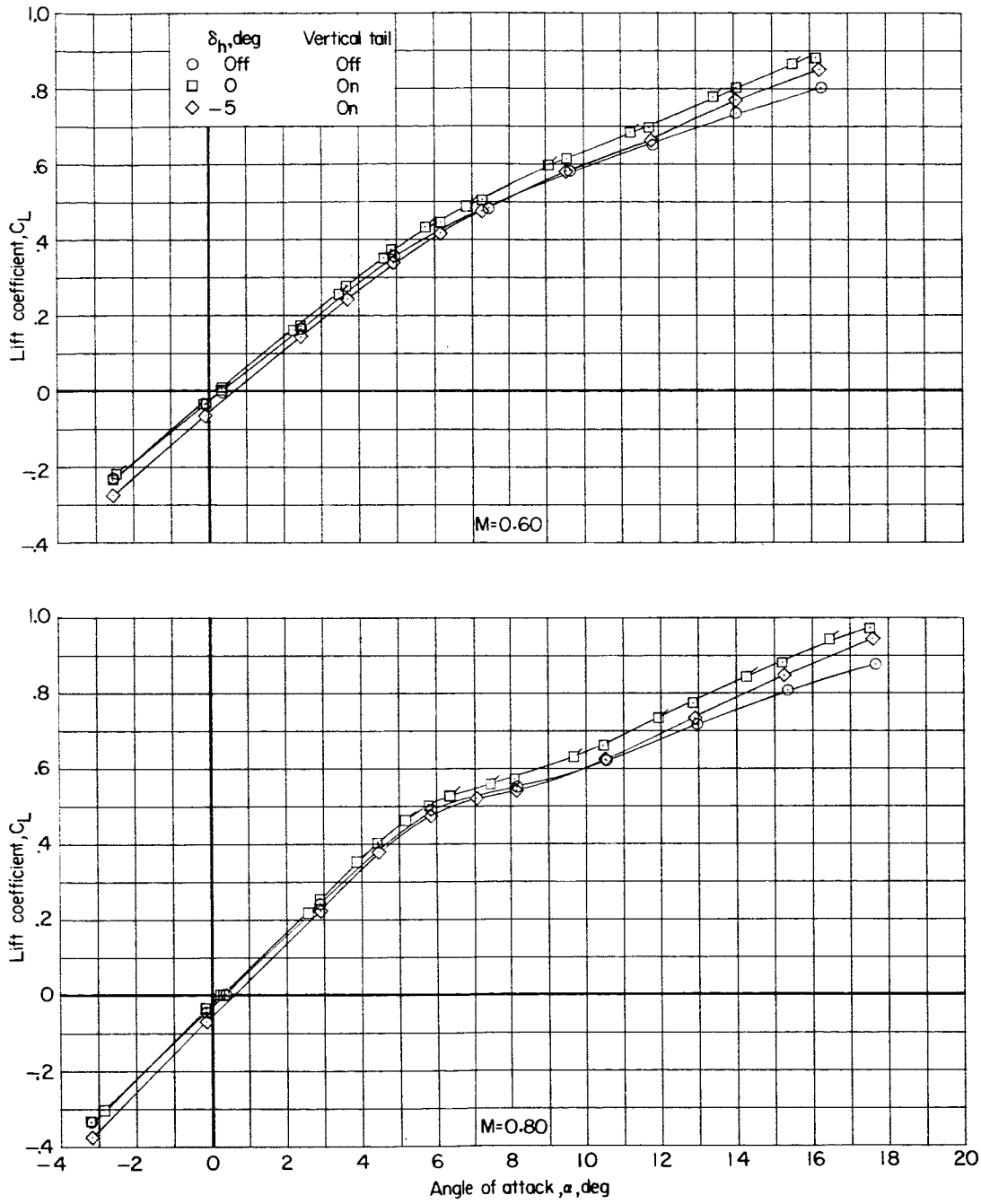

(a) C_L against α.

Figure 17.- Effect of horizontal-tail deflection on longitudinal aerodynamic characteristics of model III with 25° swept wing. Configuration BW_1VH. (Flagged symbols indicate points from repeat run.)

[redacted]

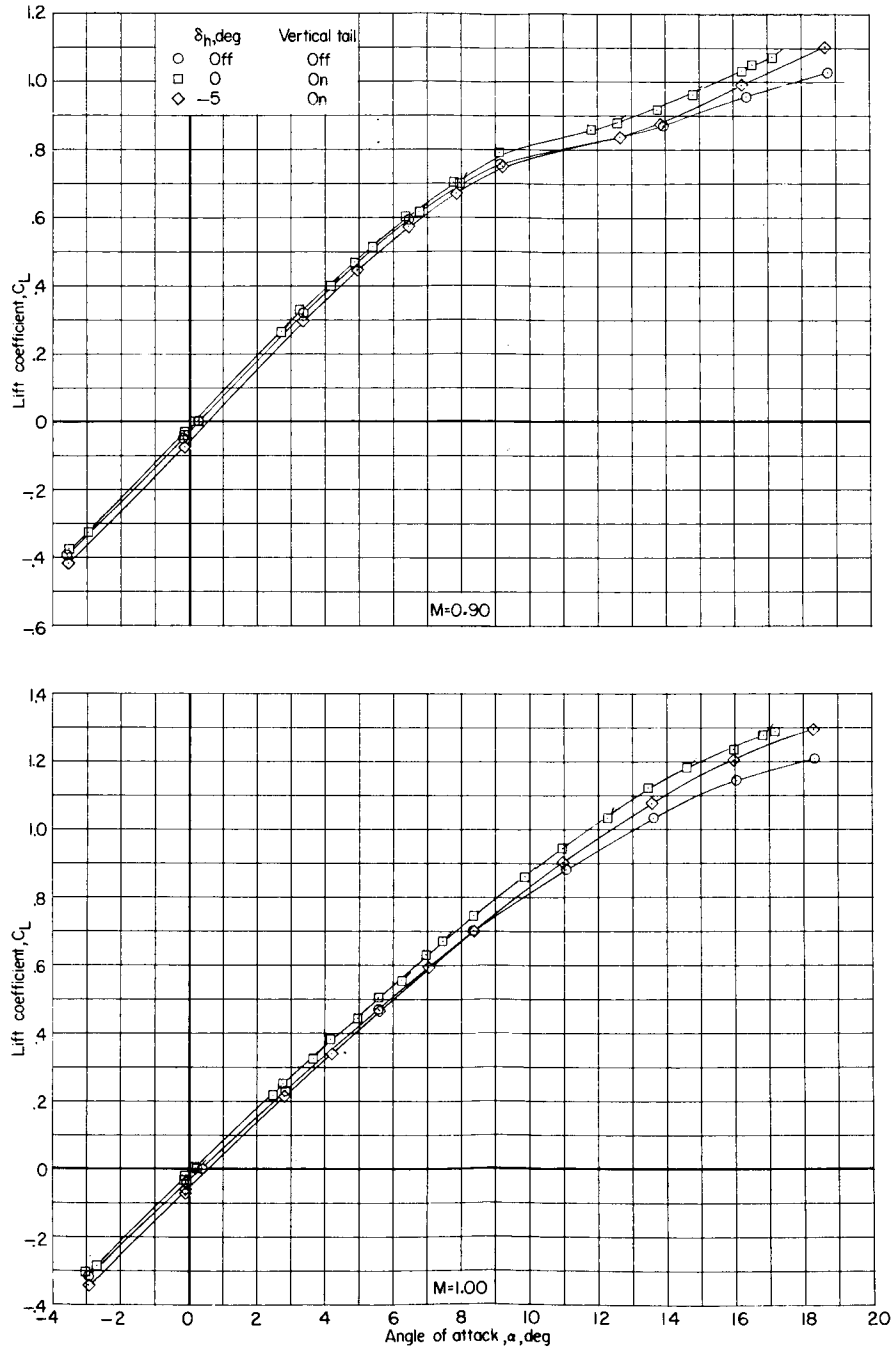

(a) Continued.

Figure 17.- Continued.

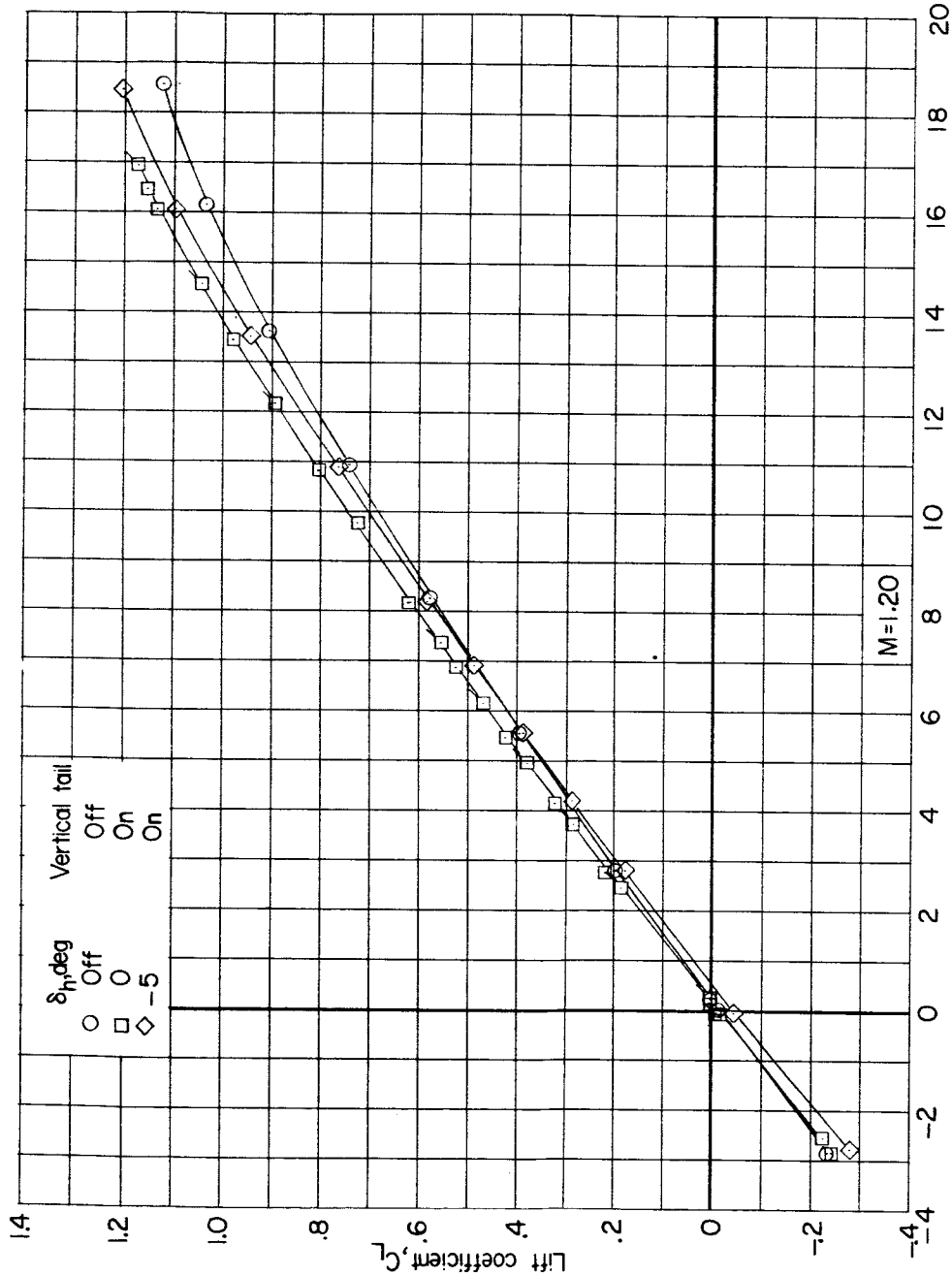

(a) Concluded.

Figure 17.- Continued.

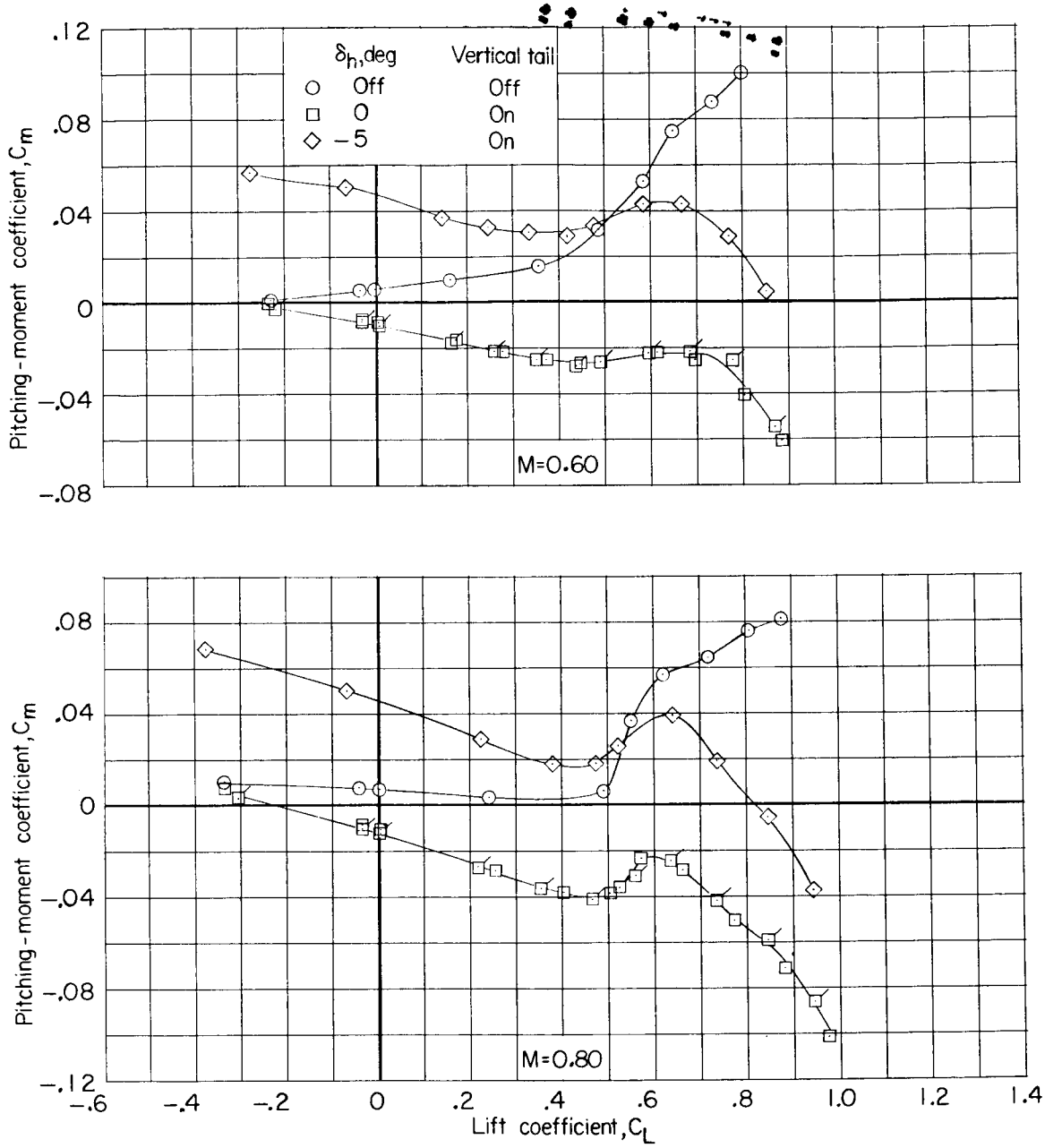

(b) C_m against C_L.

Figure 17.- Continued.

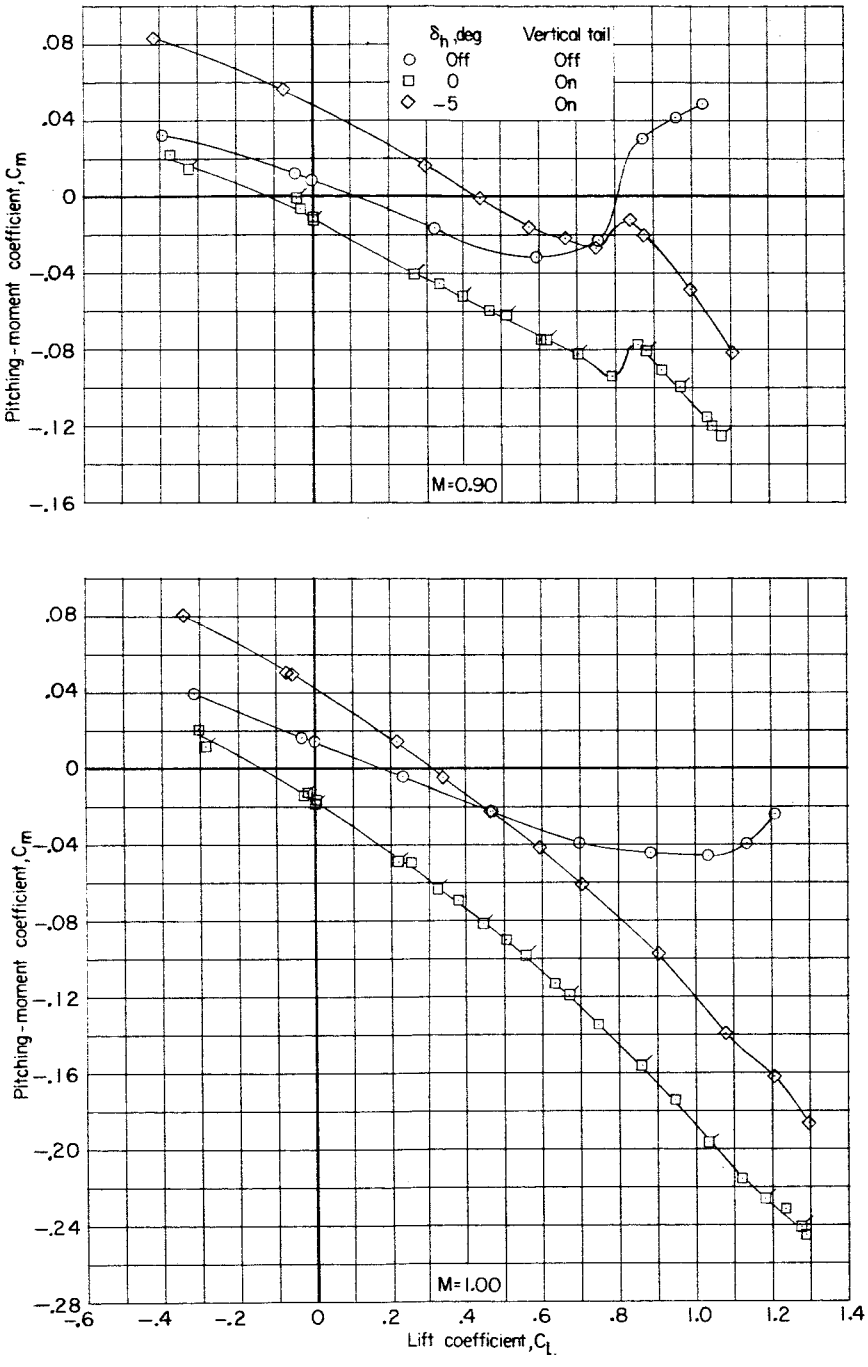

(b) Continued.

Figure 17.- Continued.

[redacted]

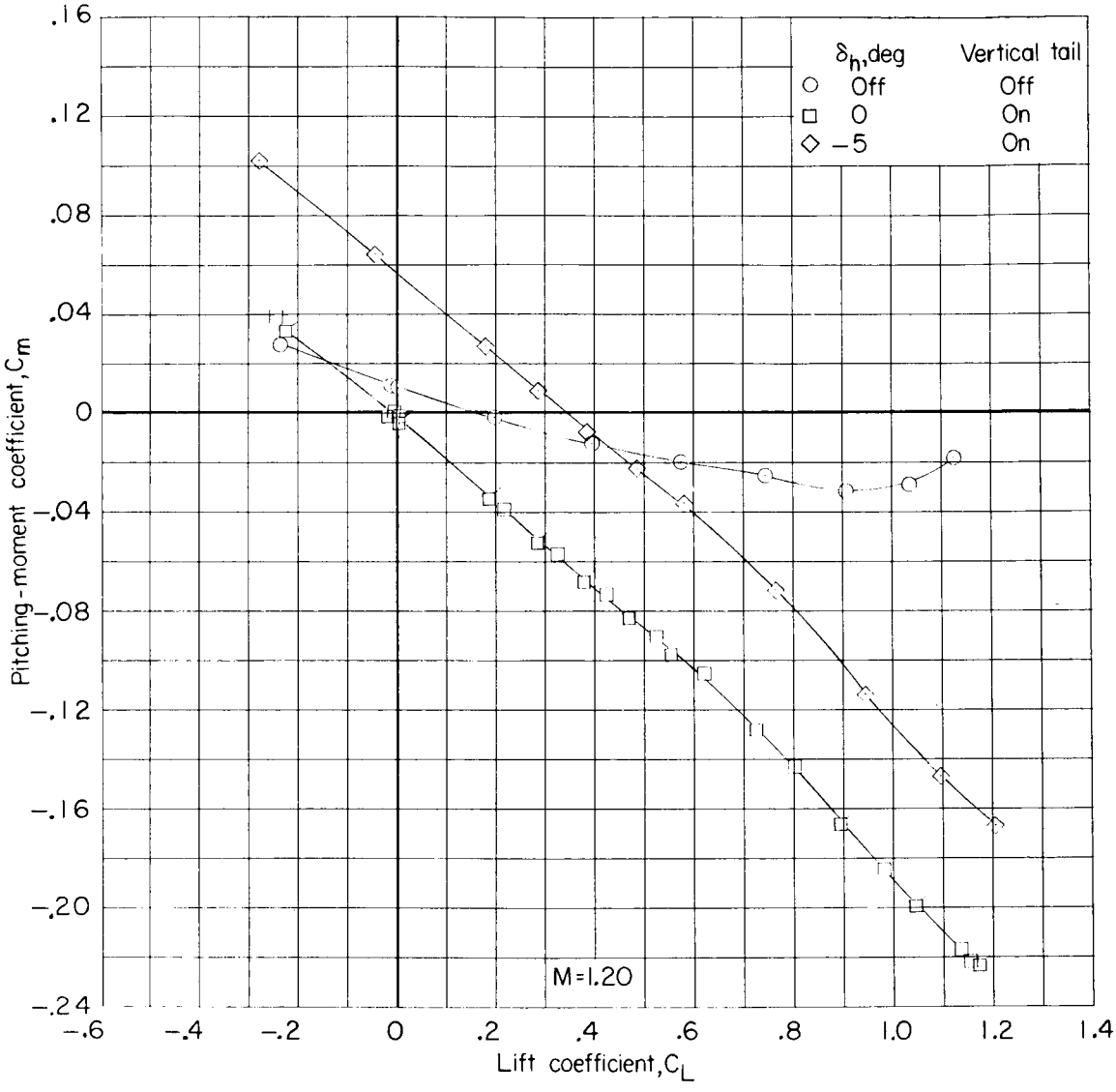

(b) Concluded.

Figure 17.- Continued.

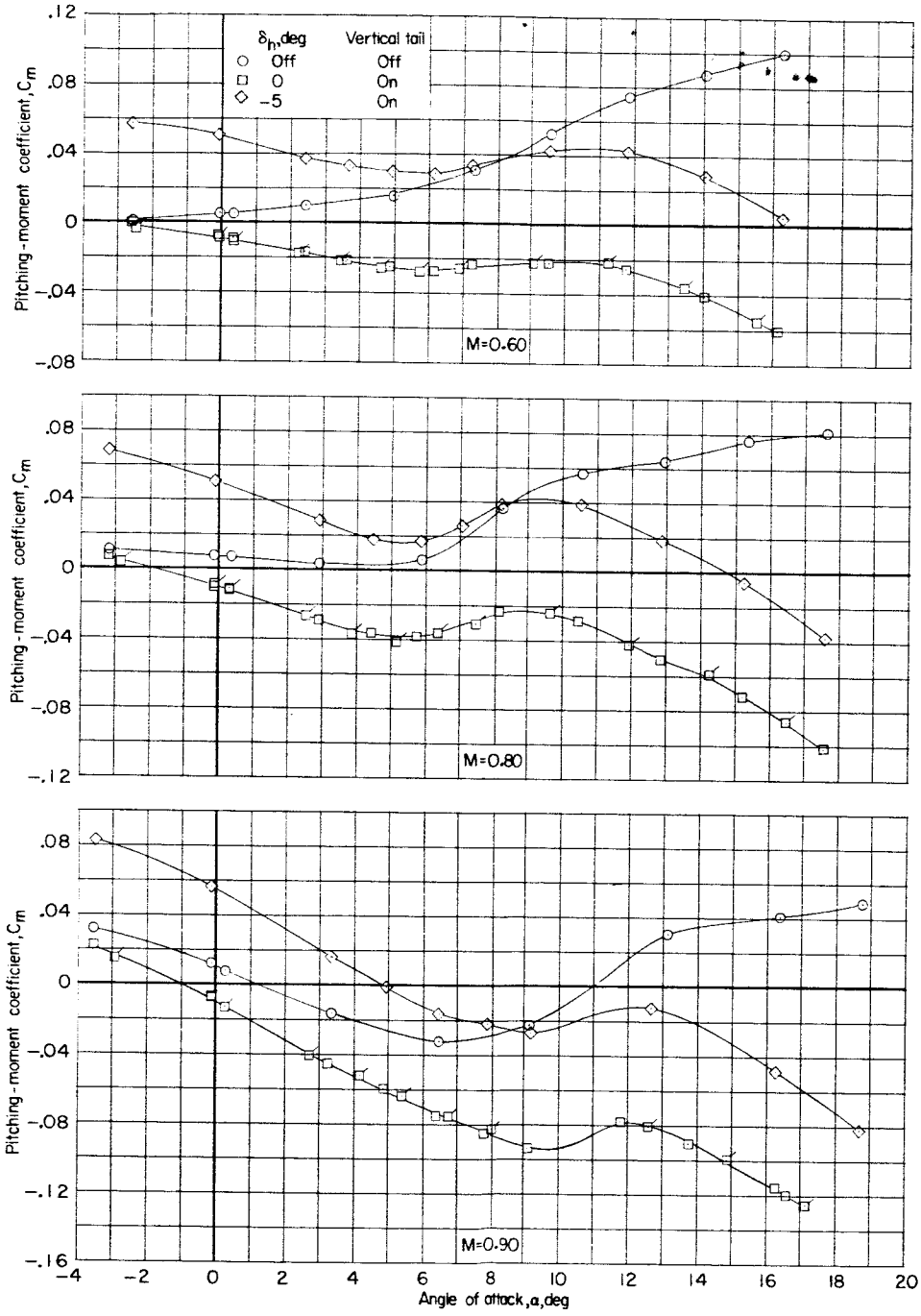

(c) C_m against α.

Figure 17.- Continued.

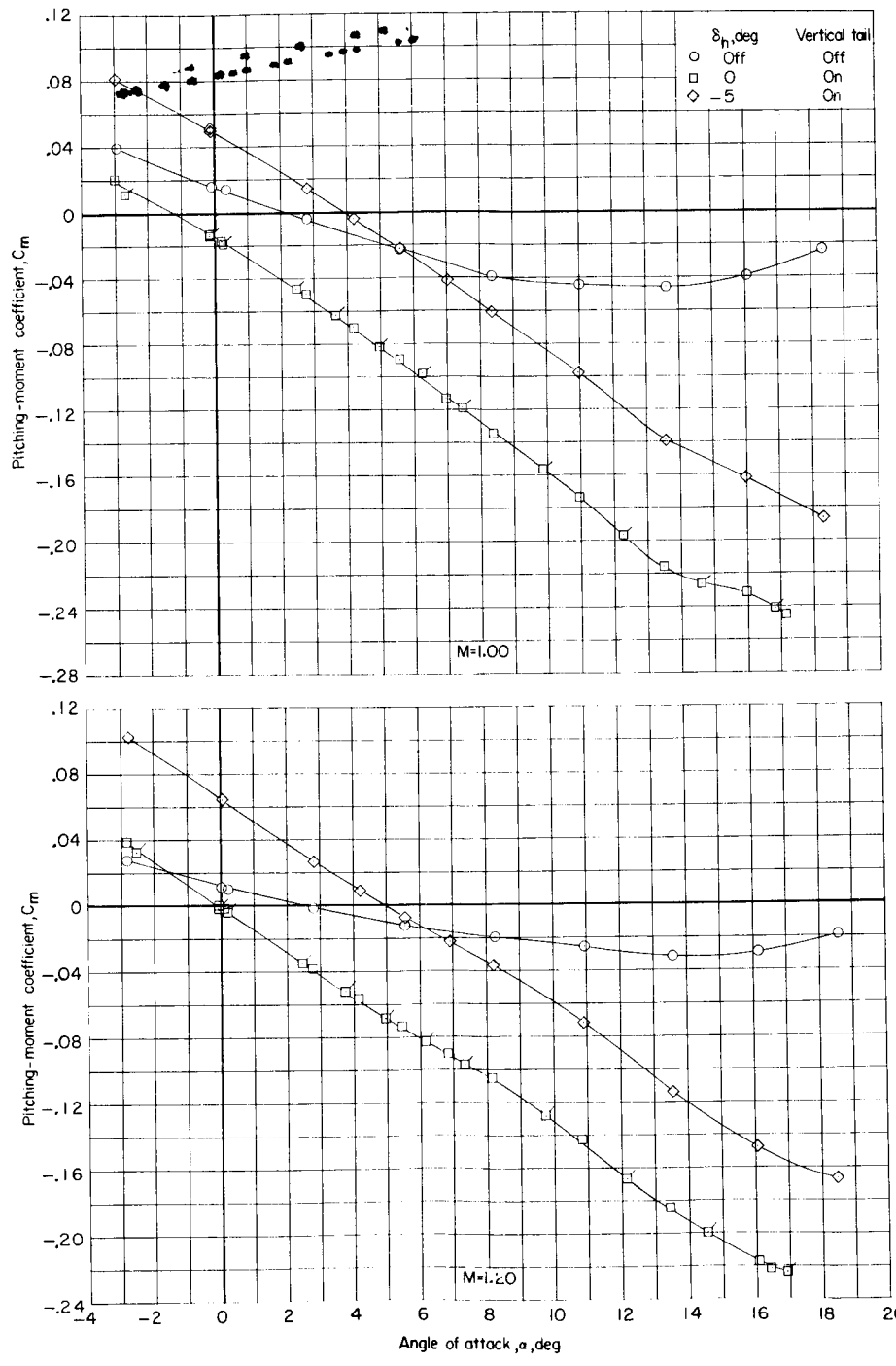

(c) Concluded.

Figure 17.- Continued.

[redacted]

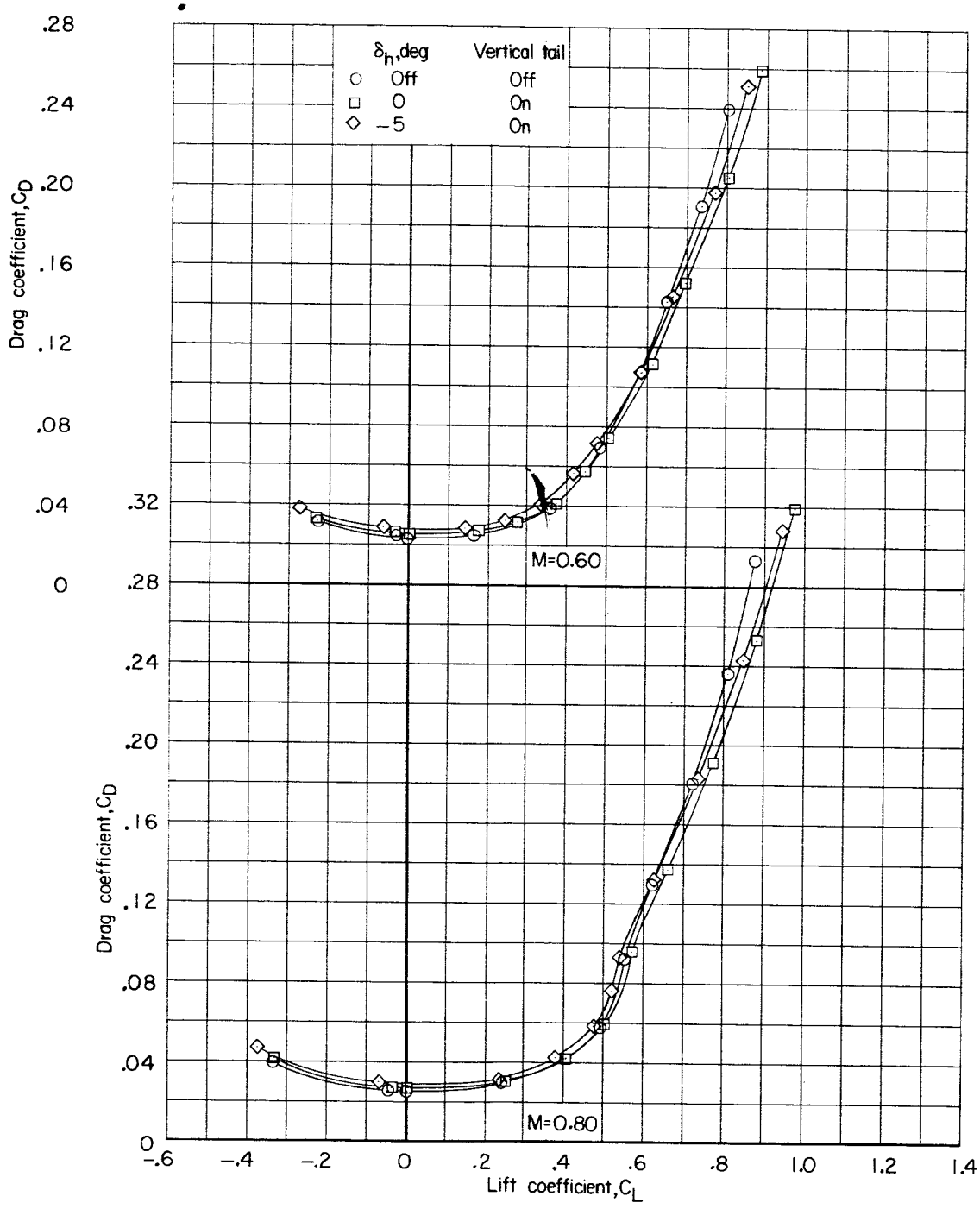

(d) C_D against C_L.

Figure 17.- Continued.

[redacted]

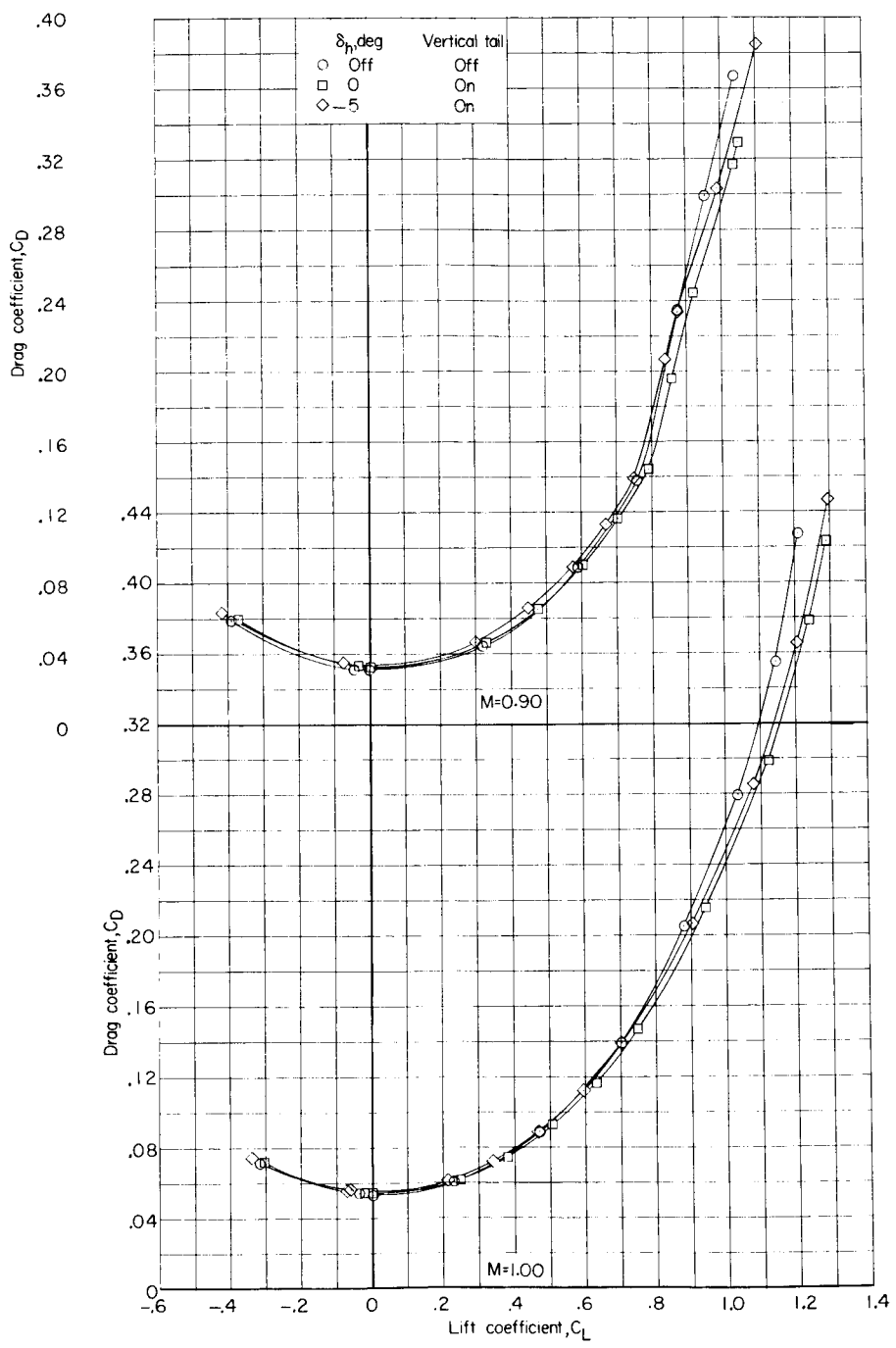

(d) Continued.

Figure 17.- Continued.

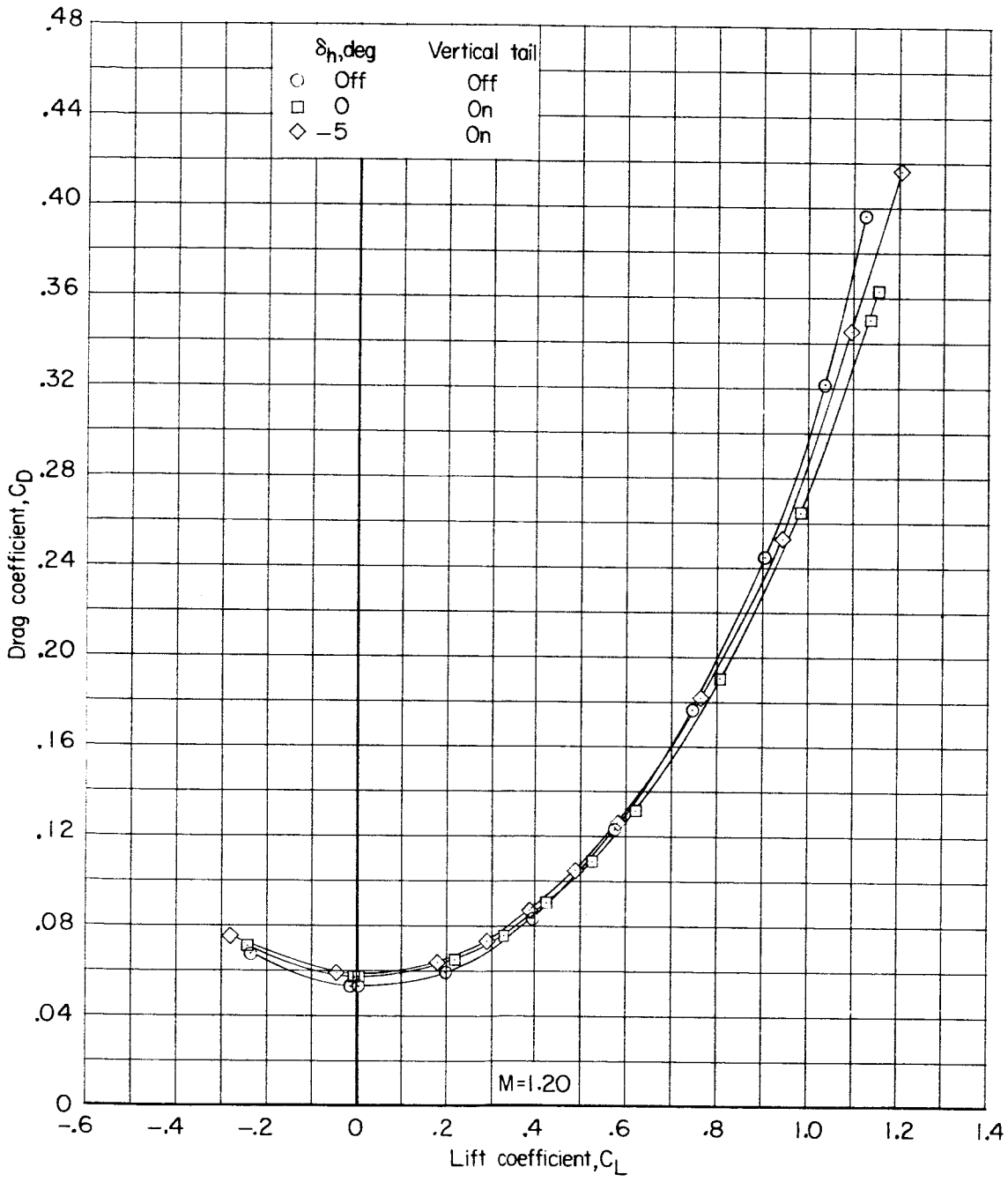

(d) Concluded.

Figure 17.- Continued.

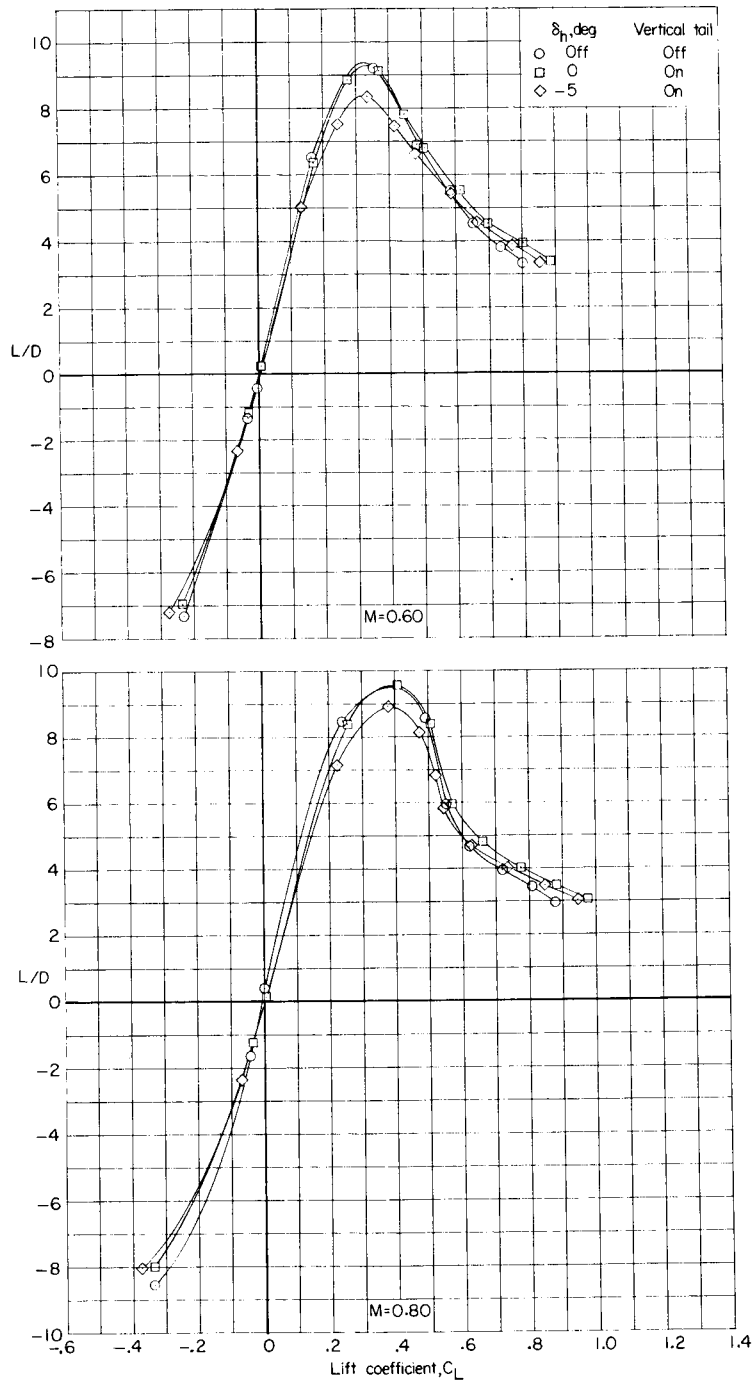

(e) L/D against C_L.

Figure 17.- Continued.

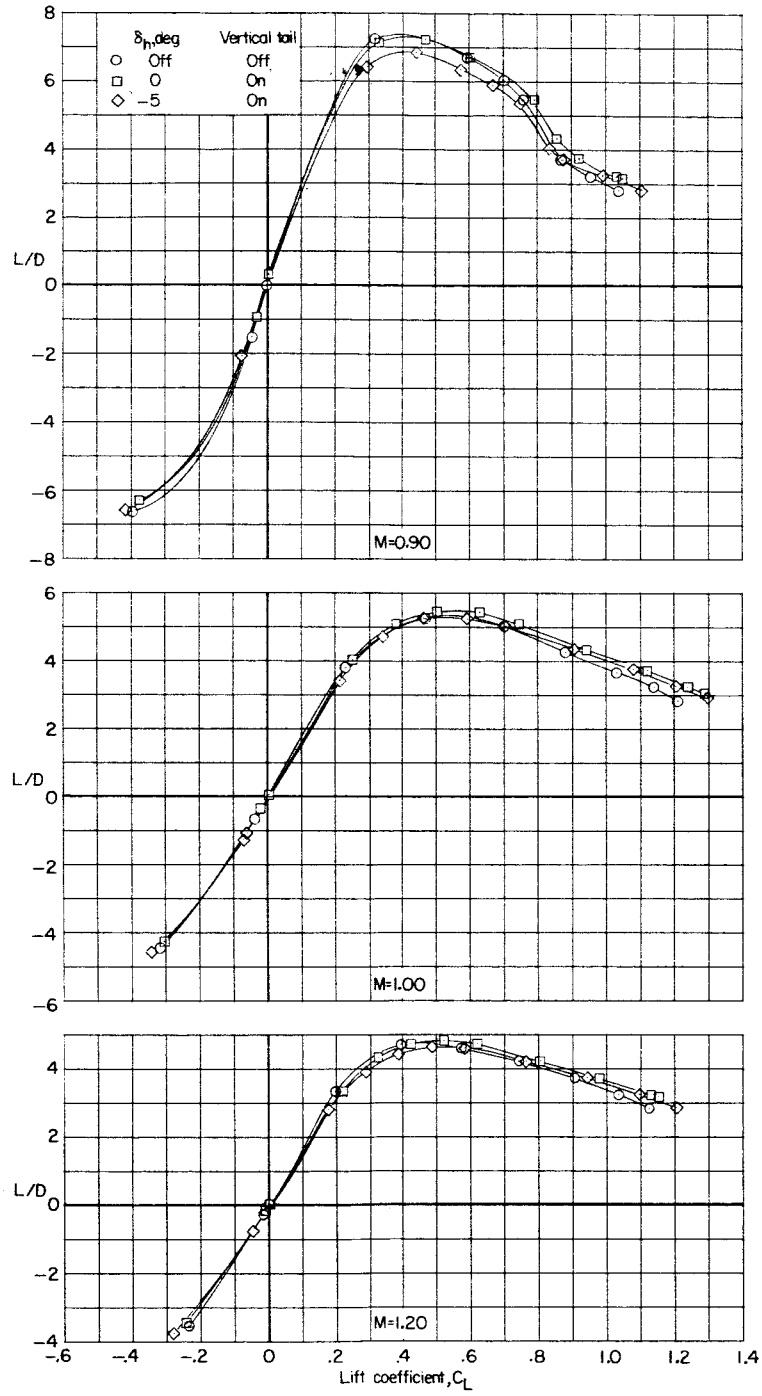

(e) Concluded.

Figure 17.- Concluded.

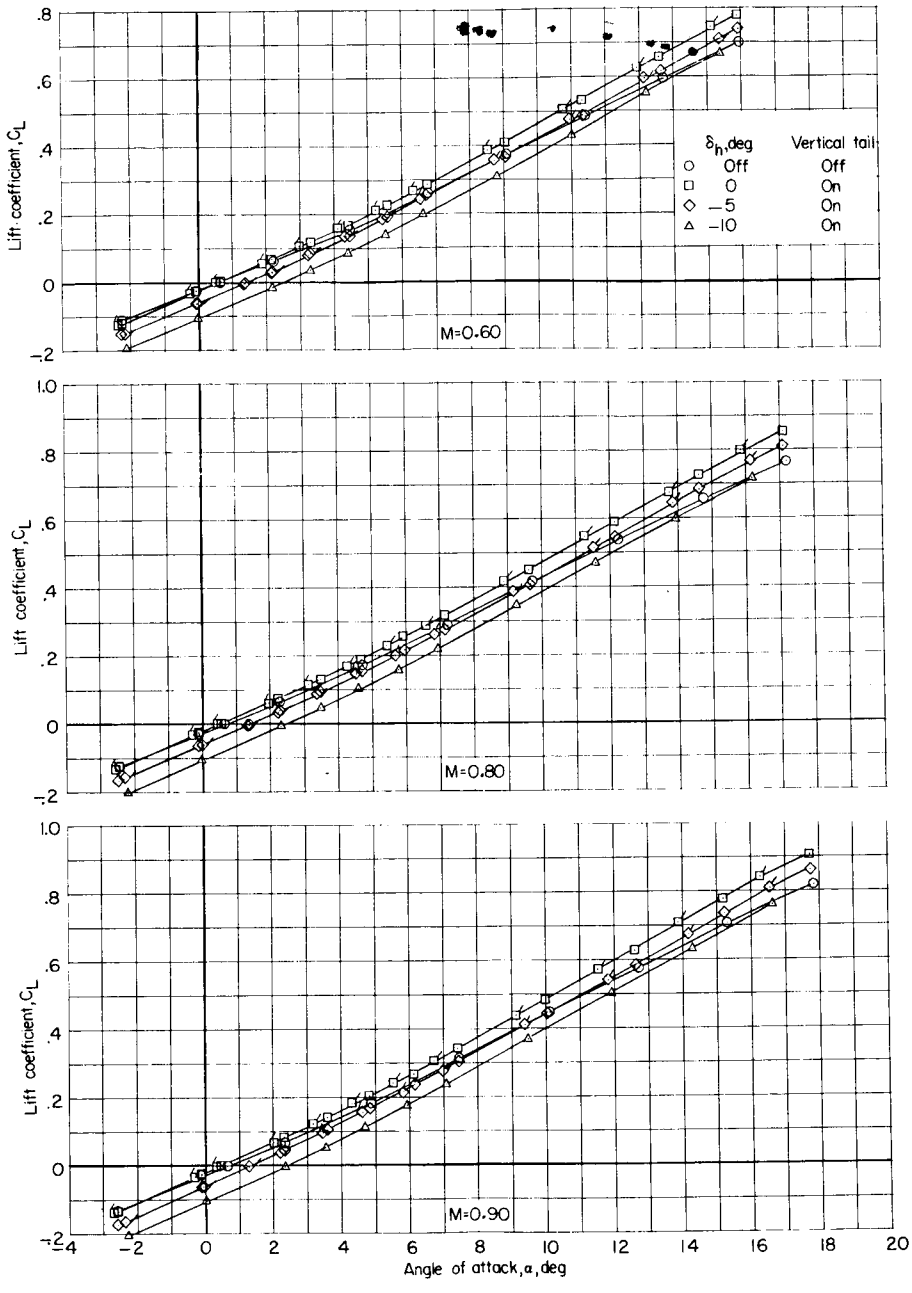

(a) C_L against α.

Figure 18.- Effect of horizontal-tail deflection on longitudinal aerodynamic characteristics of model III with 75° swept wing. Configuration BW_3VH. (Flagged symbols indicate points from repeat run.)

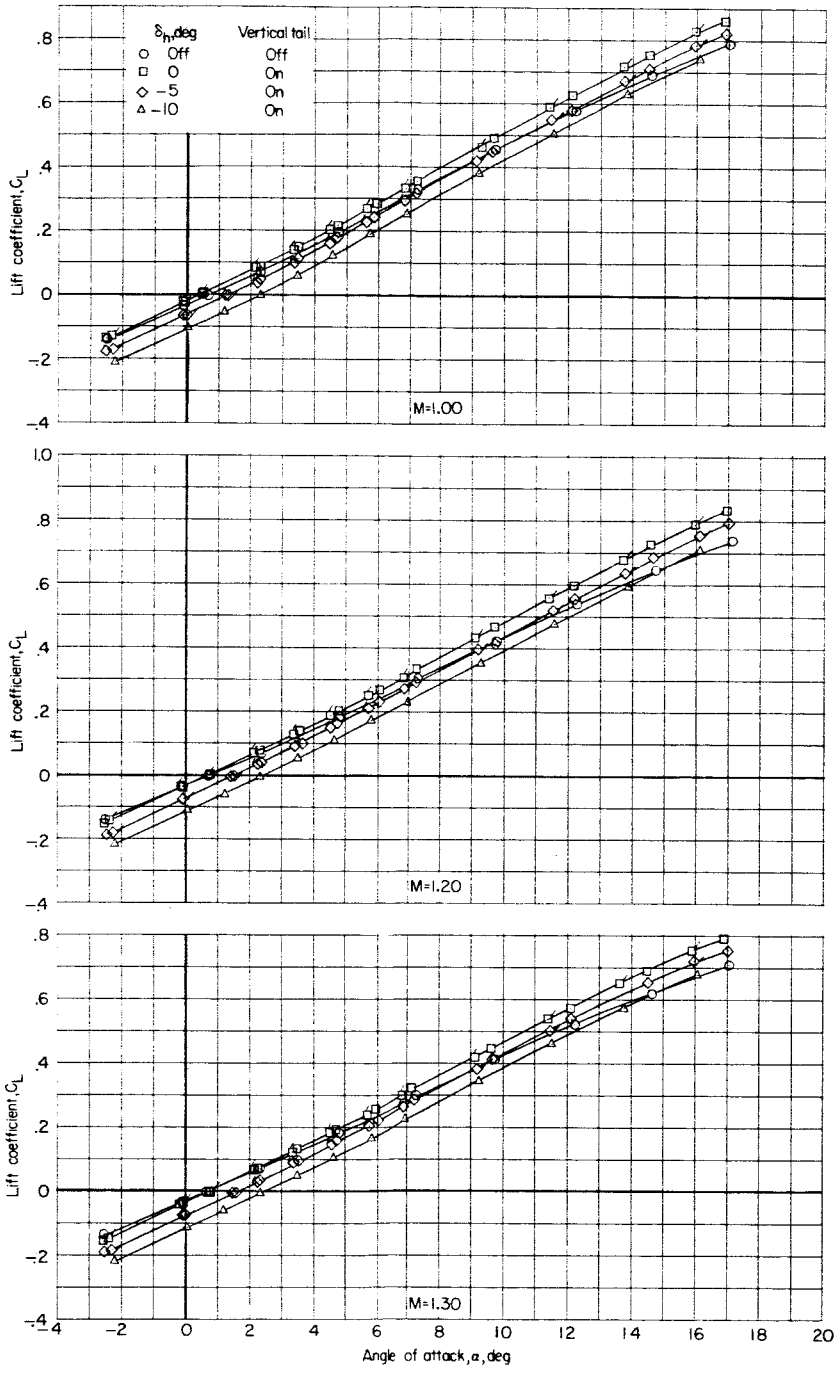

(a) Concluded.

Figure 18.- Continued.

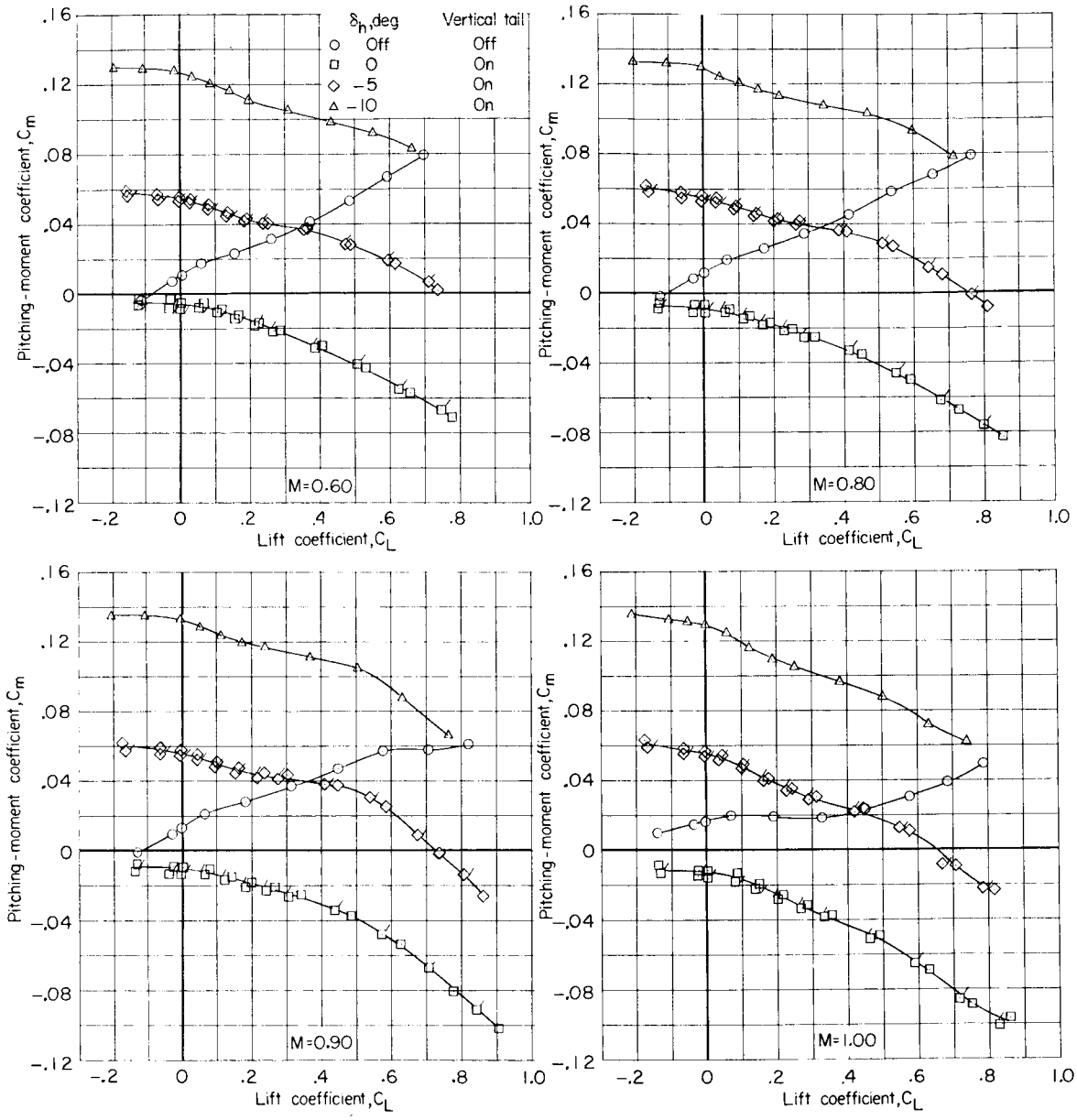

(b) C_m against C_L.

Figure 18.- Continued.

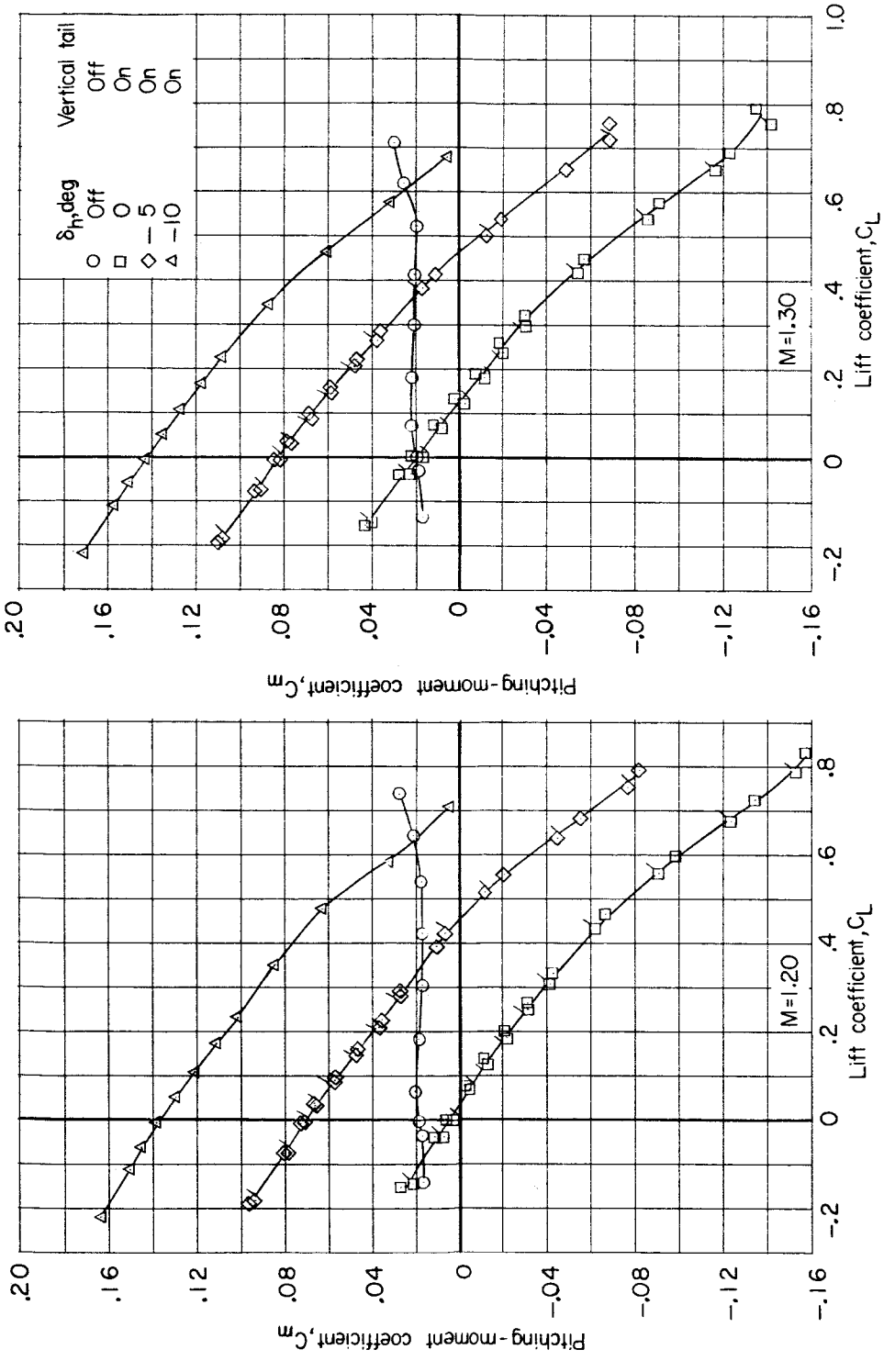

(b) Concluded.

Figure 18.- Continued.

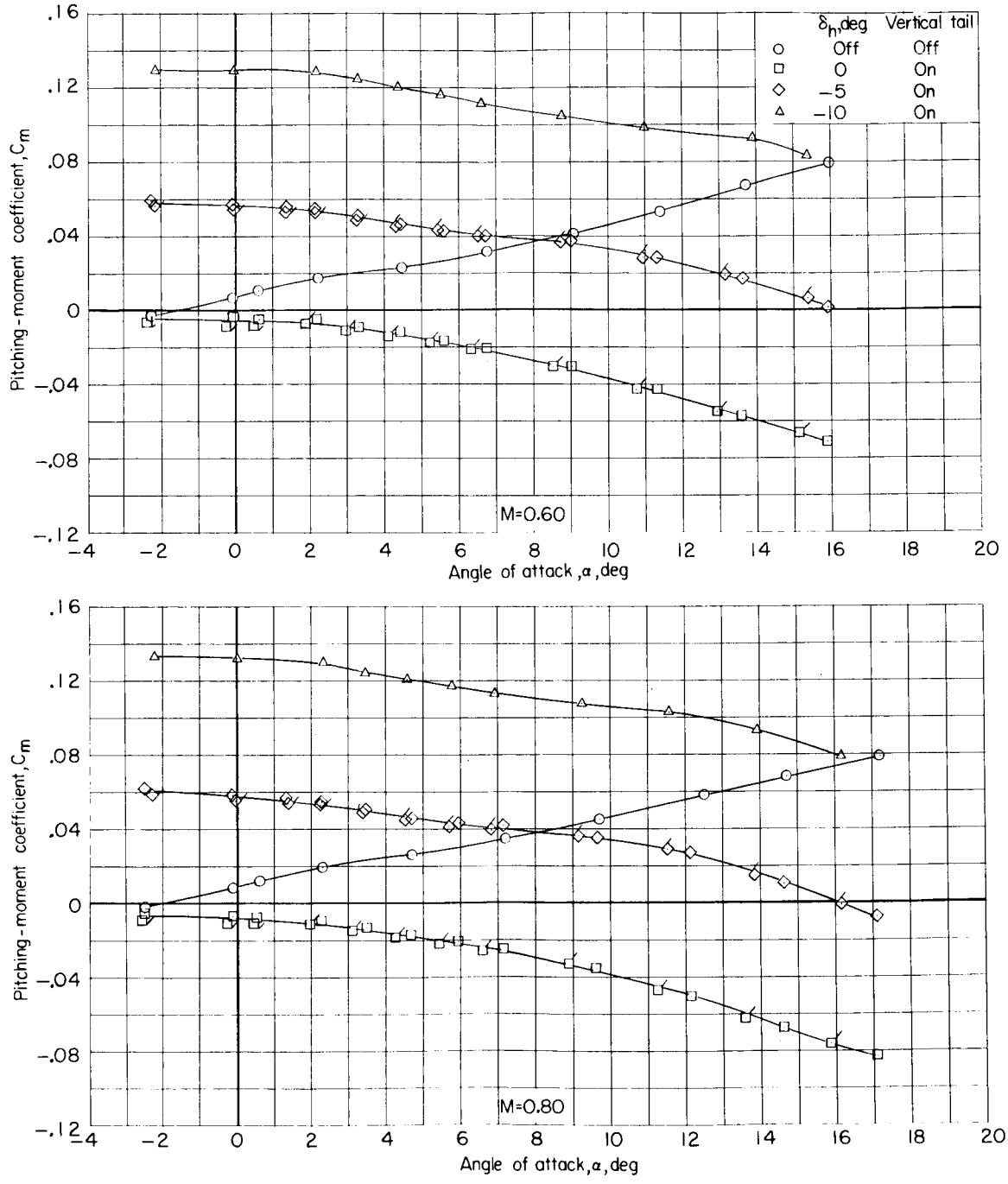

(c) C_m against α.

Figure 18.- Continued.

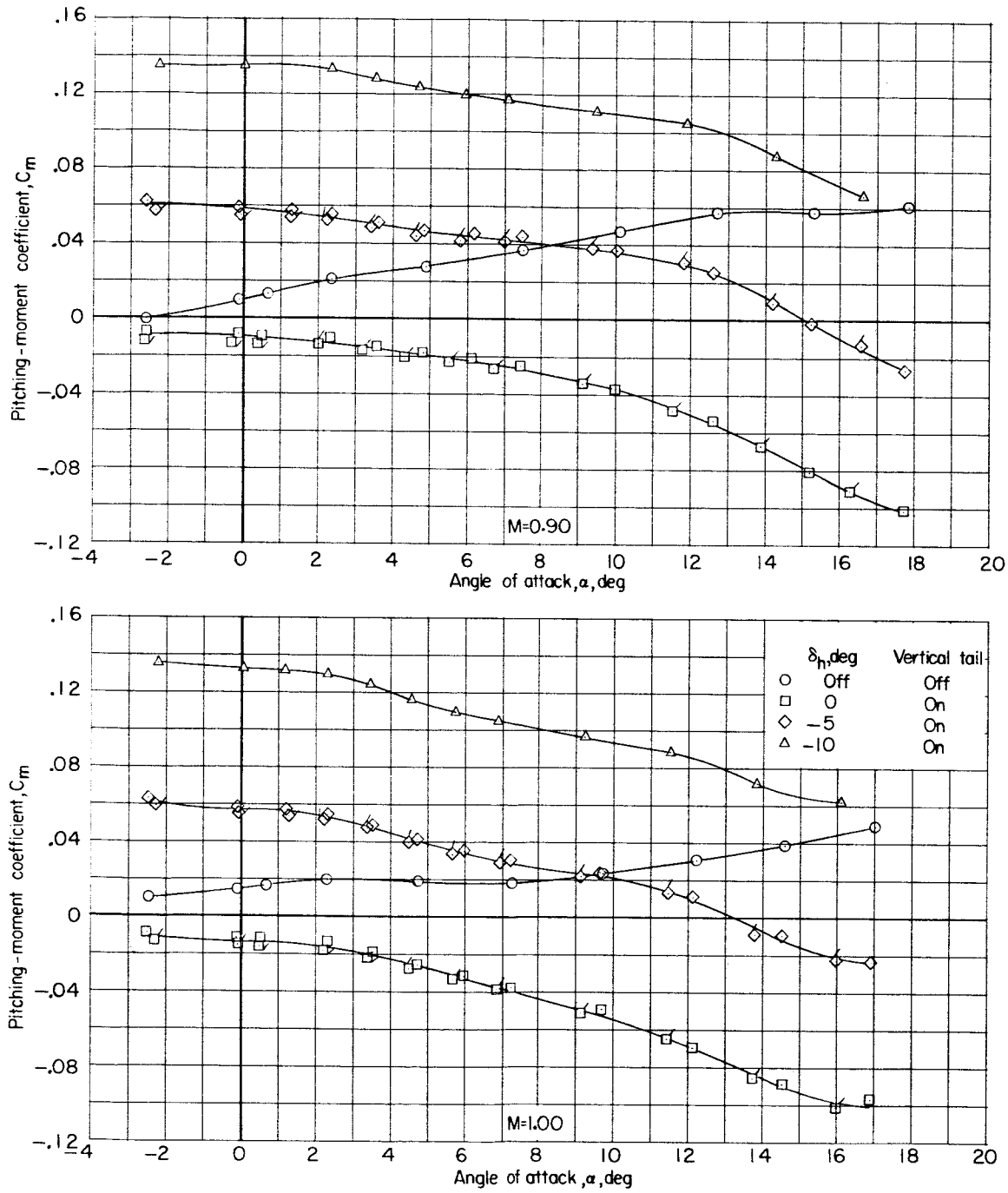

(c) Continued.

Figure 18.- Continued.

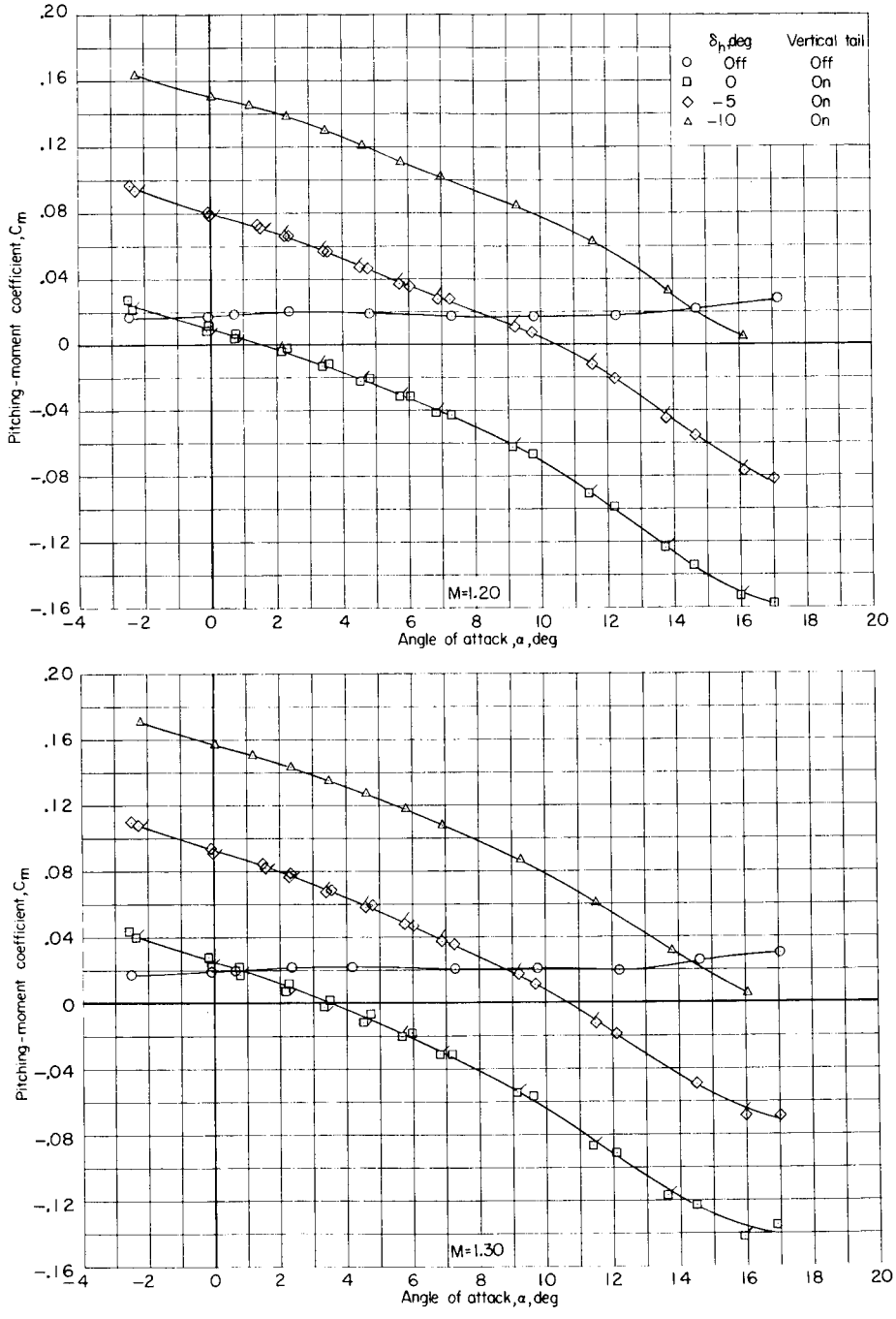

(c) Concluded.

Figure 18.- Continued.

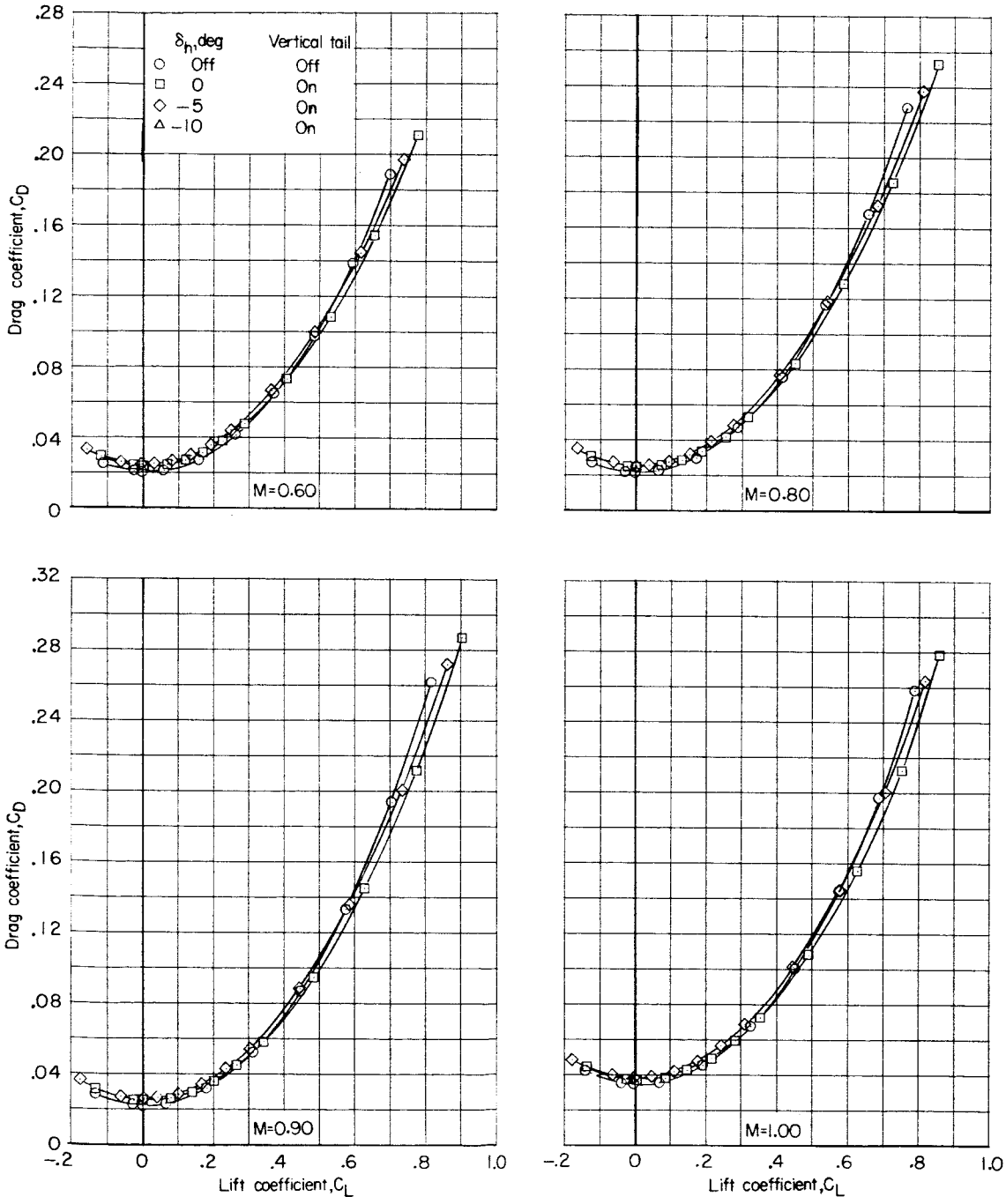

(d) C_D against C_L.

Figure 18.- Continued.

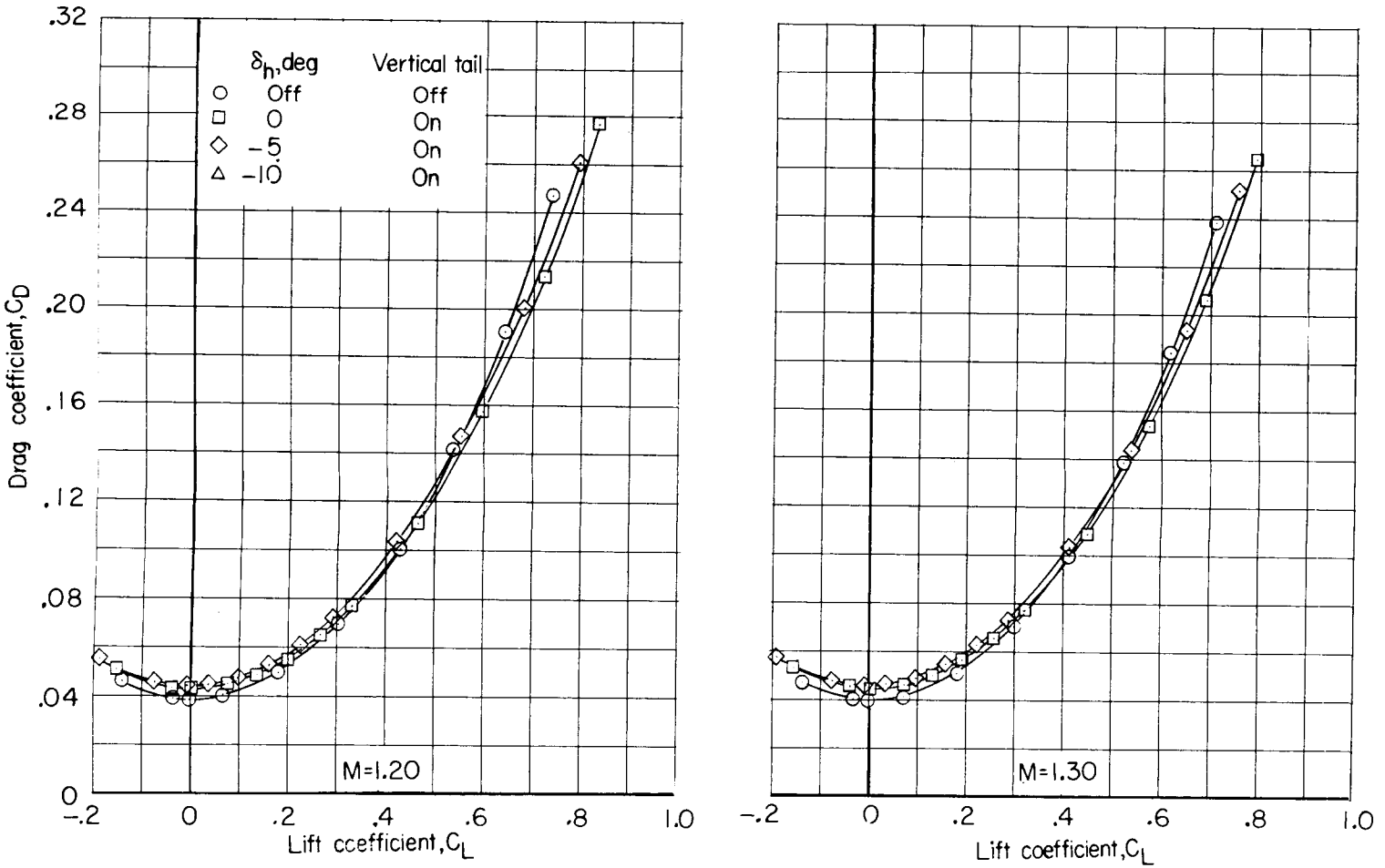

(d) Concluded.

Figure 18.- Continued.

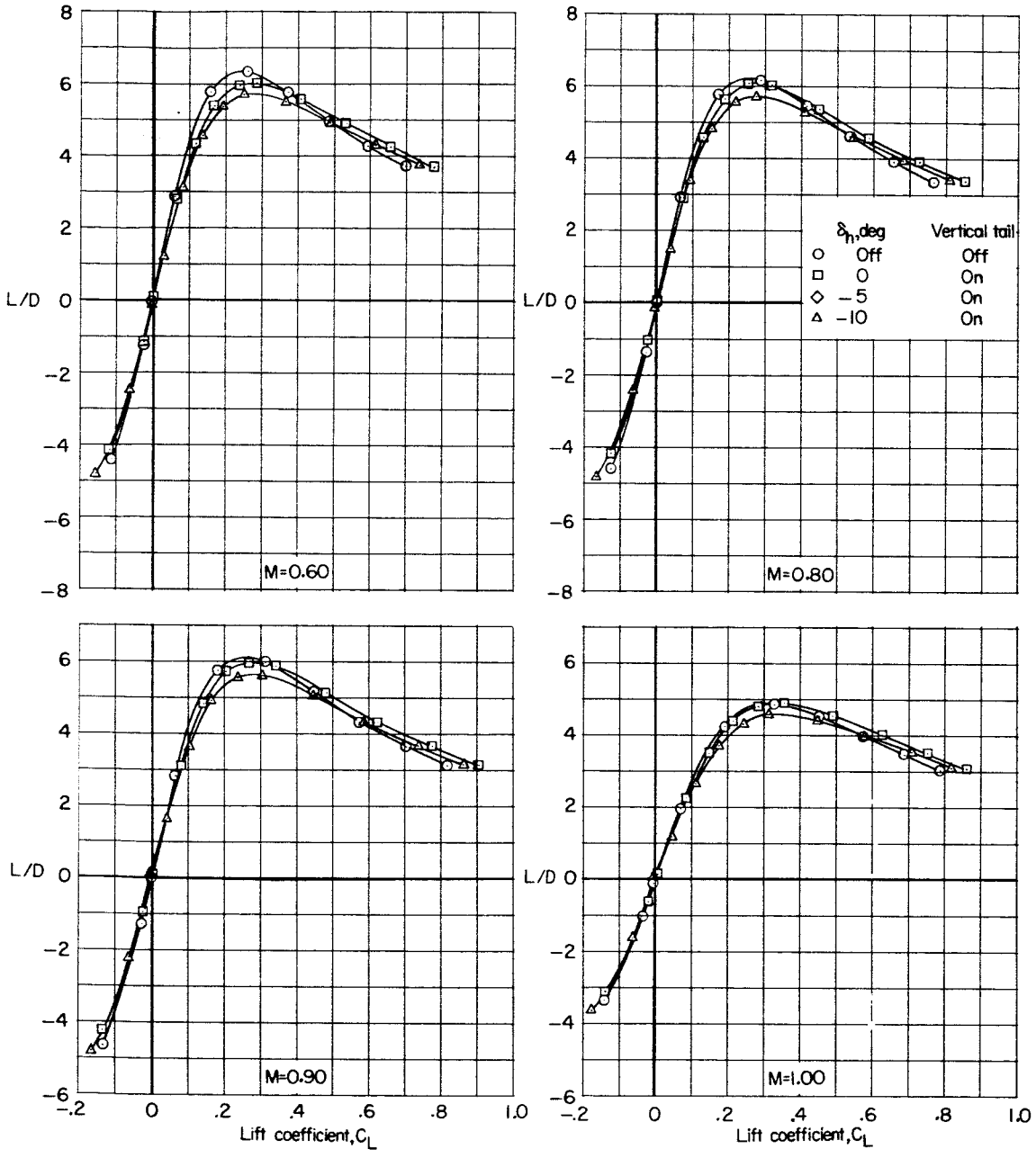

(e) L/D against C_L.

Figure 18.- Continued.

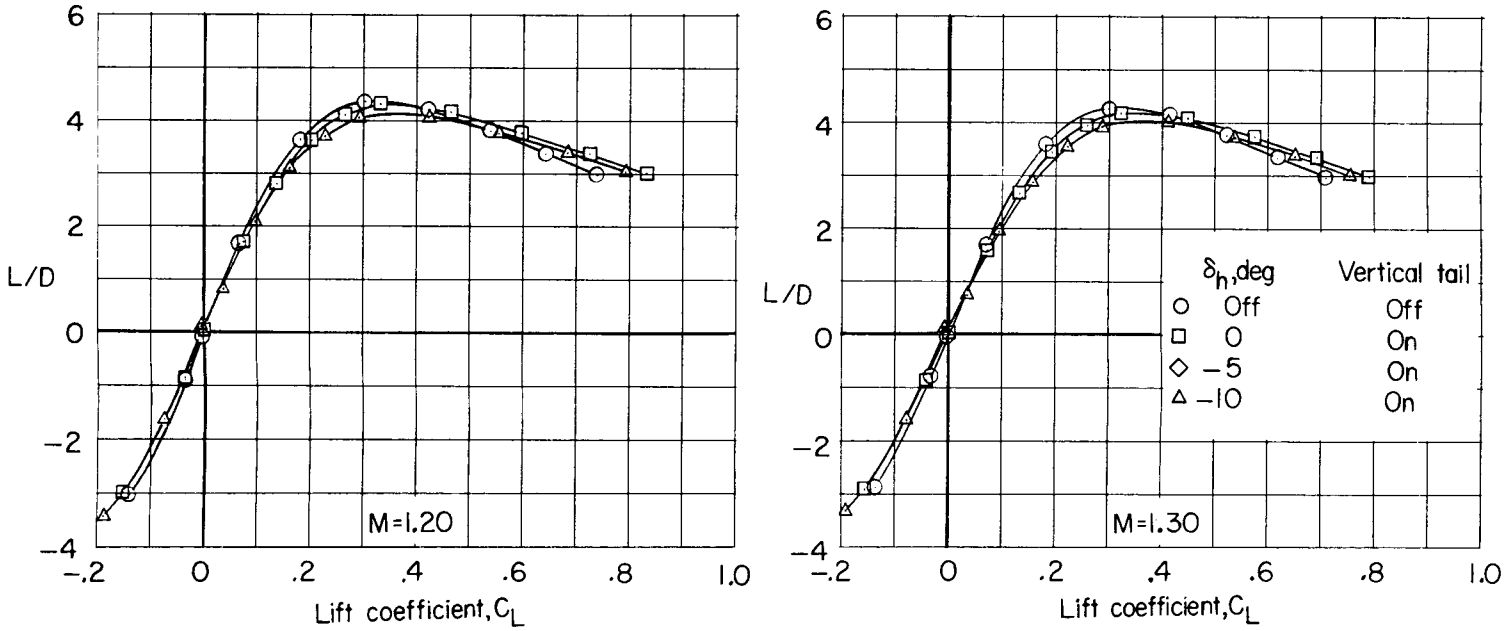

(e) Concluded.

Figure 18.- Concluded.

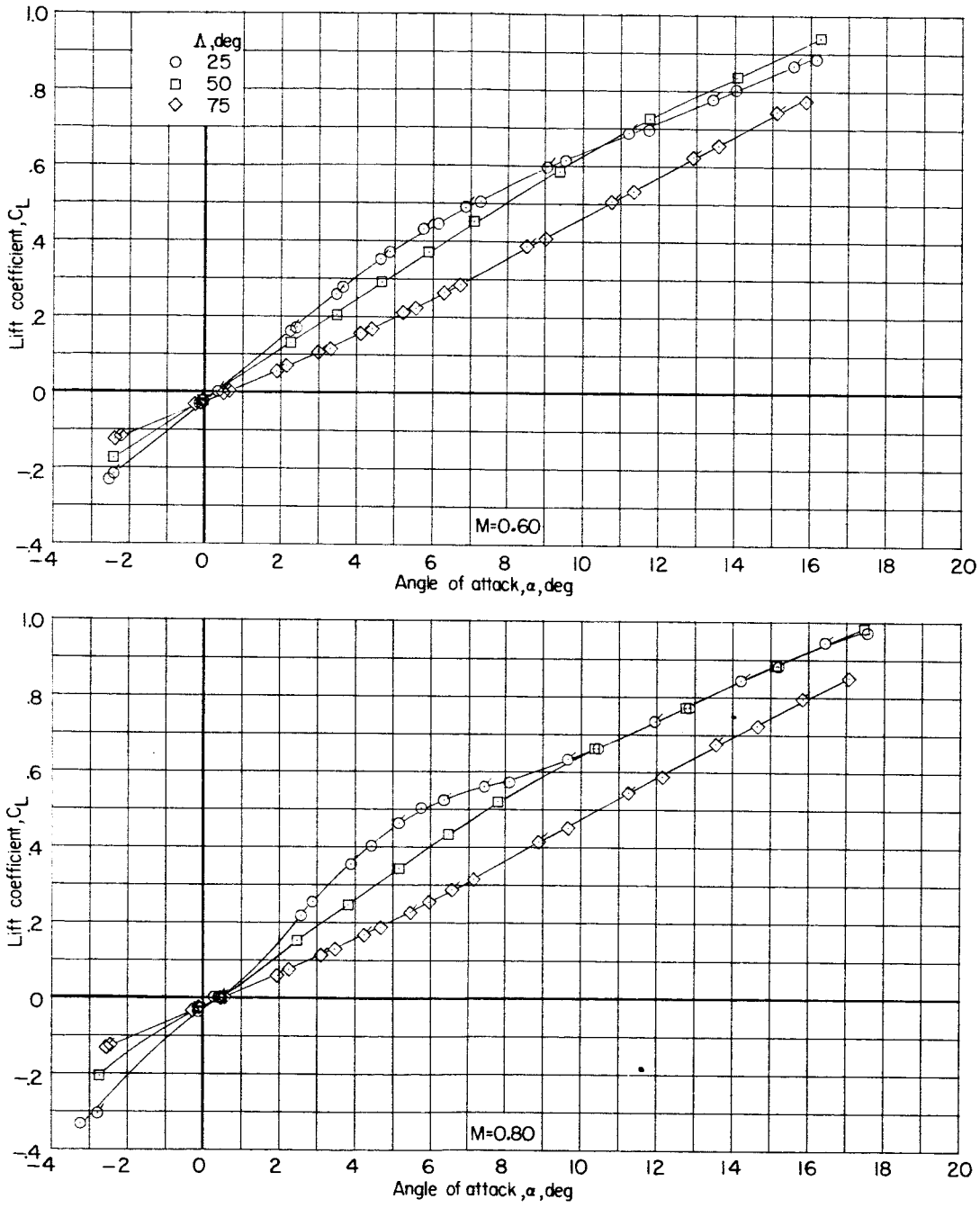

(a) C_L against α.

Figure 19.- Effect of wing sweep on longitudinal aerodynamic characteristics of model III. Configuration BWVH; $\delta_h = 0^o$. (Flagged symbols indicate points from repeat run.)

[redacted]

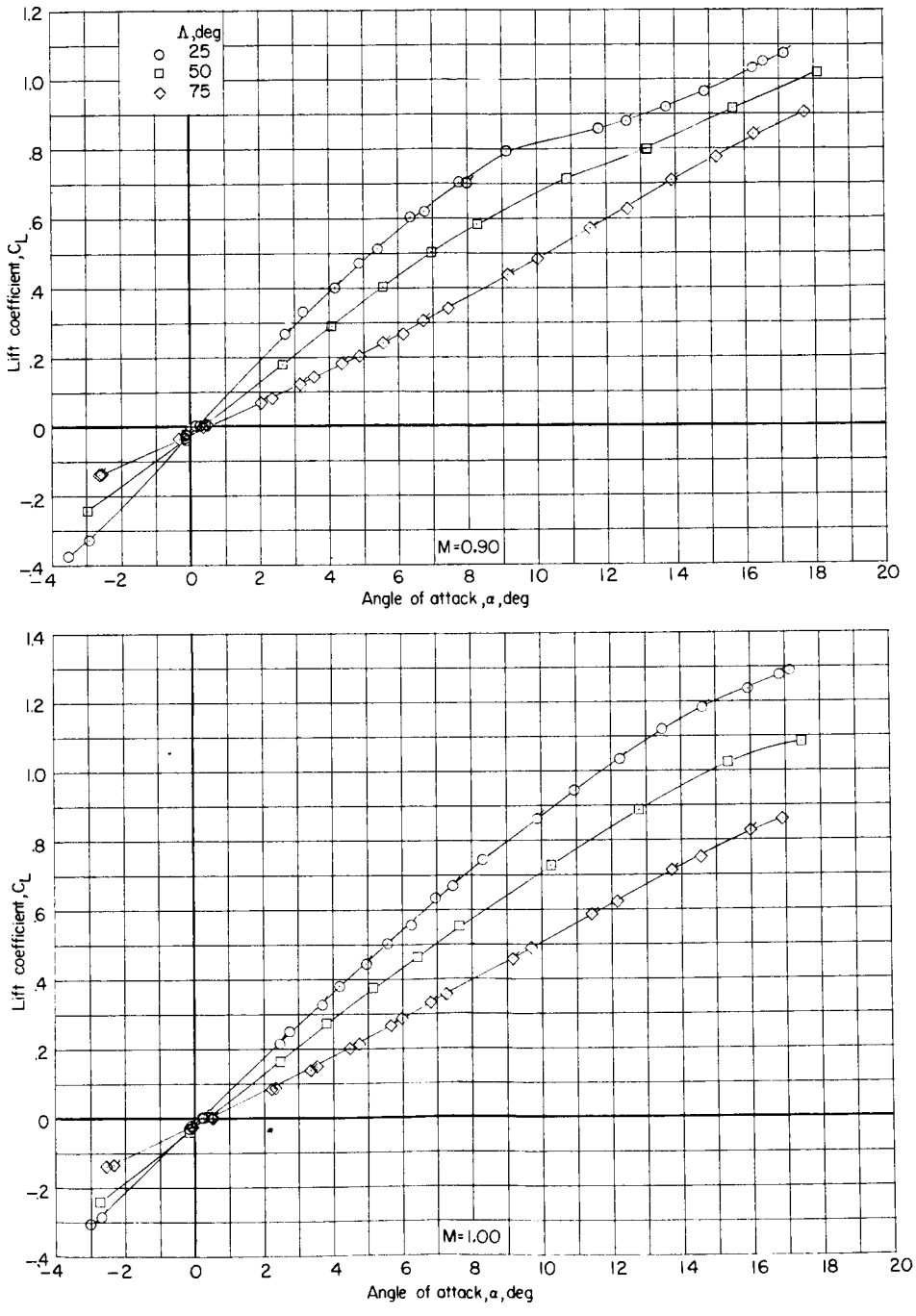

(a) Continued.

Figure 19.- Continued.

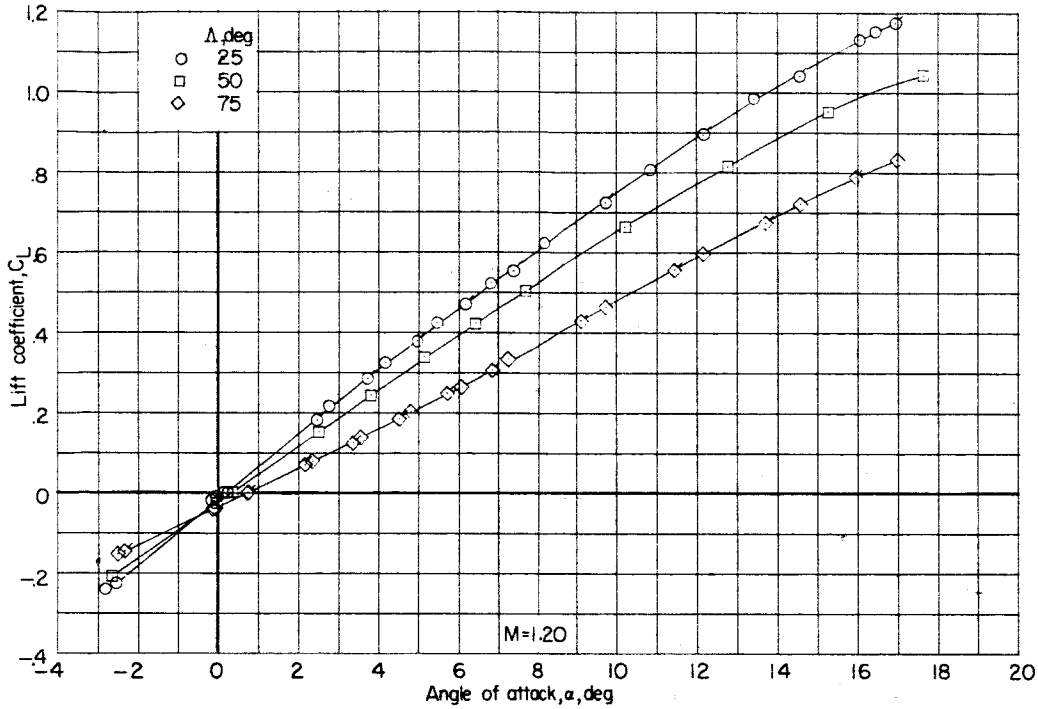

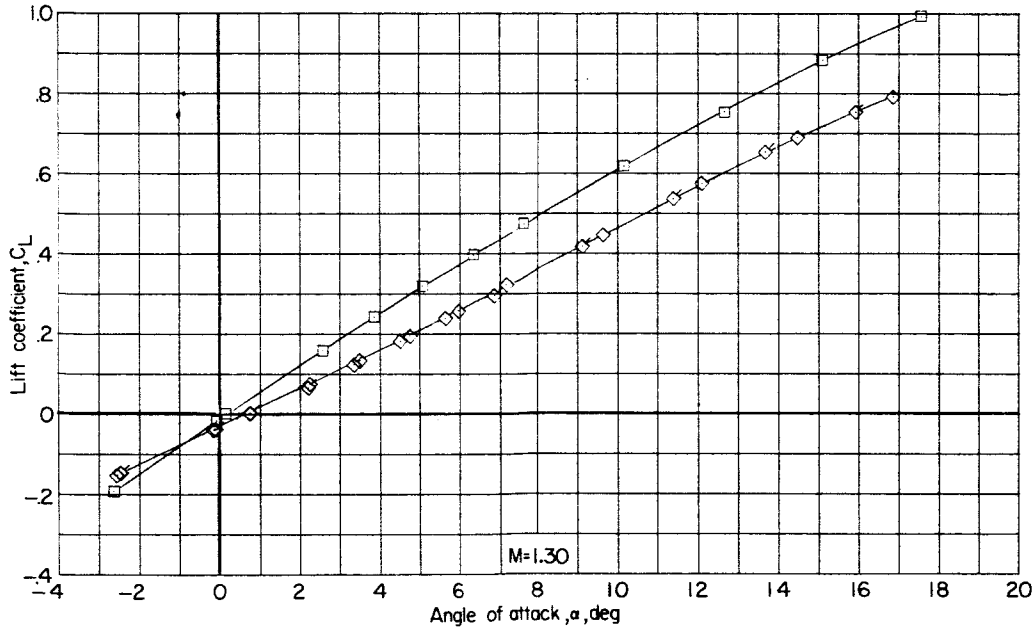

(a) Concluded.

Figure 19.- Continued.

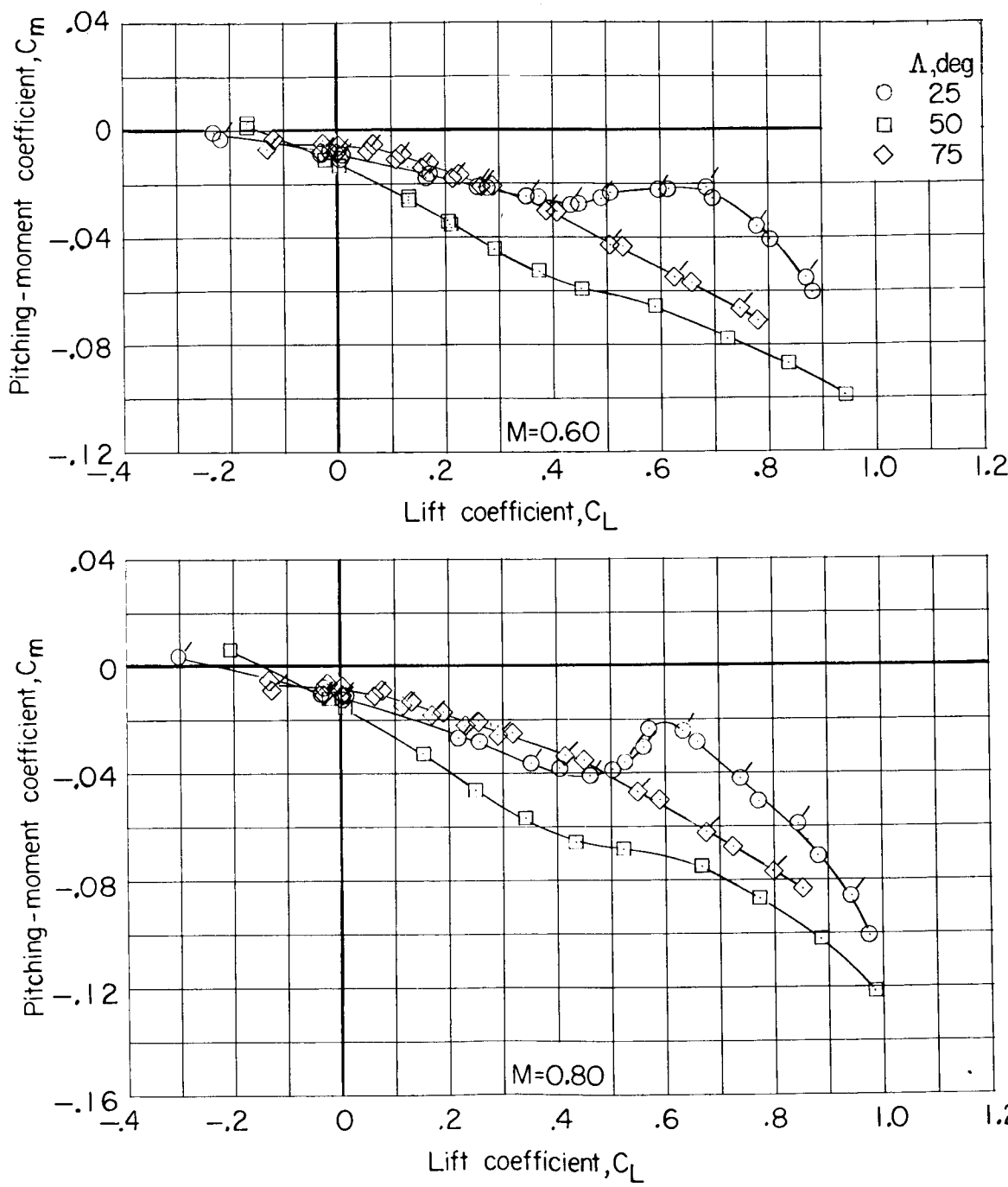

(b) C_m against C_L.

Figure 19.- Continued.

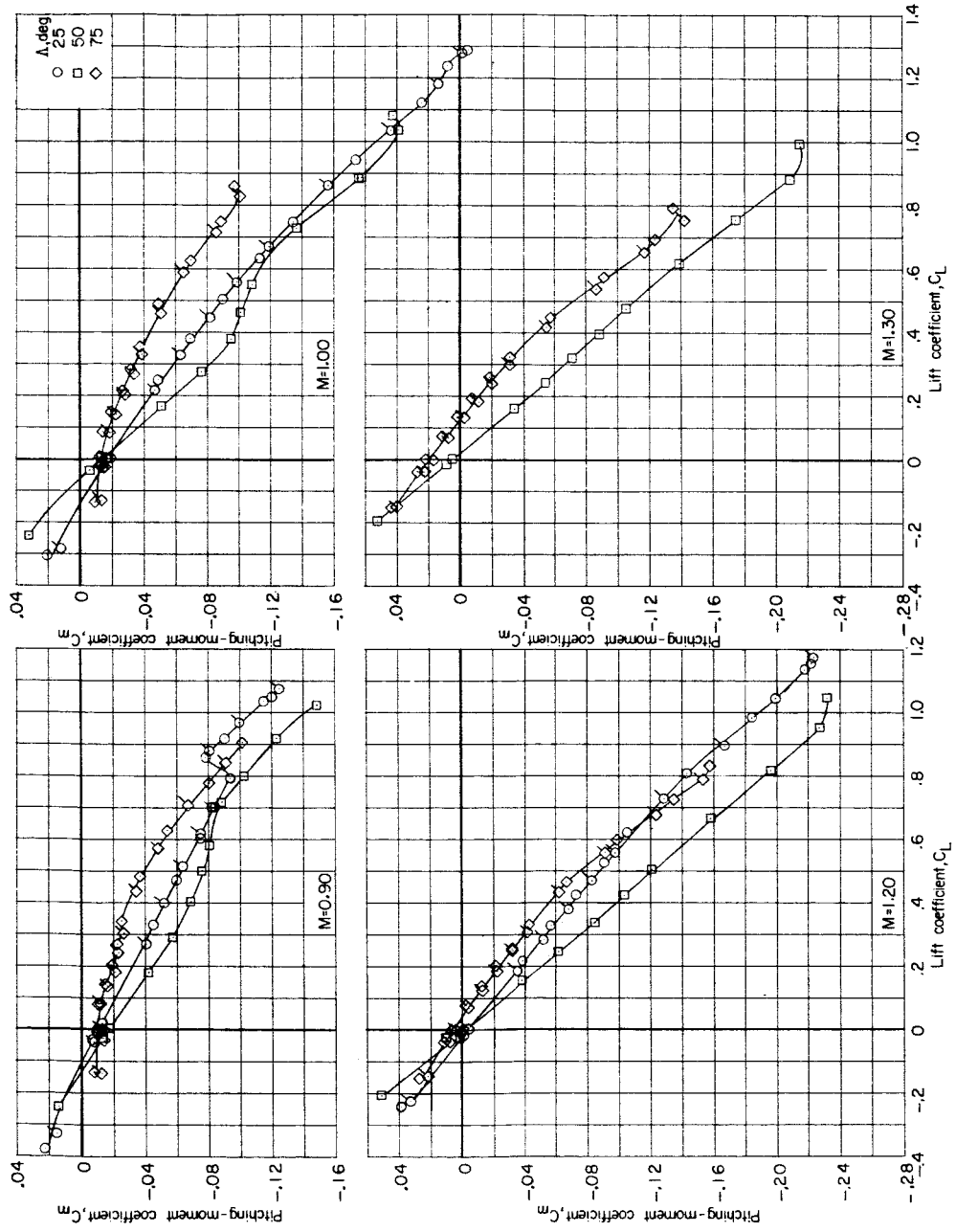

(b) Concluded.

Figure 19.- Continued.

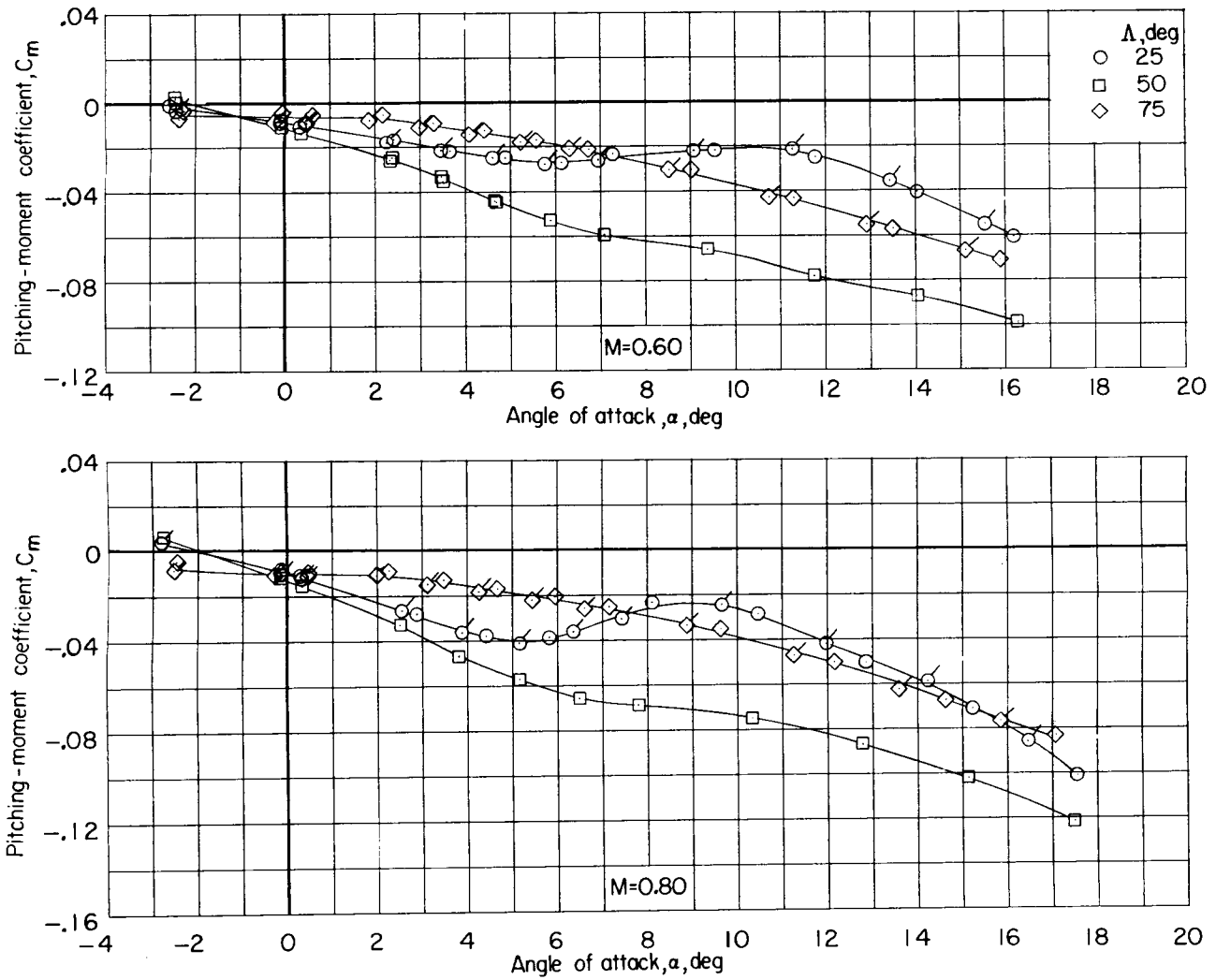

(c) C_m against α.

Figure 19.- Continued.

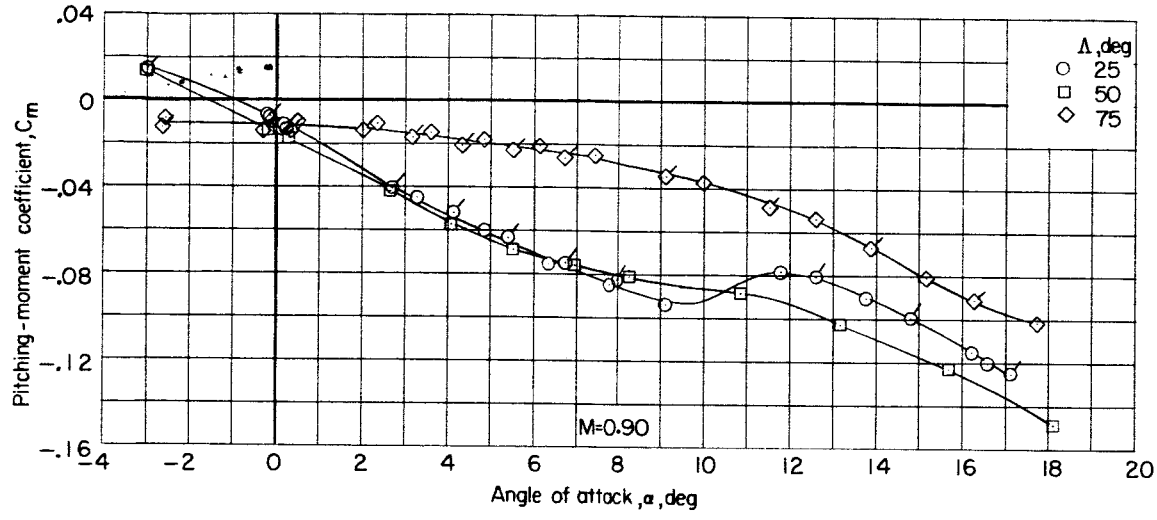

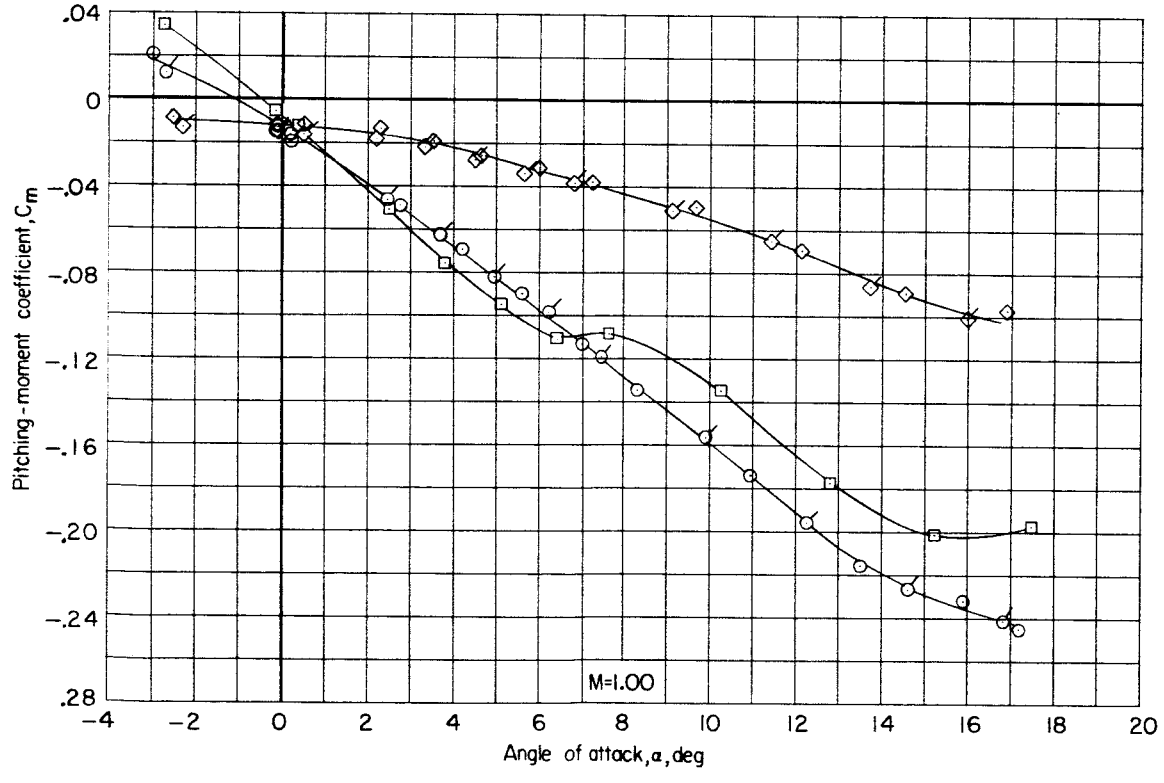

(c) Continued.

Figure 19.- Continued.

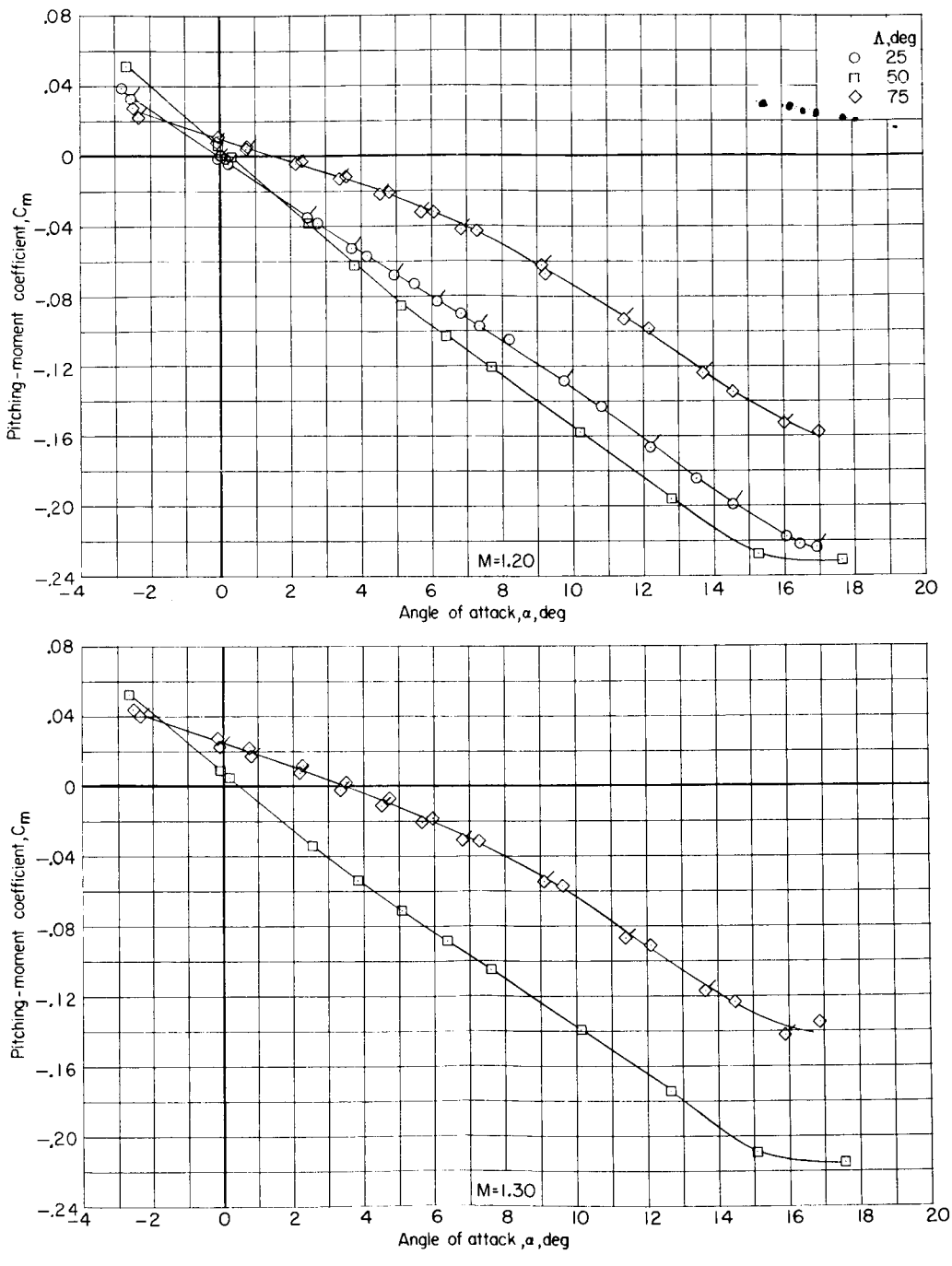

(c) Concluded.

Figure 19.- Continued.

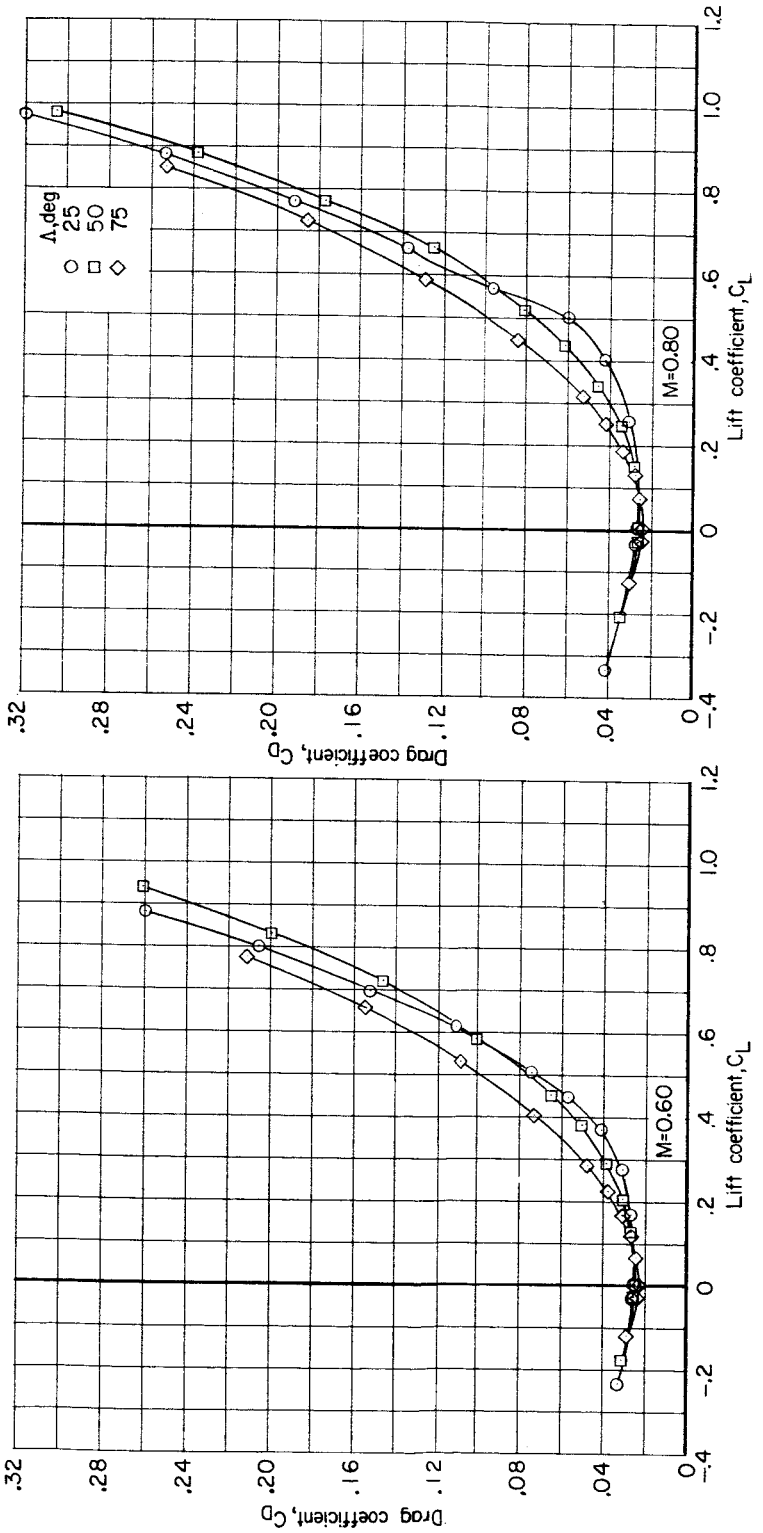

(d) C_D against C_L.

Figure 19.- Continued.

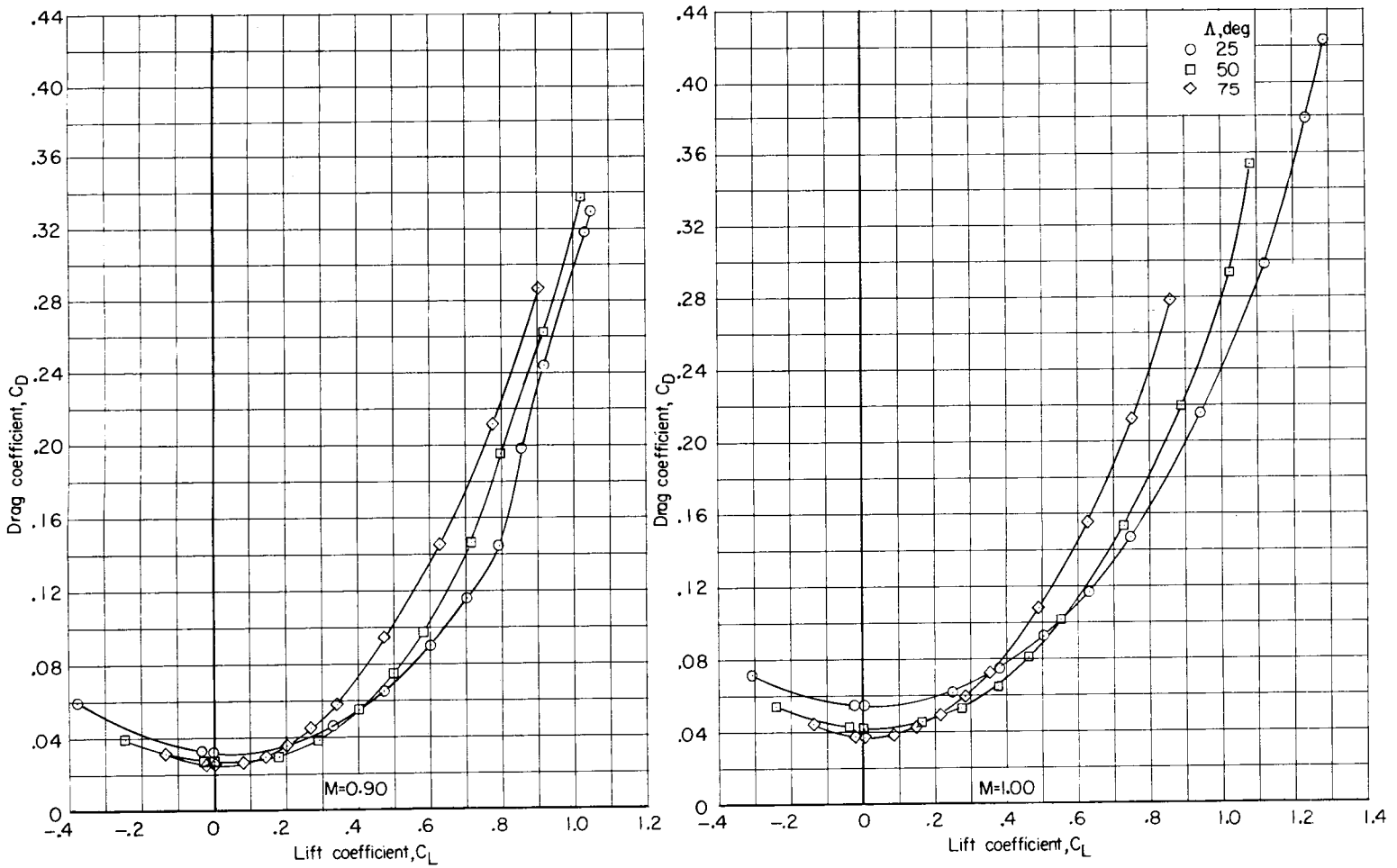

(d) Continued.

Figure 19.- Continued.

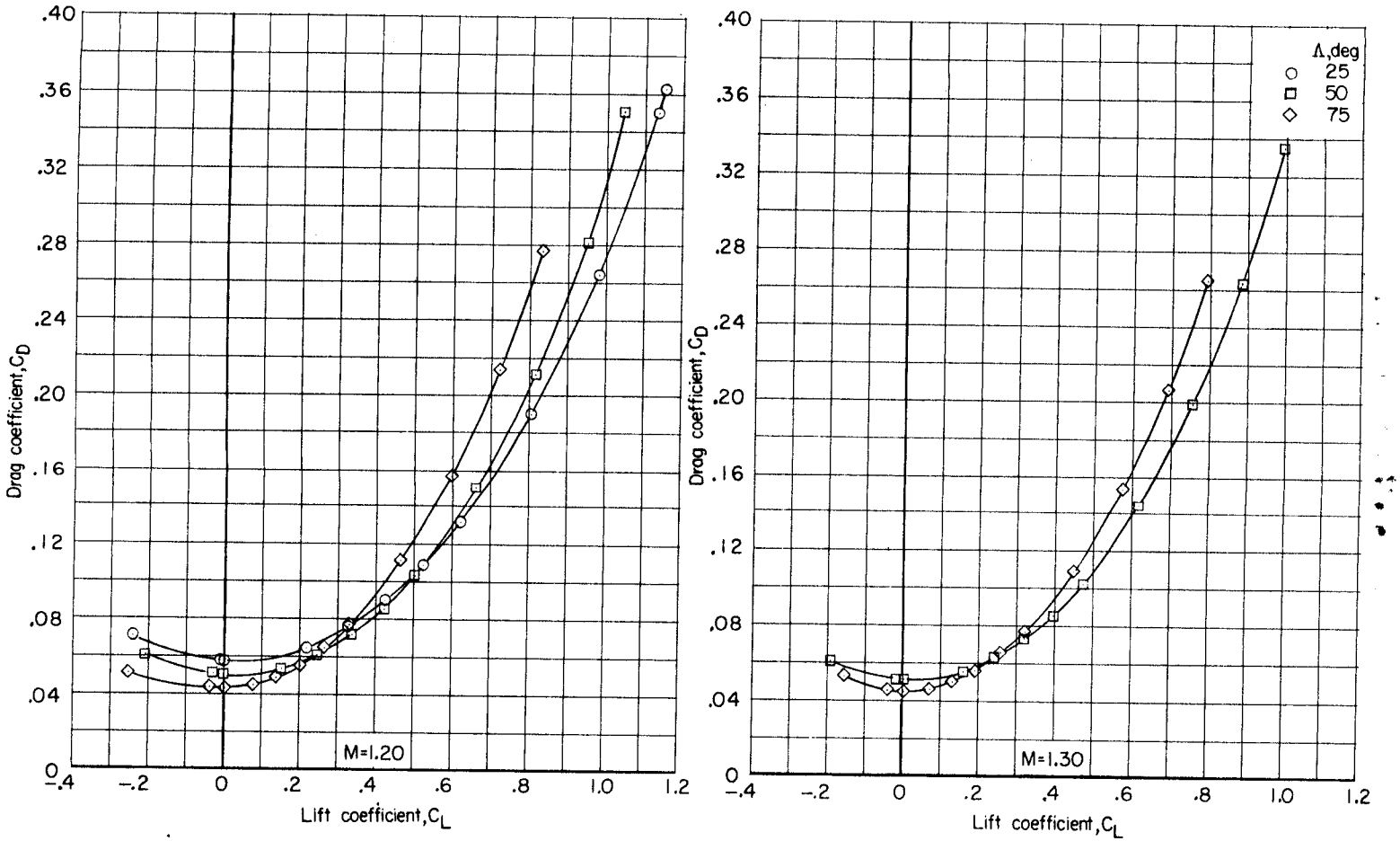

(d) Concluded.

Figure 19.- Continued.

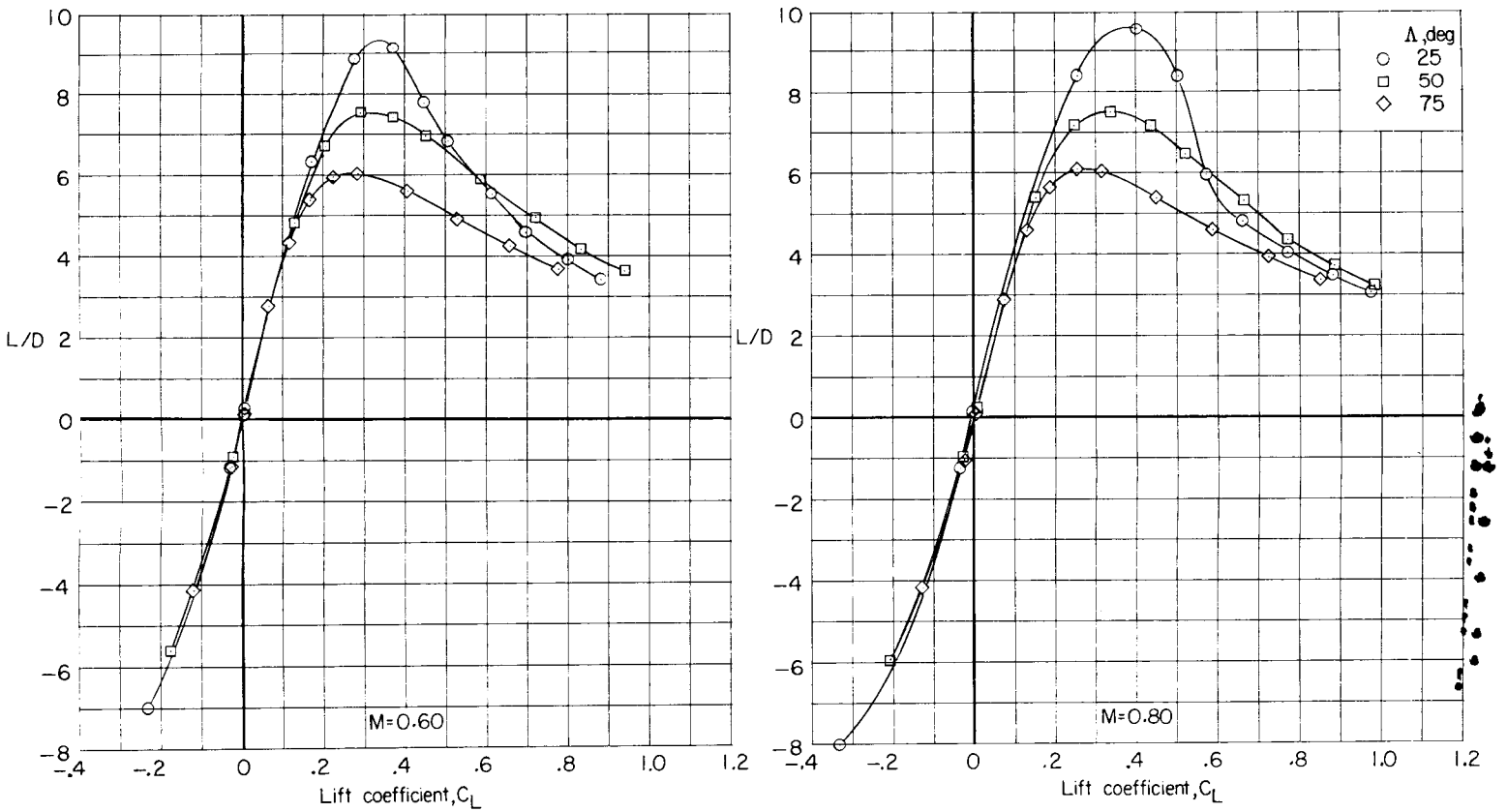

(e) L/D against C_L.

Figure 19.- Continued.

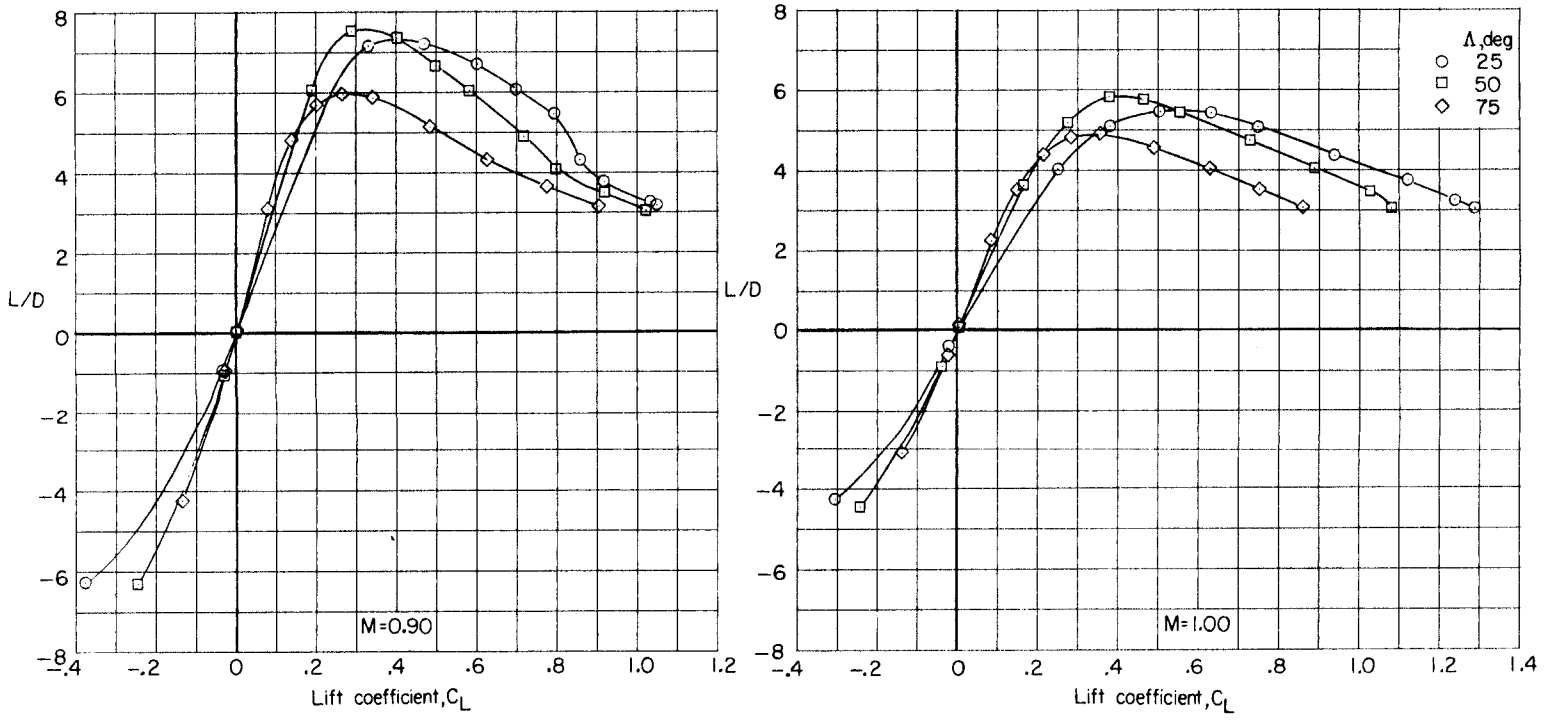

(e) Continued.

Figure 19.- Continued.

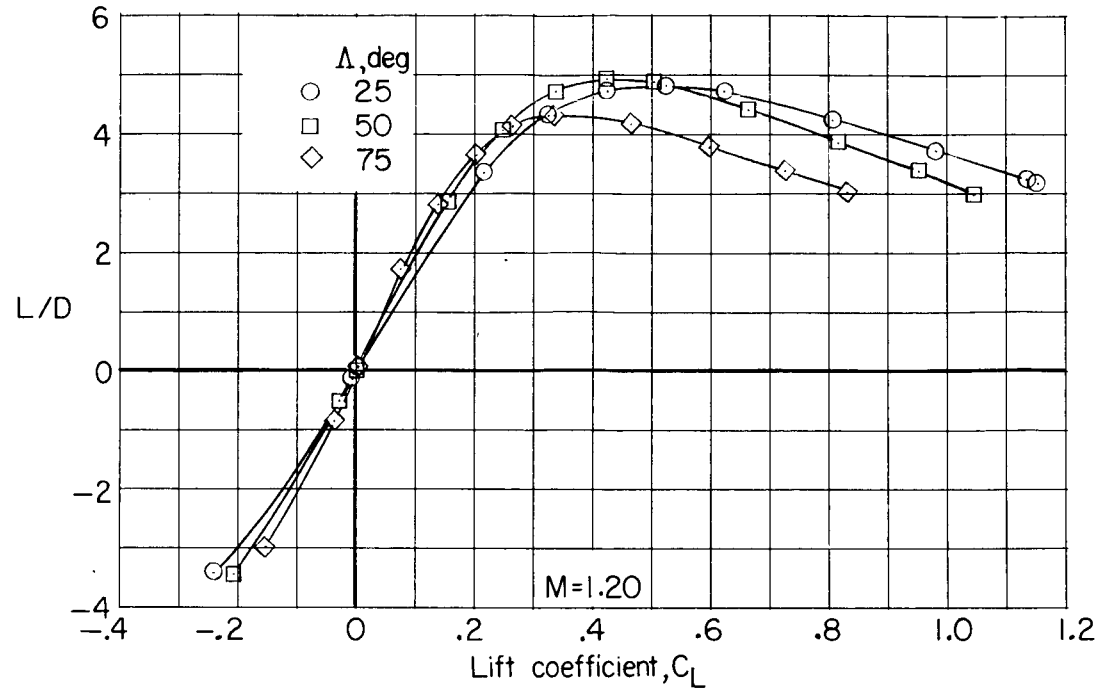

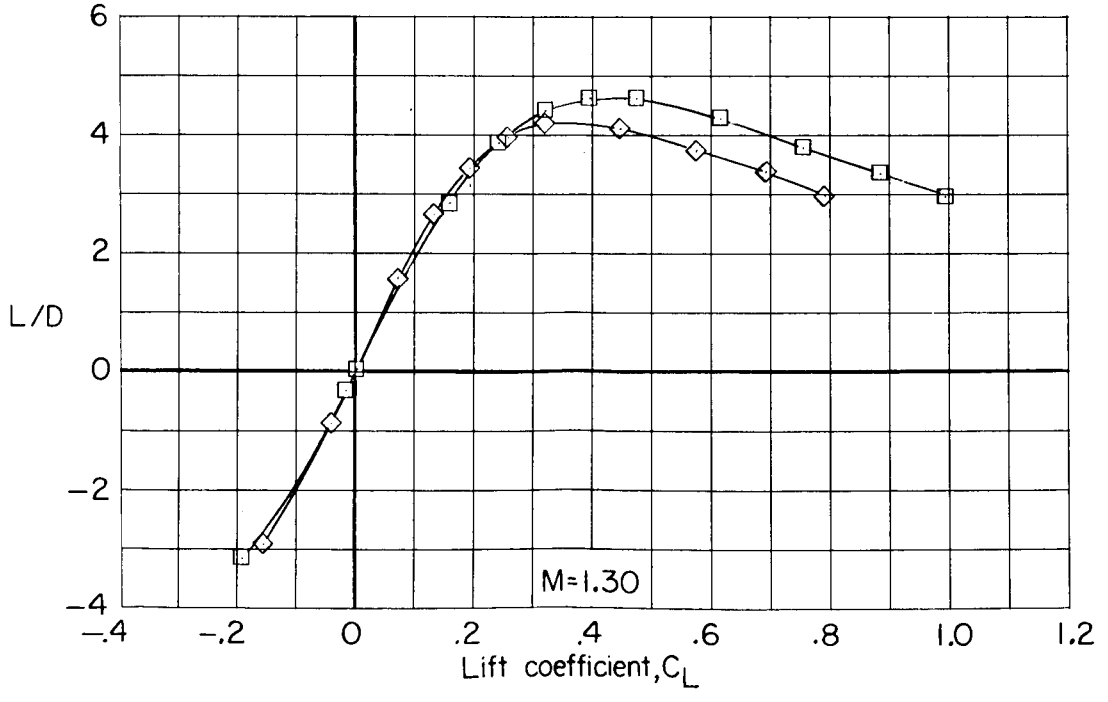

(e) Concluded.

Figure 19.- Concluded.

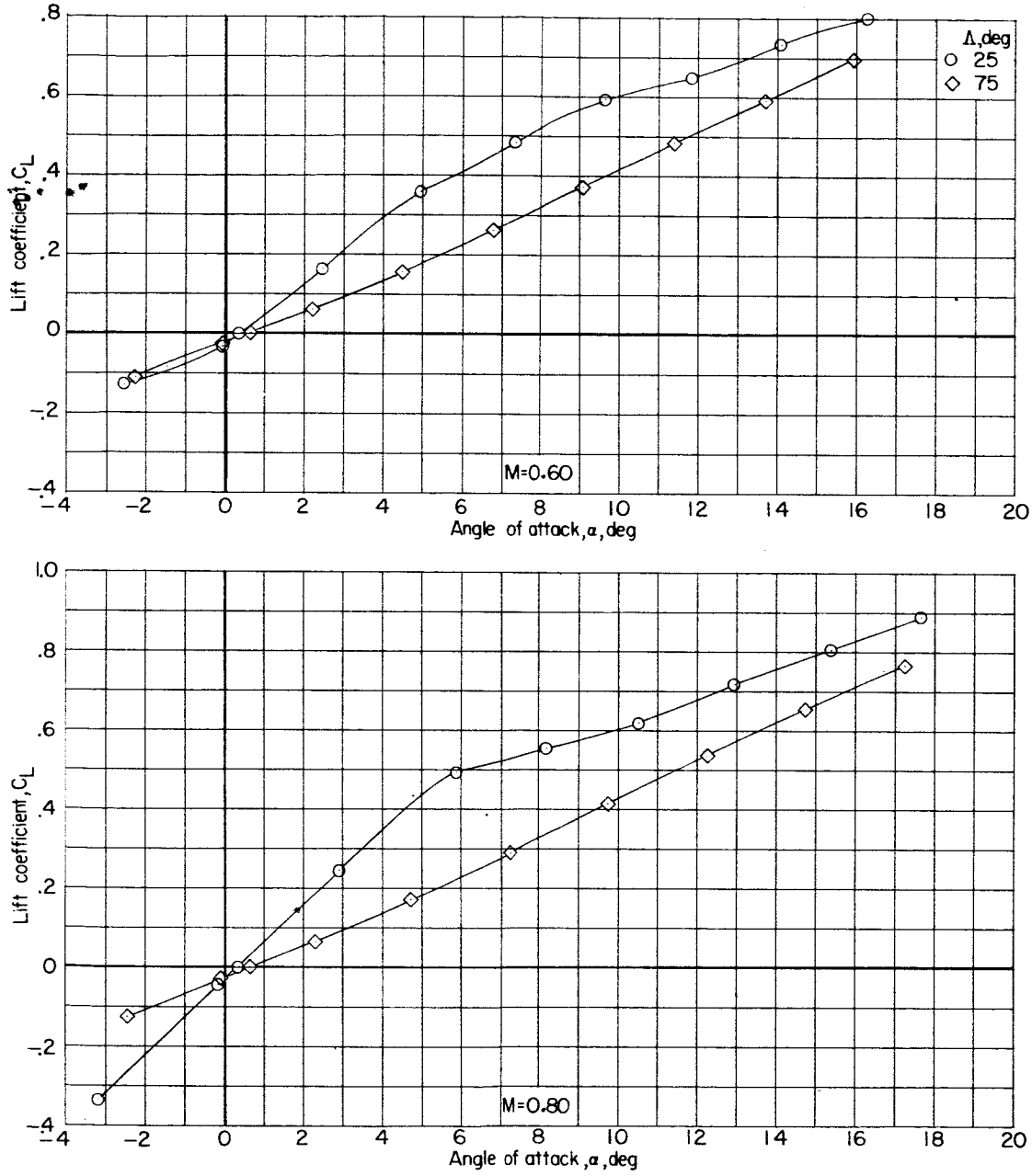

(a) C_L against α.

Figure 20.- Effect of wing sweep on longitudinal aerodynamic characteristics of model III with horizontal and vertical tails off. Configuration BW.

[redacted]

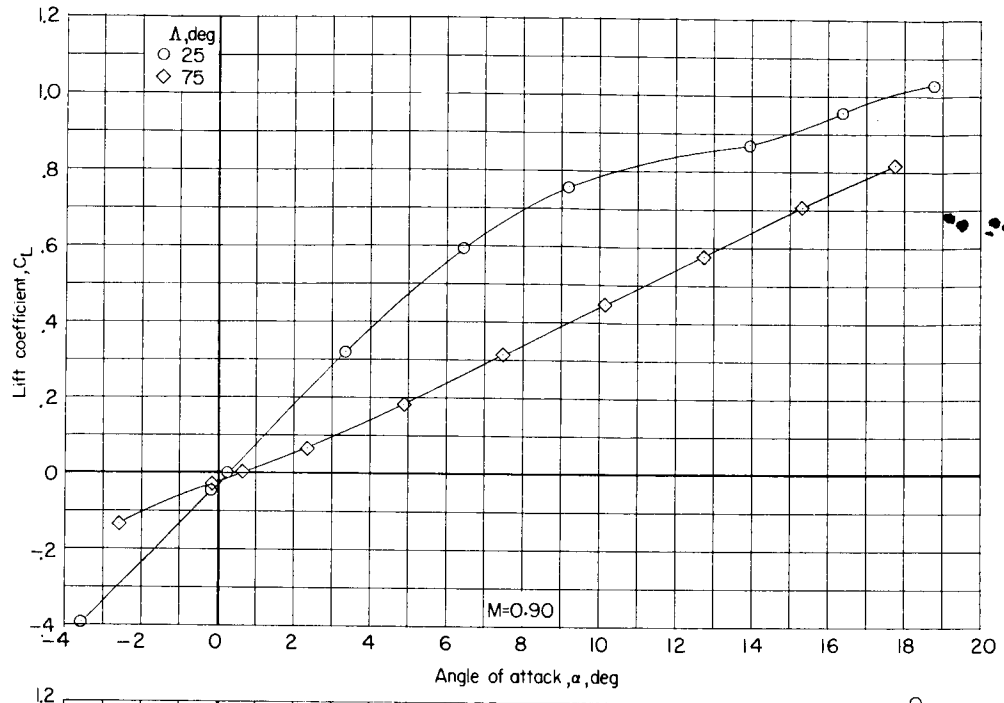

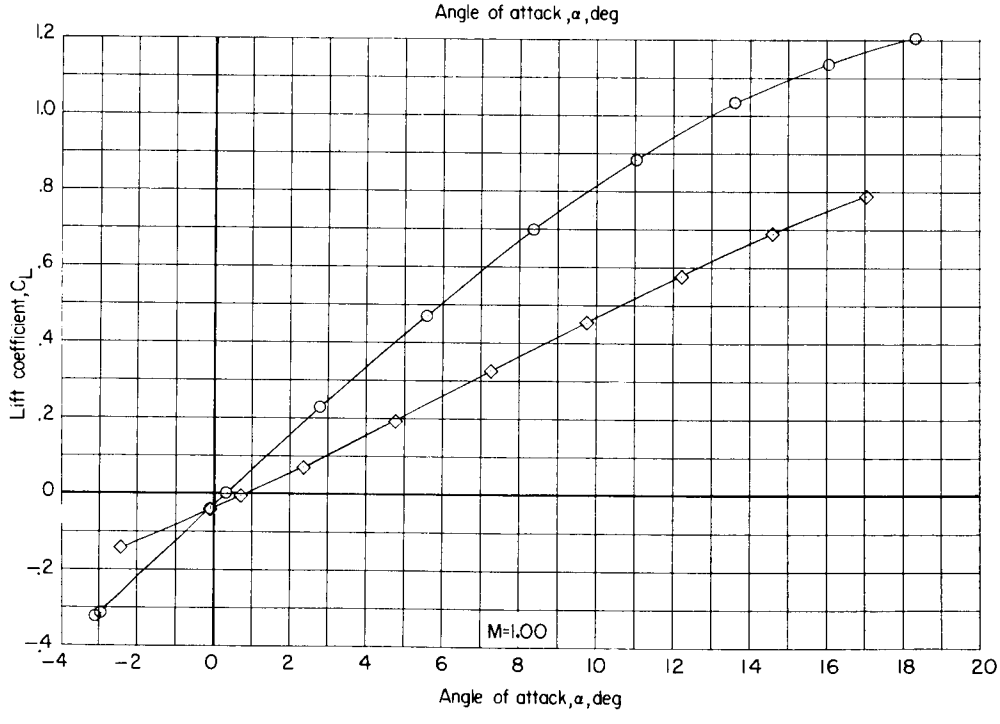

(a) Continued.

Figure 20.- Continued.

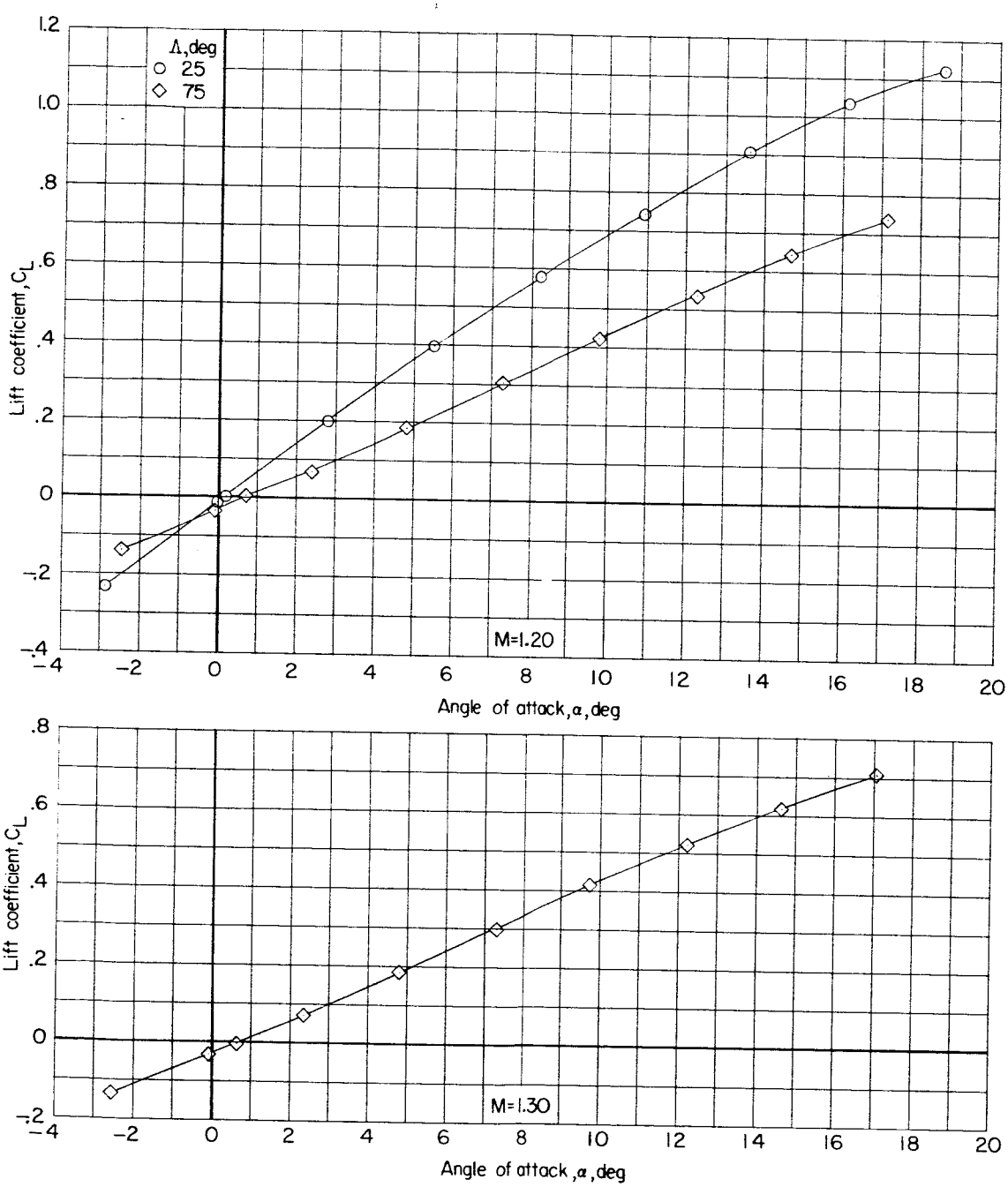

(a) Concluded.

Figure 20.- Continued.

[redacted]

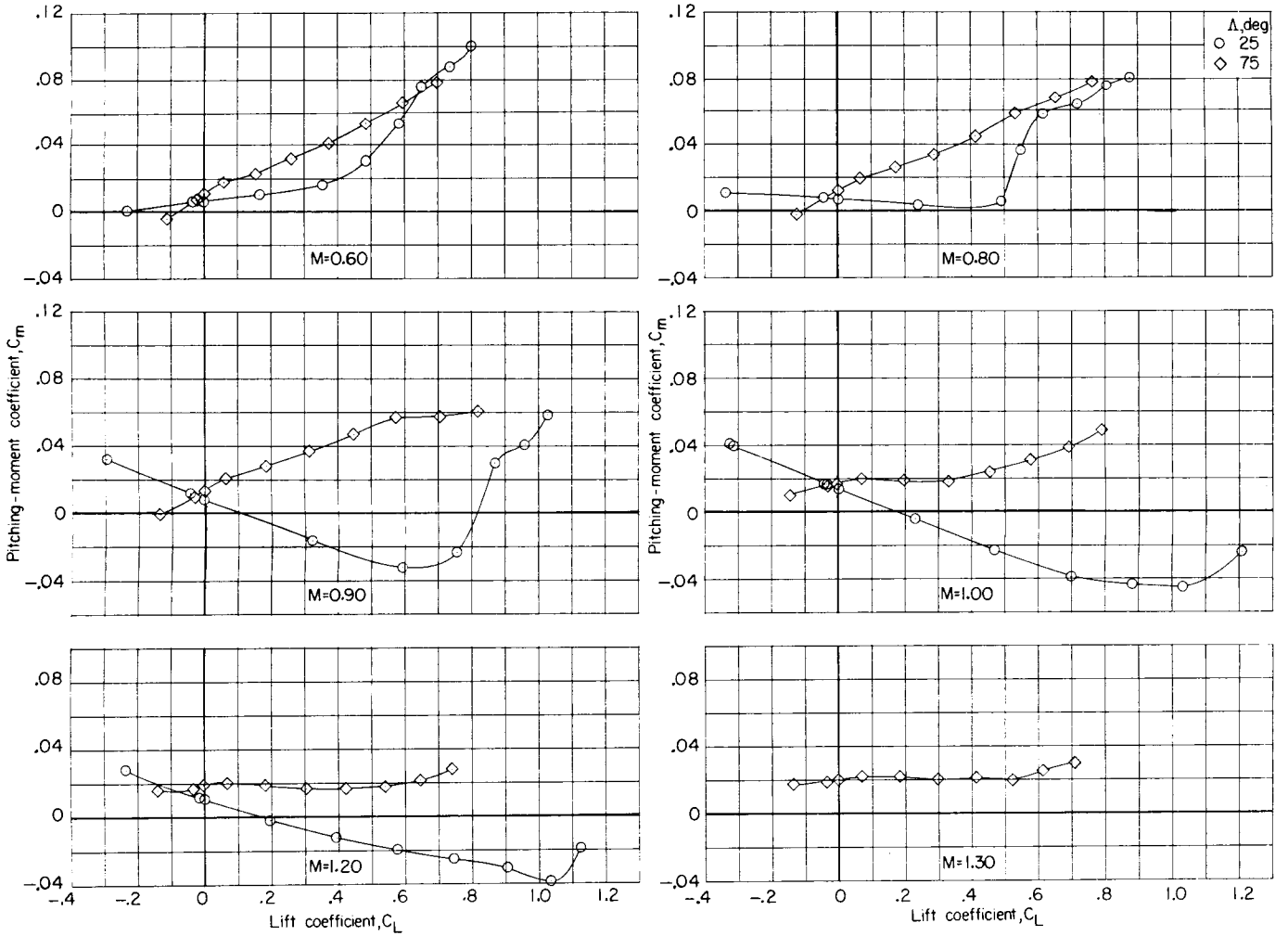

(b) C_m against C_L.

Figure 20.- Continued.

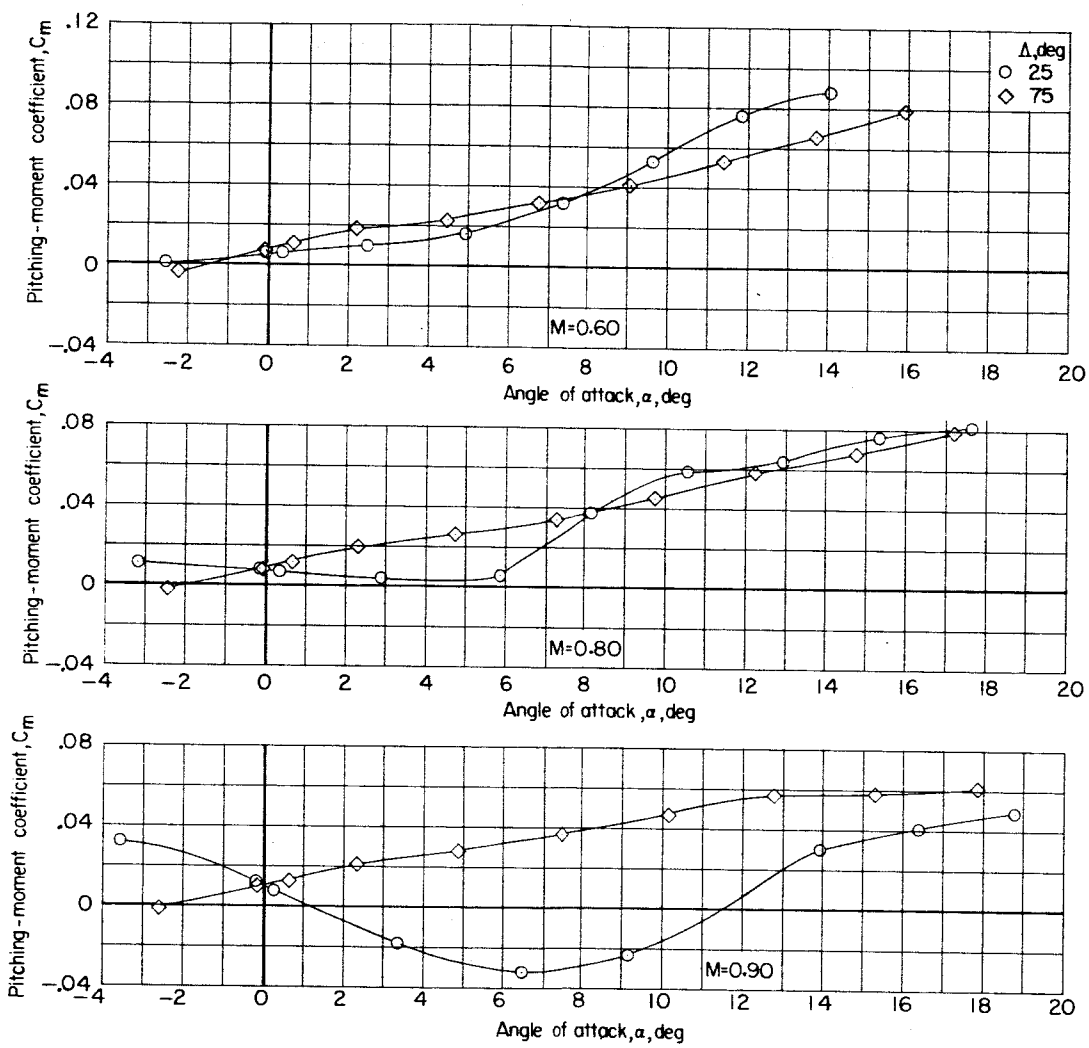

(c) C_m against α.

Figure 20.- Continued.

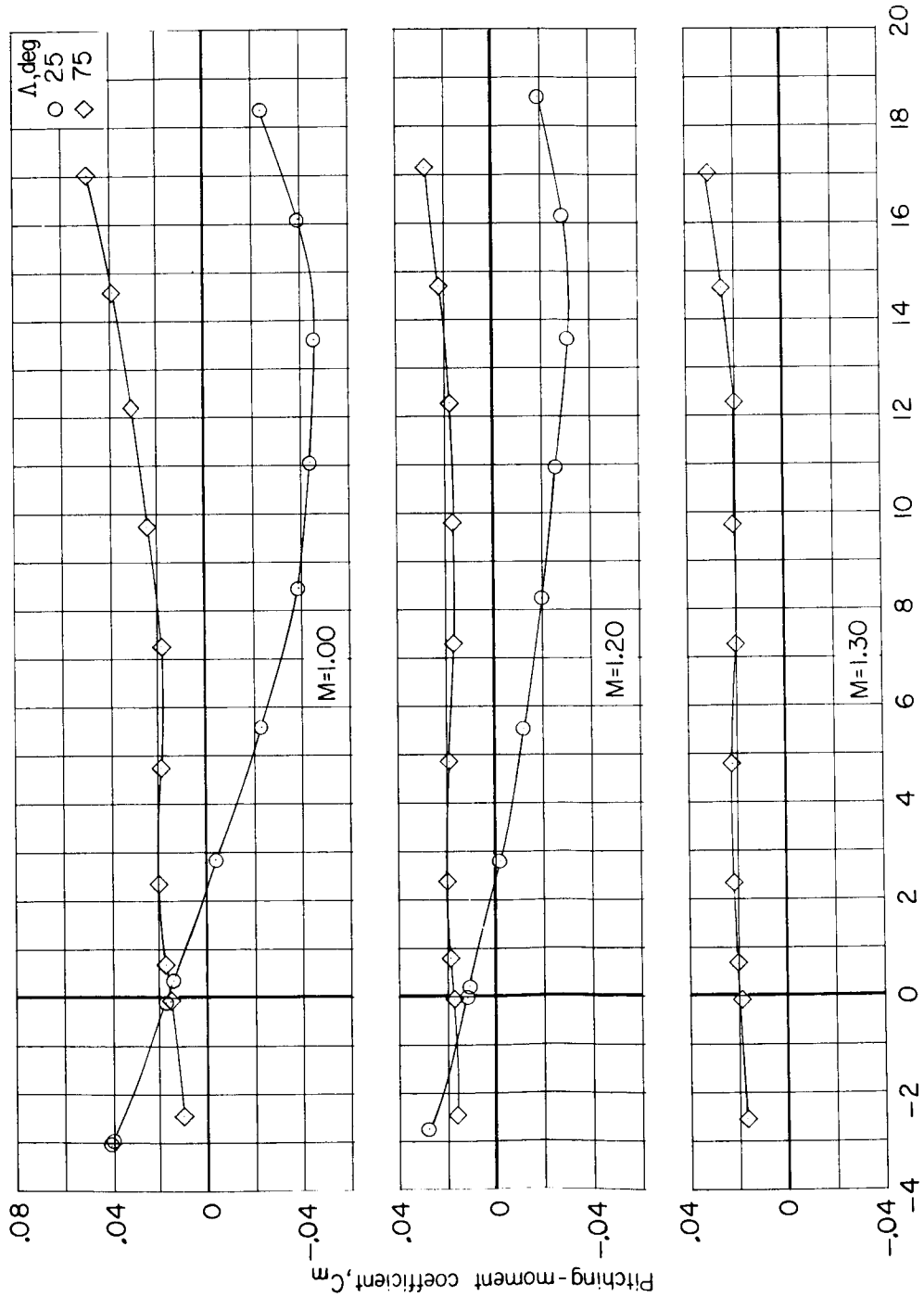

(c) Concluded.

Figure 20.- Continued.

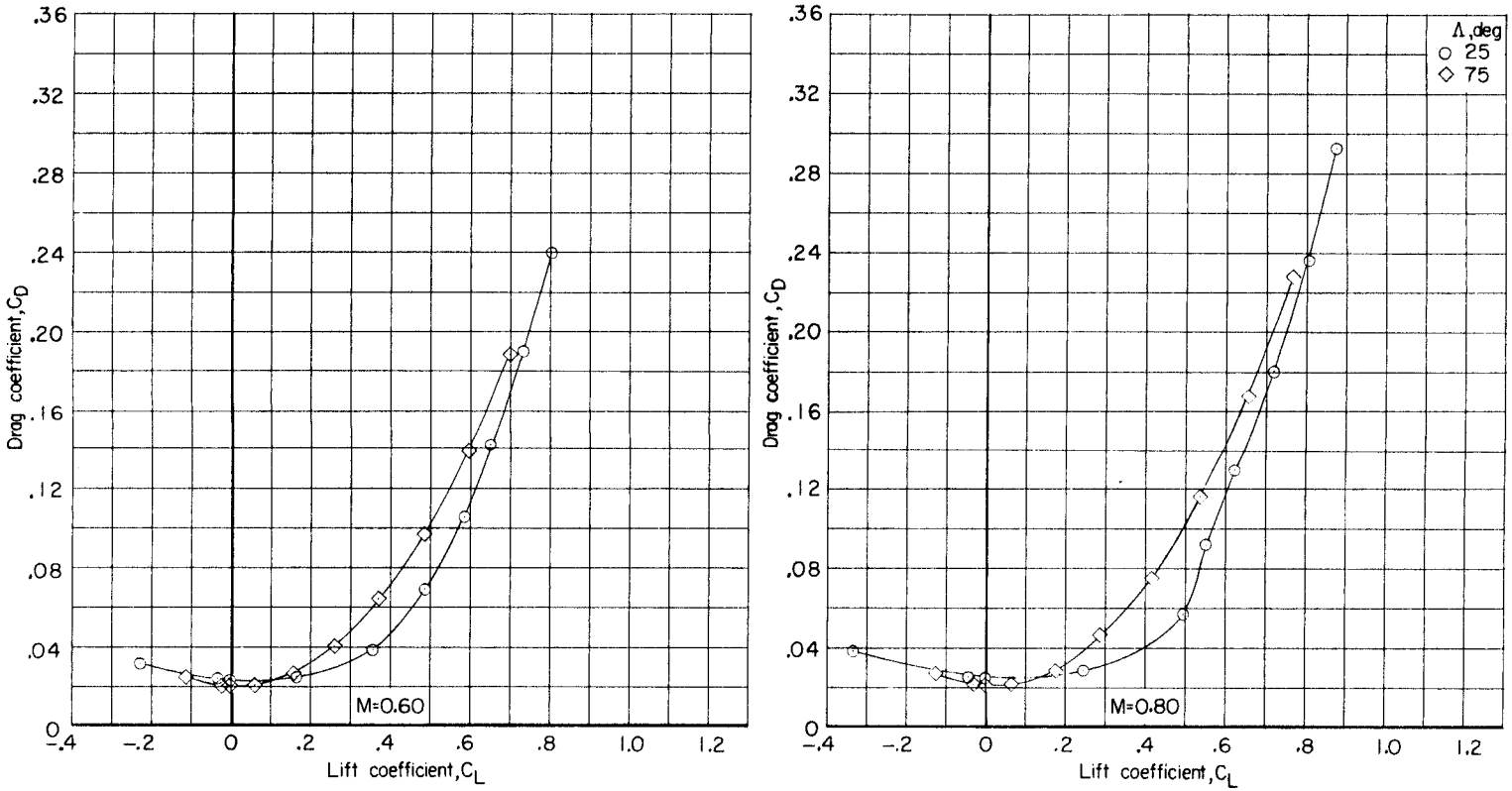

(d) C_D against C_L.

Figure 20.- Continued.

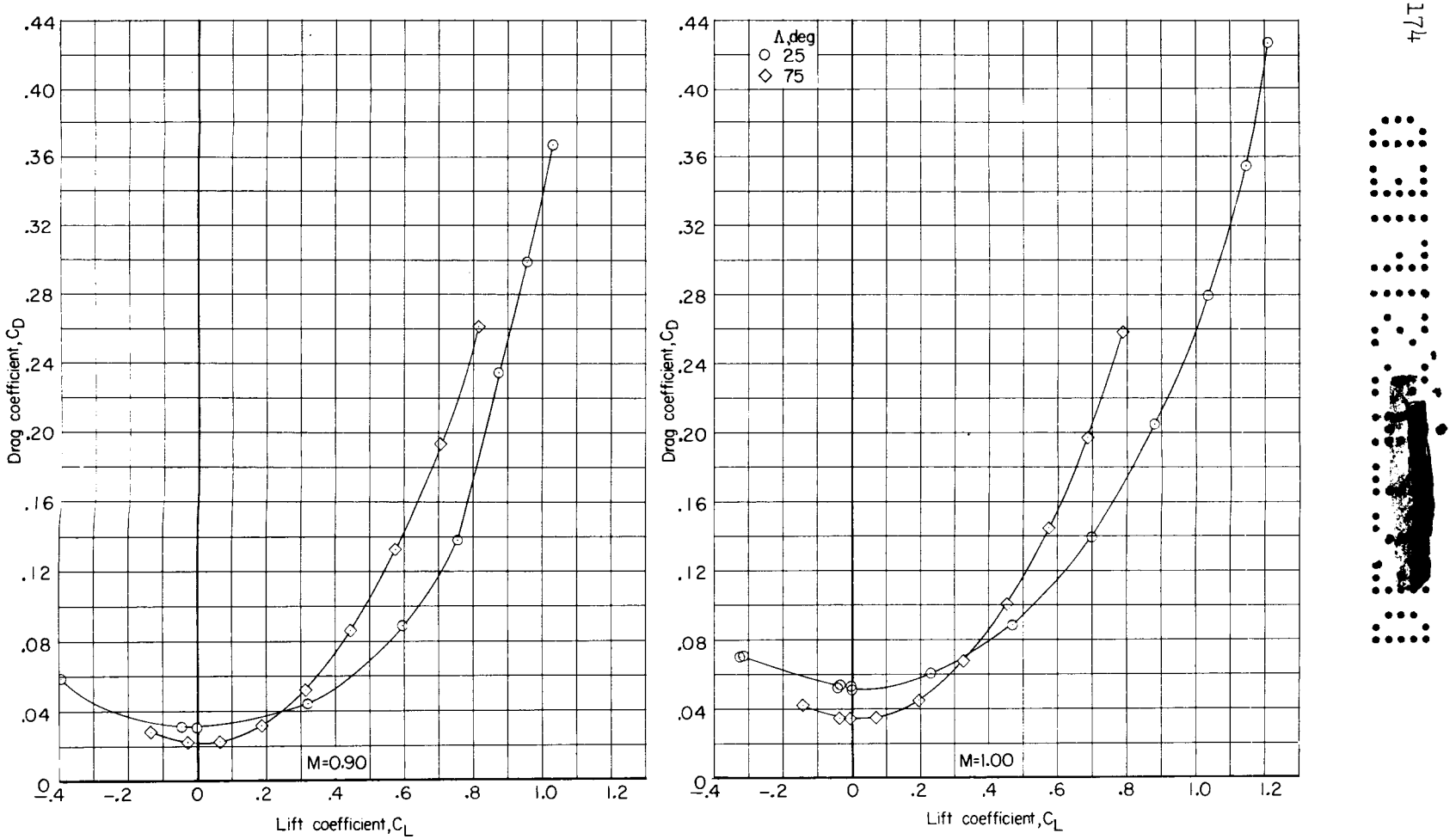

(d) Continued.

Figure 20.- Continued.

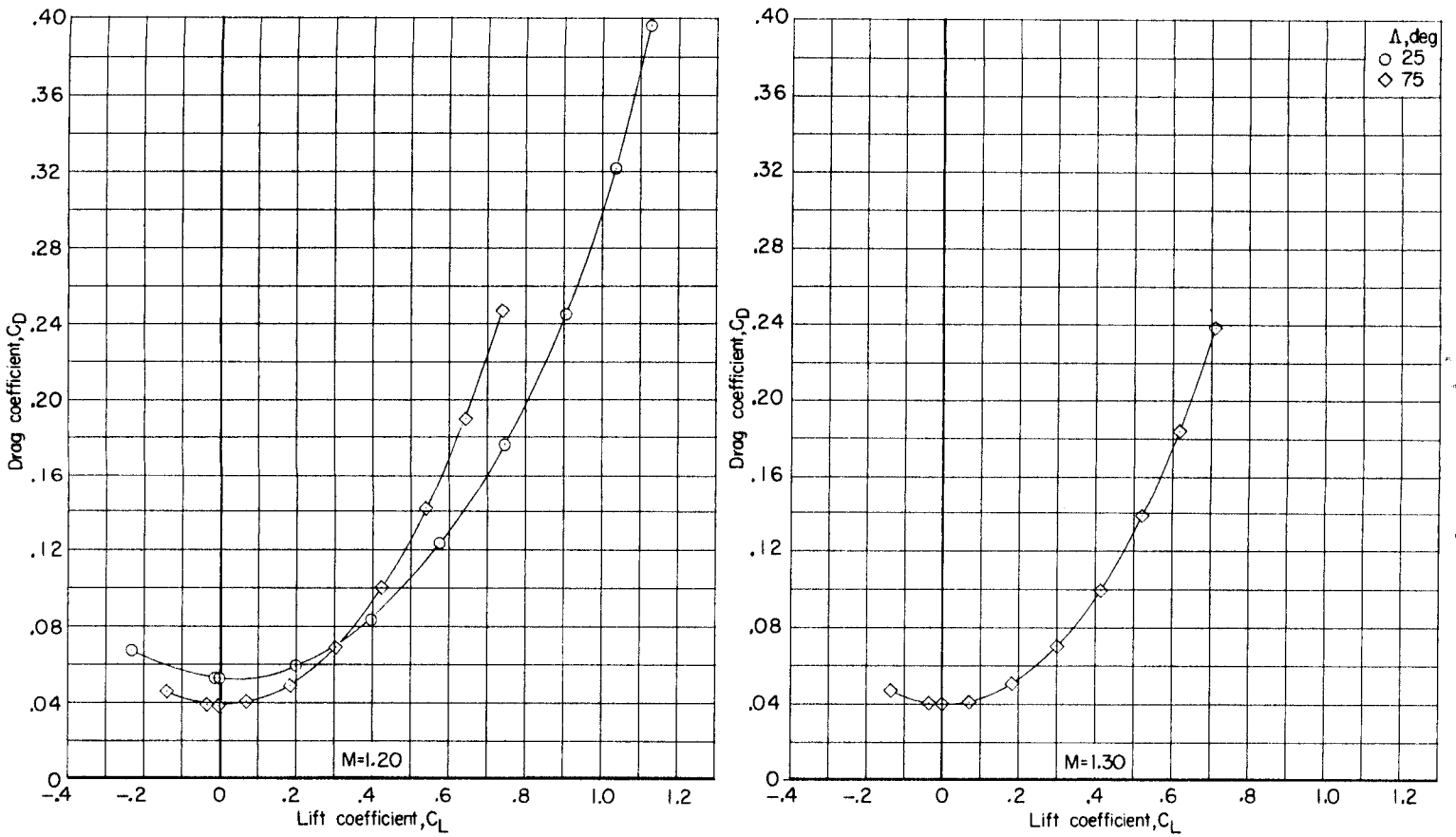

(d) Concluded.

Figure 20.- Continued.

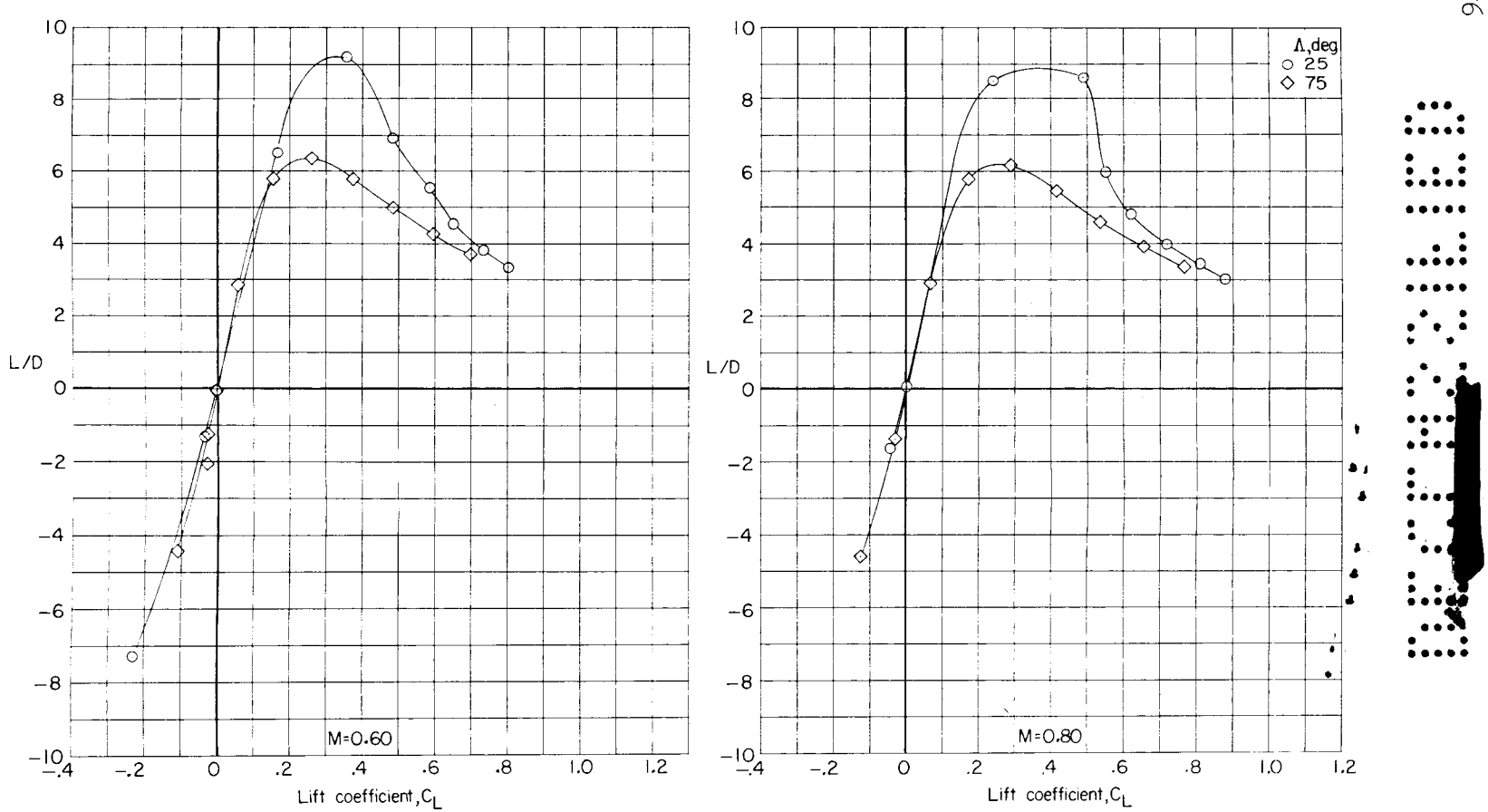

(e) L/D against C_L.

Figure 20.- Continued.

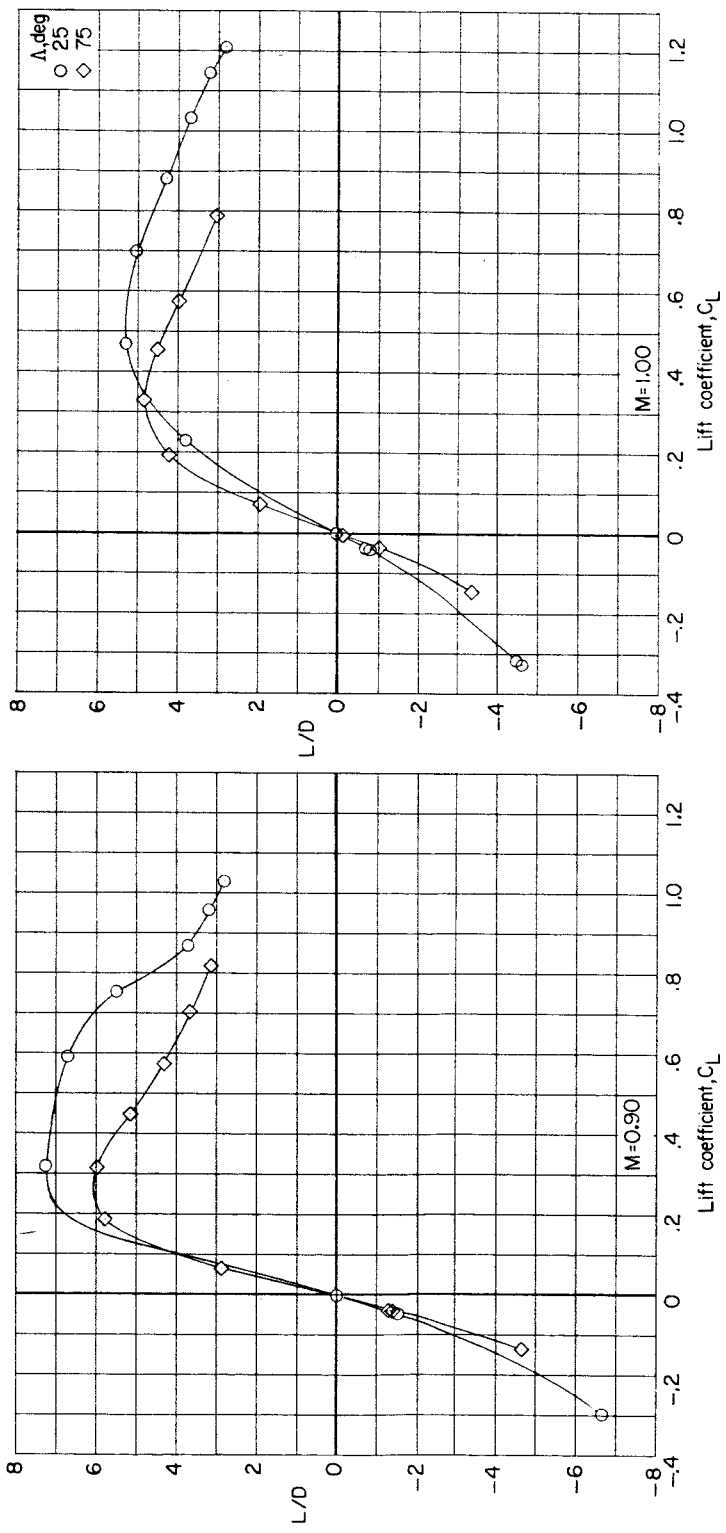

(e) Continued.

Figure 20.- Continued.

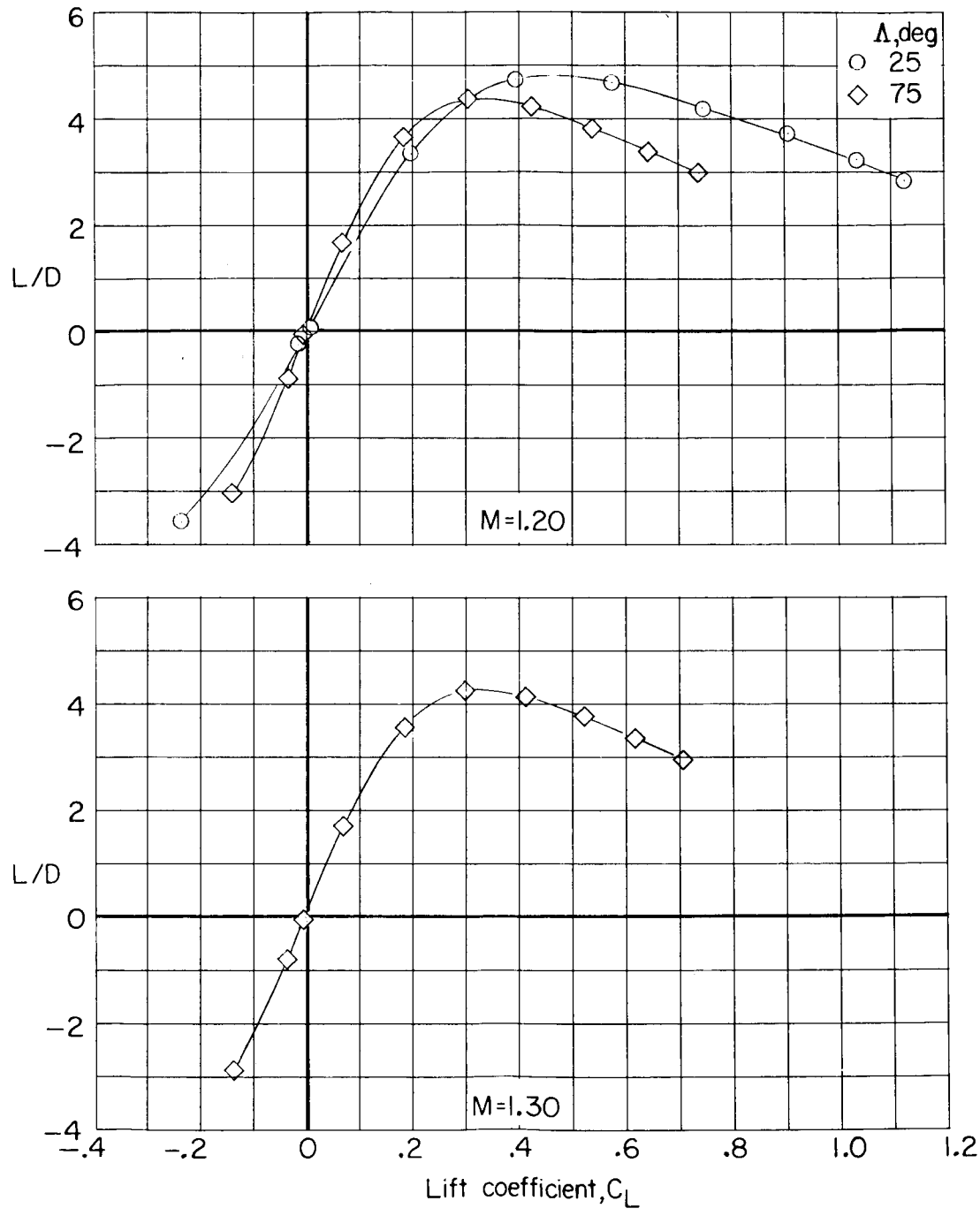

(e) Concluded.

Figure 20.- Concluded.

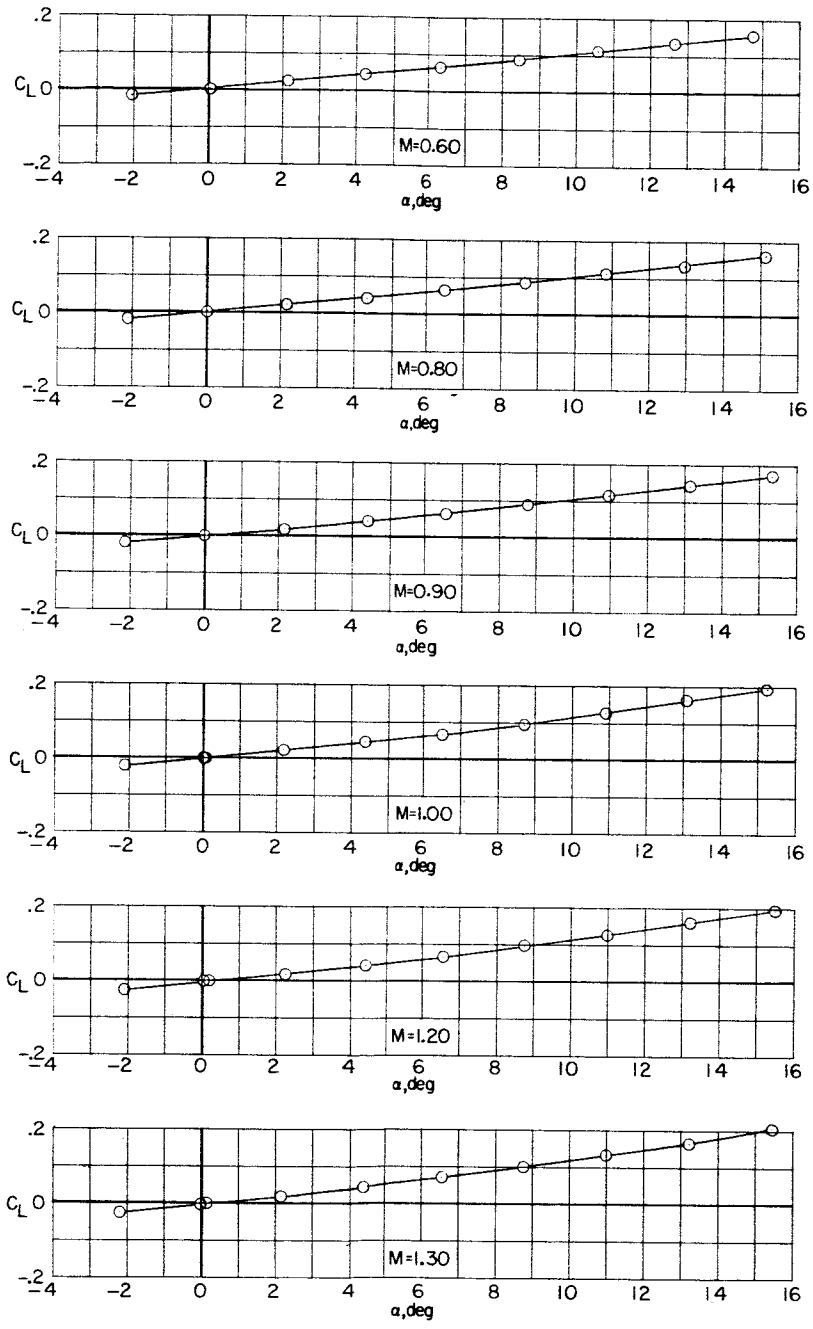

(a) C_L against α.

Figure 21.- Longitudinal aerodynamic characteristics of body alone of model III. Configuration B.

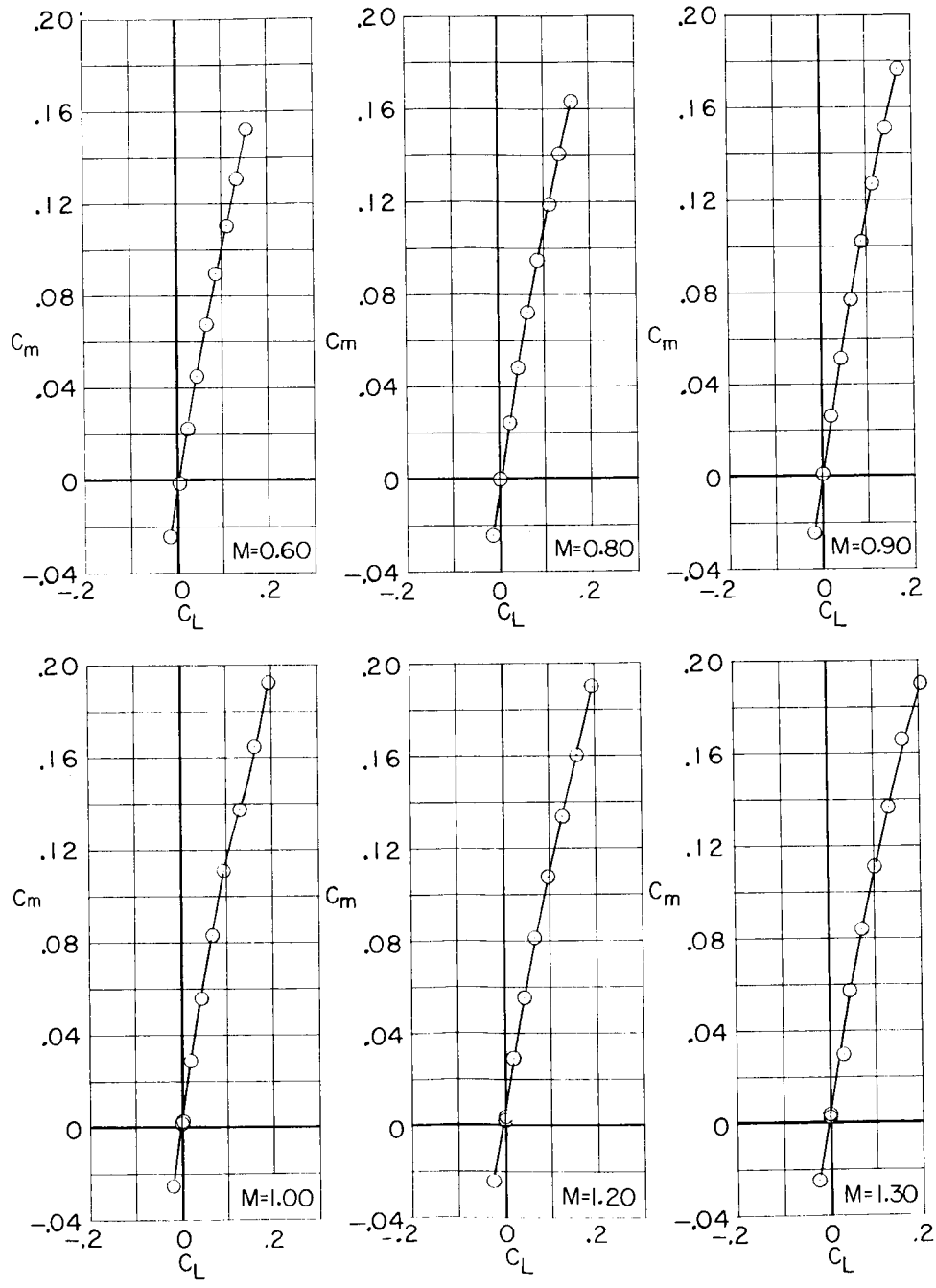

(b) C_m against C_L.

Figure 21.- Continued.

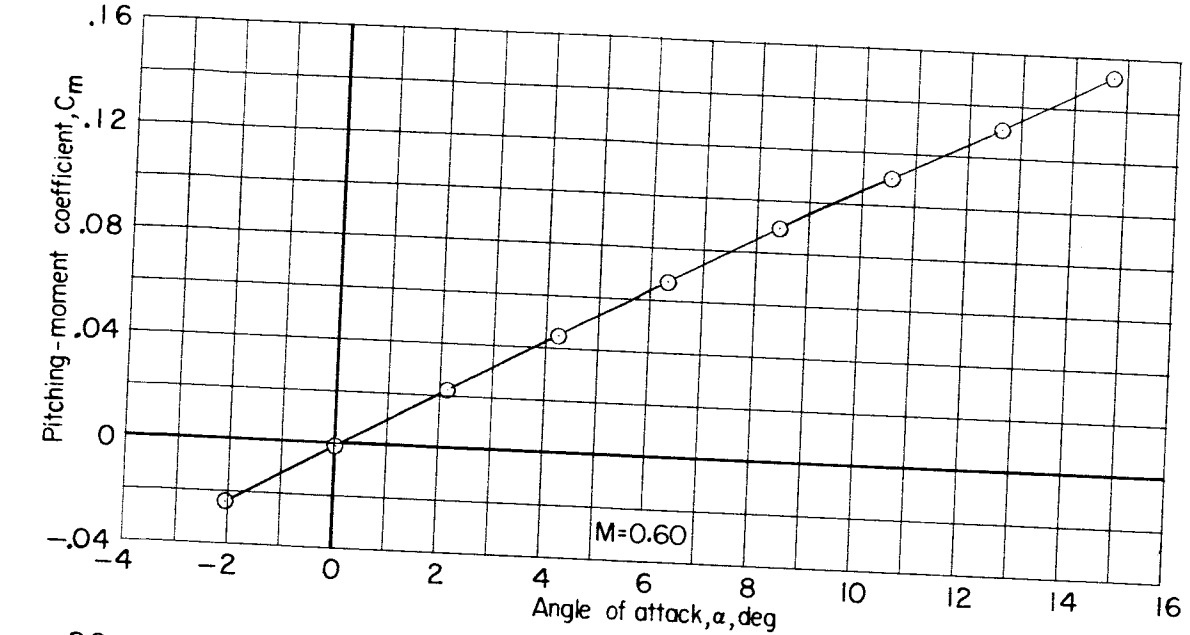

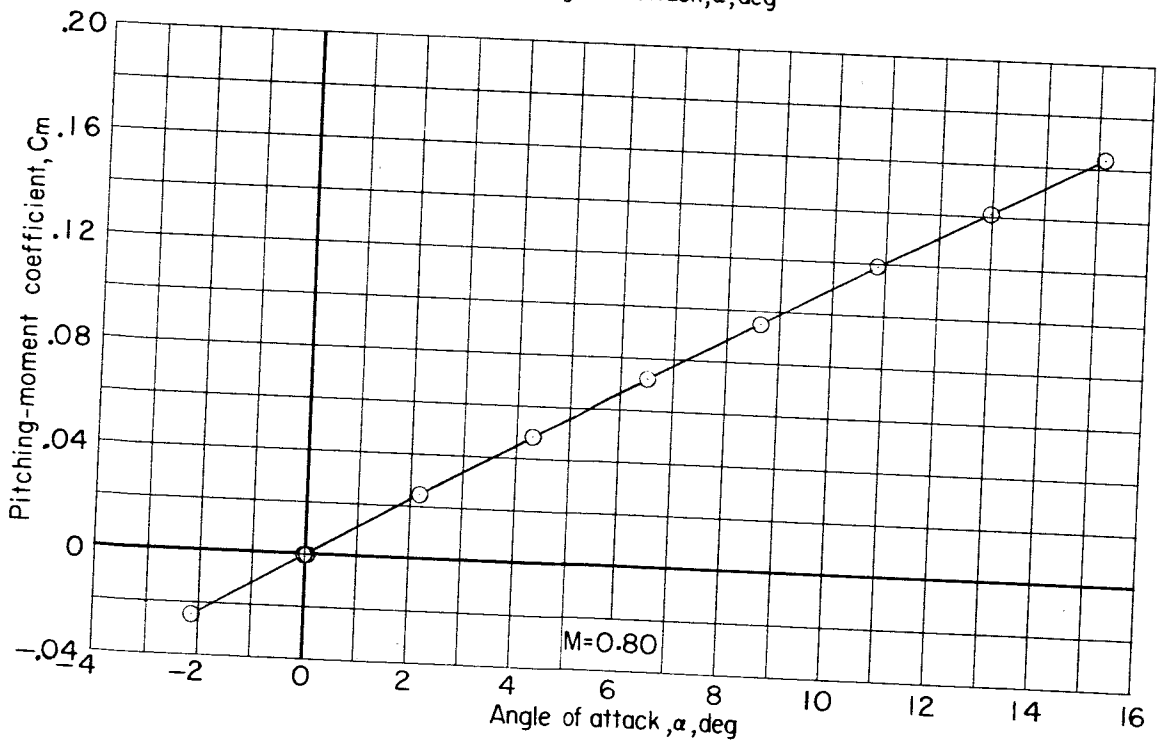

(c) C_m against α.

Figure 21.- Continued.

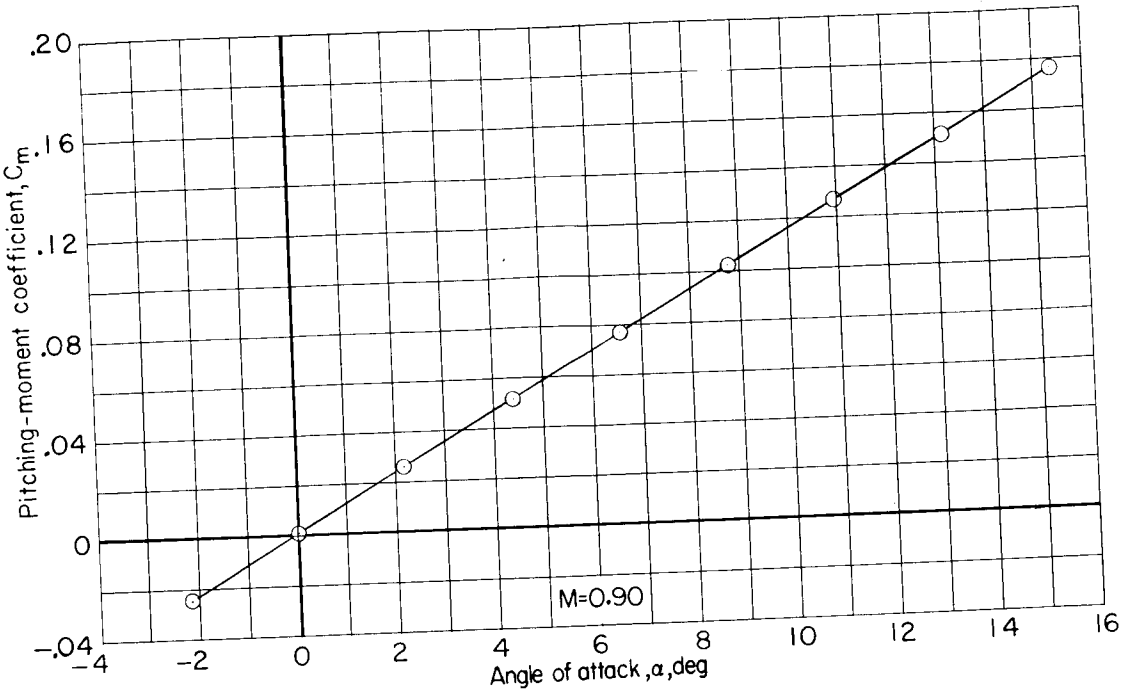

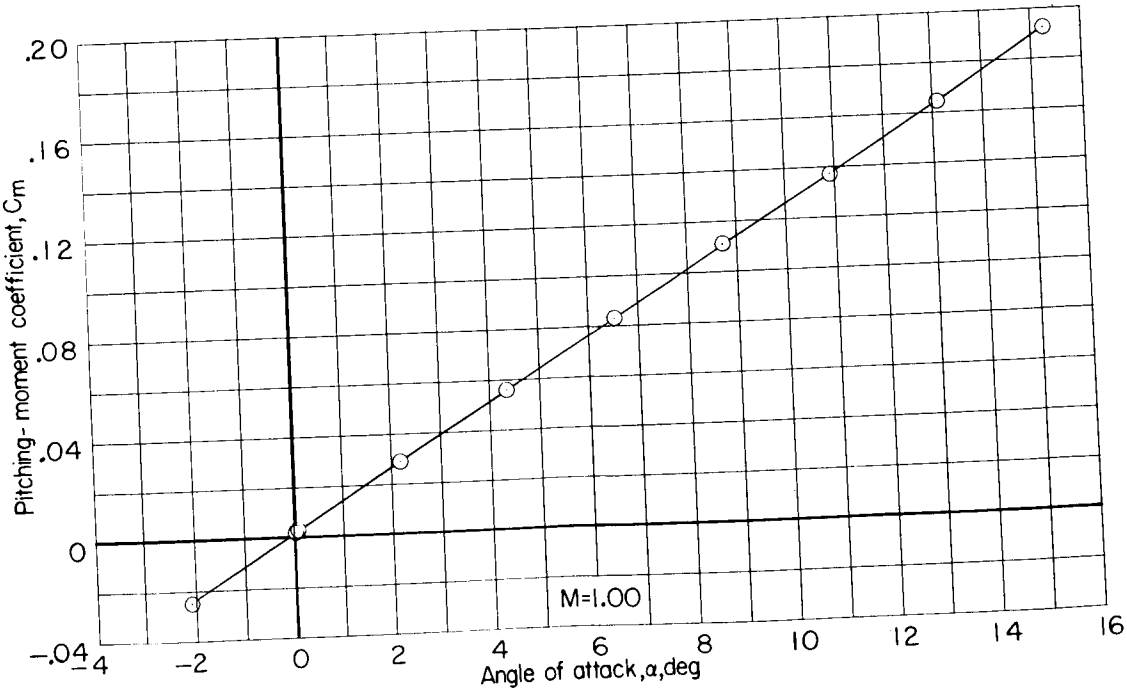

(c) Continued.

Figure 21.- Continued.

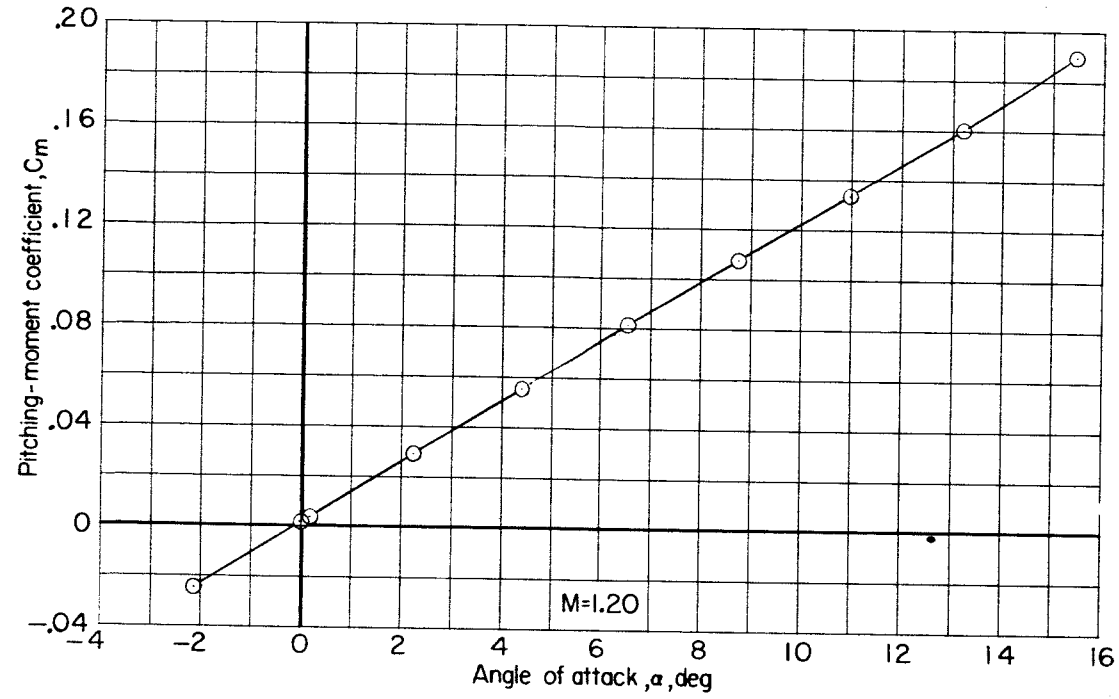

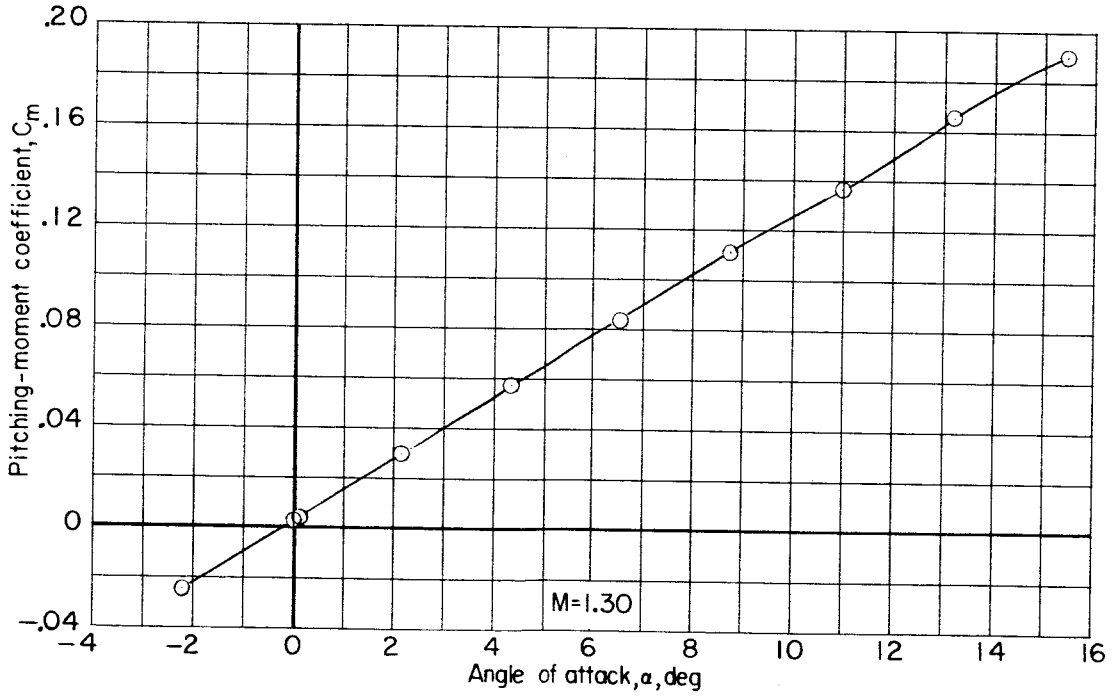

(c) Concluded.

Figure 21.- Continued.

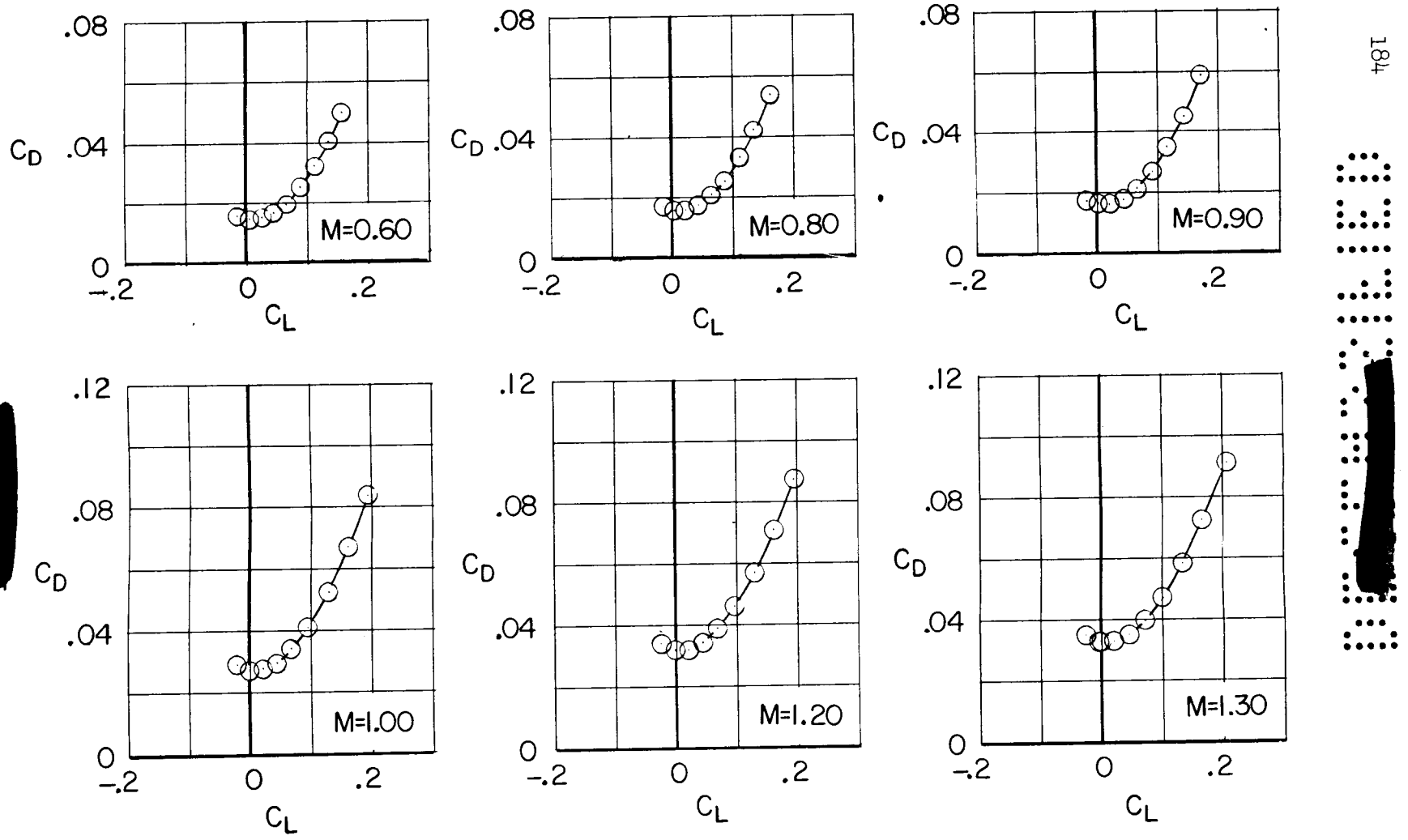

(d) C_D against C_L.

Figure 21.- Continued.

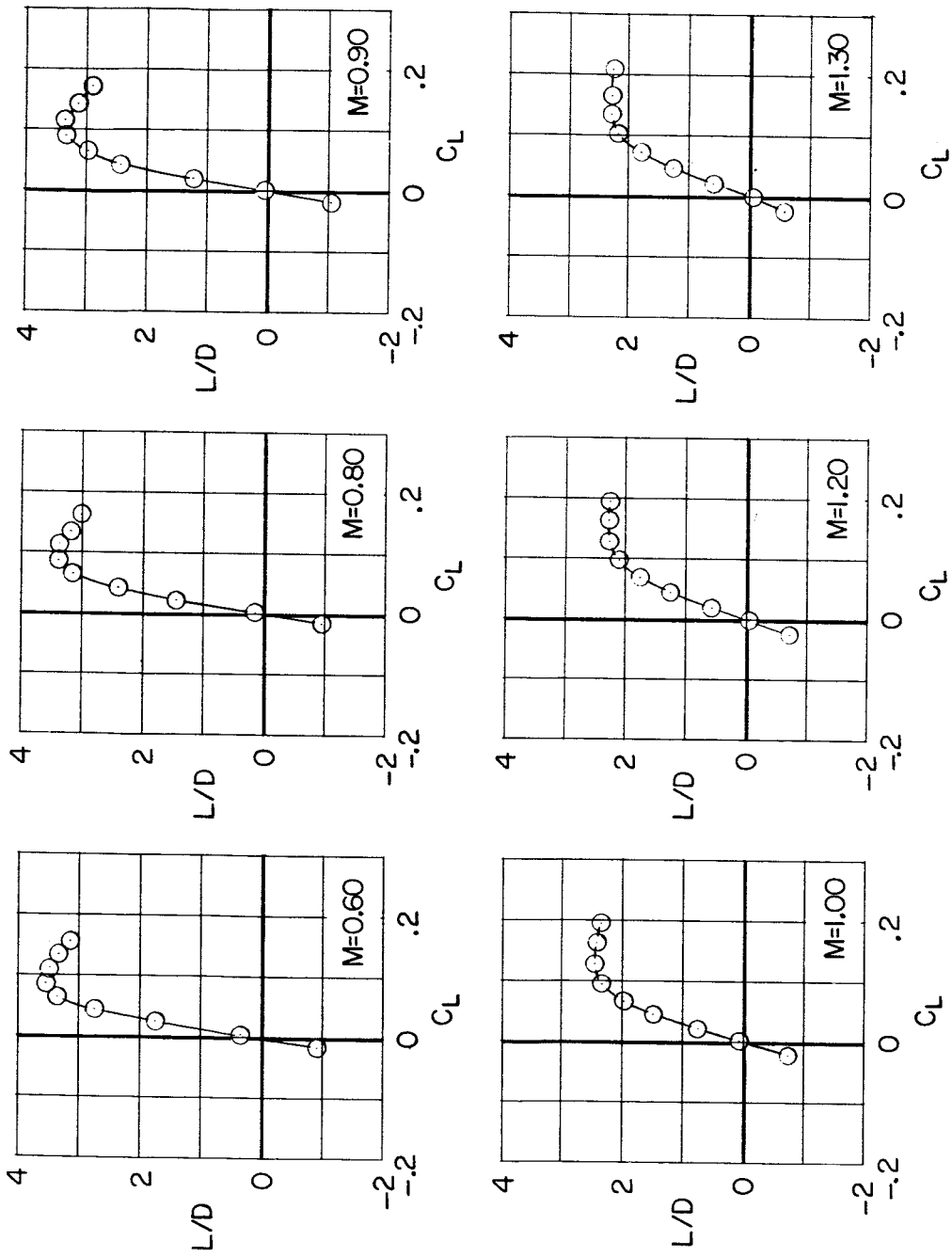

(e) L/D against C_L.

Figure 21.- Concluded.

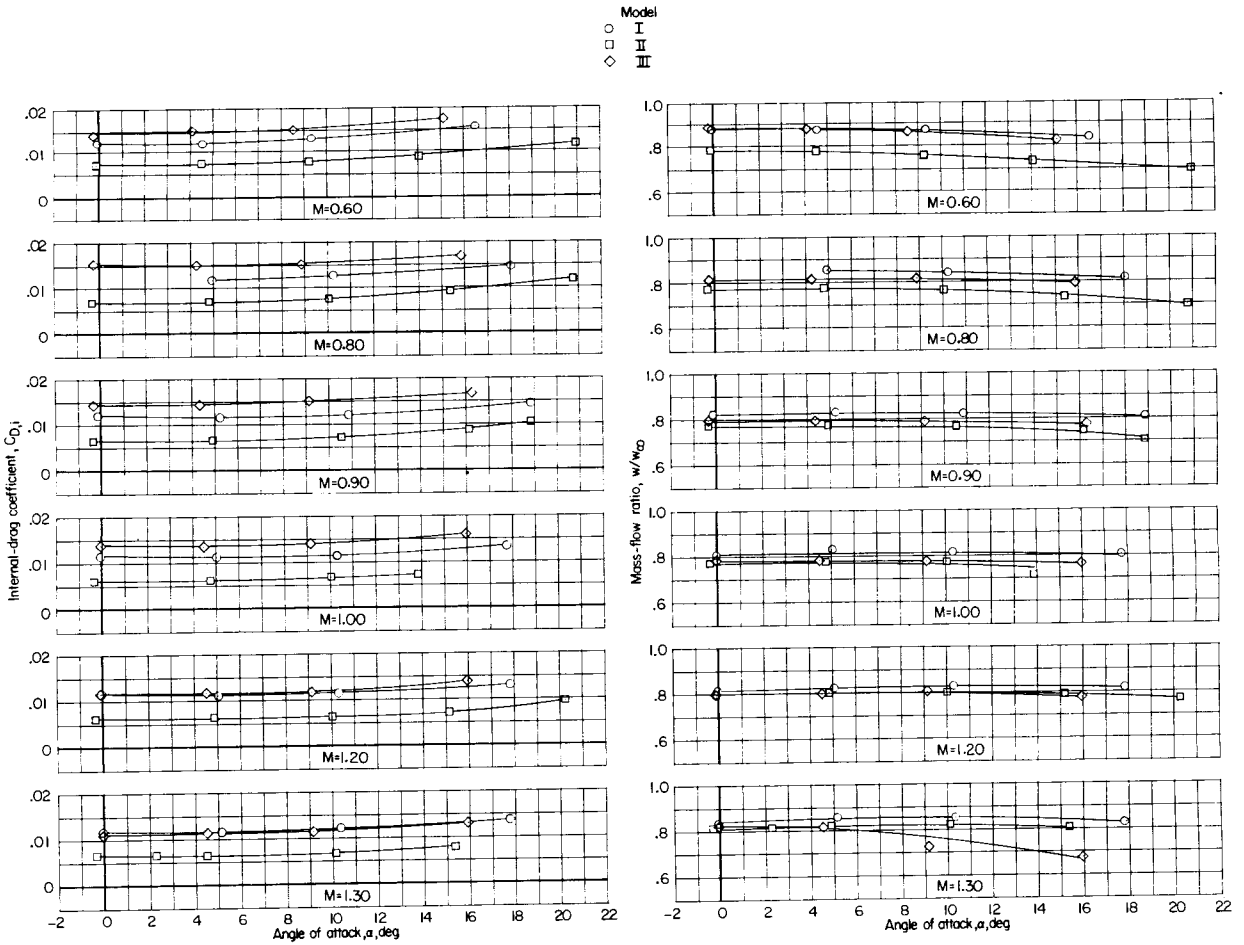

(a) $C_{D,i}$ and w/w_∞ against α.

Figure 22.- Results on internal-drag coefficient and mass-flow ratio of models I, II, and III. Configuration BVW$_3$H; $\delta_h = 0^\circ$.

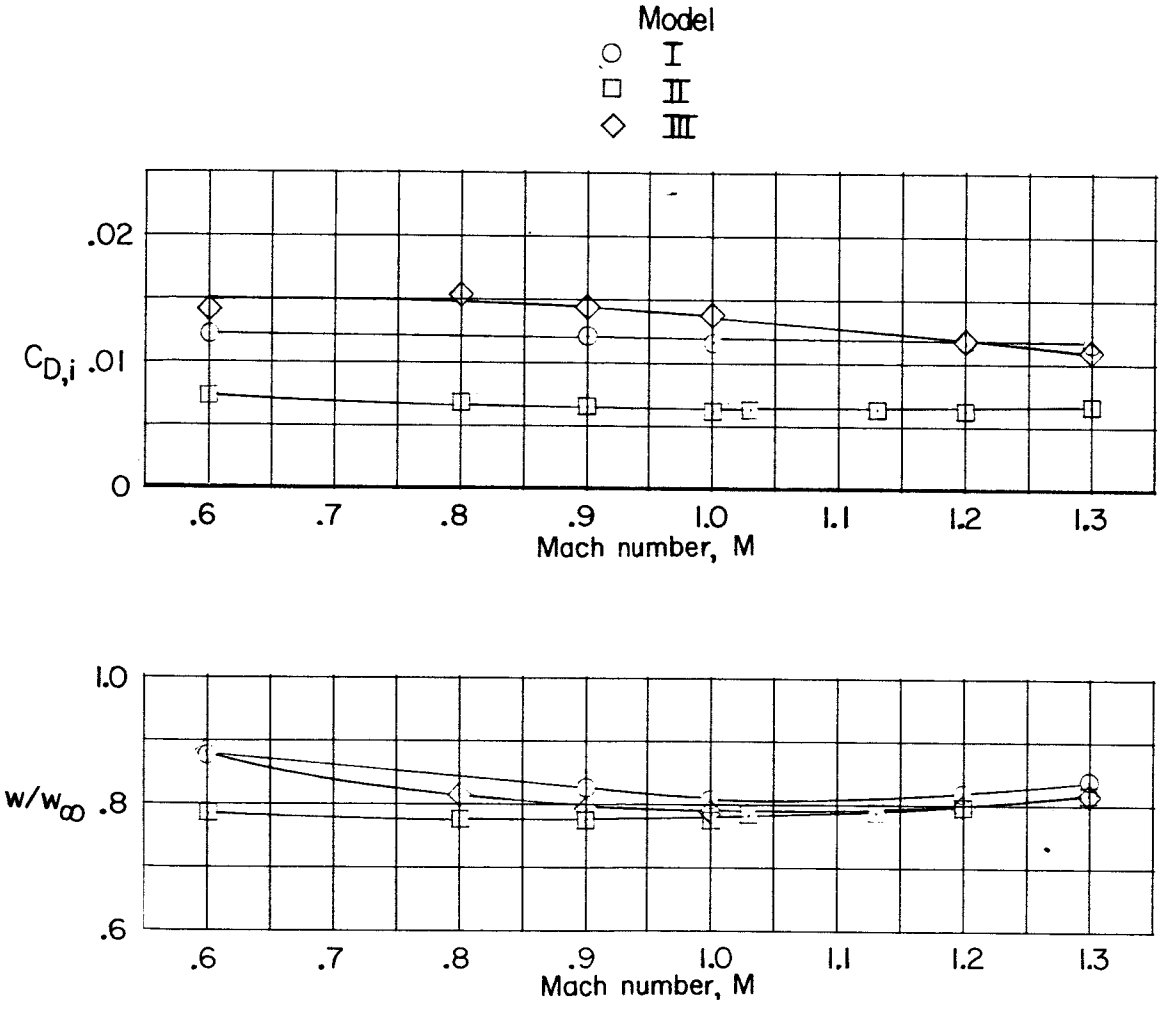

(b) $C_{D,i}$ and w/w_∞ against M; $\alpha = 0^\circ$.

Figure 22.- Concluded.

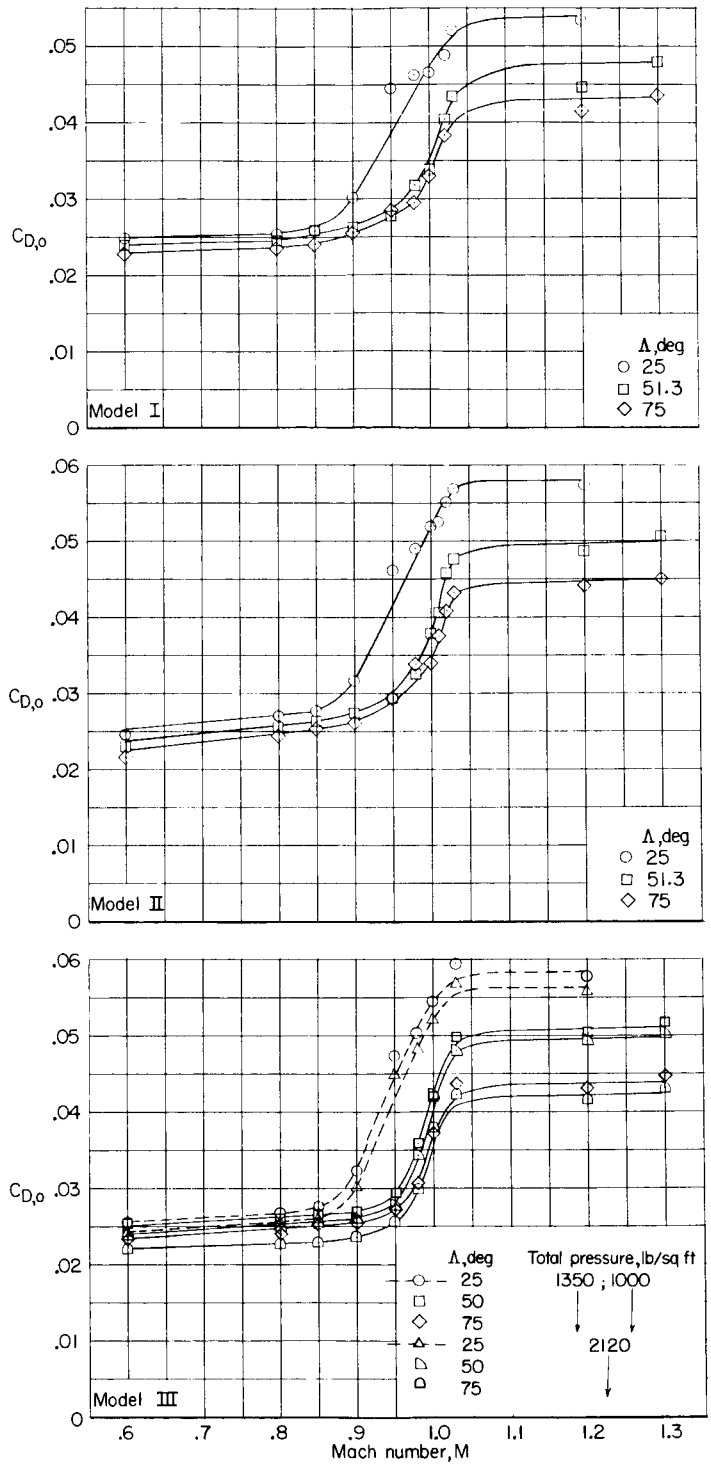

Figure 23.- Effect of wing sweep on zero-lift drag characteristics of models I, II, and III. Configuration BWVH; $\delta_h = 0^o$.

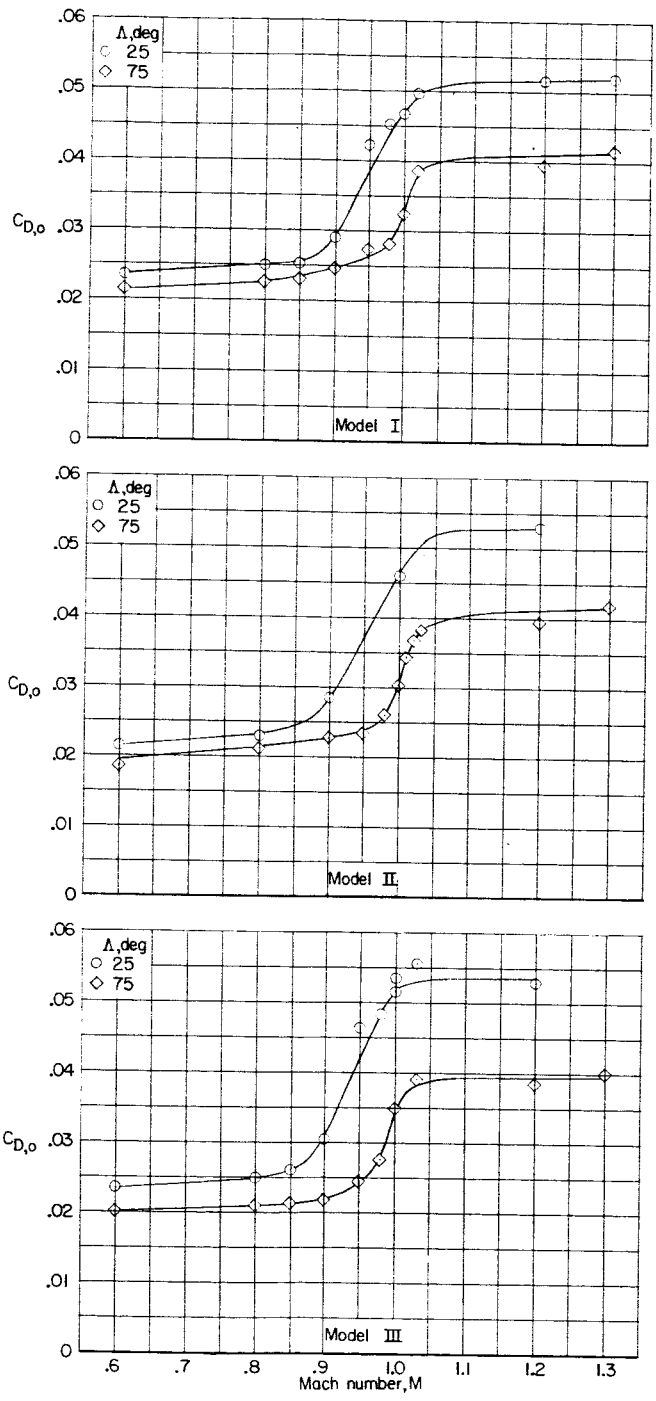

Figure 24.- Effect of wing sweep on zero-lift drag characteristics of models I and II with horizontal tail off (configuration BWV) and model III with horizontal and vertical tails off (configuration BW).

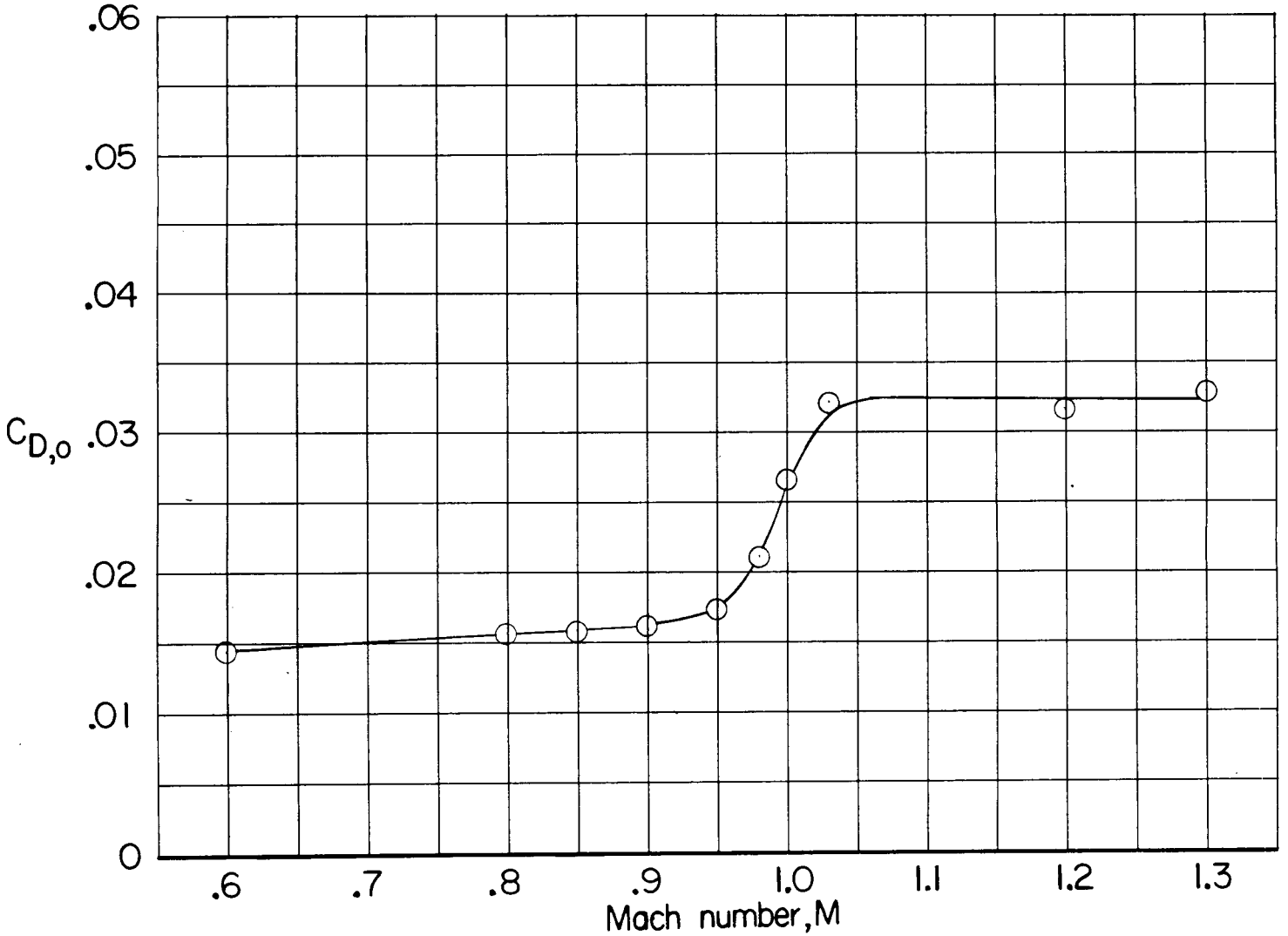

Figure 25.- Effect of Mach number on zero-lift drag characteristics of body alone of model III. Configuration B.

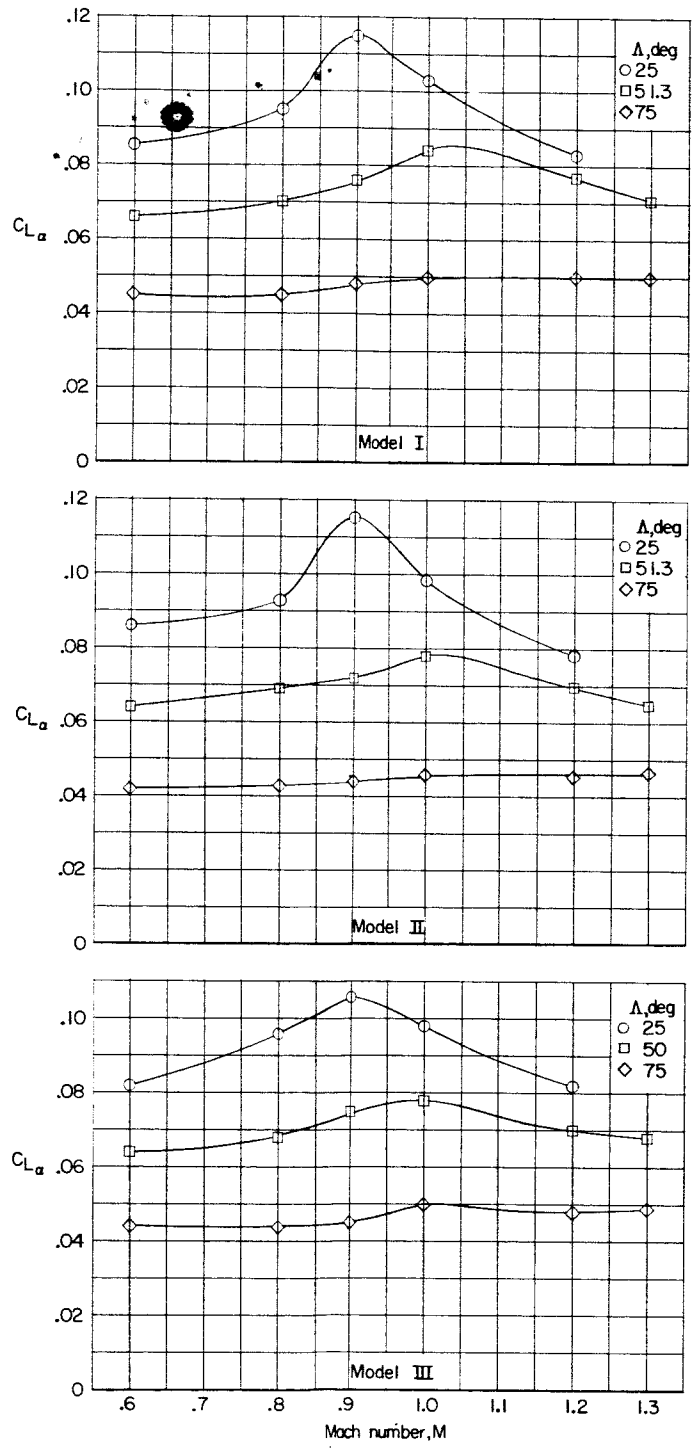

Figure 26.- Effect of wing sweep on lift-curve slope of models I, II, and III. Configuration BWVH; $\delta_h = 0^o$.

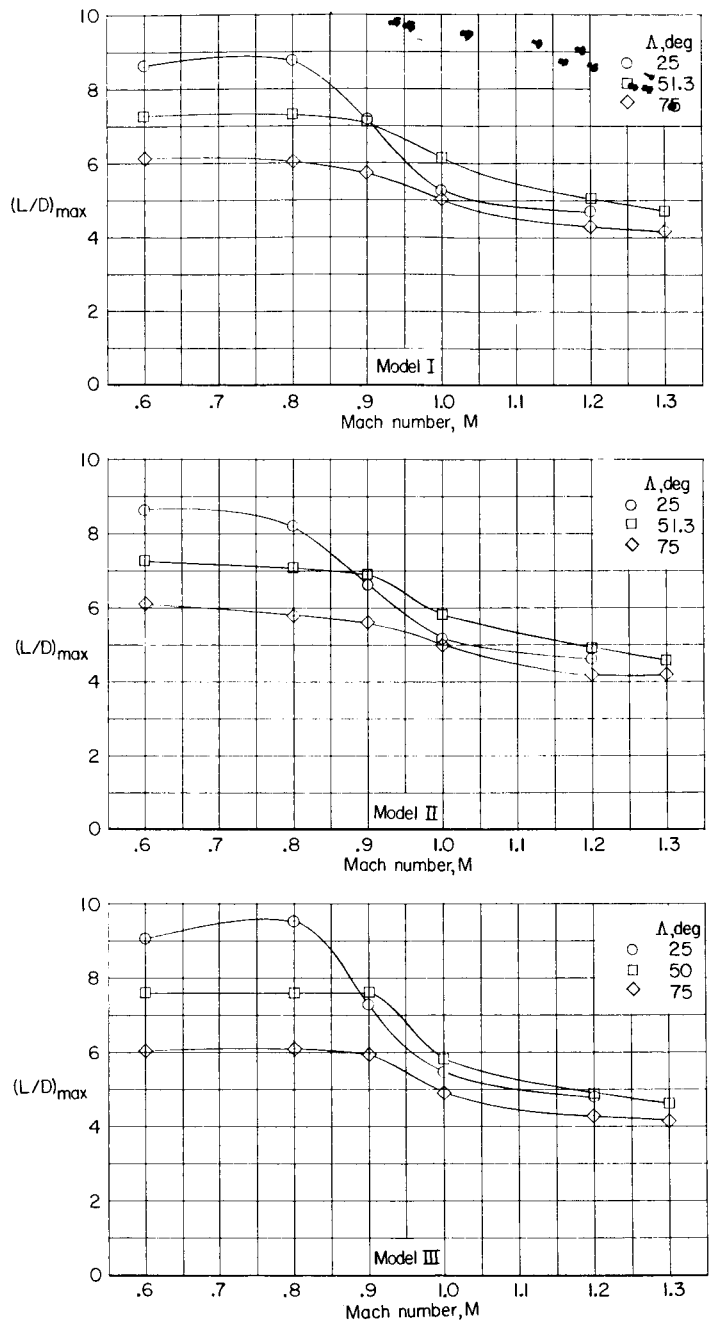

(a) $(L/D)_{max}$ against M.

Figure 27.- Effect of wing sweep on maximum lift-drag ratio of models I, II, and III. Configuration BWVH; $\delta_h = 0^o$.

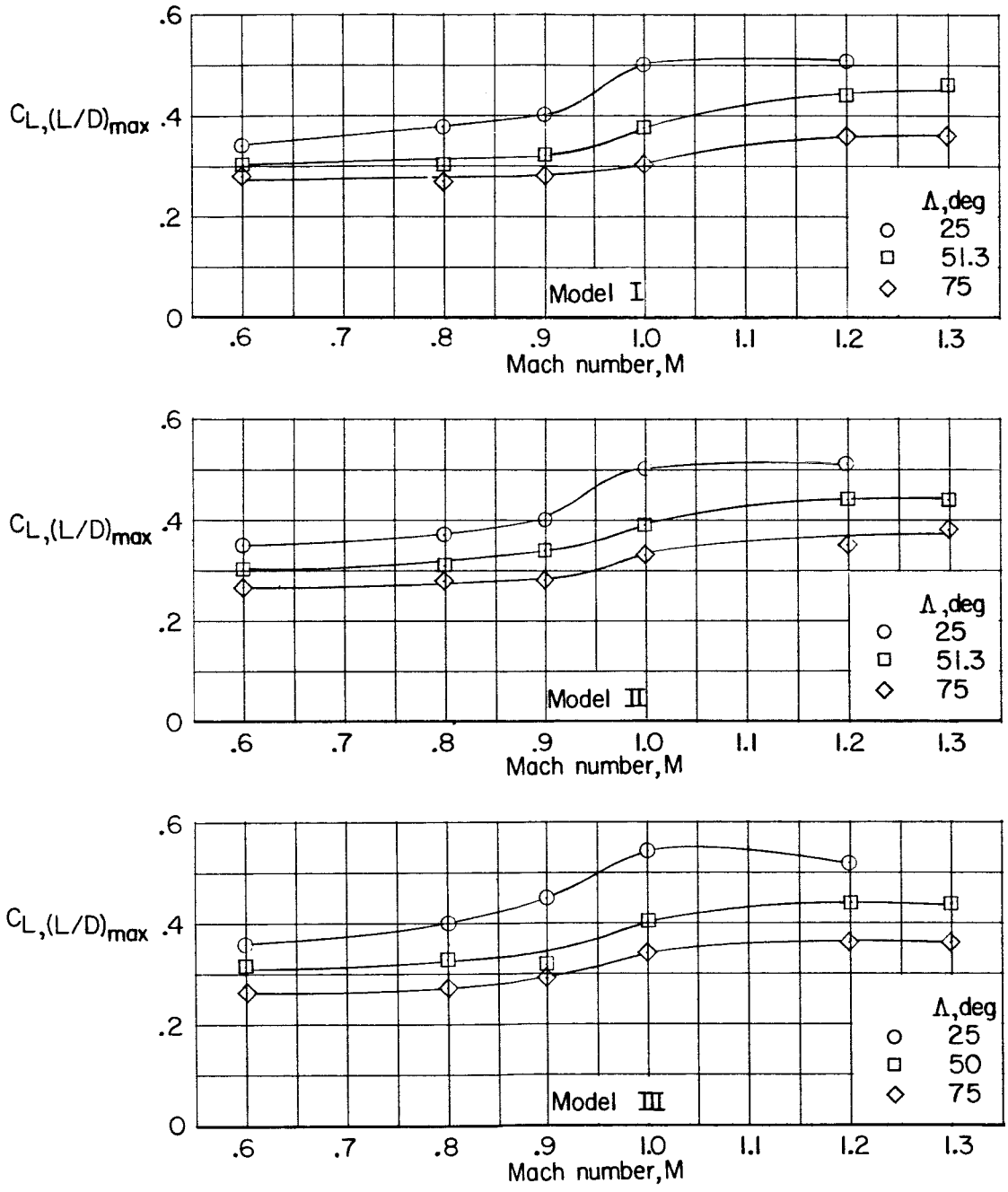

(b) C_L at $(L/D)_{max}$ against M.

Figure 27.- Concluded.

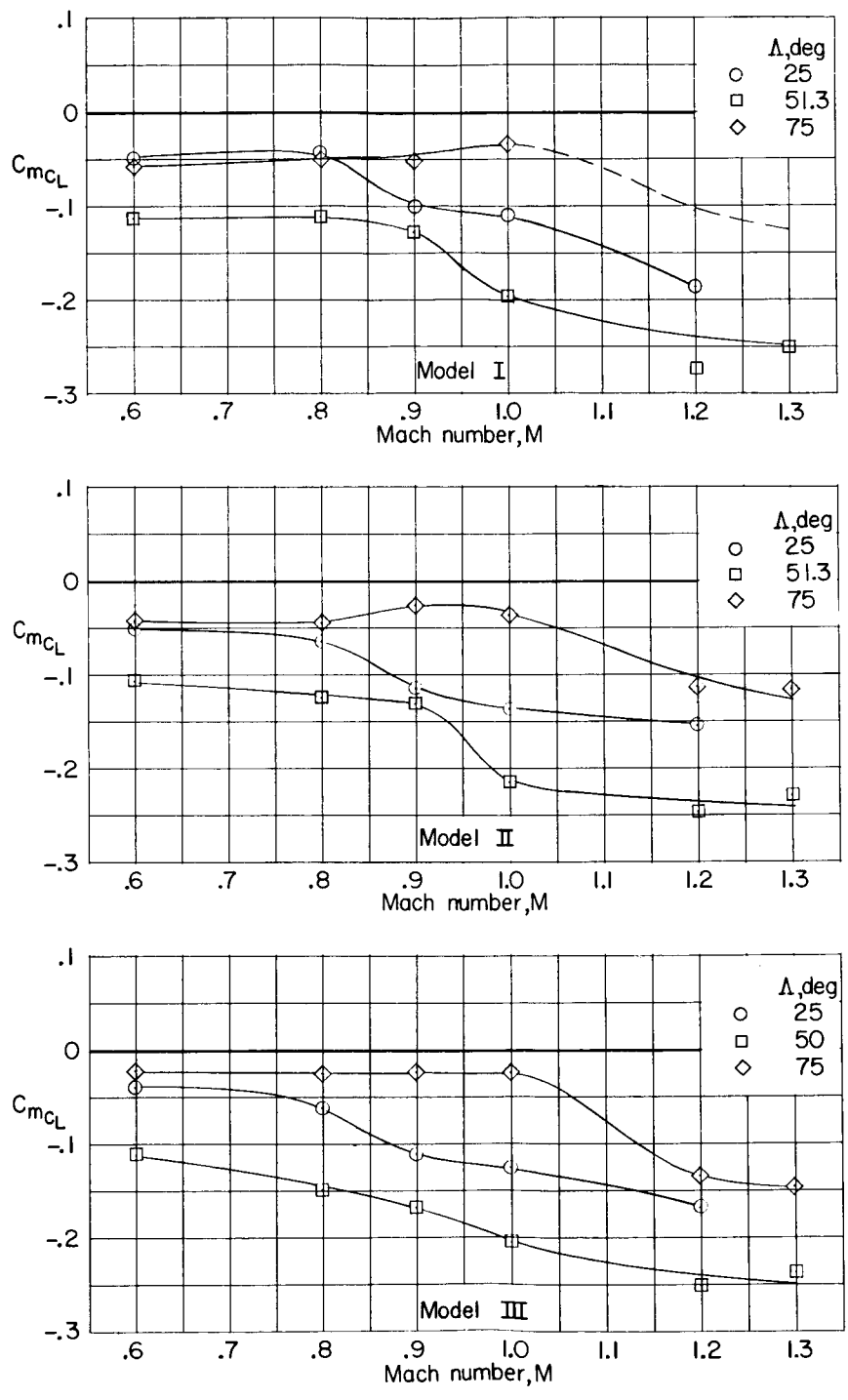

Figure 28.- Effect of wing sweep on static longitudinal-stability derivative of models I, II, and III. Configuration BWVH; $\delta_h = 0^o$.

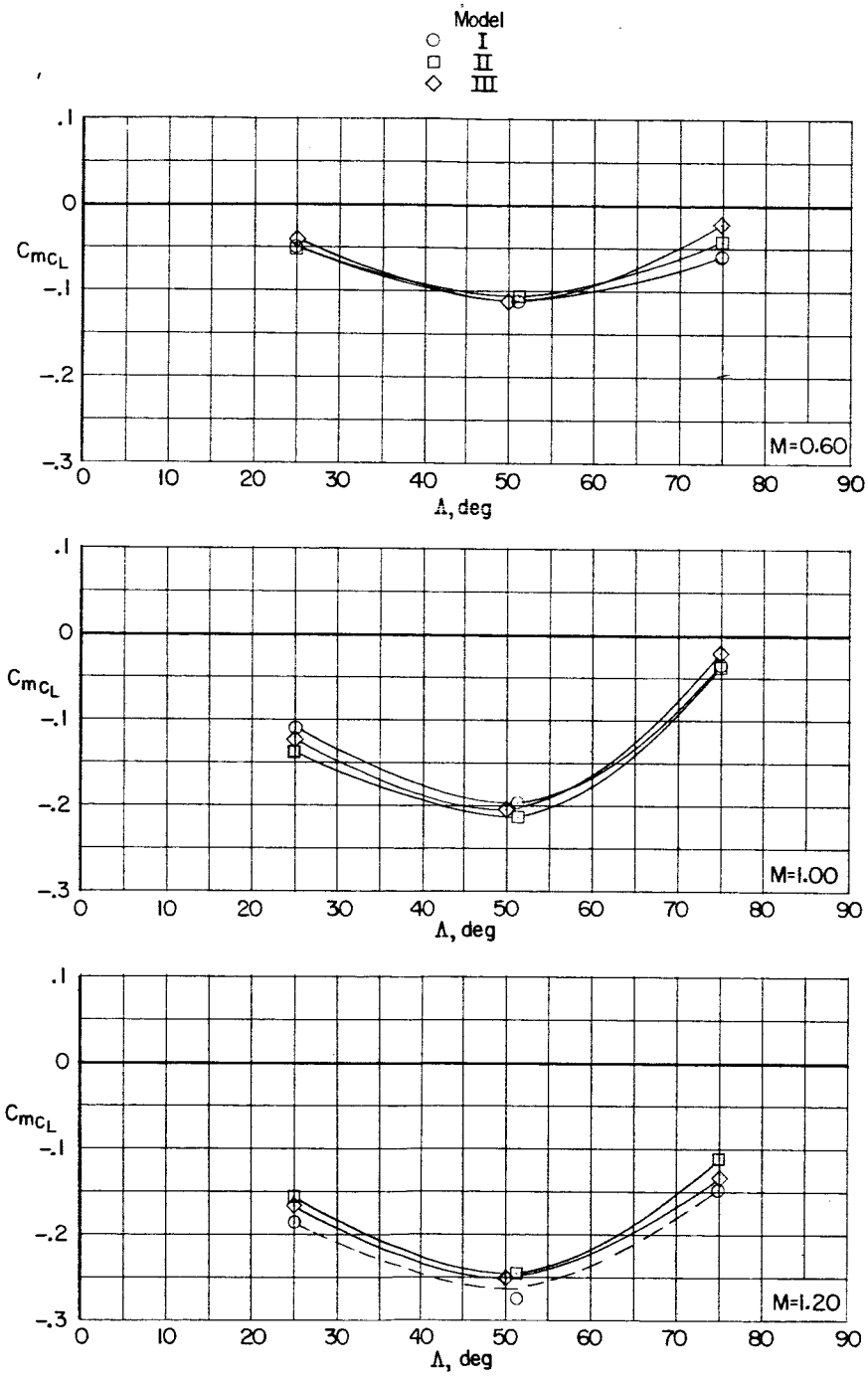

Figure 29.- Variation of static longitudinal-stability derivative of models I, II, and III with angle of sweep. Configuration BWVH; $\delta_h = 0^o$.

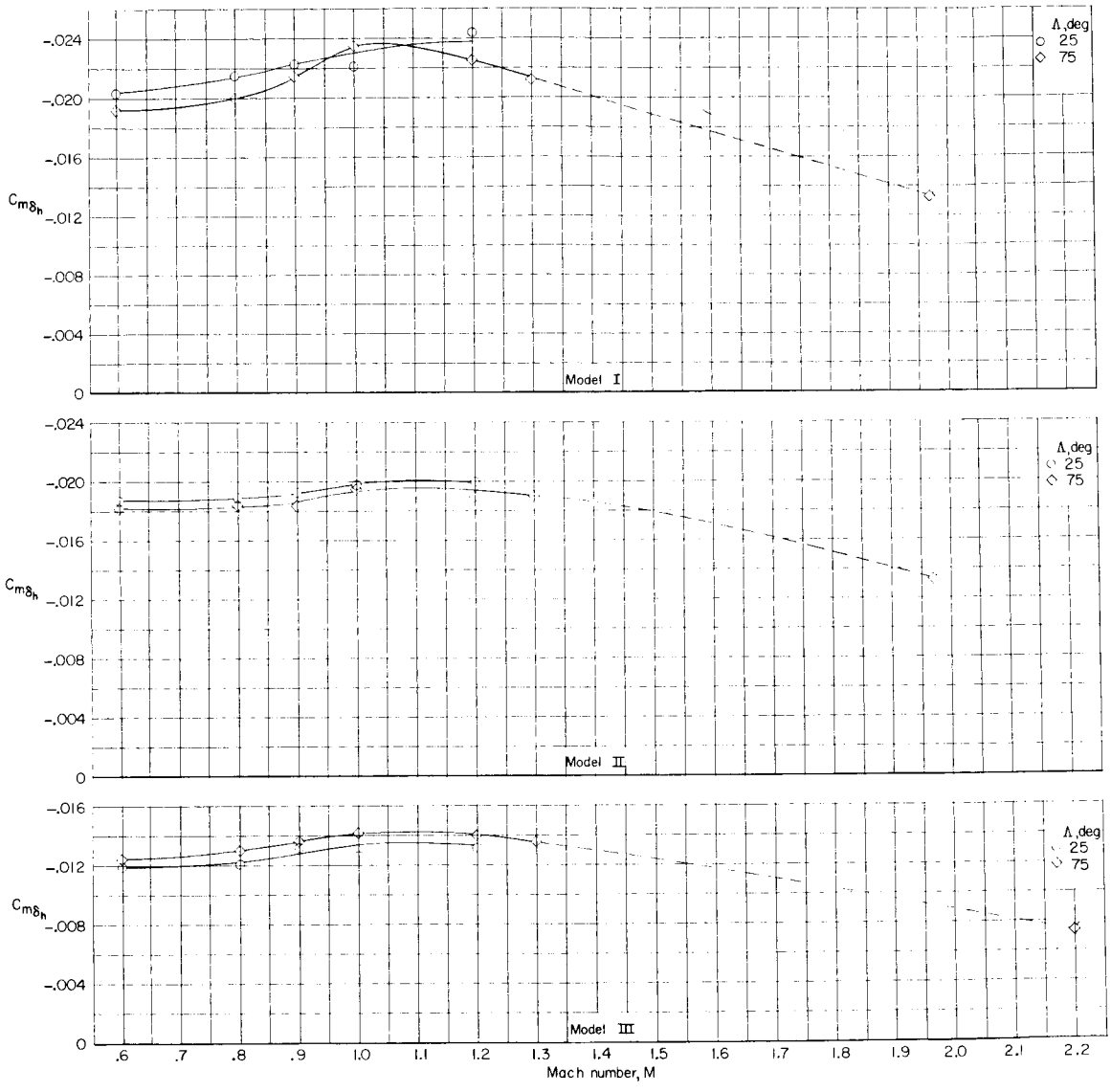

Figure 30.- Effect of wing sweep on horizontal-tail effectiveness of models I, II, and III. Configuration BWVH; $\alpha = 0^{o}$. (Flagged symbols indicate data points from refs. 10 and 11.)

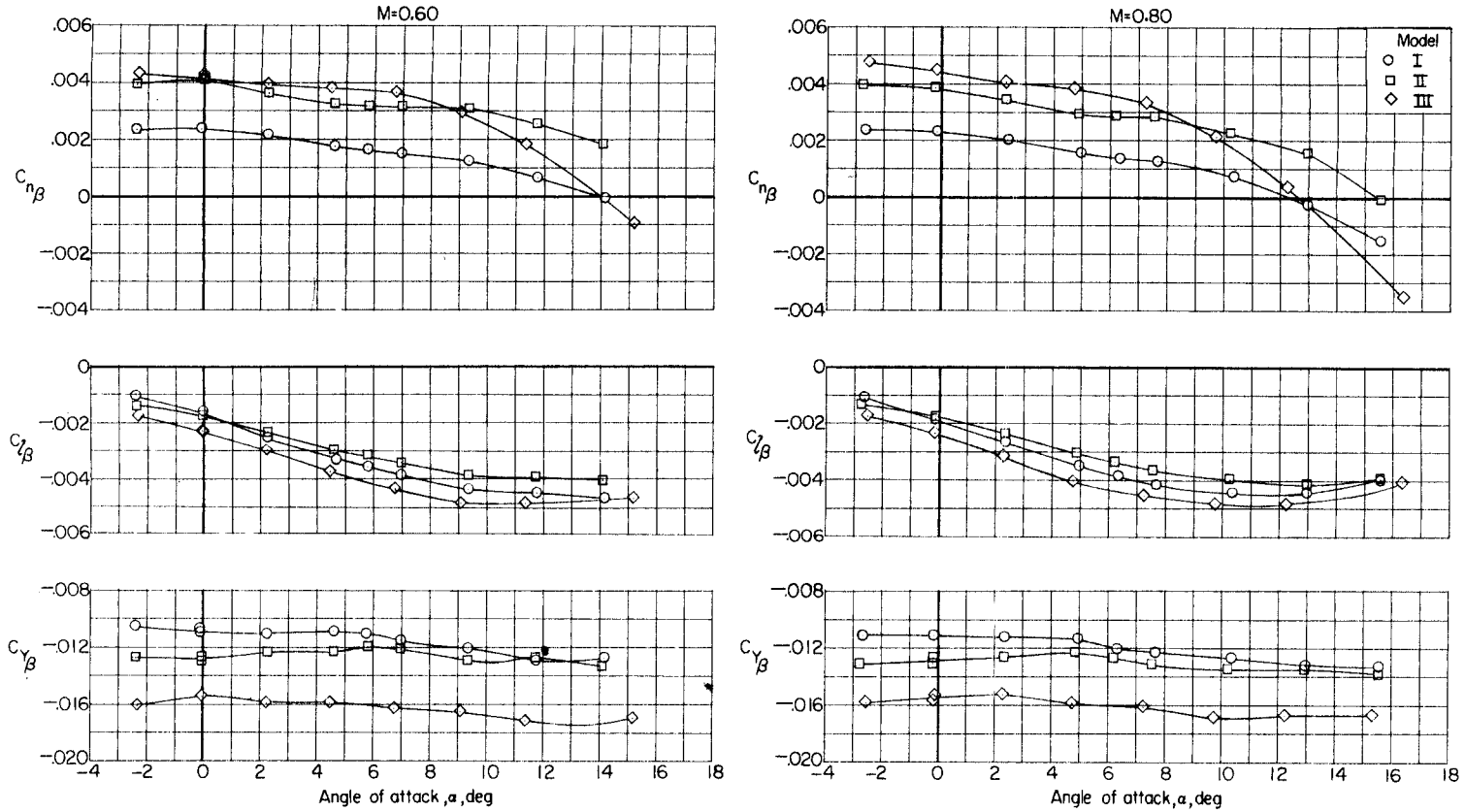

(a) C_{n_β}, C_{l_β}, and C_{Y_β} against α.

Figure 31.- Lateral-stability derivatives of models I, II, and III with 75° swept wing. Configuration BW_3VH; $\delta_h = 0°$.

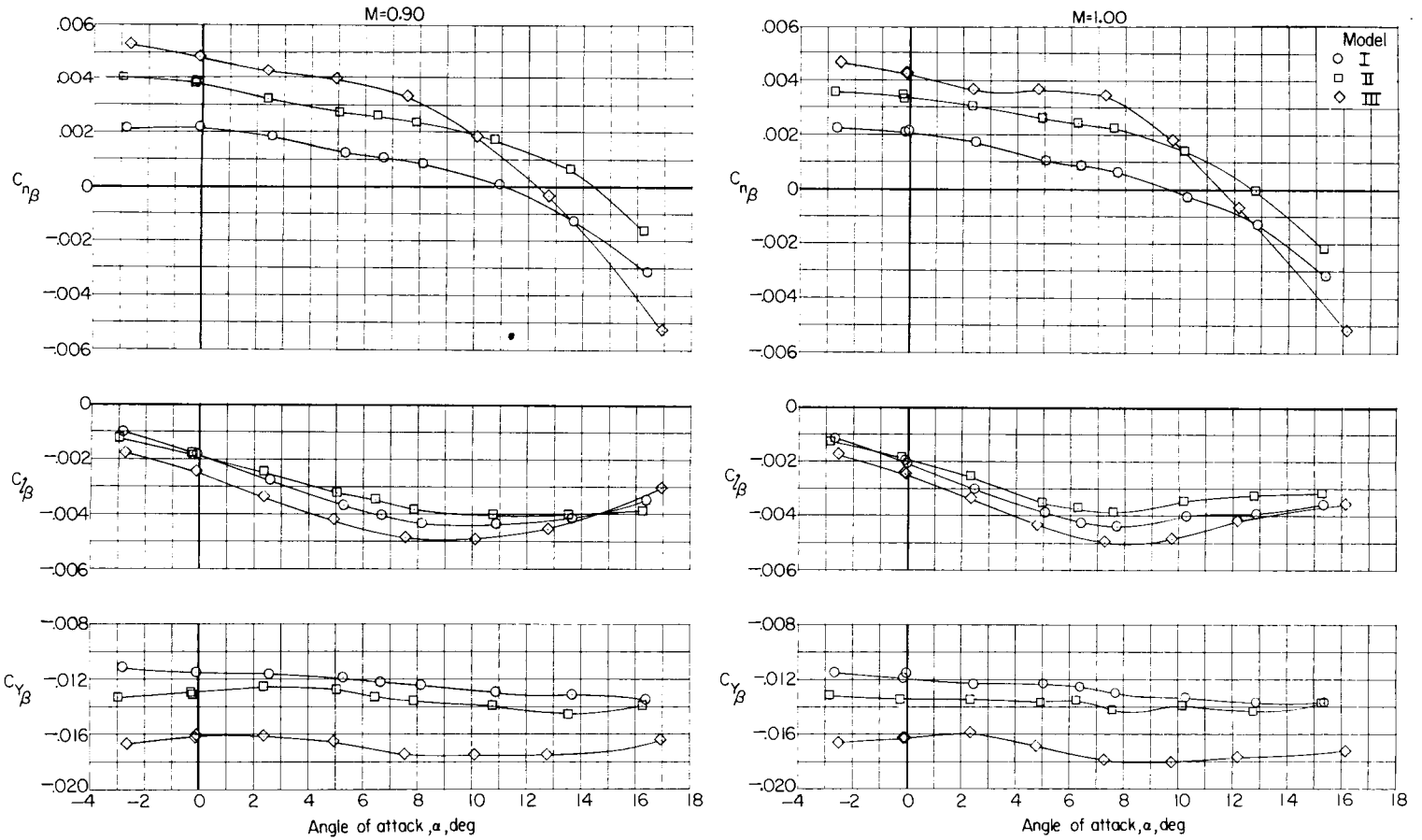

(a) Continued.

Figure 31.- Continued.

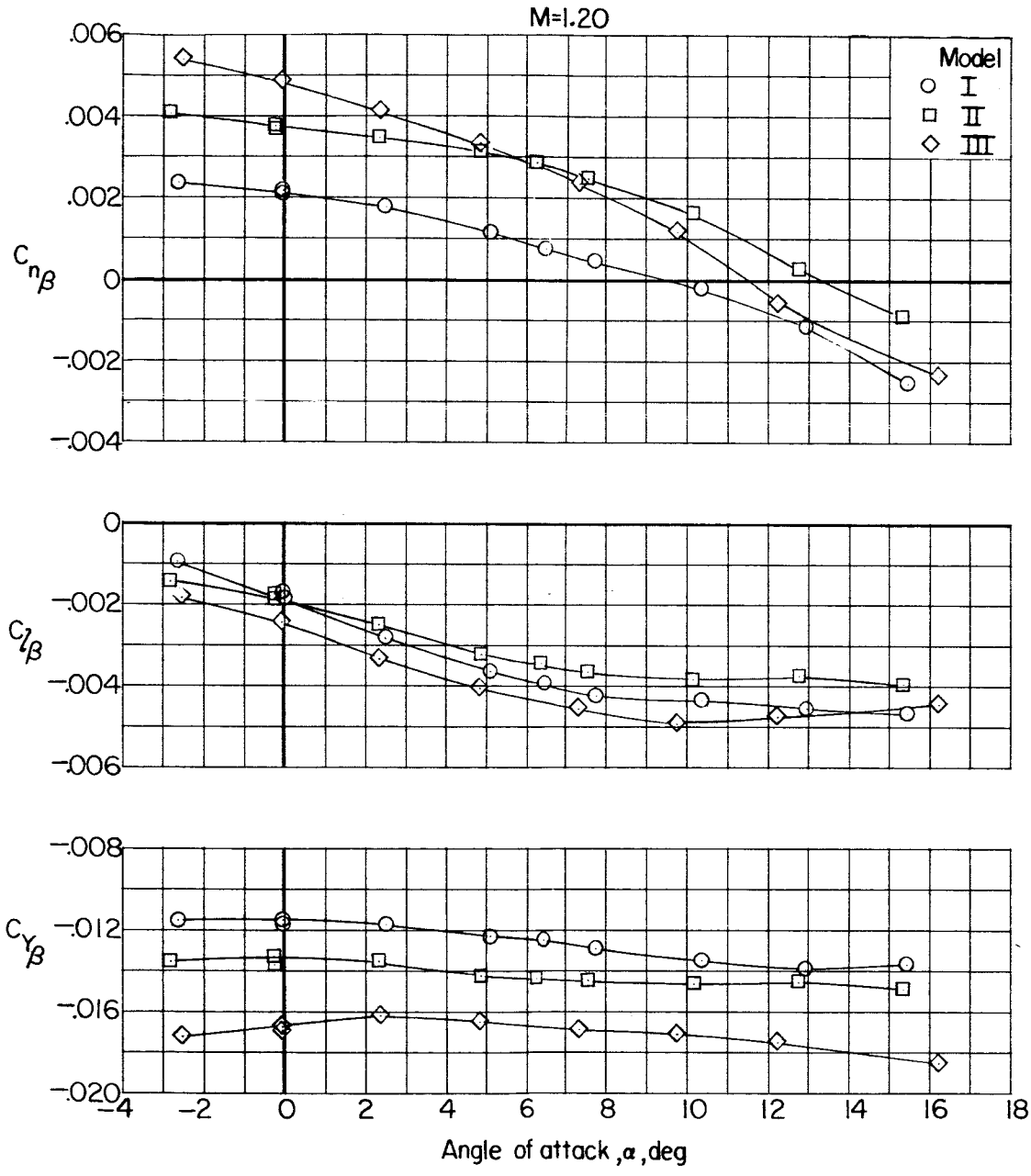

(a) Concluded.

Figure 31.- Continued.

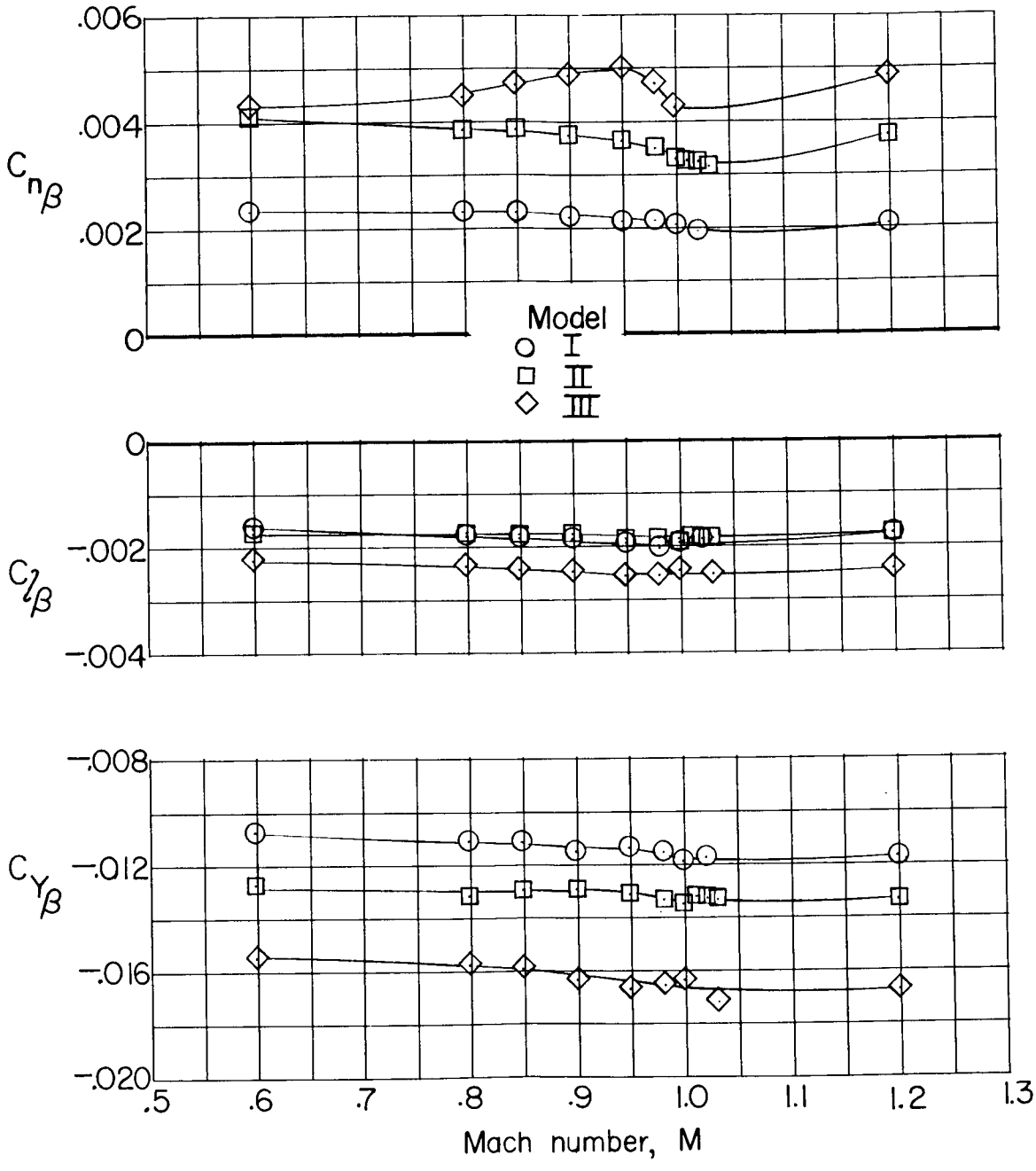

(b) C_{n_β}, C_{l_β}, and C_{Y_β} against M; $\alpha = 0^\circ$.

Figure 31.- Concluded.

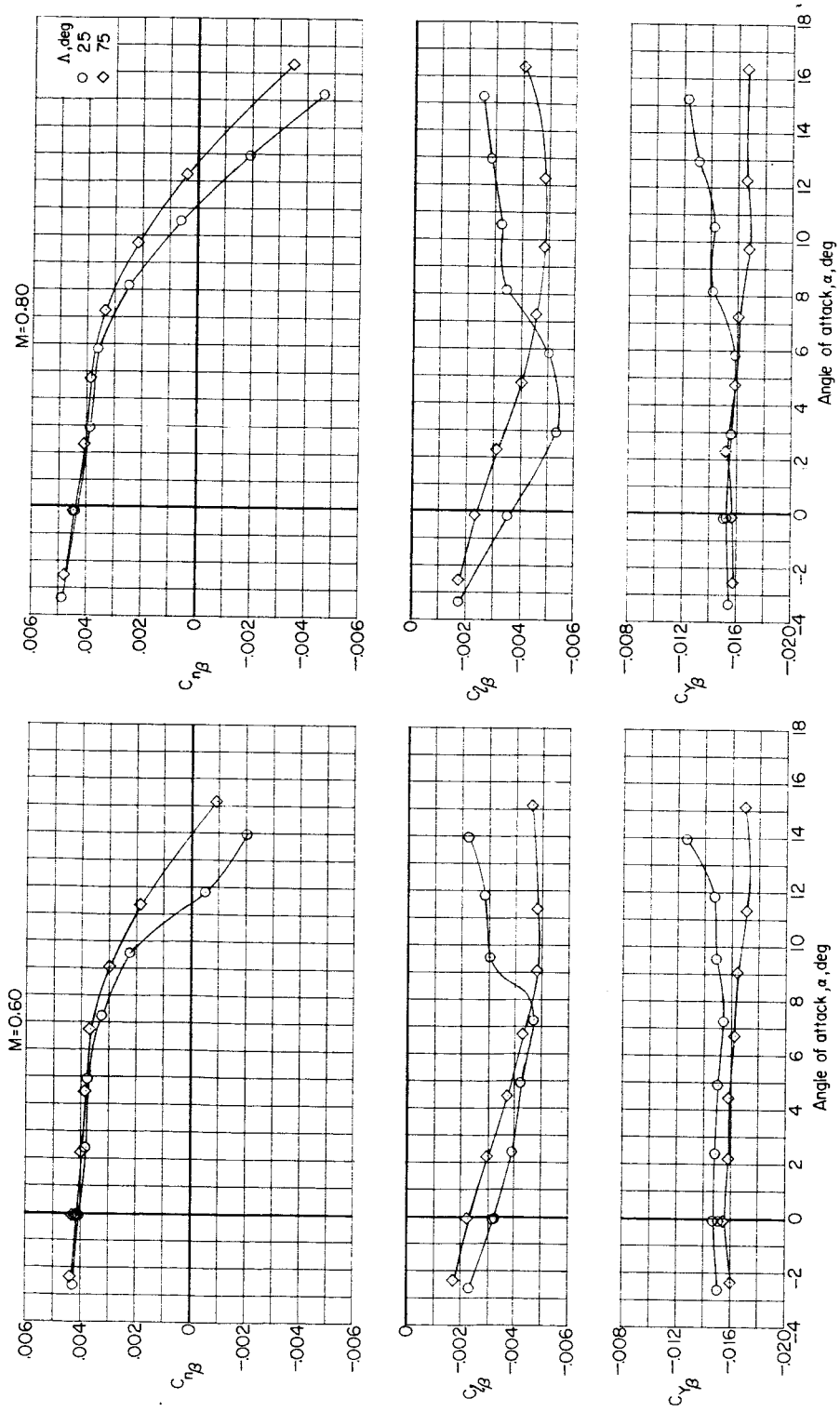

(a) C_{n_β}, C_{l_β}, and C_{Y_β} against α.

Figure 32.- Effect of wing sweep on lateral-stability derivatives of model III. Configuration BWVH; $\delta_h = 0^\circ$.

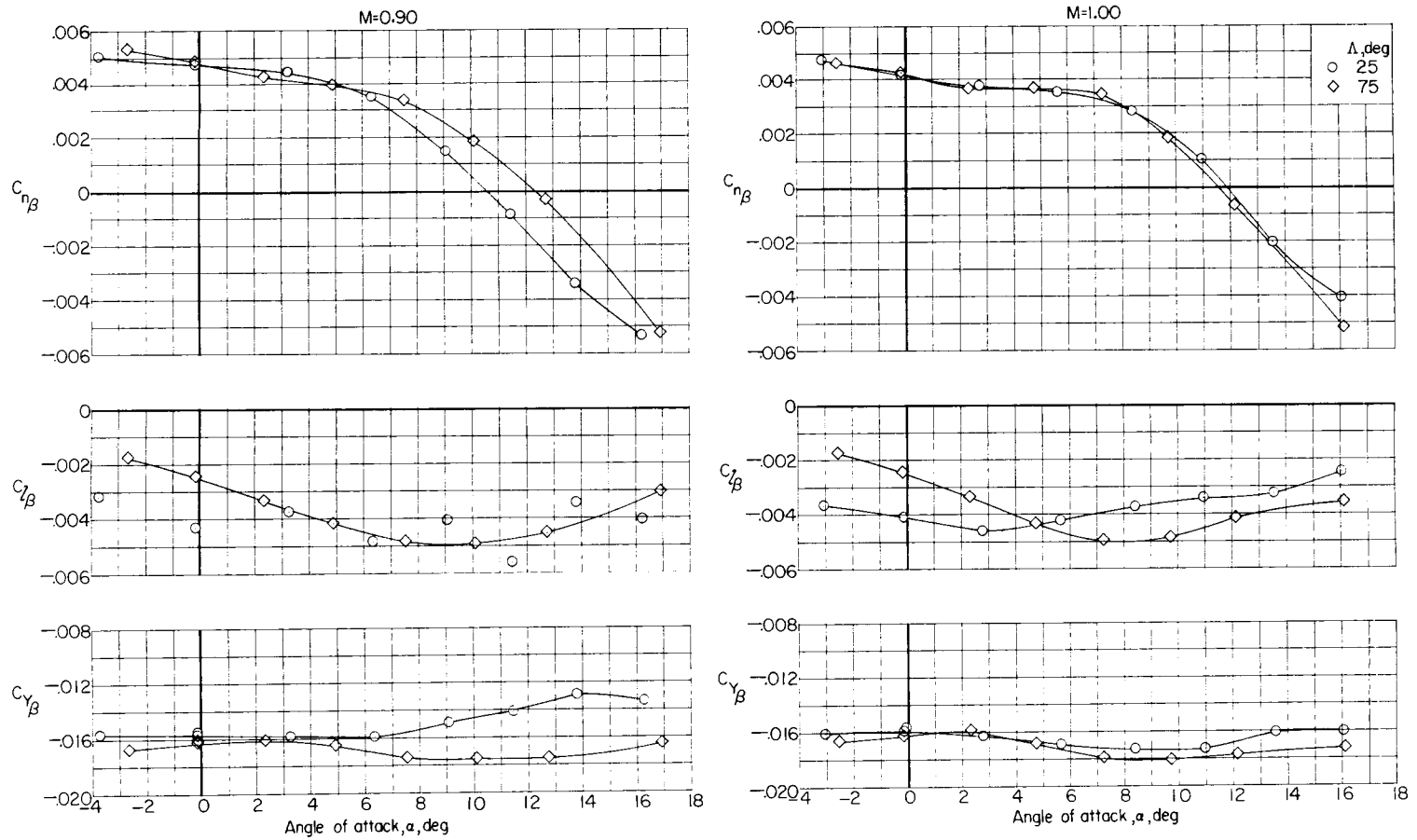

(a) Continued.

Figure 32.- Continued.

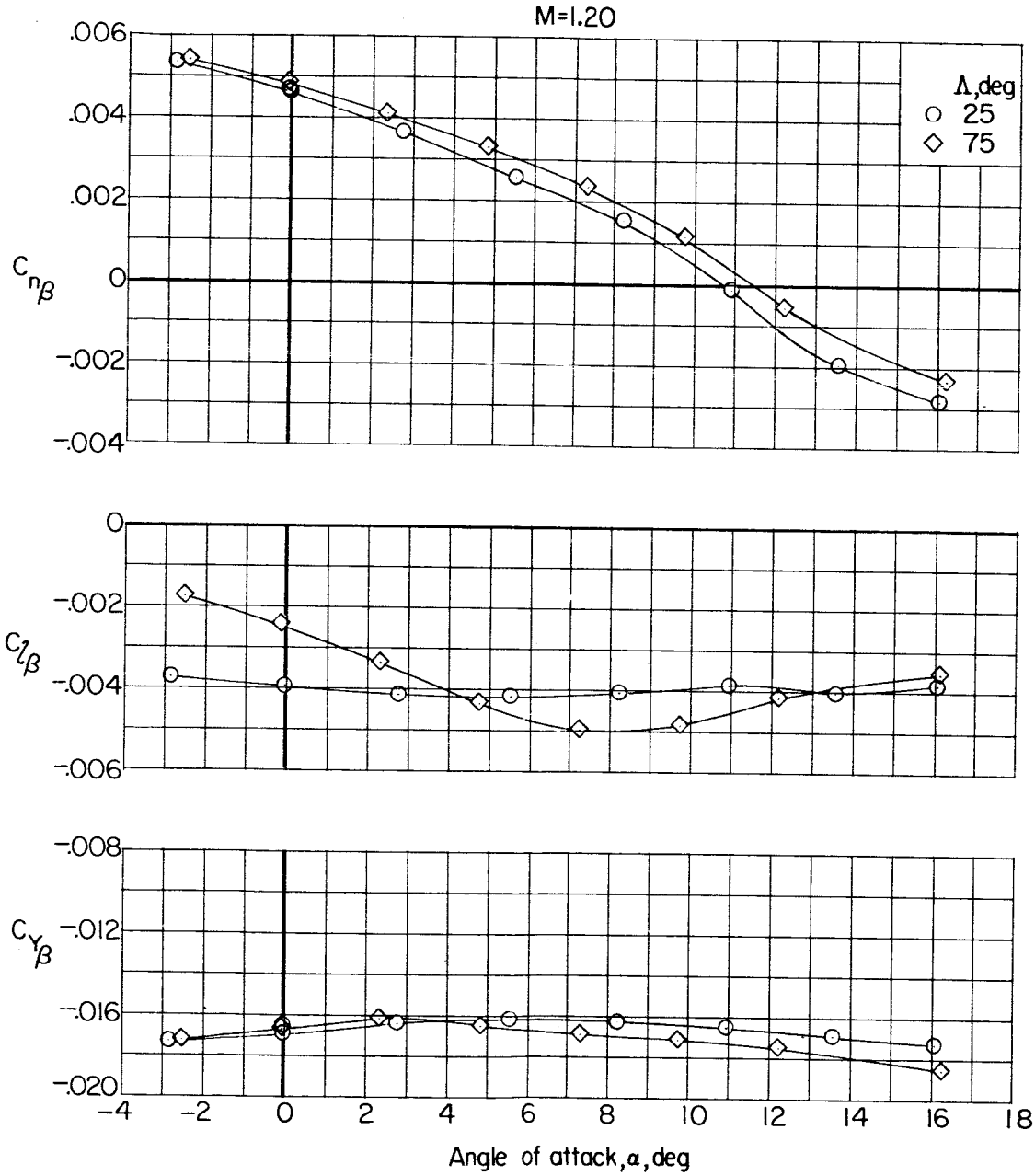

(a) Concluded.

Figure 32.- Continued.

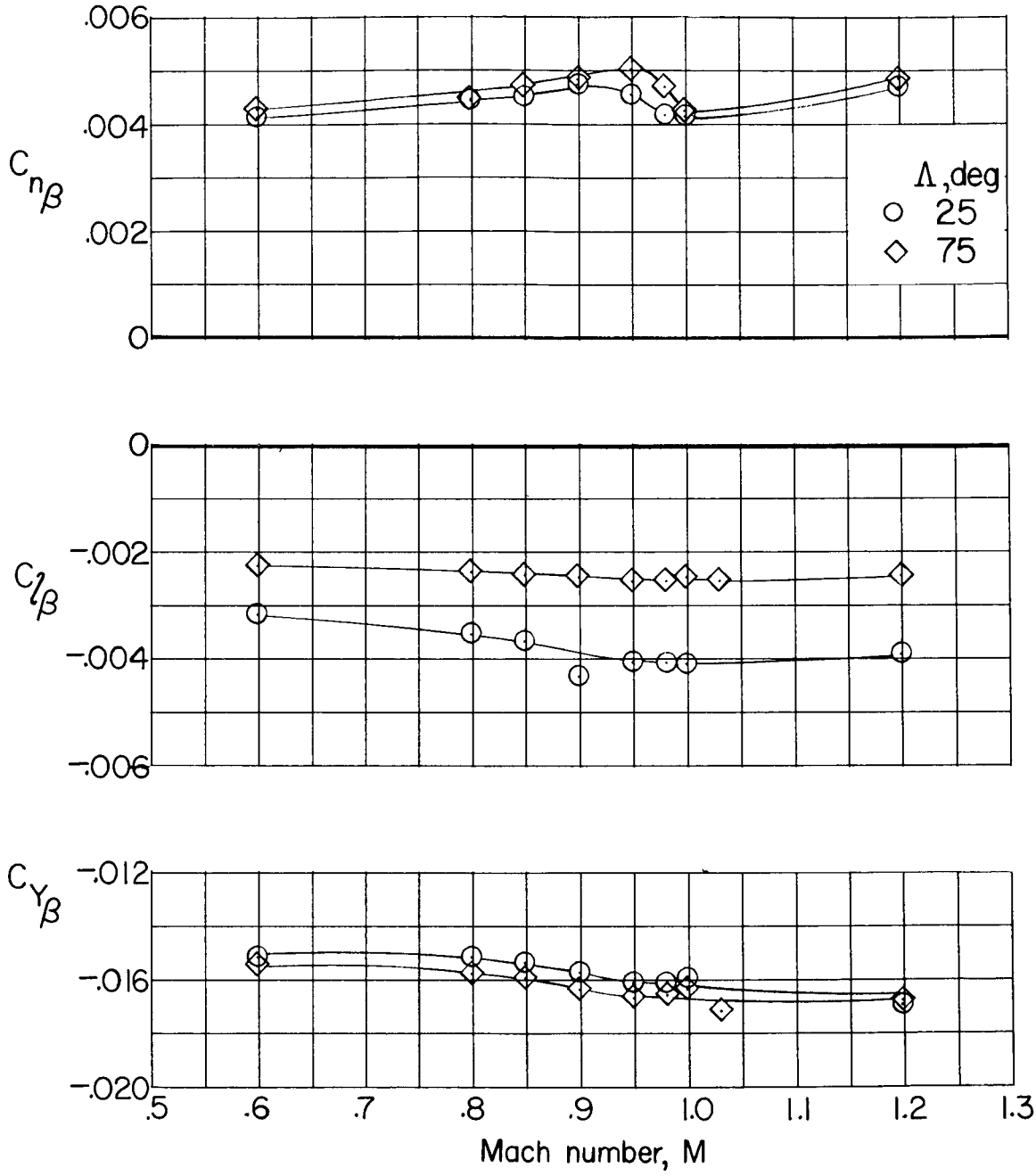

(b) C_{n_β}, C_{l_β}, and C_{Y_β} against M; $\alpha = 0^\circ$.

Figure 32.- Concluded.

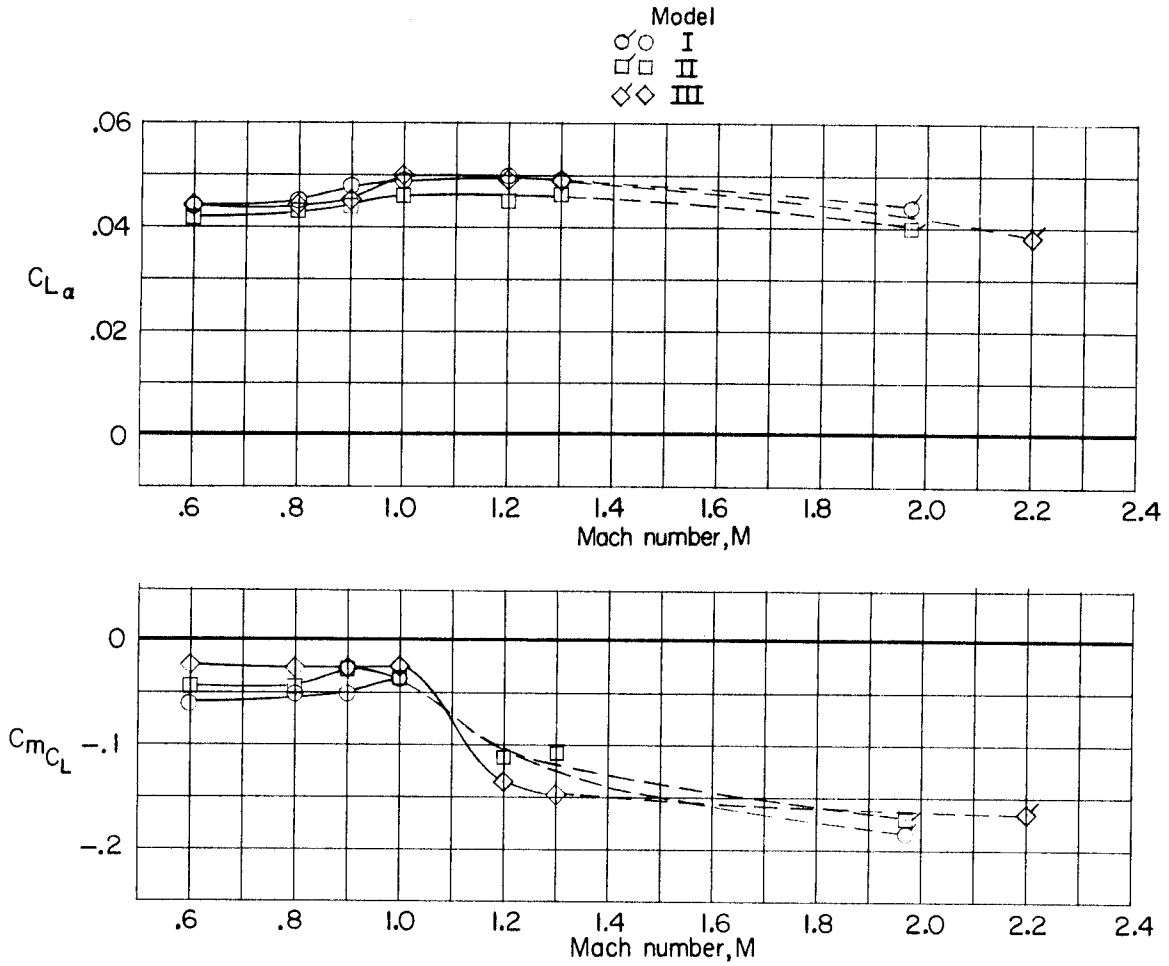

(a) C_{L_α} and $C_{m_{C_L}}$ against M.

Figure 33.- Comparison of performance and longitudinal stability of models I, II, and III with 75° swept wing. Configuration BW_3VH; $\delta_h = 0°$. (Flagged symbols indicate data points from refs. 10 and 11.)

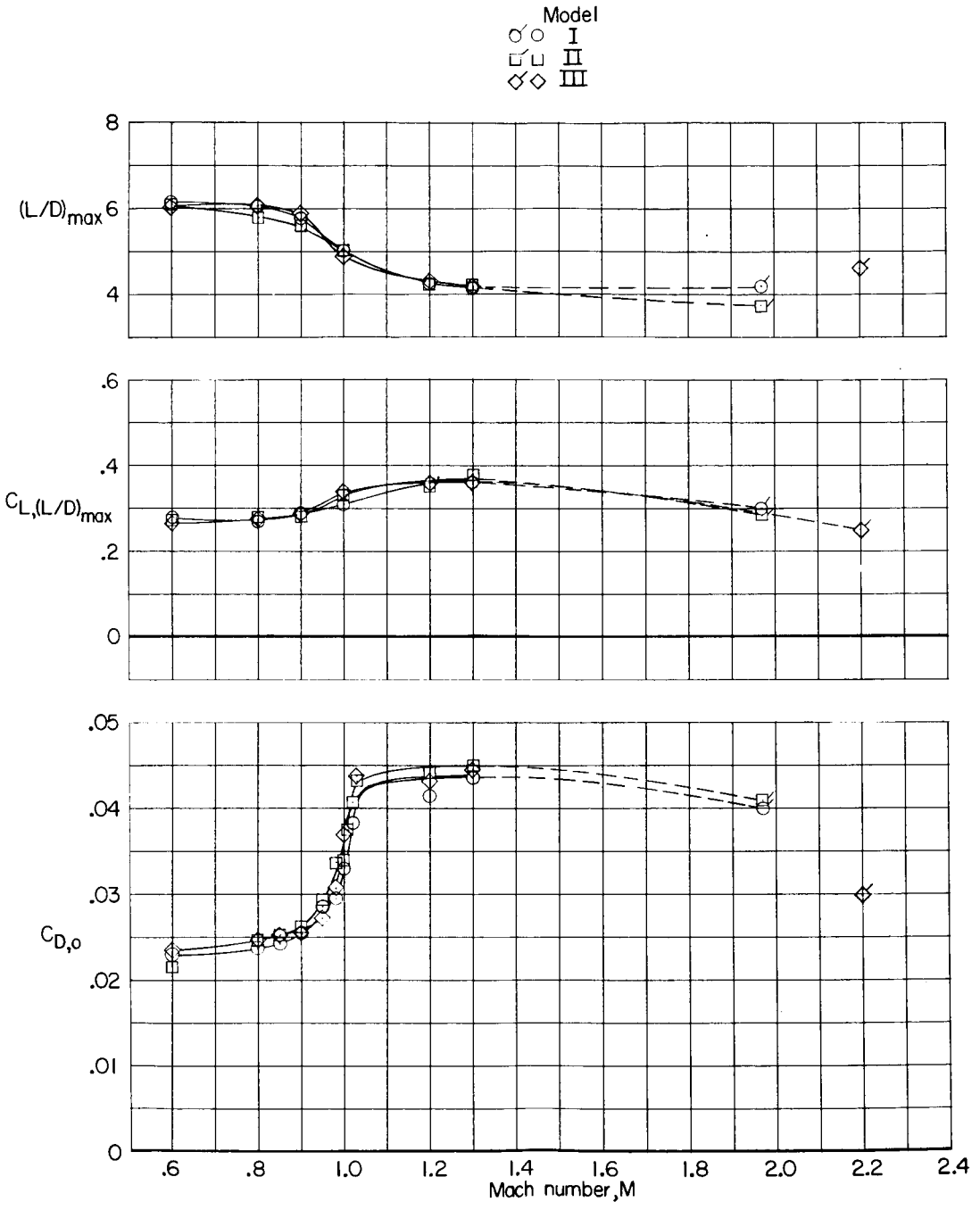

(b) $(L/D)_{max}$, $C_{L,(L/D)_{max}}$, and $C_{D,o}$ against M.

Figure 33.- Concluded.